The scaling of strong field interactions with wavelength

by

Derrek Joseph Wilson

B.S., University of Arkansas, Fayetteville, Arkansas, 2012

AN ABSTRACT OF A DISSERTATION

submitted in partial fulfillment of the
requirements for the degree

DOCTOR OF PHILOSOPHY

Department of Physics
College of Arts and Sciences

KANSAS STATE UNIVERSITY
Manhattan, Kansas

2018

Abstract

Ultrafast laser systems (pulse durations ∼10-100 femtoseconds) allow for the practical production of intense fields ($\geq 10^{14}$ W/cm^2) in a table-top, laboratory setup. The development of this technology has opened the door to studying the interaction of intense laser fields with atoms, molecules, and solid media. These experiments revealed a wealth of dynamics and interplay between the field, ion, and the freed electron, which has led to the production of first attosecond pulses and opened the field of attosecond science.

The dynamics of the electron in an intense laser field are fundamental to strong-field phenomena such as higher-order harmonic generation, high energy above threshold ionization, and non-sequential double ionization. As the electron can be strongly accelerated by the instantaneous field, the dynamics depend on both the field's amplitude and wavelength. The latter dependence comes from the fact that the period of the field increases with wavelength. Thus, the electron is accelerated for a longer time and the energy gained is proportional to the wavelength squared. Recent evidence supports the claim that the electron-field interaction at longer wavelengths must include the contribution of the magnetic field and/or the radiation pressure of the field, adding to the wealth of effects associated with strong-field interactions.

This thesis explores several routes towards fulfilling gaps in our understanding of the wavelength-scaling of strong-field interactions. I first demonstrate several important developments that reduce the complexity of generating non-sinusoidal, light transient waveforms in the near-infrared, opening the ability to tailor waveforms for more control on strong-field interactions.

Next, I demonstrate the development of a strong-field, femtosecond source at wavelengths from 5 μm to 9 μm. To date, this is the first few-cycle, strong-field ($\geq 10^{13}$ W/cm^2) source in the long-wave infrared. An important advantage to this design is the wavelength tunability,

which provides a control knob for understanding strong-field interactions across a broad wavelength range.

Afterwards, I present applications of wavelength tunable sources in strong-field absorption in semiconductors. Specifically, I measure the absorbance of a strong laser field in gallium arsenide as a function of laser polarization, which varies the density of states available to the electron. This is performed for four laser wavelengths spanning 1.2 μm to 2.4 μm. With these absorbance measurements, we can compare the dependence of the photoexcitation rate on several parameters and compare it to theory. We find that the change in absorbance with density of states deviates from theoretical predictions as the photon order for the photoexcitation increases from two to three. This could be attributed to the field modifying the energy-momentum relationship of the conduction band.

To conclude the thesis, I present simulations on a recent experimentally demonstrated technique for amplifying few-cycle electric fields. Due to the difficulty in making these sources, the model I developed includes many of the parameters involved in designing the system. This simulation can be used to plan design criteria, such as nonlinear crystal thickness, for peak performance of the amplification process.

The scaling of strong field interactions with wavelength

by

Derrek Joseph Wilson

B.S., University of Arkansas, Fayetteville, Arkansas, 2012

A DISSERTATION

submitted in partial fulfillment of the
requirements for the degree

DOCTOR OF PHILOSOPHY

Department of Physics
College of Arts and Sciences

KANSAS STATE UNIVERSITY
Manhattan, Kansas

2018

Approved by:

Co-Major Professor
Artem Rudenko

Approved by:

Co-Major Professor
Carlos Trallero-Herrero

Copyright

Abstract

Ultrafast laser systems (pulse durations ∼10-100 femtoseconds) allow for the practical production of intense fields ($\geq 10^{14}$ W/cm^2) in a table-top, laboratory setup. The development of this technology has opened the door to studying the interaction of intense laser fields with atoms, molecules, and solid media. These experiments revealed a wealth of dynamics and interplay between the field, ion, and the freed electron, which has led to the production of first attosecond pulses and opened the field of attosecond science.

The dynamics of the electron in an intense laser field are fundamental to strong-field phenomena such as higher-order harmonic generation, high energy above threshold ionization, and non-sequential double ionization. As the electron can be strongly accelerated by the instantaneous field, the dynamics depend on both the field's amplitude and wavelength. The latter dependence comes from the fact that the period of the field increases with wavelength. Thus, the electron is accelerated for a longer time and the energy gained is proportional to the wavelength squared. Recent evidence supports the claim that the electron-field interaction at longer wavelengths must include the contribution of the magnetic field and/or the radiation pressure of the field, adding to the wealth of effects associated with strong-field interactions.

This thesis explores several routes towards fulfilling gaps in our understanding of the wavelength-scaling of strong-field interactions. I first demonstrate several important developments that reduce the complexity of generating non-sinusoidal, light transient waveforms in the near-infrared, opening the ability to tailor waveforms for more control on strong-field interactions.

Next, I demonstrate the development of a strong-field, femtosecond source at wavelengths from 5 μm to 9 μm. To date, this is the first few-cycle, strong-field ($\geq 10^{13}$ W/cm^2) source in the long-wave infrared. An important advantage to this design is the wavelength tunability,

which provides a control knob for understanding strong-field interactions across a broad wavelength range.

Afterwards, I present applications of wavelength tunable sources in strong-field absorption in semiconductors. Specifically, I measure the absorbance of a strong laser field in gallium arsenide as a function of laser polarization, which varies the density of states available to the electron. This is performed for four laser wavelengths spanning 1.2 μm to 2.4 μm. With these absorbance measurements, we can compare the dependence of the photoexcitation rate on several parameters and compare it to theory. We find that the change in absorbance with density of states deviates from theoretical predictions as the photon order for the photoexcitation increases from two to three. This could be attributed to the field modifying the energy-momentum relationship of the conduction band.

To conclude the thesis, I present simulations on a recent experimentally demonstrated technique for amplifying few-cycle electric fields. Due to the difficulty in making these sources, the model I developed includes many of the parameters involved in designing the system. This simulation can be used to plan design criteria, such as nonlinear crystal thickness, for peak performance of the amplification process.

Table of Contents

List of Figures

List of Tables

Acknowledgments

There are numerous people who I must acknowledge for their help, kindness, and belief in my desire to get me to this point. My parents, Dennis and Joan Wilson, have always raised me to believe in being rewarded for hard work, and to cherish the satisfaction that comes from it. My sister, Jeanette Turley, started teaching me the alphabet when I was three days old; I must have received a knack for learning at a young age.

Julie Potter and Mike Brown were my English teachers in high school, and their ability to teach me more about life and humanity than was ever found in a text book is something I will always keep with me. I would have never learned to love physics if it weren't for a fantastically orchestrated summer class I serendipitously took at Pittsburg State University with Dr. David Kuehn. My undergraduate research advisor, Dr. Surendra Singh, pushed me to be a scientist who does their thinking for themselves and tries new things when old things don't work well. Dr. Brian Washburn has always offered words of encouragement when graduate school was getting too difficult. Adam Summers, my lab partner, has always been a great colleague and none of this work would have happened without his involvement.

My advisor, Dr. Carlos Trallero-Herrero, has been a great person to work with. His group management allowed me to explore research without restraint and, while it wasn't always successful, I was always learning new things. Carlos was a great listener and placed the well-being of his students first, while always pushing us to be our best.

Finally, I want to thank the National Science Foundation for their support through the NSF graduate research fellowship under grant number DGE-1247193. Also, the HITS laser was mainly financed by NSF-MRI grant No:1229672, with additional contributions from DOD-DURIP grant No. FA2386-12-1-3014 and DOE grant No. DE-FG02- 86ER13491. Operational cost of the laser as well as additional support for myself was provided by the Chemical Sciences, Geosciences, and Biosciences Division, Office of Basic Energy Sciences, Office of Science, U.S. Department of Energy (DOE) under Grant No. DE-FG02-86ER13491.

Dedication

A prayer to Lh'Asor, the God of Lasers.

ead us from the darkness, O my Lord. Fill our hearts with coherence, so we may walk your collimated path.

Lord of Light,
you are the fluorescence of our crystal,
the fire on our beam cards,
the burn marks on our walls.

ours is the photon that warms our hearts,
yours the mirror that guides us when
lasing is swallowed by darkness.

Defend us, Lh'Asor,
for the lab is dark and full of terrors.

Preface

This is what I mean. If unmolested, upon rising to the surface, the sperm whale will continue there for a period of time exactly uniform with all his other unmolested risings. Say he stays eleven minutes, and jets seventy times, that is, respires his seventy breaths over and over again, to a minute. Now, if after he fetches a few breaths you alarm him, so that he sounds, he will be always dodging up again to make good his regular allowance of air. And not till those seventy breaths are told, will he finally go down to stay his full term below ...

In man, breathing is incessantly going on - one breath only serving for two or three pulsations; so that whatever other business he has to attend to, waking or sleeping, breathe he must, or die he will. But the sperm whale only breathes about one-seventh or Sunday of his time.

Herman Melville, *Moby-Dick*, chapter 85

Herman Melville's famous novel has been recognized as a classic of American literature. The novel itself is more metaphor than plot, and could almost be used as much as a manual for understanding the mid 19^{th} century whaling industry as it is for literary entertainment. Thus, for every moment of excitement and suspense, there are chapters of details, explanations, and analogies. For this reason, the above passage is often considered a metaphor for Melville's writing style.

My personal experience has found this passage revealing of the scientific process. A scientist's ventures are often long and arduous, requiring us to look far into the future for our rewards. We may spend months or possibly years attempting a measurement, scanning the literature, and improving our technique, before we reach a moment of success. And just when we find this moment, it can be months again before we grasp the implications of our

results. It is only in that brief moment, the "Sunday", as Melville describes, when we have understood our discovery that we feel a moment to breathe.

A personal example of this analogy is the results presented in chapter 6. A young, less disciplined, version of myself saw this project in 2014 as a simple "send the laser beams through the crystal" and "focus the outcome in a gas chamber". It was two years before the latter part of that statement was attempted and even then, it was another 18 months before it was successful. I can say that I spent most of my time in graduate school failing before I got it right. And while it was arduous at the time, I am happy that I spent my "full term below" the surface.

While the moment of clarity, the breath taken above the ocean, is rewarding, it is important as scientists to remind ourselves that what we live for is that "full term below" the surface. In fact, this is the time where science lives. For these moments breed determination and understanding our work from new perspectives, helping us not just through the next interval, but for decades into the future.

This thesis is one of these risings, a moment to contemplate an arduous journey and broadcast the work I have performed to this point in my career. My aim with this work is to provide a clear conclusion to a challenging yet fruitful term. I plan to provide background and summaries for most of the projects I have undertaken as a graduate student, as well as provide a brief outlook on where several of these projects will continue. As I move forward into my next term, and a new generation of students begin theirs, it is my hope this document is a foundation for them to build upon.

Chapter 1

Introduction

The pursuit of understanding interactions between matter and light has been of great interest since Greek philosophers, such Aristotle and Ptolemy, theorized the physical phenomenon responsible for vision[1]. While the forerunners of the classical Greek period had yet to achieve the scientific scrutiny developed during the Enlightenment, their approaches to the subject centered on the interaction of light with the eye. During this same time, Euclid's book *Optics*, is the first recorded attempt at describing the law of reflection, and relies on postulates based on the interaction of light with reflective surfaces[2]. After the first millennium A.D., when the Arabic empire was at its height, Ibn al-Haitham wrote *The Book of Optics* where he described the law of refraction at the interface of two media[3]. From these few works, and amongst numerous others that could be included here, we conclude that when we seek to understand light, we equivalently seek to understand how light interacts with its surroundings. Despite the millennia that have passed, it remains a grand challenge in science to put light-matter interactions into new conditions that further our understanding of their nature.

To consider the importance of how light and matter interact with one another, let's consider the role of the wavelength of light involved. Figure 1.1 shows a human hand and with various materials in different wavelength regimes. Figure 1.1a shows a germanium window, a semi-metal, in front of the hand in the visible region of light (400 nm - 700

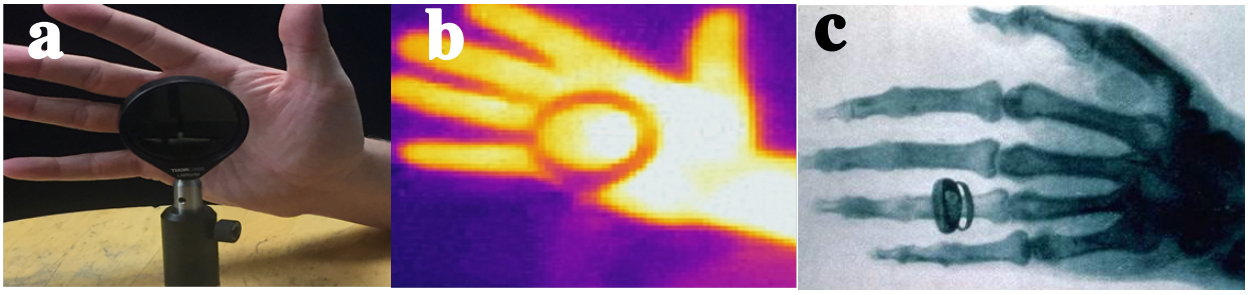

Figure 1.1: Matter's response to light is sensitive to the wavelength being used. **a** A human hand and a window of germanium held in an optical mount, illuminated under visible (400 nm-700 nm) light. The illumination shows that all materials present in this picture reflect visible radiation. **b** The same hand and window but viewed in the long wave infrared (8-15 μm). The clear difference from **a** is that, in this wavelength region, the hand is illuminating the surroundings and the germanium plate is transparent. **c** A hand with a metallic ring illuminated with X-rays. Here, the hand's flesh is now completely transparent. (Figure 1.1c Photo credit: Willam Röntgen 1896).

nm). As this range of wavelengths is familiar to our eyes, we see nothing unusual and the germanium window behaves as a metallic mirror. However, in figure 1.1b, which shows the hand and germanium in the long-wave infrared (LWIR, 8-15 μm), their behavior is completely different. The human body has a temperature of roughly 37 Celsius (99 Fahrenheit) which, according to the theory of black body radiation[1], necessitates that it naturally emits light at a wavelength of roughly 10 μm. Moreover, we see that the palm and wrist are much brighter than the fingers, indicating that they are emitting more light and hence, warmer. In addition, while the Germanium window behaved as a mirror in the visible, it acts like a dielectric in the LWIR, as it is transparent to the light emitted by the hand. On the other side of the spectrum, figure 1.1c shows the effect of imaging a hand with a metallic ring in the X-ray region. This time, the flesh of the hand is transparent, allowing us to produce a clear image of the bones. Because of this, the ring seemingly "floats" around the ring finger, which is largely opaque to the X-rays.

We see that, even under these very simple scenarios, the wavelength we choose to study matter with has a profound effect on what we will uncover about the system. It is interesting

[1]This is the same effect responsible for the sun's light emission, though because the sun is much hotter, the wavelength is much shorter.

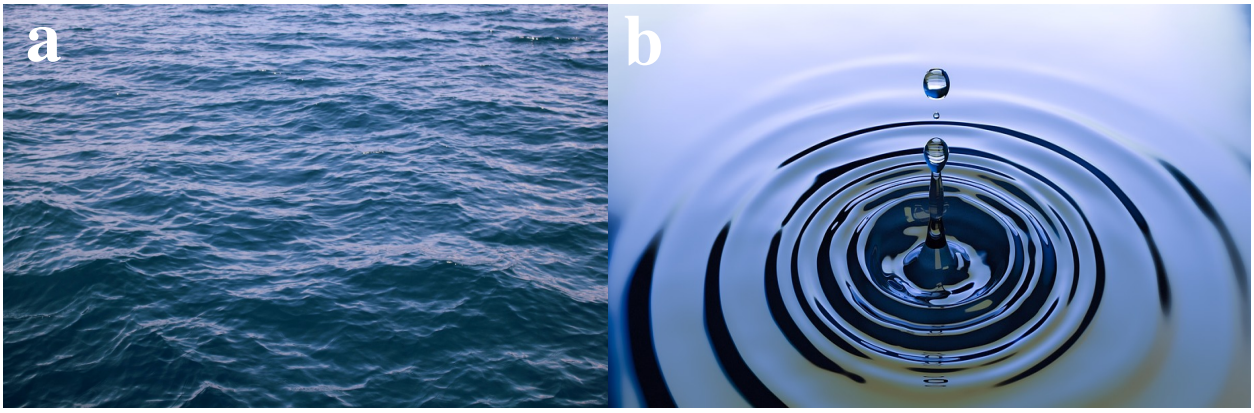

Figure 1.2: ***a*** Typically, waves emanating from lamps and other sources have a stochastic nature to the radiation, as exemplified by the nature of waves created on the surface of a lake or sea **b** When a wave is generated in a controlled manner, as shown here, we see that it has a highly reproducible nature and well defined properties. (Both images in this figure are released free of copyrights under Creative Commons CC0.)

to note that while each wavelength provides insight into the composition and behavior of the system, the incorporation of all these studies provides us with a much deeper understanding than any individual photograph. Thus, we can conclude that we learn more from nature when studying light-matter interactions across a large range of wavelengths rather than confining our experiments to a limited range.

While ambient light provides us some understanding of nature, much more precise measurements can be made when light has well defined properties. In figure 1.2a, we see an example of waves with stochastic properties. Here, the waves are sourced from many locations: e.g. wind, reflections from the shore line, amongst others, resulting in a random pattern that is generally weak and hard to predict. This is similar to the ambient light sources we use in our daily lives, such as light bulbs. On the other hand, figure 1.2b, shows a wave generated from a single source, perhaps a rock dropped in a pool. In this case, their is a well defined wave front, velocity, and amplitude. These waves are closer in resemblance to what is produced from a laser.

When light sources have well defined field characteristics, they can give a clearer measurement of matter's response. For instance, when light is made with a highly confined frequency, known as a "monochromatic" field, the frequency can be used to measure time.

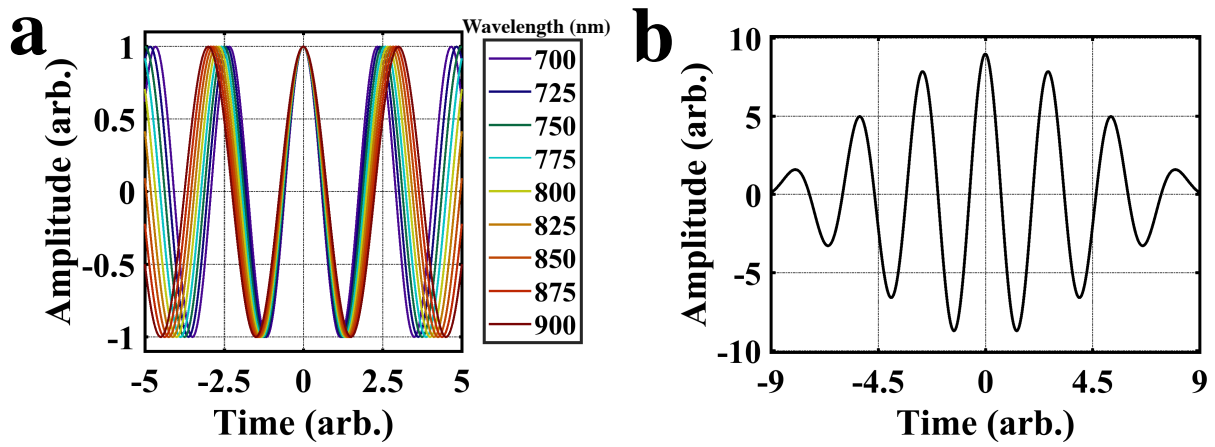

Figure 1.3: **a** Frequencies of light from 700 nm - 900 nm where all frequencies have a peak amplitude at $t = 0$ fs. As we move further from the center, the individual frequencies begin to destructively interfere due to the difference in their periods. **b** When the frequencies in part **a** are summed into a single field, as shown here, their constructive and detractive interference produces a single pulse of light.

Just as a pendulum in a clock could infinitely keep time if its frequency never changed, the light field of a truly, single frequency field, never deviates. Unlike the pendulum, light waves are responsible for the most precise measurements of time, with the current record standing at 1 part in 10^{19} seconds[4].

Another way to study matter is with light waves made up of a substantial number of frequency components. In this case, we must consider an additional property of waves concerning the nature in which they overlap, known as superposition. This is illustrated in figure 1.3, where several fields with unique frequencies in figure 1.3a are summed together to produce a new field, shown in figure 1.3b. When this is done with millions of waves with neighboring wavelengths, we find that they produce a much stronger amplitude for several neighboring crests and troughs, but further away, they destructively interfere. Thus, when all the fields are overlapped for maximum amplitude at a given crest or trough, we can say they are *in phase*.

This pulsed nature of a light wave has offered a substantial contribution to our understanding of matter. These days, light can be pulsed to as short as several tens of attoseconds ($1 \text{ as} = 10^{-18}$ s). To consider how short of an amount of time one attosecond is, consider that

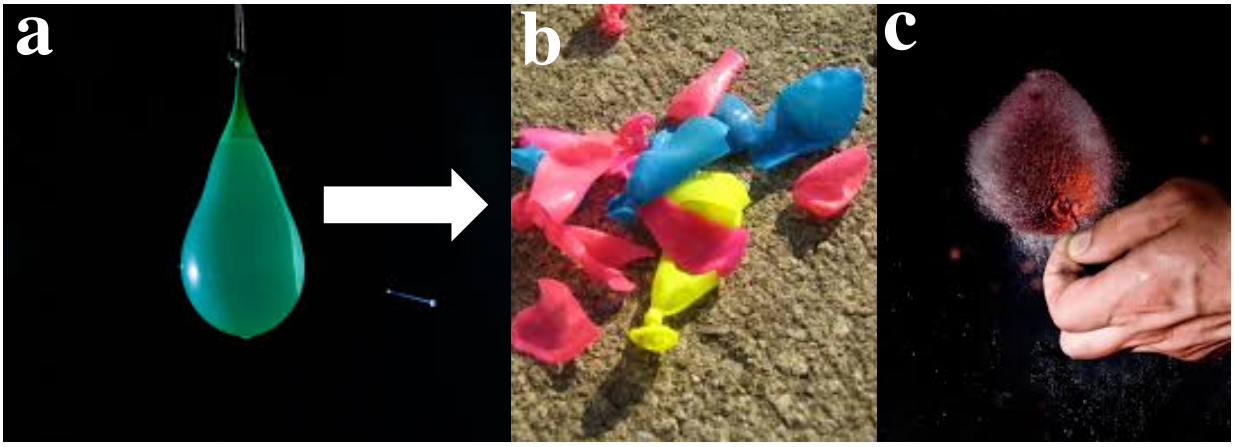

Figure 1.4: **a** With low timing resolution, we will only see the initial and final states of some fast event, such as the popping of the water balloon shown here. **b** When we increase the timing resolution, as with a high speed camera, the dynamics of the event are clearly visible. Having tools with the resolution to capture fast events allows us to understand how their nature, (Images in this figure are released free of copyrights under Creative Commons CC0.)

there is one billion nanoseconds in a singe second, which seems like a lot to my imagination. But one nanosecond is composed of one billion attoseconds, so an attosecond is a very short amount of time!

These short pulses can be used to understand how matter responds in time to some stimulus. A simple way to think of this is to consider the pulse as a high speed camera. A typical camera takes 16 or perhaps 32, images every second. If something happens faster than that, it will simply appear as a blur and we will only see the initial and final states of the event. This is illustrated in figure 1.4a, where we see a needle directed at a water ballon. With the unaided eye the balloon will pop "instantaneously" and we will only see broken remnants of the balloon, as shown in figure 1.4b. With a very high speed cameras, on the other hand, we can take over a thousand images in a second, revealing dynamics that are not visible to the naked eye. In figure 1.4c, the camera is capable of showing the dynamics of the balloon as it disintegrates, and reveals much more about the event than a standard camera could. In our case, the laser pulse gives us information about the dynamics in a window of time specified by its duration. A shorter pulse acts as a "faster"[2] camera and allows us to

[2]The term "ultrafast" science refers to the discipline of using short pulses to study light-matter interactions

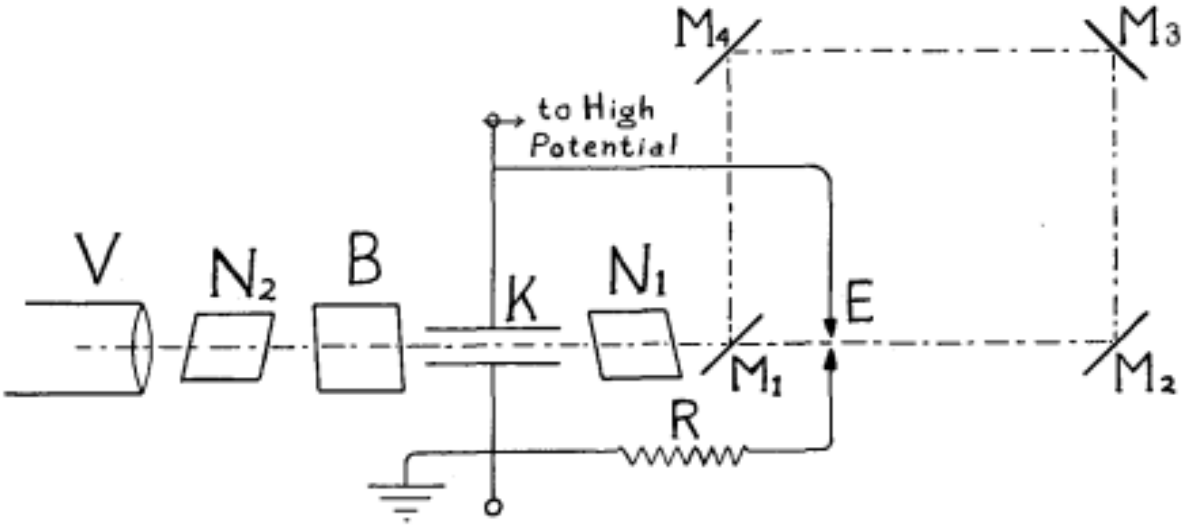

Figure 1.5: Layout for the first ultrafast measurement using pulsed light. E - gap between wires, produces flash, M_i - the i^{th} mirror guiding the pulse, R - resistor, N_i - polarizer, K - Kerr cell, B - Double image polarizing prism, V - observation viewport. Reproduced from [5].

reveal dynamics occurring on shorter time scales.

The first demonstration of measuring material dynamics in time with pulsed light fields was performed in 1899 by Abraham and Lemoine[6], and their setup is shown in figure 1.5. At the time, scientists were studying the Kerr effect, a property of some materials where birefringence is formed by applying a DC field to the material. Where some materials, such as glass, required several seconds for the Kerr effect to build up, liquids, like CS_2, typically had no visible build up time. They designed an experiment, shown in figure 1.5, so that a pulsed light field, generated by an arc from two wires held closely together (labeled "E" in the diagram), is synchronized with moment the DC field is shut off on Kerr cell (K). A set a mirrors (M_1-M_4) guide the pulsed light field into K, allowing for an increase or decrease in the distance it travels before entering the material. Time and distance are related by

$$t = d/c, \tag{1.1}$$

in time. It can become a bit of a misnomer, however, as it is often used to describe the pulses themselves, which are no faster than ordinary light. However, the dynamics uncovered by an "ultrashort" pulse are certainly "ultrafast".

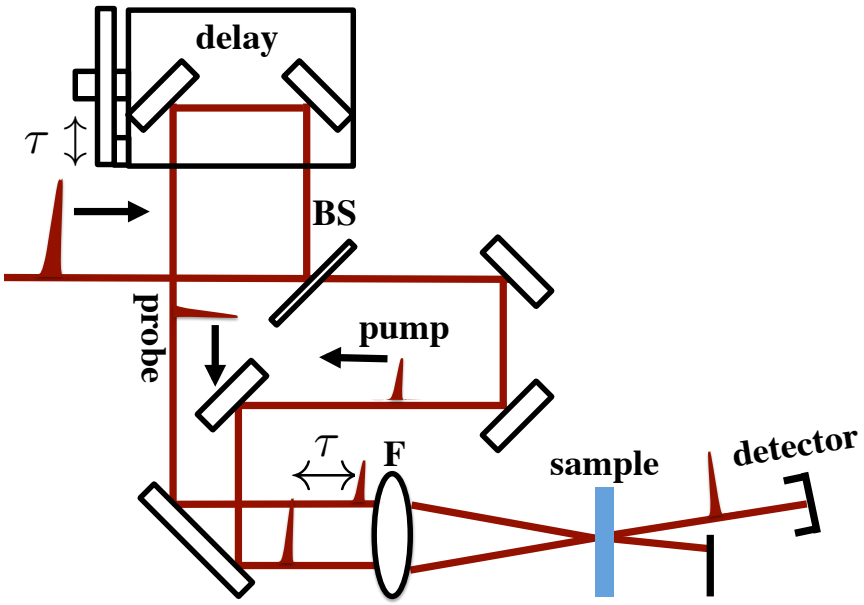

Figure 1.6: One example of a non-collinear layout for a pump probe experiment. In this case, the laser pulse is split into two arms. One arm, the pump, excites the sample. The second pulse is scanned in time with respect to the probe using a set of mirrors on a translational stage. After observing the sample at time τ, the probe can be measured with a detector. BS - beam splitter, τ - delay, F - focusing lens.

where t is the time, d is the distance traveled by the light pulse, and c is the speed of light, which is approximately $2.9979 \cdot 10^8$ meters per second. Because E and K are synchronized, changing d for the mirror path allows the pulsed light to sample K at a different point in time. With this, they were able to determine that the Kerr effect in CS_2 dissipates on a timescale of 10 nanoseconds or less! Later, when lasers were invented, it was realized that the response was in the picosecond regime, as they were actually measuring the width of the pulse generated from the spark. Still, it is rather amazing to realize that measuring dynamics to the precision of a nanosecond has been possible for well over a century. We could argue that, with this experiment, the field of "ultrafast" science was born.

Still, ultrafast science did not see its breakthrough until the invention of the laser in 1960[7]. As lasers produce not only energetic, coherent radiation, but deliver it in a highly confined direction, they have become the principle tool for ultrafast experimental studies. It wasn't long after their invention that lasers could be pulsed to picosecond (10^{-12} s)[8] and

even femtosecond (10^{-15} s) durations[9]. They were immediately put to use in experimental studies and used in a technique later known as "pump-probe", shown in figure 1.6. This method uses two pulses, one to initiate the dynamics (pump) and the second to sample the matter's reaction at different points in time (probe). When pulses reached the femtosecond time scale, pump-probe was capable of imaging chemical reactions and dynamics. These breakthroughs gave rise to the field of "femtochemistry" and led to Ahmed Zewail being awarded the Nobel Prize in Chemistry in 1999[10].

Because femtosecond pulses are short, they can be very powerful while only having modest pulse energies. For instance, the laser I use, called the High Intensity Tunable Source, has a 25 femtosecond pulse with 20 mJ of energy in each pulse. This delivers a peak power of 0.7 Terawatts, which is more than 300 times more power than the Three Gorges Dam, the largest power station in the world, and about 10 % of the world's electrical power capacity[11]. Lasers with this magnitude of peak power can reach intensities which alter an atom, molecule, or solid material, allowing for dynamics that wouldn't occur with weaker fields. For instance, the Coulomb potential of the atomic nucleus' can be suppressed, liberating the electron and allowing it to accelerate in the electric field of the laser. These dynamics are responsible for several exciting phenomena, including the production of highly energetic, pulsed electrons, and attosecond pulses through the process of higher-order harmonic generation (HHG)[12].

It is in the region of ultrashort, "strong-field" science that I will explore light-matter interactions in this thesis. In particular, a large part of this work is dedicated to providing light-source technology that can extend strong-field experimental studies into new wavelength regimes. In particular, the basis of much of this work requires the development of a state-of-the-art Terawatt class laser, which is described in chapter 4. Afterward, in chapter 5, I will cover the development of a new method for producing non-sinusoidal, light-transient waveforms. This method takes a technique that has been successfully applied towards visible and UV waveforms, and applies it toward generating similar waveforms in the NIR, which has a number of advantages for strong-field science.

In chapter 6 I will discuss the development of a new light source capable of studying strong-field science in the long-wave infrared (LWIR, $8-15$ μm). This source has the added

benefit of being tunable across an octave of central wavelengths spanning the 5 μm to 9 μm range while maintaining pulses possessing only a few oscillations of the electric field. We demonstrate the usefulness of this source for strong-field science by performing ionization experiments on xenon gas across its entire wavelength range.

Afterwards, we will look into applications of strong laser fields by studying the wavelength-scaled nature of the strong-field photoexcitation in semiconductors in chapter 7. By varying the wavelength, the intensity, and the density of states that the electron experiences, we can study the dependence of photoexcitation on these three essential parameters. We find there is a dependence on photon order that is not described by traditional calculations, and could arise from the inclusion of a better description of the electron's dispersion properties.

To conclude the thesis, I will then provide an outlook on the future of my research in chapter 8 based on the work shown in previous chapters. In particular, my motivation for developing novel laser sources using nonlinear optics has prompted me to research a new light amplification technique which has a number of advantages over the state-of-the-art methods. Due to the complex nature of this system, I have developed a primitive method of modeling the nonlinear optical setup as a means to optimize the conversion efficiency and tailor the system to a desired outcome.

Before digging into the results discussed in this thesis, I will take some time to provide background for those who are unfamiliar with certain aspects of this work. In particular, I want to emphasize phenomena that are relevant for guiding the results as they are currently formulated. In chapter 2, I will describe various details of strong-field interactions in atoms, molecules[3] and solids. In particular, I will cover the essential mechanisms for photoionization (photoexcitaion) in atoms (solids). I will also cover the essentials of solid structure, and properties of a solid that are required to understand how it interacts with a strong laser field. Finally I will offer a comparison on the similarities and differences of these interactions between solids and atoms/molecules.

Afterwards, I will discuss the relevant topics of ultrafast optics in chapter 3. I will cover the construction of an ultrashort pulse and methods of characterizing the electric field. Then

[3]Most of the discussion is focused on atoms, and not molecules, but there is much overlap.

I will discuss nonlinear optics and the techniques that are used to make new wavelengths using difference frequency generation. Finally, I will conclude with an overview of self-phase modulation and its application to few-cycle pulse generation.

Chapter 2

Strong-field interactions with matter

This chapter introduces the interaction of strong laser fields with various media.

2.1 Atoms and Molecules

The first theoretical work on the ionization of atoms and molecules where the photon's energy falls below the ionization threshold was performed by Maria Goeppert-Mayer in 1931 [13]. She treated the field as a perturbation with respect to the Coulomb potential, $V(\mathbf{r})$, which is given by

$$V(\mathbf{r}) = -\frac{1}{4\pi\epsilon_0}\frac{e}{|\mathbf{r}|} \tag{2.1}$$

where e is the charge of the electron and ion (as experienced by the highest bound electron), ϵ_0 is the permittivity of free space, and $|\mathbf{r}|$ is the distance between the electron and core. This is represented in figure 2.1. Specifically, for the case where two photons are absorbed, Goeppert-Mayer showed that the absorption rate was proportional to E_0^2, where E_0 is the strength of the field. The general case for multi-photon absorption, where n photons are required, is found to be proportional to I_0^n.

However, as the field strength increases, we can no longer treat it as a perturbation, as

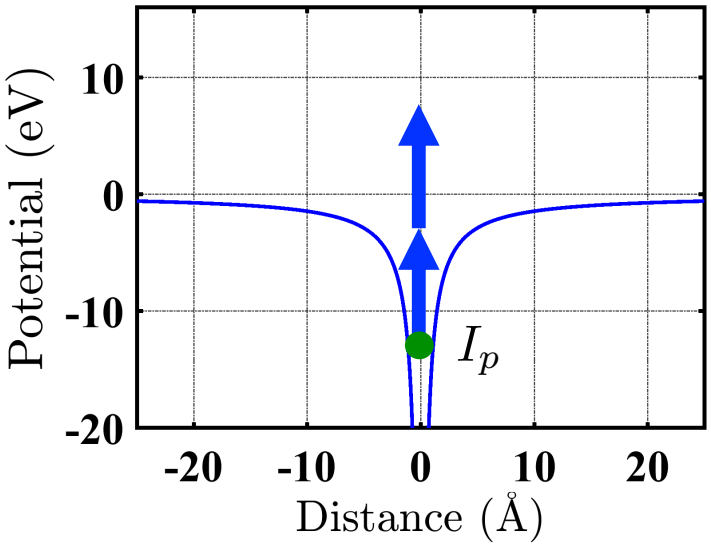

Figure 2.1: The Coulomb potential, with an electron (green) residing at a depth I_p. The two blue arrows indicate photons from a field with their height indicating their energy. Since each has an energy less than I_p, one photon is not enough for the electron to be freed. Instead, the electron can be freed from the Coulomb well by absorbing two photons.

it will begin to impart a large contribution to the total potential. As this is the regime strong-field science deals with, we require a more complete picture of the system if we want to understand the experimental outcomes. To start, let's simplify things by considering the case when the wavelength of the field, $E(t)$, is much larger than the atomic dimension ($\approx$Å).[1] Using the length gauge we can invoke the dipole approximation [13], and the potential due to the field is

$$V_E(\mathbf{r}) = \mathbf{E}(t) \cdot \mathbf{r}. \tag{2.2}$$

Then the total potential becomes

$$V_T(\mathbf{r}) = V_E(\mathbf{r}) + V(\mathbf{r}). \tag{2.3}$$

[1] We also need to keep in mind that excluding contributions from the magnetic field puts a limit on the maximum intensity and wavelength, which have a somewhat complicated interdependence that are discussed elsewhere. [14]

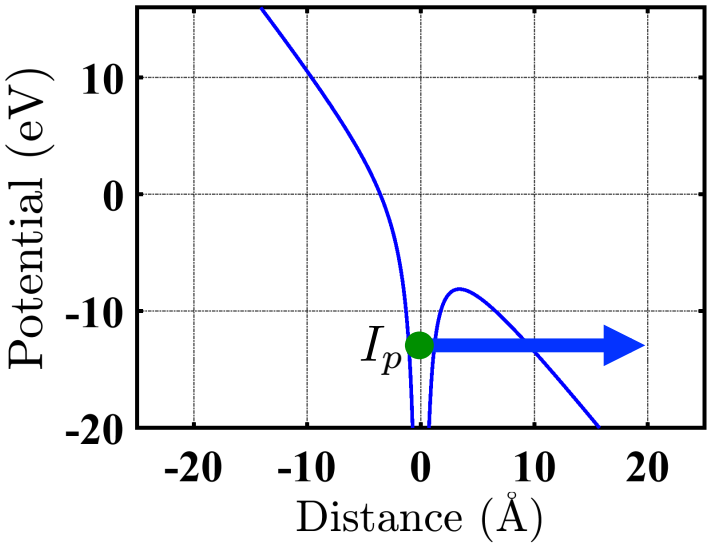

Figure 2.2: The full potential for an electron (green) residing at a depth I_p in a Coulomb well under the influence of a strong, slowly oscillating, laser field. In this case, the Coulomb well is distorted strongly enough that the electron can be freed via tunneling, indicated by the path shown on the blue arrow.

If we have a linearly polarized laser field, then many processes can be approximated as one dimensional so that $\mathbf{r} \to r$, $\mathbf{E}(t) = E_0 \cos(\omega t)\hat{\mathbf{x}}$. This case is shown in figure 2.2. Here we see that ionization can be performed by the electron tunneling through the now distorted Coulomb well and into the continuum, where it is primarily under the influence of the laser field. The case for tunneling under the influence of a DC field was solved in the early days of the laser and is found to have a rate $\propto \exp[-1/E_0]$ so that as E_0 increases, the rate increases exponentially[15;16].

2.1.1 Ionization regimes according to Keldysh Theory

While the two cases presented in section 2.1 give us insight into the phenomenon of ionization, we need a much more complete description if we want to understand the interaction of atoms and molecules with strong laser fields. In treating the regime where ionization occurs under the influence of a strong field, we need to make some assumptions if we wish to have an analytical relation. As anyone working with quantum mechanics knows, perturbation theory

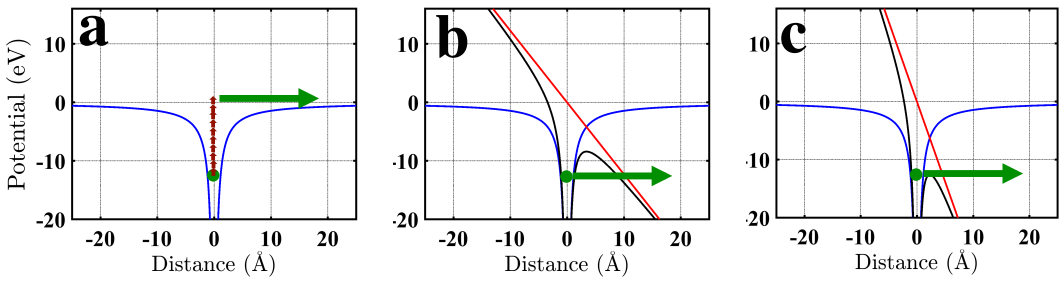

Figure 2.3: Three ionization regimes according to Keldysh **a** Multiphoton **b** Tunneling **c** Over the barrier.

is the work horse for producing reasonable calculations without resorting to the full time-dependent Schrödinger equation. However, as we just stated in the previous section, we are attempting to no longer include the field in this manner.

This conundrum is treated by tackling the problem in reverse. If we now consider a strong field, we can include it through its full form and include the Coulomb well as a perturbation. This is known as the strong field approximation (SFA), and was pioneered in the early days of the laser[17–19]. In SFA, it is useful to introduce a dimensionless parameter, γ, where[17]

$$\gamma = \sqrt{\frac{\omega^2 2 m_e I_p}{e^2 E_0^2}} = \sqrt{\frac{I_p}{2U_p}}, \tag{2.4}$$

ω is the frequency of the laser, m_e is the electron's mass, and I_p is the ionization potential, which describes how deep inside the Coulomb well the electron resides before ionization. U_p is known as the ponderomotive potential, and we will derive it and discuss its consequences in section 2.1.2.

A full derivation of the ionization rate calculation is long and many approaches are found in the literature[17–21]. However, the principle mechanisms of the calculations are shown in figure 2.3 and described in more detail in the following subsections.

Multiphoton

With strong laser fields, we can extend the two-photon picture in figure 2.1 to include many photons. In this scenario, shown in figure 2.3a, $V_E(r)$ (red) distorts the potential around the

Coulomb well (blue), as shown by $V_T(r)$ (black). Because the field is very strong, it is possible for the electron (green) to be freed by absorbing a large number of photons. However, the field is not so strong that tunneling is a dominate feature. This is seen by the fact that the tunneling length (the width of the barrier the electron needs to tunnel through) is large.

Tunneling

When we turn up the field strength, $V_T(r)$ can be bent far enough that the electron can tunnel through the barrier, as shown in figure 2.3b. This is an important regime for strong-field physics, as the electron has the possibility of interacting with the ion through recollisions, which are described later.

Over the barrier

If we continue to increase the the strength of the field, $V_E(r)$ will distort the Coulomb well enough that there is no longer a barrier between the electron and the continuum. That is, the electron can freely disperse into the continuum. This is shown in figure 2.3c.

We find that multi-photon and tunneling ionization are just two limiting cases of a continuum of ionization possibilities, where intermediate cases are a mix of both tunneling and multi-photon processes. To distinguish between the two cases, we consider the value of γ, which is $\ll 1$ in the tunneling regime and $\gg 1$ in the multi-photon.

2.1.2 The role of the electron

There are many interesting processes due to the dynamics of an electron driven by a strong-field. To start, let's determine the cycle-averaged energy gained by an electron in an AC field. To do this, we will consider the electron under the influence of simple harmonic motion with frequency ω. The force, in one dimension, then goes as

$$F(t) = eE\exp(-\mathrm{i}\omega t) = m_e a(t), \tag{2.5}$$

since this is harmonic motion, the position of the the electron $x(t)$ is easily given from the acceleration as

$$x(t) = \int \left[\int a(t)dt \right] dt = -\frac{1}{\omega^2} a(t) = -\frac{1}{\omega^2} \frac{eE}{m_e} \exp(-\mathrm{i}\omega t). \tag{2.6}$$

Then the kinetic energy gained by the electron is proportional to the time-averaged velocity squared ($\langle v(t)^2 \rangle$) and we find

$$U_p = \frac{1}{2} m_e \left\langle v(t)^2 \right\rangle = \frac{1}{2} m_e \left\langle \left(\frac{d}{dt} x(t) \right)^2 \right\rangle \tag{2.7}$$

$$= \frac{1}{2} m_e \frac{1}{2} \frac{e^2 E^2}{m_e^2 \omega^2} = \frac{1}{4} \frac{e^2 E^2}{m_e \omega^2}, \tag{2.8}$$

We can express this in terms of the intensity, I, by replacing E^2 with $2I/(\epsilon_0 c)$ where ϵ_0 is the permittivity of free space and c is the speed of light:

$$U_p = \frac{e^2}{2 m_e \epsilon_0 c} \frac{I}{\omega^2}. \tag{2.9}$$

This is known as the ponderomotive energy, and it has several important consequences which will be discussed individually.

Above threshold ionization

Freed electrons can be accelerated away from the atom, resulting in an energy spectrum known as above threshold ionization (ATI)[22]. For intensities corresponding to the multi-photon regime, these distributions result in a discreet electron energy spectra, called ATI peaks, with energy separations that are the same as the laser's photon energy. One physical picture for ATI is that, once freed from the Coloumb potential, the electron does not stop absorbing photons from the field and, hence, has energy spectra characterized by the band-width of the laser up to a cut-off energy of twice U_p[23;24]. An alternative description of ATI is stems from the laser pulse consisting of many field oscillations, and that it is the interference of the electrons from successive field cycles that result in the evenly spaced peaks[25;26].

Rescattering

For a linearly polarized field, the electron can accelerate back towards the ion core under the fields subsequent half-cycle. The field can accelerate the electron so that it gains a substantial amount of kinetic energy in the process. This energetic electron can interact with the ion core in a number of ways, which we can jointly refer to as rescattering events.

In one scenario, the electron imparts a portion of its kinetic energy to deeper bound electrons in the ion core. This can result in either leaving the ion in an excited state (known as rescattering excitation[27]) or, when the electron has gained enough energy, the removal of one or more of the deeper bound electrons in the ion core. This latter process is known as non-sequential double (multiple) ionization (NSDI)[28]. We can also observe elastic rescattering, which can produce electrons with energies much higher than the $2U_p$ cut-off given for ATI[29].

Rescattering processes have also been shown to depend strongly on the laser field's polarization[30;31]. Rescattering processes are most efficient for linearly polarization, as the field acts to drive the electron back toward to parent ion. On the other hand, elliptically polarized fields give the electron a displacement and can dramatically reduce the probability of rescattering.

Higher-order Harmonic Generation

Finally, a very important process is higher-order harmonic generation (HHG), which has been described with a semi-classical, three-step model[12]. We have already discussed the first two steps, which are the tunneling ionization by a strong laser field, and the subsequent acceleration of the electron in the field's potential.

In the third step, the electron recombines with the parent ion core, emitting a high energy photon in the process. This process can result in a harmonic plateau, which, depending on the laser wavelength, intensity, and target, delivers a spectrum spanning 10-1500 eV[32]. HHG has a cutoff law where the maximum yielded photon energy, $E_{co}^{(HHG)}$, is given by

$$E_{co}^{(HHG)} = 3.17U_p + I_p, \tag{2.10}$$

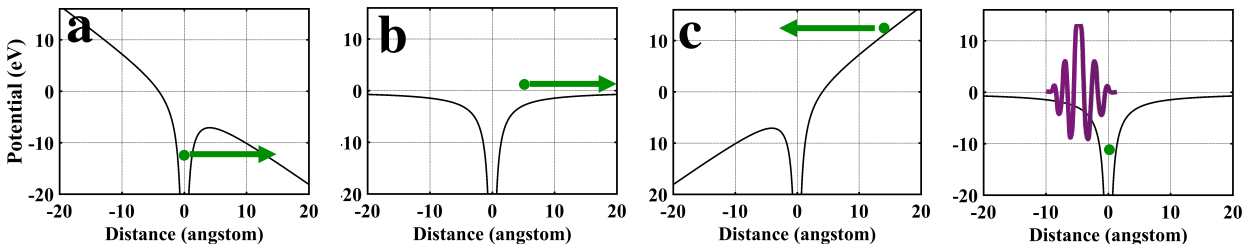

Figure 2.4: Three step model. **a** The electron (green) undergoes tunnel ionization. **b** At some later time, $E(t)$ is zero, the electron continues to move away from the ion core. **c** In the subsequent half cycle of $E(t)$, the field has the opposite sign, accelerating the electron back to the core. **d** The electron recombines, emitting a high energy photon (purple).

where I_p is the ionization potential[12;33]. The steps of HHG are shown in figure 2.4.

2.1.3 The role of the laser field's wavelength

In section 2.1.2, several important phenomena related to strong laser fields and their induced dynamics on electrons were described. Of particular interest for us are the dynamics associated with the electron's rescattering processes, as they provide ultrafast, strong-field physics with important tools. In particular, the ability of HHG to yield a plateau of harmonics spanning a broad range in the XUV and soft X-ray regions has allowed for the production of pulses with attosecond duration[34]. This is responsible for the birth of the field of attosecond physics, which utilizes techniques such as attosecond streaking[35], attosecond transient absorption spectroscopy[36], and attosecond X-ray absorption fine structure spectroscopy[32]. All these methods require HHG as a source for XUV to soft X-ray flux.

Besides HHG, a recent technique known as laser induced electron diffraction (LIED) has emerged, allowing for the imaging of molecules using rescattered electrons. Because the de Broglie wavelength for highly energetic electrons can be much less than the atomic spacings in a molecule, the rescattered electrons can be used to recover an image of the molecule after they diffract off the molecular structure. This is the essence of scanning electron microscopy[37;38]. However, because the electrons are generated and rescattered in less than a cycle of the laser field, the technique allows for attosecond timing resolution[39;40].

This unparalleled combination of spatial and timing resolution has been shown to recover molecular dynamics, such as dissociation, on these time scales.

Techniques like LIED and HHG are strongly dependent on the wavelength of the laser. While U_p increases linearly with intensity, it increases quadractically with the laser's wavelength. In both these applications, the intensity can only be increased so much before rescattering events are detrimentally affected. Thus, if high energy photons or electrons are desired, we need laser sources with much longer wavelengths.

2.2 Extension to solids

Strong-field science is not limited to atomic and molecular systems. In addition to the extensive research on plasmas etc.[41–43], the last decade has witnessed several experiments demonstrating strong laser field interactions on solid media which are closely correlated to processes described in section 2.1[44;45]. Under these conditions, there exists several analogies between the strong-field interactions of atoms and molecules with their solid counterparts. At the same time, the properties of solid materials can allow for new phenomena.

Solid materials come in numerous shapes and forms, making it difficult to classify all their properties in a unified way. For this reason, when I discuss solid media, I will limit the discussion to only bulk crystalline materials[2]. Bulk crystals have been intensively studied for over a century, making them a great candidate to bring the strong-field studies discussed in section 2.1 into a new material class.

In this section, I want to introduce a few concepts that are essential for our understanding of interactions in solids. This includes a derivation of the allowed energies in a periodic lattice and the inclusion of a strong laser field into the lattice. In the next section, I will cover several models for the photo-induced excitation rates in solids.

[2]Another class of solids, known as nanoparticles, have also become increasingly interesting in strong-field science. We will only refer to effects with macroscopic crystalline systems here.

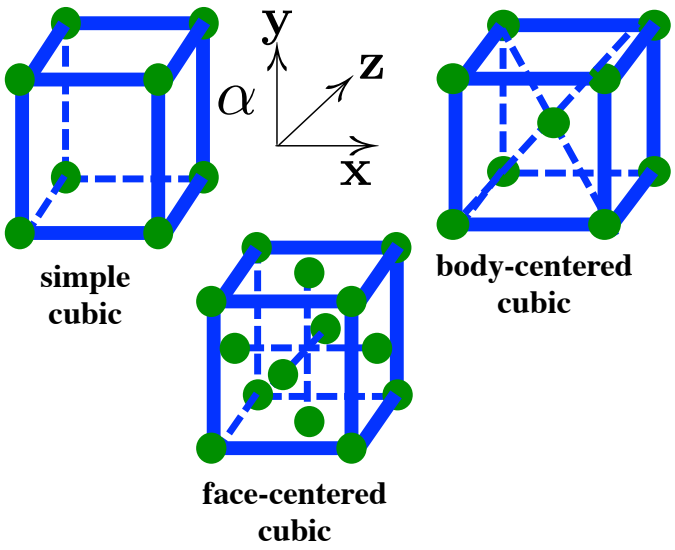

Figure 2.5: The three unit cells. On the top left is the simple cubic structure, with nuclei located on only the corners. The other two, face-centered and body-centered cubic, do not have vanity issues. Rather, their names describe the position of additional ions within the cell.

2.2.1 Solid structure

Crystalline solids consist of an infinitely repeating arrangement of atoms with a fundamental building block known as a unit cell[46;47]. The three units cells shown in figure 2.5 are simple-cubic, body-centered cubic, and face-centered cubic. The green circles represent the location of the ion while the blue lines indicate bond lengths. We can produce every crystalline structure by simply varying the bond lengths and bond angles of these three unit cells.

Solid state physics can quickly become complicated, and it is often required to perform advanced numerical computations to determine the properties of a particular crystal. However, because crystals are infinitely repeating, we can exploit their periodicity to unravel some of their generic behavior. In particular, we can find a set of vectors that indicate the position of all subsequent unit cells.

As an example, let's consider the simple-cubic lattice in figure 2.5 with a bond length α. Let's choose the origin to be, say, one of the corners of the cell, it doesn't really matter where, so long as all subsequent cells are defined the same way. Then every unit cell in the

entire lattice is defined by the following vector

$$\mathbf{R} = n_x\mathbf{x} + n_y\mathbf{y} + n_z\mathbf{z}, \tag{2.11}$$

where n_x, n_y, n_z are integers from $-\infty$ to $+\infty$, the axes are defined in figure 2.5, and the axes are of length α. This is a representation of the crystal in position, but it is often more useful to consider the lattice in reciprocal (momentum) space. We find the reciprocal lattice for the simple cubic lattice to be

$$\mathbf{G} = n_x\frac{2\pi}{\alpha}\hat{\mathbf{i}} + n_y\frac{2\pi}{\alpha}\hat{\mathbf{j}} + n_z\frac{2\pi}{\alpha}\hat{\mathbf{k}}, \tag{2.12}$$

where the vectors $\hat{\mathbf{i}}, \hat{\mathbf{j}}, \hat{\mathbf{k}}$, are unit vectors of length one along the x, y, and z axes, respectively.

This periodicity gives us a powerful relation that allows us to greatly simplify solutions to the time independent Schrödinger equation (TISE):

$$\left(-\frac{\hbar^2}{2m_e}\nabla^2 + V(\mathbf{r})\right)\Psi = E\Psi, \tag{2.13}$$

where Ψ is the electron wave function under the influence of the potential $V(\mathbf{r})$, $\hbar$ is Planck's reduced constant, m_e is the electron's mass, and E is the total energy. However, we know from the periodicity that $V(\mathbf{R} + \mathbf{r}) = V(\mathbf{r})$, meaning that if the crystal is a repeating structure, then so too is the potential energy experienced by an electron moving throughout the lattice. This consequence gives rise to Bloch's theorem, which states that

$$\Psi(\mathbf{r}) = \exp(\mathrm{i}\mathbf{k}\cdot\mathbf{r})u(\mathbf{r}), \tag{2.14}$$

where $u(\mathbf{r}+\mathbf{R}) = u(\mathbf{r})$, meaning that all solutions for $\Psi(\mathbf{r})$ under the potential $V(\mathbf{r})$ can be made from a combination of a periodic wave function, $u(\mathbf{r})$, and a plane wave. Proof for this theorem can be found throughout the literature[46–48].

To dive straight into solving the TISE for a true crystal, even with our knowledge of Bloch's theorem, would be time consuming and wouldn't allow us to focus on the important

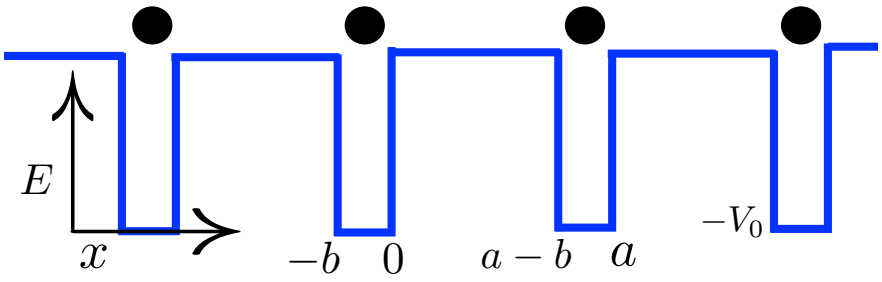

Figure 2.6: The Kronig-Penny potential.

consequences of a periodic lattice. Instead, let's consider the 1D Kronig-Penny model, which is explained in numerous resources[47;49] and shown in figure 2.6. The model consists of a periodic arrangement of square wells with separation a, width b, and depth $-V_0$. We can write this potential, $U(x)$, as

$$U(x) = \begin{cases} 0, & an < x < (a-b)(n+1) \\ -V_0 & an - b < x < an, \end{cases} \tag{2.15}$$

for $n \, \epsilon \, \mathbb{Z}$. Problems of this nature are easily handled with undergraduate level mathematical techniques[50]. For $E > 0$ in the regions where $U(x) = 0$, say from $0 < x < a - b$, the TISE tells us that the wave function is

$$\Psi(x) = A_1 \exp(\mathrm{i}\kappa x) + A_2 \exp(-\mathrm{i}\kappa x), \tag{2.16}$$

$$\kappa^2 = \frac{2m_e E}{\hbar^2}, \tag{2.17}$$

with A_1 and A_2 to be determined. Meanwhile, in a region where $U(x) = -V_0$, say $a - b < x < a$, we find that

$$\Psi(x) = B_1 \exp(\mathrm{i}\eta x) + B_2 \exp(-\mathrm{i}\eta x), \tag{2.18}$$

$$\eta^2 = \frac{2m_e(E + V_0)}{\hbar^2}, \tag{2.19}$$

where again, B_1 and B_2 are to be determined. A solution to these equations is found by invoking the usual conditions, that $\Psi(x)$ and $\frac{d}{dx}\Psi(x)$ are continuous, at a given boundary, say at $x = 0$. An additional set of equations can be found from Bloch Theorem, giving us a system of four equations for four unknown coefficients. The solution is found from placing these coefficients in matrix form;

$$\begin{bmatrix} 1 & 1 & -1 & -1 \\ \kappa & -\kappa & -\eta & \eta \\ \mathrm{e}^{\mathrm{i}(\kappa-k)(a-b)} & \mathrm{e}^{-\mathrm{i}(\kappa+k)(a-b)} & -\mathrm{e}^{-\mathrm{i}(\eta-k)b} & -\mathrm{e}^{\mathrm{i}(\eta+k)b} \\ (\kappa-k)\mathrm{e}^{\mathrm{i}(\kappa-k)(a-b)} & -(\kappa+k)\mathrm{e}^{-\mathrm{i}(\kappa+k)(a-b)} & -(\eta-k)\mathrm{e}^{-\mathrm{i}(\eta-k)b} & (\eta+k)\mathrm{e}^{\mathrm{i}(\eta+k)b} \end{bmatrix} \begin{bmatrix} A_1 \\ A_2 \\ B_1 \\ B_2 \end{bmatrix} = \begin{bmatrix} 0 \\ 0 \\ 0 \\ 0 \end{bmatrix}. \tag{2.20}$$

To solve this, we find the determinant[47], and after a lot of boring algebra we find

$$\cos(ka) = \cos(\eta b)\cos(\kappa(a-b)) - \frac{\kappa^2+\eta^2}{2\eta\kappa}\sin(\eta b)\sin(\kappa(a-b)), \tag{2.21}$$

which is a transedental equation for the dispersion relation, i.e. the relationship of momentum (k) to energy (E). We can arrive at a simpler solution, as shown in Kittle[47], when $b \to 0$, $V_0 \to \infty$, so that $bV_0 = C$, where C is a constant. This means that $\eta^2 b = C$, but $\eta b \to 0$. The dispersion relation reduces to

$$\cos(ka) = \cos(\kappa a) - C\frac{a}{2}\,\mathrm{sinc}(\kappa a) \leftrightarrow \text{R.H.S.} \tag{2.22}$$

In this last term, $\mathrm{sinc}(x) = \sin(x)/x$ and R.H.S. is an abbreviation for the right hand side of the transcendental equation shown in 2.22. Because the left hand side oscillates between ± 1, the only valid solutions are when R.H.S. is within this range.

Figure 2.7 shows the behavior and eigenenergies for two of the infinite number of solutions that are possible for equation 2.22. Both figure 2.7a and 2.7c show R.H.S. for $C = 20$, but with $a = 10$ Å for 2.7a and only 2.5 Å for 2.7c. Because of the periodic nature of the potential, solutions for $E(k)$ are represented in terms of $E(k')$, where $k' = k - G$. We find

that the possible energies for both systems result in a series of energy bands and energy gaps. For figure 2.7b, the gap at the bottom is only about 0.4 eV, and there are numerous additional gaps between 0-10 eV. However, figure 2.7d has a nearly 4 eV gap for the lowest lying band, and more than a 10 eV gap between the first and second bands.

We also find that, for small momentum, $E(k')$ is approximately parabolic, so that it behaves as a free particle which has a dispersion relation $E(k') = \frac{\hbar^2}{2m_e}k'^2$. However, at the band edge, this approximation fails, as the concavity of the curve flips and has a derivative of zero at the band edge (i.e. at $k' = \pm\pi/a$). This can have a profound effect on how solids behave under the influence of strong laser fields, as we will see in section 2.3.1.

Dielectrics versus semiconductors

It is common in solid state physics for the lowest bands to be completely filled, followed by the higher bands to be completely empty, when the system is in the ground state. Let's just assume then that the two lowest bands in figure 2.7b are filled. The gap between the second (filled) and third (empty) bands is only about 1 eV, meaning that an electron only needs a small amount of energy to reach the first excited band. We call this a semiconductor because it only requires a small DC voltage in order for the electrons to be liberated from ground state band (i.e. the valence band) into the excited band (i.e. the conduction band). Once in the conduction band, the electron is then free to move about the crystalline lattice. Meanwhile, in figure 2.7d, if the first band is filled but the second empty, then the electron needs over 10 eV to be excited. We call these systems insulators, because the DC voltages required for electrons to conduct electricity are so enormous that the material damages before it ever occurs.

For true three dimensional materials, there are a number of parameters that dictate whether or not a material is an insulator, semiconductor, or other material[3]. However, lattice spacing is one of many parameters dictating the band spacing and, in general, the band gap increases as the lattice constant (i.e. a) decreases.

[3]A metal is simply a material where a band is partially filled, allowing for almost instantaneous flow of electrons with applied voltage.

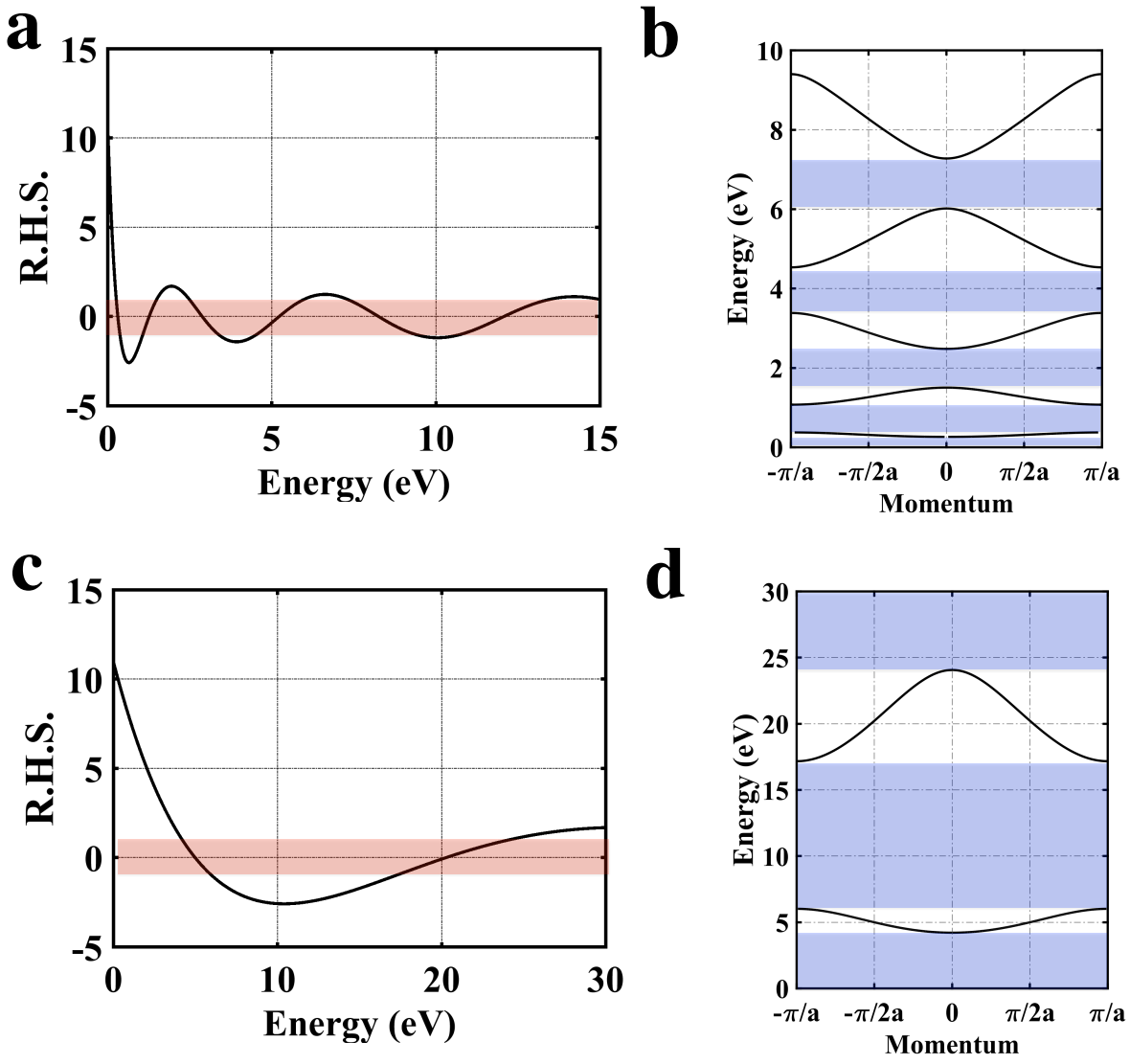

Figure 2.7: Bands resulting from two solutions to the Kronig-Penny potential. **a** R.H.S for a= 10 Å. Only when R.H.S. falls within the red-shaded regions is there a solution. **b** $E(k)$ under the periodic delay potential, the blue shaded regions indicate forbidden energies, and the height of the blue shaded regions indicate the band gap. **c** R.H.S for a= 2.5 Å. Only when R.H.S. falls within the red-shaded regions is there a solution. **d** $E(k)$ under the periodic delay potential. The blue shaded regions indicate forbidden energies and the height of the blue shaded regions indicates the band gap.

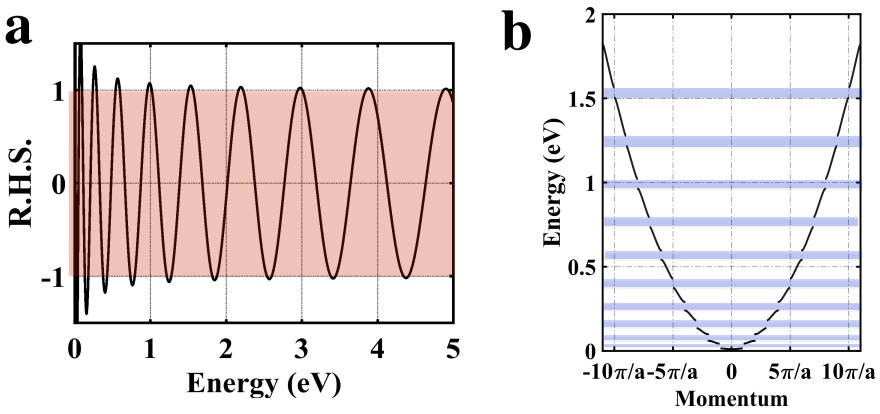

Figure 2.8: **a** R.H.S. for a band with lattice constant $a = 50$ Å. **b** $E(k)$ under the periodic delay potential with lattice constant $a = 50$ Å.

If we extend a to a large distance, then the action of the potential should become less pronounced and the electron should feel more like a free particle. We see this in figure 2.8, where we have plotted R.H.S. and $E(k)$ for a =50 Å. We see that the gaps in $E(k)$ have decreased significantly in width and separation, while the overall dispersion closely resembles that of a free particle.

Denisty of states

Lattice spacing and the overall band structure also modifies the density of states that an electron can occupy at a given energy. Obviously, if the energy corresponds to a band gap, a region where no states exists, then that density is zero. However, in regions where the band allows for electron occupation, we must consider the available states, as this determines the rate of excitation dynamics that we will discuss in section 2.2.2 and 2.3.

We know that the electron propagates with a group velocity $v_g = \frac{d\omega}{dk}$, which is easily found from the energy-momentum dispersion relations

$$v_g = \frac{1}{\hbar}\frac{dE(k)}{dk}. \tag{2.23}$$

It is useful to write the force, $\mathcal{F}$, on an electron in a lattice as $\mathcal{F} = m^* a$, with a the acceleration and m^* the effective mass. We are then prompted to take a time derivative of

v_g,

$$a_g = \frac{dv_g}{dt} = \frac{1}{\hbar}\frac{d}{dt}\frac{dE(k)}{dk} = \frac{1}{\hbar}\frac{dk}{dt}\frac{d^2E(k)}{dk^2}. \tag{2.24}$$

Because $\mathcal{F} = \frac{dp}{dt} = \hbar\frac{dk}{dt}$, with p as the electron momentum we find that

$$\mathcal{F} = \hbar^2\frac{dk^2}{d^2E(k)}a_g = m^*a_g. \tag{2.25}$$

However, due to the nature of the derivative we often write m^* as

$$\frac{1}{m^*} = \frac{1}{\hbar^2}\frac{d^2E(k)}{dk^2}. \tag{2.26}$$

From here, we see that, although the electron has a true mass, m_e, it does not necessarily behave with that mass when it is moving about a periodic potential. This phenomenon is explained a little more in section 2.2.2, but the periodic lattice basically requires the electron to oscillate within the region of $k = -\pi/a$ to $k = +\pi/a$, with a being the lattice constant. Because of this, the electron feels a repulsive action due to the dispersion relation of the particular band it resides in, which is described by the "effective" mass.

We can find a "back-of-the-envelope" relation for how m^* is related to the density of states. To start, consider that in a thin energy region, $dE(k)$, the density of states $D\{E(k)\}$ is related to the number of electronic states that can occupy the given volume dV. Because electrons have spin, two electrons are available and we find

$$D\{E(k)\}dE(k) = \frac{2}{dV}. \tag{2.27}$$

Now, because of Heisenberg's uncertainty relation, we find that, in three dimensions,

$$\delta x\delta p_x\delta y\delta p_y\delta z\delta p_z = dVdV_p \sim h^3, \tag{2.28}$$

where dp_i is the momentum in the i^{th} coordinate, dV_p is the momentum volume, and h is

Planck's (not reduced) constant. We can simplify this by considering an isotropic momentum, i.e. $V_p = \frac{4}{3}\pi p^3$. Then, since the kinetic energy in the band can be found using m^*, we find that

$$V_p = \frac{4}{3}\pi \left[2E(k)m^*\right]^{3/2}, \tag{2.29}$$

and we can put everything together to find that the density of states is

$$D\{E(k)\} = \frac{8\pi}{h^3}\sqrt{2}m^{*3/2}\sqrt{E(k)}. \tag{2.30}$$

Thus, if the electron has a momentum $E(k = 0) = E_0$, then the density of states at the bottom of the conduction band is

$$D\{E_0\} = \frac{8\pi}{h^3}\sqrt{2}m^{*3/2}\sqrt{E_0}, \tag{2.31}$$

and we can see that m^* for a particular band has a direct influence on the density of states.

2.2.2 Solids under the influence of strong fields.

Now that we understand the structure influencing electrons in a periodic lattice, we can get a brief overview of the important dynamics that electrons can undergo in these systems.

Bloch oscillations and intraband dynamics

When an electron is in the conduction band and under the influence of an external DC field, F, it experiences a force in the direction dictated by the field. If we say that $\mathbf{F} = F\hat{\mathbf{x}}$, it acquires momentum $p(t) = -eFt$. And if the electron started with $p_0 = -\pi\hbar/a$, then it will cross the Brillouin zone in time

$$\tilde{T} = \frac{2\pi\hbar}{eaF}. \tag{2.32}$$

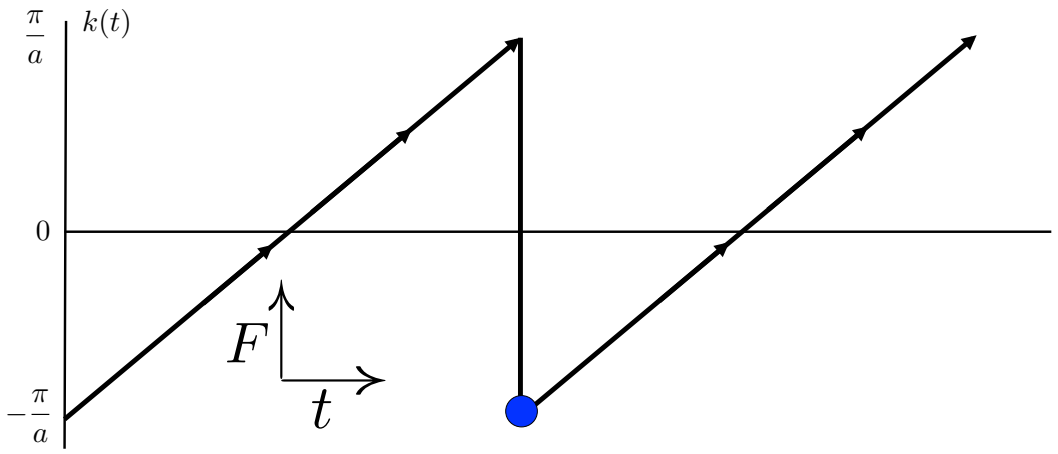

Figure 2.9: Pictogram describing Bloch oscillations. The first Brillouin zone of the reciprocal lattice is on the y-axis and time is displayed on the x-axis. The electron moves under F with a constant accelerating, so that $k'(t)$ increases linearly. When $k' = \frac{eF\tilde{T}}{\hbar}$, the momentum shifts back by the value of the reciprocal lattice vector, G, and the process is reinitiated.

The periodicity has some seemingly counterintuitive consequences. We might be lead to believe that after $\tilde{T}$, the momentum would continue to increase; but this is not the case because the electron already possesses the maximum momentum supported by the particular band it resides in. Also, it cannot simply "jump" to the next band (we are assuming that F is not too large at this point). What Bloch found all those years ago with his nice theorem is that the electron reaches a new state on the opposite side of the lattice! In other words at time $\tilde{T}$,

$$k' = \frac{eF\tilde{T}}{\hbar} - 2\pi/a \tag{2.33}$$

This process is illustrated in figure 2.9.

These dynamics lead to the electron oscillating in the lattice with a frequency $\omega_B = \frac{eaF}{\hbar}$, known as the Bloch frequency. Here we were only concerned with a DC field, if the field were to oscillate at a frequency ω, then the electron experiences an additional "quiver" energy, which we will describe in section 2.3.

Interband dynamics

We find that, just as we have several mechanisms describing transitions between bound states and the continuum in atoms and molecules, there exists methods of transitioning between valence and conduction bands for semiconductors and dielectrics.

Much of this discussion follows that of section 2.1.1. There, we saw that multiphoton and tunneling are just two extremes of a generalized description of atomic and molecular ionization. Here, we similarly find that the excitation from the valence to conduction band for a semiconductor/insulator also exhibits multiphoton and tunneling mechanisms, as shown in figure 2.10 for a one dimensional Coulomb lattice. As before with atoms and molecules, these two phenomena are extreme cases for a general excitation rate, which can be described by the Keldysh parameter for solids[17], γ_s, as

$$\gamma_s = \frac{\omega\sqrt{m_r^*\Delta}}{eF}, \tag{2.34}$$

where Δ is the band gap between the valence and conduction band and m_r^* is the electron-hole pair effective mass, which is defined as

$$\frac{1}{m_r^*} = \frac{1}{m_c^*} + \frac{1}{m_v^*}. \tag{2.35}$$

As we saw in section 2.2.1, m^* is related to the density of states in the given band. Because we are talking about transitions between different bands, we can see that m_r^* is a metric for describing the overall density of states available for the system. For example, if $m_c^* \to 0$, then $m_r^* \to 0$ and the rate of transition is very small, simply because it is limited by the number of states the electron can occupy in the conduction band.

2.3 Strong-field photoexcitation rates in solid media

In this section, we will explore the interaction of strong laser fields with solid media and, in particular, crystalline solids. Specifically, we are interested in the excitation rate of the elec-

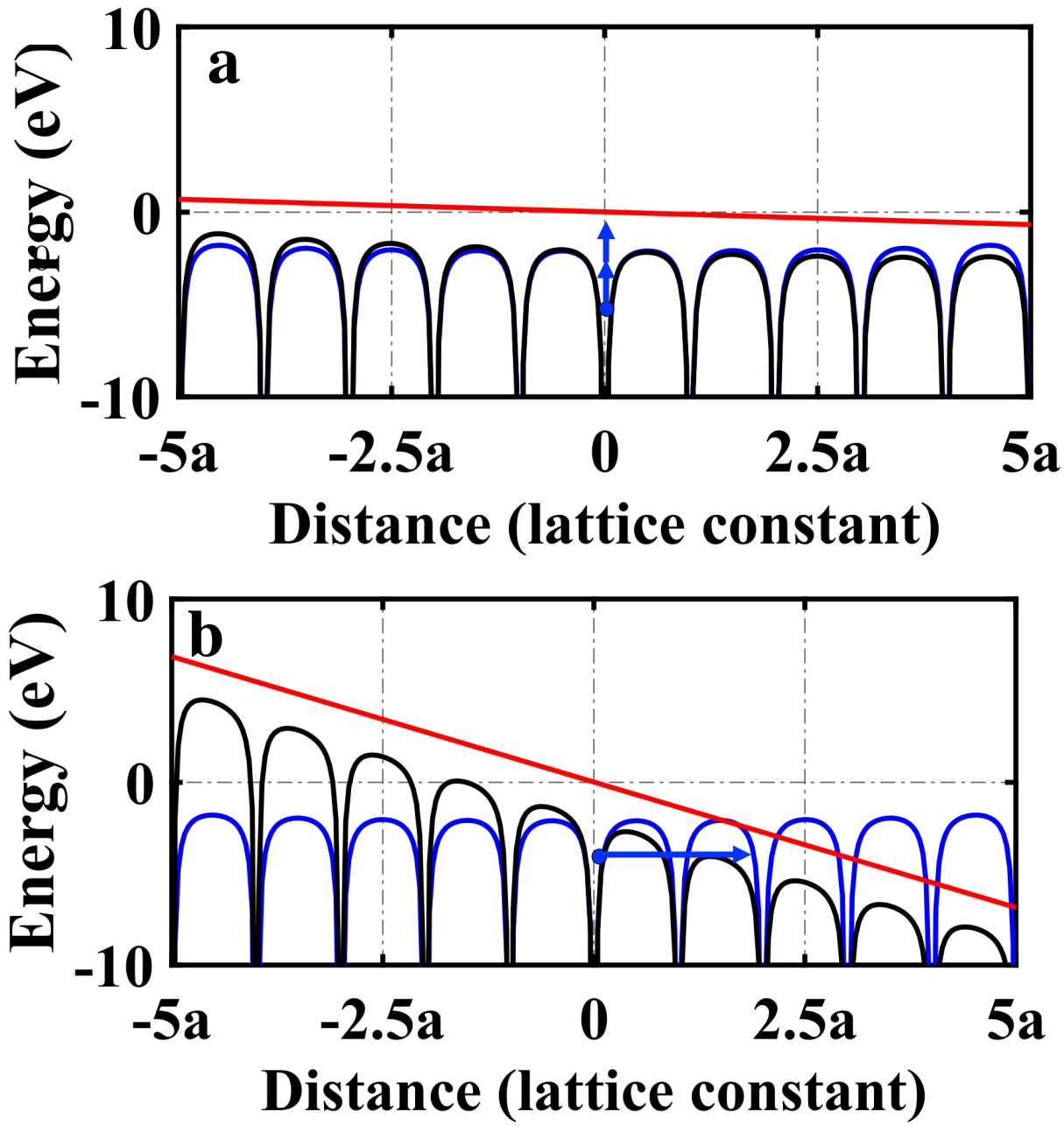

Figure 2.10: In both **a** and **b**, the blue line indicates the undisturbed potential for a one dimensional Coulomb lattice, the red line is the field potential, and the black line is the total potential. **a** Multi-photon excitation to conduction band. **b** Tunneling excitation to conduction band.

tron between the valence and conduction band, which will be described in a similar fashion as atoms and molecules were in section 2.1[17]. The main feature differing these calculations is the choice of how to describe the band. We will go through the physical consequences that occur when one band is chosen versus another and describe their limitations.

2.3.1 Three common band models

One of the main underlying features for a derivation of the photoexcitation rate is the choice of band structure. There are three examples of bands used in the literature[51;52] that I will go through in this section, the parabolic, the non-parabolic (Kane), and the cosine.

Parabolic

In the simplest scenario, we can consider direct band gap materials, and utilize the basic assumption that the electron starts with a small momentum when undergoing an excitation from the valence to conduction band. In the vicinity of small momenta, a direct band gap material possesses a dispersion relation much like a parabola,

$$\epsilon_P(\mathbf{k}) = \Delta\left(1 + \frac{\hbar^2 \mathbf{k}\cdot\mathbf{k}}{2m^*\Delta}\right), \tag{2.36}$$

where $\epsilon_P(\mathbf{k})$ is the parabolic band with momentum wave vector $\mathbf{k}$, Δ is the band gap energy, and m^* is the electron-hole pair effective mass (also known as the reduced effective mass).

When the electron is driven by a linearly polarized, strong laser field in the conduction band, we can largely regard its motion as one dimensional, and hence, $\mathbf{k} \to k$. We will take this to be the case through the rest of this section. Once in the conduction band, the electron takes on a field driven quasi-momentum,

$$k(t) = k_0 - \frac{eF}{\hbar\omega}\sin(\omega t), \tag{2.37}$$

where e is the electron charge, F is the amplitude of the electric field, $\hbar$ is Planck's reduced constant, ω is the field frequency, and t is time. Under these conditions, $\epsilon(k)$ takes on a

cycle-averaged, field driven form:

$$\epsilon(k_0)_{eff} = \frac{1}{T}\int_0^T \epsilon\left(k_0 - \frac{eF}{\hbar\omega}\sin(\omega t)\right) dt, \tag{2.38}$$

with T as the period of the field. We call this quantity the effective band gap. As shown in equation 2.38, this is a general relation independent of the band-model and was originally proposed by Keldysh to derive photoexcitation rates[17]. It will be the main quantity used to describe the role of band structure. In the case of the parabolic band, $\epsilon(k)^P_{eff}$ takes on the form

$$\epsilon(k)^P_{eff} = \Delta\left(1 + \frac{\hbar^2 k^2}{2m^*\Delta} + \frac{1}{4\gamma_s^2}\right) = \epsilon_P(k) + \frac{\Delta}{4\gamma_s^2}, \tag{2.39}$$

with γ_s as Keldysh's adiabatic parameter, as described earlier. This result is shown in figure 2.11 for intensities in the range of $10^{10} \leftrightarrow 10^{12}$ W/cm^2 for gallium arsenide (GaAs), which

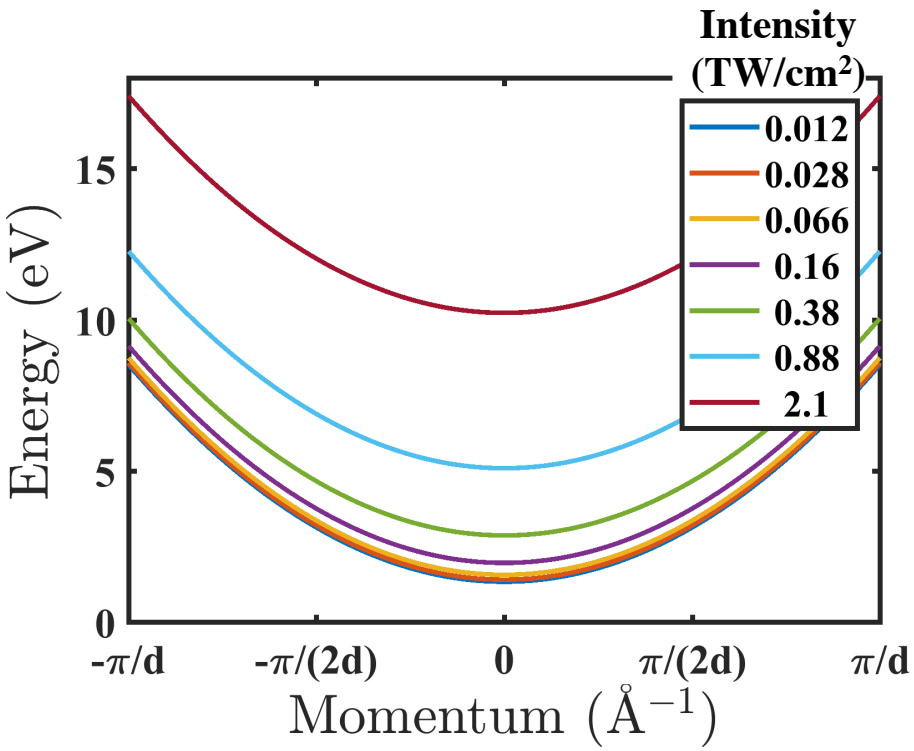

Figure 2.11: The parabolic band, $\epsilon^P_{eff}(k)$, under the influence of a laser field with intensities in the range of $10^{10} \leftrightarrow 10^{12}$W/cm^2. The x-axis is shown in momentum with d as the lattice spacing constant.

has a 1.3 eV band gap, driven by a field with a wavelength of 1180 nm, and plotted against momentum, with d as the lattice spacing constant. We see that the effective band gap increases, slowly at first, but becomes dramatically larger at high intensities. The use of the parabolic band for optical interactions with solid state materials is wide ranging and has proven to be an effective model under many conditions[53;54], especially with relatively weak field interactions. However, we will see in the following sub sections that more complete descriptions demonstrate more complicated behavior than the parabolic model.

Non-parabolic (Kane) band

Another widely used approach for describing a band is the cleverly named non-parabolic band. Because this name is rather dull, most people turned to calling it the Kane band, after its original founder[55]. The Kane band is described in one dimension as

$$\epsilon_{NP}(k) = \Delta\sqrt{1 + \frac{\hbar^2 k^2}{2m^*\Delta}}, \tag{2.40}$$

which is just $\sqrt{\Delta \cdot \epsilon_P(k)}$. Under this change, We still maintain the property of parabolic dispersion for small momenta,

$$\epsilon_{NP}(k) \approx \Delta\left(1 + \frac{\hbar^2 k^2}{4m^*\Delta}\right) \qquad (k \text{ is small}), \tag{2.41}$$

but does not scale to high energies as quickly for large k as $\epsilon_P(k)$. Although the Kane band does not satisfy all conditions across the entire Brillouin zone (notably, the continuity at the zone's edge), $\epsilon_{NP}(k)$ is more satisfactory for larger k than $\epsilon_P(k)$.

Using equation 2.38, we find that the effective band for the Kane model as

$$\epsilon^{NP}_{eff}(k) = \Delta\frac{2}{\pi}E\left(\frac{1}{\sqrt{1+\gamma_s^2}}\right)\left(\frac{\sqrt{1+\gamma_s^2}}{\gamma_s} + \frac{\gamma_s}{\sqrt{1+\gamma_s^2}} + \frac{\hbar^2 k^2}{2m^*\Delta}\right), \tag{2.42}$$

where $E(\theta)$ is the complete elliptic integral of the second kind.

This is shown for several intensities in figure 2.12. Unlike $\epsilon^P_{eff}(k)$, there is a stark contrast

in the change of the band with increasing intensities, beyond the offset of the band gap. The overall structure of the band begins to flatten out. Let's recall the physical meaning of equation 2.38, which is the cycle-averaged energy of the electron under the influence of the laser field. For the parabolic band the case was simple, regardless of where the electron initially lies in the band, its energy increases by the same amount. In the Kane band, we see that while the energy for small k increases, the cycle-averaged energy for electrons at the zone boundary can, counterintuitively, decrease.

One consequence of this behavior is that the density of states increases as the intensity of the field increases. Because the rate increases both with more intense fields and higher density of states, and the density of states (i.e. m^*) also increases with field intensity, a sort of "positive feedback" occurs where photoexciation increases much more dramatically. Measurements have shown that the Kane band is a realistic description of the influence of

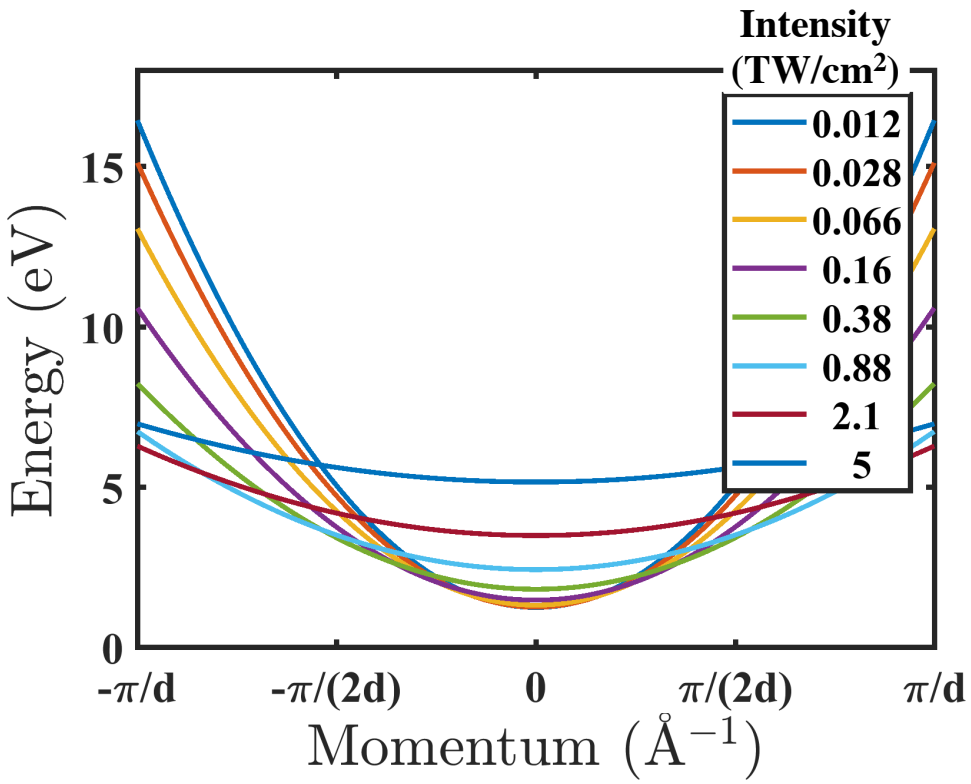

Figure 2.12: *The Kane band, $\epsilon_{eff}^{NP}(k)$, under the influence of a laser field with intensities in the range of $10^{10} \leftrightarrow 10^{12}$ W/cm^2. The x-axis is shown in momentum with d as the lattice spacing constant.*

strong laser fields than the parabolic model[56].

Cosine band

The final model we will discuss which has been used for strong-field photoexcitation rates is the cosine band[51]. In one dimension it is written as

$$\epsilon_{cos}(k) = \Delta\left(1 + \frac{\hbar^2}{\Delta m^* d^2}\left(1 - \cos(dk)\right)\right). \tag{2.43}$$

This has some immediately notable features. First, the cosine band is periodic in momentum space. Second, the cosine band is continuous at the band edge ($\pm\pi/d$). Several important materials, especially dielectrics, can be well represented by the cosine band through the entire Brillouin zone.

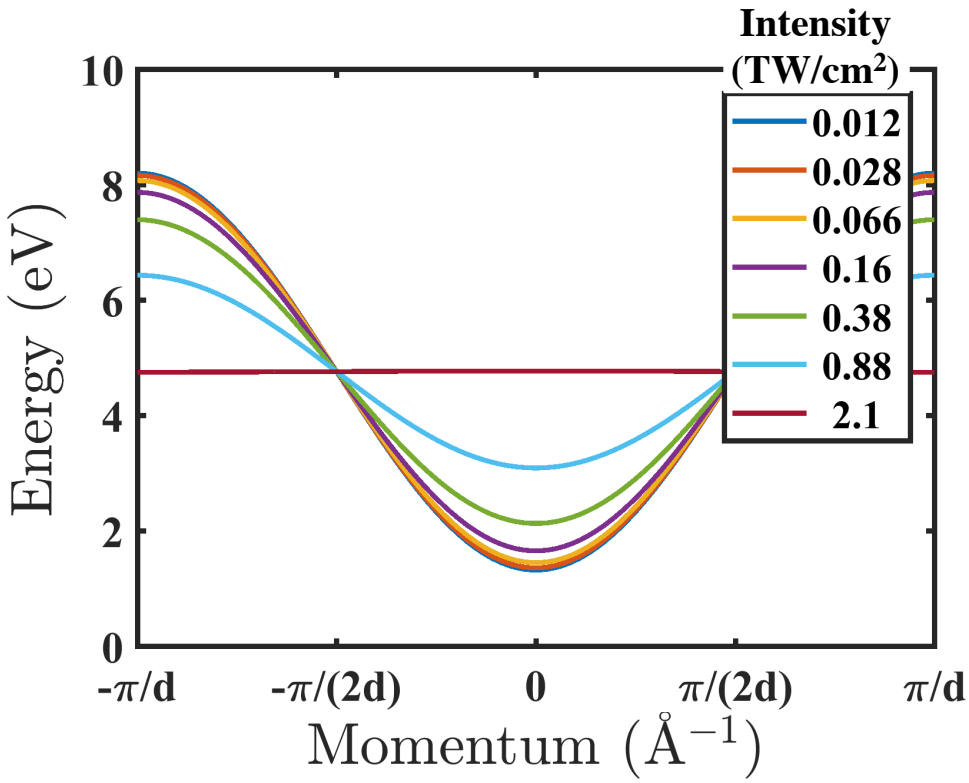

Figure 2.13: The cosine band, $\epsilon^{cos}_{eff}(k)$, under the influence of a laser field with intensities in the range of $10^{10} \leftrightarrow 10^{12}$W/cm^2. The x-axis is shown in momentum with d as the lattice spacing constant.

As before, we can derive the effective band using equation 2.38,

$$\epsilon_{eff}^{cos}(k) = \Delta\left(1 + \frac{\hbar^2}{\Delta m^* d^2}(1 - J_0(\chi))\cos(kd)\right), \tag{2.44}$$

where $J_0(\alpha)$ is the zeroth order Bessel function of the first kind and χ,

$$\chi = \frac{eFd}{\hbar\omega}, \tag{2.45}$$

is the modified adiabatic parameter. As with the Kane band, we see again that the cycle-averaged energy modifies the band's dispersion properties with electrons near the Γ point undergoing an increase in energy and electrons near the edges decreasing in energy. At the same time, m^*[4] significantly increases as it depends on the concavity of the band. At 2.1 TW/cm^2 for the conditions of GaAs under the influence of a field with a wavelength of 1180 nm, m^* approaches a singularity[5] . This singularity has been proposed as a real physical phenomenon, so long as the material can be adequately described with the cosine band, and is thought to describe the onset of damage[57;58].

Another feature of the cosine band is that it no longer depends on Keldysh's adiabatic parameter. Under the conditions of γ_s alone, reducing ω by a factor of two has the same effect on the photoexcitation rate as reducing m^* by four or increasing F by two. In other words, the ionization rate only depends on γ_s and there exists no additional interdependence between ω, F, and m^*. This is not the case with the cosine band, which depends on the modified adiabatic parameter, χ. This is important because χ considers the role of the electron being driven to the edge of the Brillouin zone, where it can undergo a Bloch oscillations[6]. This is important because, even with the same value of γ_s, longer wavelengths have an increased probability of driving an electron to the band edge despite possessing a lower intensity. This is demonstrated with $\epsilon_{eff}^{cos}(k)$ for two wavelengths with the same value of γ_s in figure 2.14.

[4]And therefore, the density of states, see section 2.2.1.
[5]See section 2.2.1.
[6]See section 2.2.2

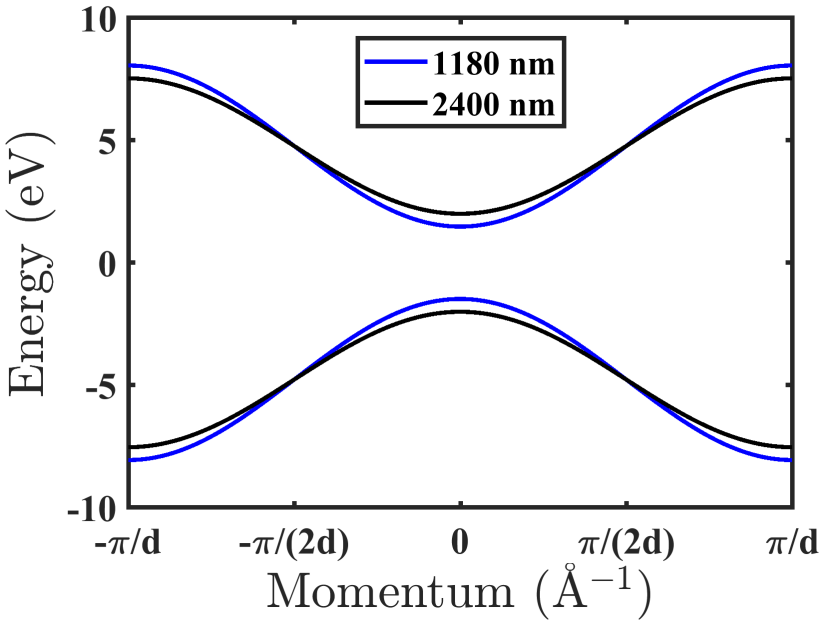

Figure 2.14: The cosine band under two wavelengths 1180 nm (blue) and 2400 nm (black). Both bands have the same adiabatic parameter $\gamma_s = 0.66$ but their dispersion properties are different due to an increase in Bloch oscillations for the longer wavelength.

2.3.2 Comparing the Kane and cosine bands

The photoexcitation rate, w, describes the probability of an electron undergoing photoexcitation (per unit time and volume), given the various parameters for the particular model at hand. These rates are given in the literature[17;51;58] and, due to their length and complexity, writing them out in this thesis is not necessary. Instead, we can solve for w as a function of laser intensity for both bands under the same conditions, as shown in figure 2.16, and understand the features based on the principles from section 2.3.1.

In figure 2.15 the rate for the cosine band is shown in blue and the rate for the Kane band is shown in black. These are given for conditions corresponding to gallium arsenide ($\Delta = 1.4$ eV), along the [100] axis ($m^* = 0.063m_e$) for a field wavelength of 2500 nm. When the intensity of the driving field is low, the two bands are essentially the same apart from a constant proportional offset where w for the cosine model is always higher than w for the Kane model. When the intensity reaches the 0.1 TW/cm^2 range, w for both models

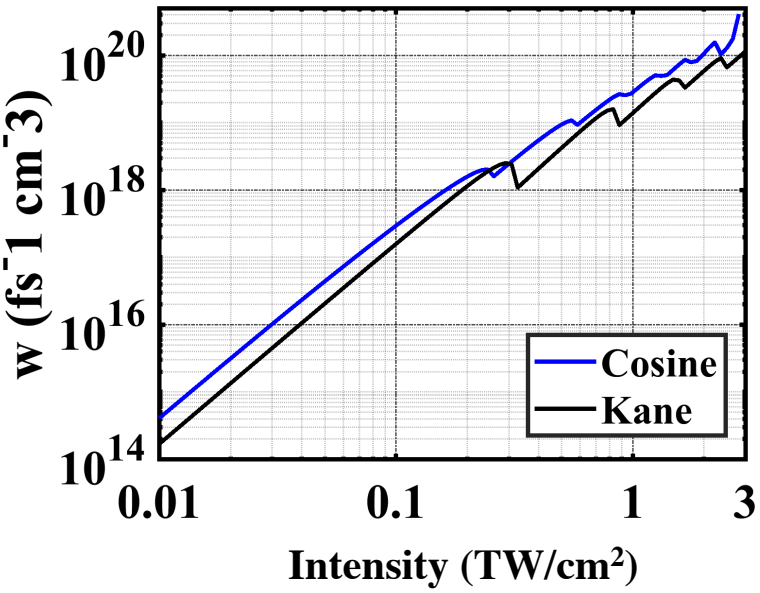

Figure 2.15: Photoexcitation rates for the cosine and Kane bands for $m^* = 0.063m_e$, corresponding to m^* for Gallium Arsenide along the [100] axis, and a field wavelength of 2500 nm.

experiences abrupt dips, with the cosine model experiencing dips at lower intensities and more frequently than the Kane model. These dips are associated with channel closings, which occur when the effective band gap ($\epsilon_{eff}^{BG} = \epsilon_{eff}(k = 0)$) has an energy such that

$$\epsilon_{eff}^{BG} = n\hbar\omega \tag{2.46}$$

with $n \in \mathbb{Z}$ and ω the frequency of the laser field. Comparing figures 2.12 and 2.13 we see that ϵ_{eff}^{BG} changes more rapidly than it does for the Kane band, which explains this feature of figure 2.15. The rates continue through several more channel closings up through the low 1 TW/cm^2, until w for the cosine model reaches a singularity. This corresponds to an intensity where the cosine band is flat, as shown for an intensity of 2.1 TW/cm^2 in figure 2.13. Thus, we expect that, where the two models should qualitatively agree at low intensities, there should be stark contrast in the photoexcitation rates given by the two models when the

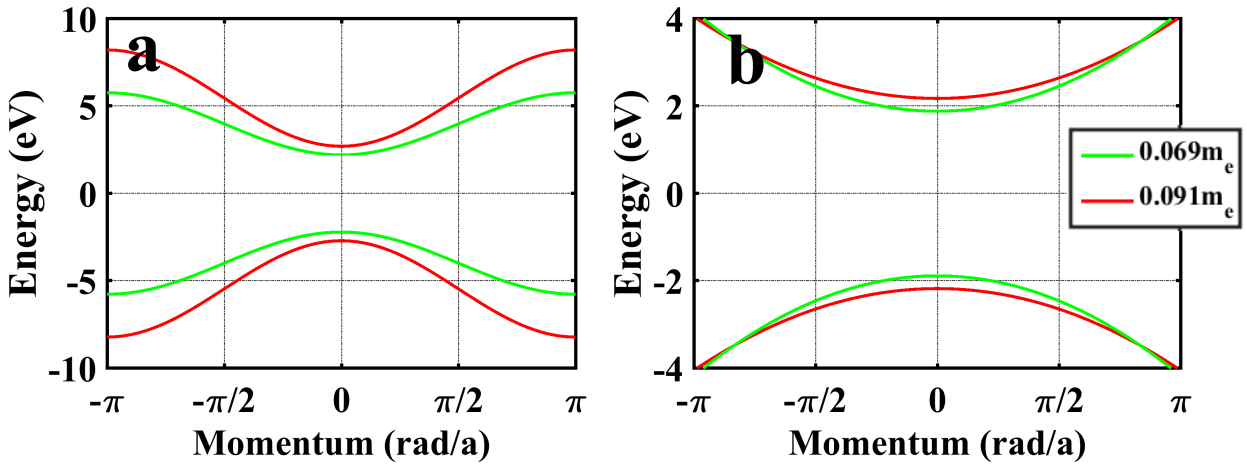

Figure 2.16: **a** The cosine band for minimum (green) and maximum (red) value of m^* in GaAs at an intensity of 0.5 TW/cm^2 at 2500 nm **b** The Kane band under the same conditions.

fields are intense[7].

In addition to the dependence on the intensity, we can also understand strong laser field interactions with various bands by changing the electron-hole pair's effective mass, m^*. As many materials experience a large change in the density of states with crystalline orientation, this can be easily accomplished by varying the laser polarization [44;45;59–61].

A principle feature of the experiments carried out in section 7.1 is that we can change the initial density of states (i.e., m^*, see section 2.2.1) via rotating the polarization incident on the crystalline surface. By doing this at various intensities and wavelengths, we have a measurement that determines how photoexcitation varies with all of its dependencies. As described in section 2.3.1, a large difference between the Kane band and the cosine is that the photoexcitation rate in the Kane model only depends on γ_s, implying that our measurements for the same value of γ_s should be identical. However, as shown in figure 2.14, the cosine band has a photo excitation rate that depends on χ, so that it will not necessarily predict the same behavior.

Since our measurements primarily revolve around the changing of m^*, we can get an

[7] 0.1 - 1 TW/cm^2 for conditions posed for gallium arsenide. This value will change depending on what system is being modeled.

idea about the difference between the band models by comparing how the initial density of states influences the band dynamics. In figure 2.16a the cosine band is plotted for minimum (green) and maximum (red) value of m^* in GaAs at an intensity of 0.5 TW/cm^2 at 2500 nm. Likewise figure 2.16b shows the results under the same conditions for the Kane band.

As we already saw in figure 2.14, the cosine band can have different $\epsilon_{cos}(k)$ despite γ_s being the same. This can be explained by the fact that the cosine band takes better account for the contribution of Bloch oscillations, which have a strong frequency dependence. Unlike the cosine band, the Kane model does not include these effects due to the lack of describing the entire Brillouin zone. It turns our that $\epsilon_{NP}(k)$ is identical so long as γ remains constant. These effects may be responsible for the measurements we find in chapter 7.

2.4 Comparing Solids with Atoms and Molecules

As a conclusion to this chapter, I will summarize the discussion on atoms, molecules, and solids by offering comparisons between the general behavior[17].

For the purposes of this thesis, atoms and molecules are studied in isolation (i.e. they interact only with the field, not with each other). We focus on interactions where the laser has a photon energy that is small compared to the ionization potential for a bound electron, the bound electron is freed through some ionization process, and the now free electron is accelerated by the field in the continuum. In solids, we focus on processes where a strong laser field excites a bound electron to the conduction band through multi-photon absorption, where it is bound to the lattice and can be accelerated by the electric field. At first, there appears to be dramatic differences between these two scenarios. However, they possess conceptual similarities because, in the conduction band, the electron is "quasi-free" to move around the lattice. It is the close spacing between the atoms in the lattice that allow for this, as can be seen with the black line in figure 2.10 permitting free movement of bound ($E < 0$) states. Of course, when the electron is freely moving in the lattice, it still experiences the weak periodic potential. So, where the freed electron from an atom/molecule sees a smooth continuum, the quasi-free electron in the conduction bands sees a "bumpy" surface which

gives rise to the numerous effects we discussed in sections 2.2 and 2.3.

When the electron is under the influence of the laser field in the continuum or conduction band, we see that in both scenarios, the ponderomotive, or "quiver" energy, is an essential parameter giving rise to the rich dynamics in either system. Whereas U_p is a straightforward calculation for the continuum, the effective band gap, which is roughly analogous to U_p for a solid, depends largely on the band's dispersion properties. This means that in atoms/-molecules, the quiver energy is purely influenced by the field but in a solid, this energy depends on a combination of the field and lattice potential.

Solids and molecules have another commonality in that they consists of two and/or three dimensional arrangement of nuclei. In section 2.2.1, we find that the density of states in a solid is governed by the band structure, and that this has a strong dependence on the arrangement of the atoms in the unit cell. Similarly, the electron density in a molecule is distributed anisotropically across the structure, and is key to understanding many chemical reactions. Numerous experiments involving the alignment of molecules with a laser in time have demonstrated that the ionization rate in a molecule is proportional to the electron density along the laser's polarization axis[62;63]. In the same way, the photoexitation rate in a solid depends on the effective mass, which is an analogous description of this charge density, and has been shown in numerous studies to dependent on the alignment of the laser fields polarization with the lattice[44;45;59–61].

Thus, when we talk about strong-field interactions in atoms and molecules as opposed to solids, there are many overlapping similarities. The main difference always comes back to how the inclusion of a periodic potential in a solid, versus a true continuum in an atom/molecule, effects the physics.

Chapter 3

Ultrafast Optics

In chapter 2, we discussed the principles behind how materials systems respond to intense light. In this chapter, I will shift towards how the light involved in these interactions is produced. Most of the topics in this chapter are brief introductions that are important for understanding the content of the experimental results presented in chapters 4 through 8.

I will start with an introduction to ultrafast optics, covering briefly how to get a femtosecond laser field. Because this thesis pertains to strong laser fields, we require amplification of these fields. An overview of this technique, known as chirped-pulse amplification, is given. I will then discuss the role of carrier envelope phase, which is important when the laser pulse duration approaches the period of the central wavelength. Because femtosecond pulses are faster than the response time of electronics, all optical measurements are required for measuring their pulse durations. I will briefly cover the common techniques used in my lab for characterizing ultrafast laser fields.

After we have covered these general principles, we can briefly cover nonlinear optical phenomena, which are essential in creating the variety of wavelengths used in the experiments covered in later chapters. We will start with the general concept of nonlinear optics and discuss how it arises physically. Then we will cover difference frequency generation, which allows us to create longer wavelengths, and self phase modulation, which allows us to generate shorter pulses.

3.1 Introduction to ultrafast optics

We will cover the main properties of ultrafast pulses and their generation. There will also be a brief overview of chirped-pulse amplification (CPA) and how it is performed in our laser.

3.1.1 Ultrafast pulses

Ultrafast laser fields, for the discussion of this thesis, are electric fields with durations under 1 picosecond ($1{\cdot}10^{-12}$ s) with frequencies in the infrared and optical regime (1 THz-1 PHz). While electric fields can carry very complex structure, for the sake of understanding the principles it is best that we start with something simple. We can write down an electric field in time as a Gaussian,

$$\mathcal{E}(t) = E_0 \exp\left(-2\ln(2)\frac{t^2}{\Delta\tau^2}\right)\exp(\mathrm{i}\omega_0 t), \tag{3.1}$$

where $\mathcal{E}(t)$ is the field in time, t, E_0 is the amplitude, $\Delta\tau$ is the pulse width, and ω_0 is the angular frequency of oscillation[1]. We will use the common convention for defining $\Delta\tau$ so that it represents the pulse width in terms of the full-width half maximum (FWHM) of the *intensity* ($I(t) = \mathcal{E}(t)^*\mathcal{E}(t)$). It is frequently the case that many of the fields we work with in the laboratory can be sufficiently described in this manner. We can equivalently express the electric field in the frequency domain,

$$\tilde{\mathcal{E}}(\omega) = \tilde{E}_0 \exp\left(-2\ln(2)\frac{(\omega-\omega_0)^2}{\Delta\omega^2}\right), \tag{3.2}$$

where $\tilde{\mathcal{E}}(\omega)$ is the field in frequency, ω, and $\Delta\omega$ is the FWHM of the spectrum, which is often referred to as the bandwidth. These two representations are related to one another via

[1]Frequency, commonly denoted as ν, is so often multiplied by 2π that I always use angular frequency. From here on, I will always refer to angular frequency as frequency.

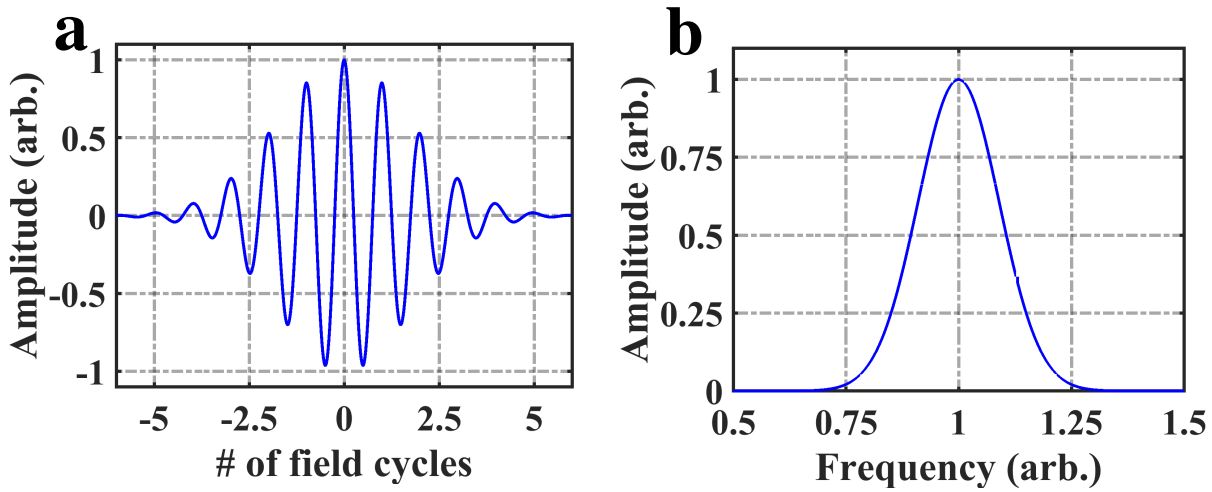

Figure 3.1: **a** Time domain electric field (equation 3.1) **b** Frequency domain electric field, or spectrum (equation 3.10)

a Fourier transformation,

$$\mathcal{E}(t) = \mathcal{F}.\mathcal{T}.\left\{\tilde{\mathcal{E}}(\omega)\right\} = \frac{1}{\sqrt{2\pi}}\int_{-\infty}^{\infty}\tilde{\mathcal{E}}(\omega)\exp(\mathrm{i}\omega t)d\omega, \tag{3.3}$$

$$\tilde{\mathcal{E}}(\omega) = \mathcal{I}.\mathcal{F}.\mathcal{T}.\left\{\mathcal{E}(t)\right\} = \frac{1}{\sqrt{2\pi}}\int_{-\infty}^{\infty}\mathcal{E}(t)\exp(-\mathrm{i}\omega t)dt. \tag{3.4}$$

It is useful to derive a relation between $\Delta\tau$ and $\Delta\omega$. To do so, we starting by performing the Fourier transform on equation 3.1

$$\tilde{\mathcal{E}}(\omega) = \frac{1}{\sqrt{2\pi}}E_0\int_{-\infty}^{\infty}\exp\left(-2\ln(2)\frac{t^2}{\Delta\tau^2}\right)\exp(\mathrm{i}(\omega_0-\omega)t)dt. \tag{3.5}$$

The solution to this integral can be worked out, or just looked up in a table

$$\tilde{\mathcal{E}}(\omega) = \frac{1}{\sqrt{2\pi}}E_0\sqrt{\frac{\pi\Delta\tau^2}{2\ln(2)}}\exp\left(-\frac{(\omega-\omega_0)^2\Delta\tau^2}{8\ln(2)}\right) = \tilde{E}_0\exp\left(-\frac{(\omega-\omega_0)^2\Delta\tau^2}{8\ln(2)}\right). \tag{3.6}$$

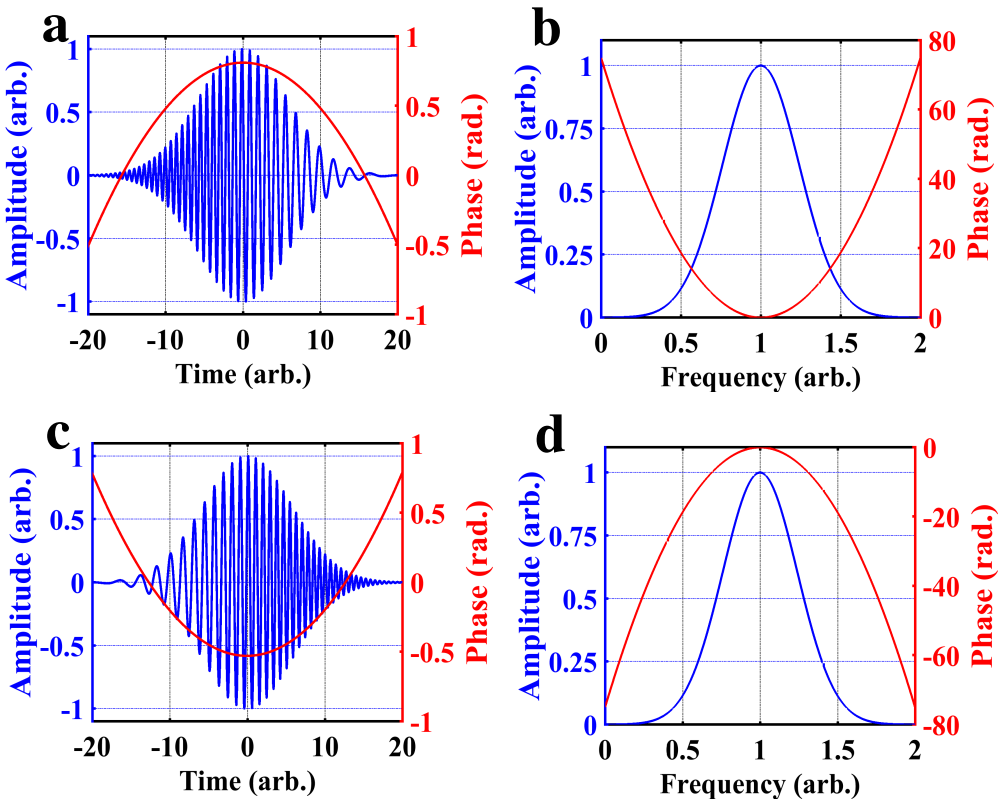

Figure 3.2: **a** Time domain electric field with positive group delay dispersion (GDD), **b** Spectrum for **a**, **c** Time domain electric field with negative GDD, **d** Spectrum for **c**.

And we simply equate the terms in the exponentials for equations 3.2 and 3.6:

$$2\ln(2)\frac{(\omega-\omega_0)^2}{\Delta\omega^2} = \frac{(\omega-\omega_0)^2\Delta\tau^2}{8\ln(2)}, \tag{3.7}$$

$$\Delta\tau\Delta\omega = 4\ln(2). \tag{3.8}$$

Which says that, for an electric field with no higher order phase, the product of the FWHM in time and the FWHM in spectrum is constant. That is, an electric field with a larger spectral bandwidth supports a shorter electric field in time. Consequently, in order to have a certain pulse duration, there is a minimum amount of spectral bandwidth required. For instance, if I want a 30 femtosecond pulse, I need $\Delta\omega = 9{\cdot}10^{13}$ rad/s.

At this point, we have not yet considered the effect of higher order phase for our derivation of electric fields. With very short pulses, all frequency components must be precisely in phase

for a pulse to reach its shortest duration, which we often refer to as its Fourier transform limited (FTL) duration. While we can get close to this, typically, there is always some slight phase relationship between the components. This arises from the pulse traveling through a material, or by propagating through a geometrically arranged optical setup, such as a stretcher. When attempting to generate short laser fields, it is imperative that we have ways to measure these phase relationships. I will go over how these are measured in section 3.3, but for now it is important that we see how the phase effects our fields.

We can include phase into our electric field by writing 3.1 as

$$\mathcal{E}(t) = E_0 \exp\left(-2\ln(2)\frac{t^2}{\Delta\tau^2}\right)\exp(\mathrm{i}\omega_0 t + \mathrm{i}\phi(t)), \tag{3.9}$$

where $\phi(t)$ is the time domain phase. There is also a corresponding phase in frequency, $\phi(\omega)$, that can be found after[2] taking the Fourier Transform,

$$\tilde{\mathcal{E}}(\omega) = \tilde{E}_0 \exp\left(-2\ln(2)\frac{(\omega-\omega_0)^2}{\Delta\omega^2}\right)\exp(\mathrm{i}\omega_0 t + \mathrm{i}\phi(\omega)). \tag{3.10}$$

It is possible to treat this problem with either $\phi(t)$ or $\phi(\omega)$. However, it is much more intuitive to consider what happens to individual frequency components and then determine the resulting effects on electric field's time-domain characteristics. For this reason, we will treat this problem with $\phi(\omega)$. While the the spectral components of our field may not be FTL, they are not random either. Assuming that $\phi(\omega)$ is infinitely differentiable, we can do a Taylor expansion on $\phi(\omega)$ at ω_0,

$$\phi(\omega) = \phi_0 + \alpha\omega + \beta(\omega-\omega_0)^2 + \gamma(\omega-\omega_0)^3 + \epsilon(\omega-\omega_0)^4 + ..., \tag{3.11}$$

where the terms ϕ_0, α, β, γ, and ϵ indicate the magnitude of that specific term. It turns out that ϕ_0 and α do not affect the pulse duration[3] and, typically, only the next several terms

[2] It is worth noting here that $\phi(t) \neq \mathcal{F}.\mathcal{T}.\{\phi(\omega)\}$, meaning that the relationship between phase in either domain is not so simple. We will see in the next two examples that $\phi(\omega)$ and $\phi(t)$ have completely different relationships.

[3] α can be shown to describe the pulse delay in time. We will see in section 3.2 that ϕ_0 is related to the

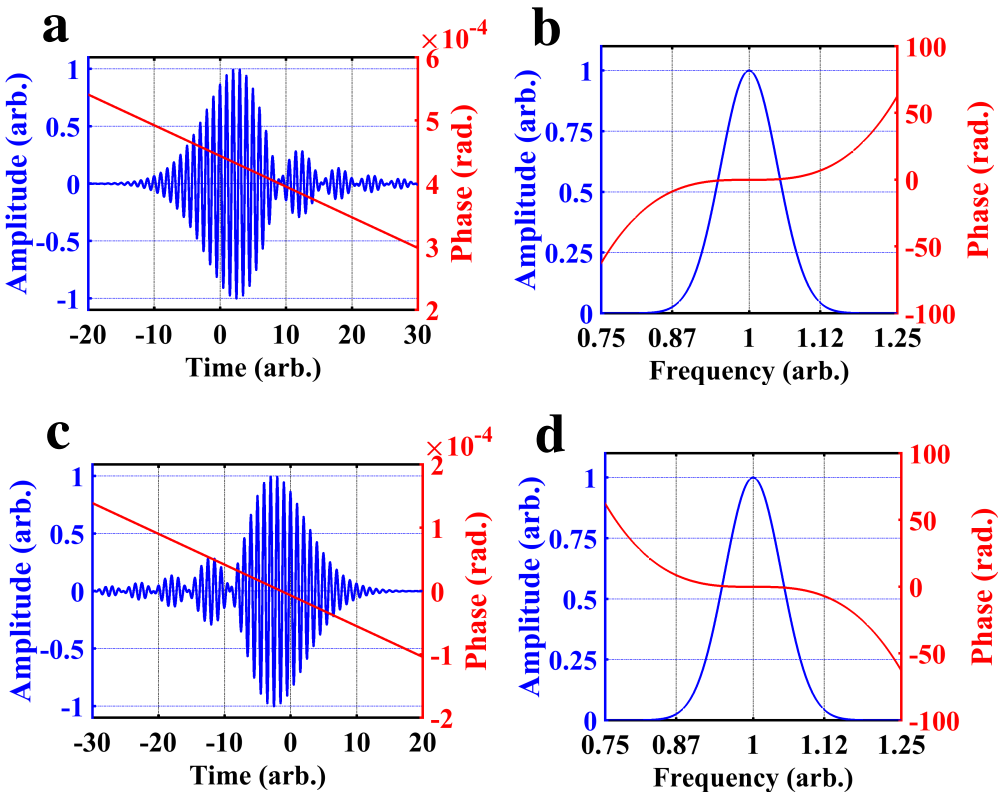

Figure 3.3: **a** Time domain electric field with positive third order dispersion (TOD), **b** Spectrum for **a**, **c** Time domain electric field with negative TOD, **d** Spectrum for (c).

are required for describing a pulse's dispersion. For instance, β, which is known as the group delay dispersion (GDD), has the ability to stretch a pulse to a duration of $\Delta\tau_{out}$,

$$\Delta\tau_{out} = \Delta\tau\sqrt{1+\left(\frac{4\ln(2)\beta}{\Delta\tau^2}\right)^2}. \tag{3.12}$$

Figure 3.2b shows the applied chirp to the spectrum and the resulting time domain electric field is shown in figure 3.2a. Not only has the pulse been stretched, but the electric field oscillates at a different frequency on the left hand side versus the right hand side. This is where "chirp" gets its name, as it has an analogy to the changing pitch of bird calls. Also, despite being a quadratic term, the frequencies are linearly stretched across the envelope, hence the name, linear chirp. We can also compare figures 3.2a and 3.2c and notice that

carrier envelope phase.

their chirp is opposite in behavior, which is due to the sign. We usually refer to positive (negative) chirp as when the lower (higher) frequencies come first in the field, as shown in figure 3.2a. It is also useful to consider how the electric field is influenced by the third order dispersion (TOD) term in equation 3.11. This is demonstrated in figure 3.3. We see that the electric field has a very different response to γ as opposed to β, as γ doesn't change the frequency in time, but adds "satellite" pulses. As with the chirp for β, the sign of the γ determines which side of the main pulse the satellites reside.

While orders higher than GDD and TOD can influence the field, in our lab we typically find these two to be the most dominate terms of equation 3.11. Besides minimizing the pulse duration, we also want to reduce GDD and TOD because the additional characteristics of the pulse can negatively influence an experiment. Because GDD preferentially delivers some frequencies before others, and TOD can deliver a satellite pulse to an experiment before the main event, these electric fields can alter the interaction in complicated ways.

There are a few ways to control dispersion. First most ultrafast lasers are designed with a compressor system (see figure 3.5), which acts to control dispersion using the geometric arrangement of a grating or prism set. Because the dispersion changes depending on what experiment is being performed, the compressor acts to pre-compensate these effects so that the experiment is delivered an FTL pulse[64]. Another method which is especially useful when we want high energy, very short pulses, is chirped mirrors. These are optical mirrors with a sophisticated arrangement of dielectric coatings which compensate for phase by causing certain frequencies to travel further than others. After many bounces, pulses as short as a few femtoseconds can be made without reducing the pulse energy[65;66]. Finally, if we are fortunate to work in certain wavelength regimes, the dispersion relationship of some materials can actually compensate the phase. This is by far the simplest technique as the arrangement only requires transmitting the pulse through the material with a thickness that is adequate in providing the correct compensation[67–69].

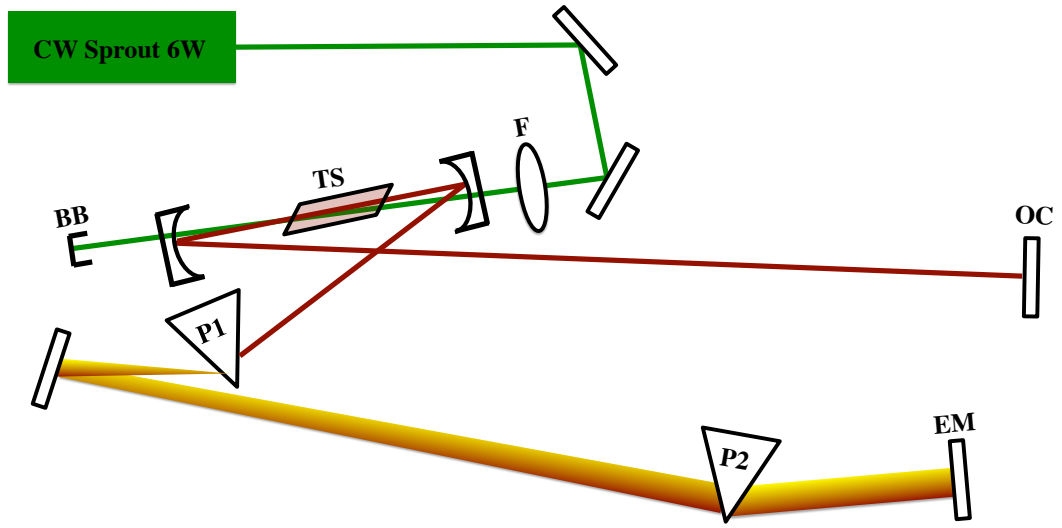

Figure 3.4: Layout of the oscillator for the laser in chapter 4.

3.1.2 Ultrafast pulse generation

We now have a good understanding of how an ultrafast pulse behaves. However, we have not yet discussed how they are created. To do so requires a laser with adequate properties. For the last 25 years, this has been the Ti:Sapphire (Ti:Sapph) laser[70]. A schematic of the layout for the Ti:Sapph in the HITS lab is shown in figure 3.4 and was developed by KM labs in the early 90's[70;71]. The Ti:Sapph has been the workhorse in in strong-field science due to its ability to directly produce fields approaching 10 femtoseconds.

We have not discussed the processes behind how a laser works, for that, there are numerous resources[72;73]. I intend to only cover the basics that apply to the lasers used in this thesis, as our interest is less in the most general principles of laser operation and more in the application of lasers for energetic, femtosecond field production. A laser is a result of the coherent production of photons. When a collection of electrons in some medium are excited, they will have some rate at which any one can spontaneously decay back into their ground state, emitting a photon. If this photon passes through the medium, it has the ability to induce emission in neighboring electrons in a process known as stimulated emission. This is the critical phenomenon behind laser operation, as photons emitted in the process of

stimulated emission are coherent with one another.

Thus, a laser contains three critical components. First, it has a medium with excitable electrons. Second, it has some method of pumping these electrons to their excited states. Finally, it has a pair of mirrors forming a cavity around the medium. This cavity is stable so that light passing between the mirrors cannot escape and is required to pass through the medium hundreds or thousands of times before escaping through one of the mirrors, which we call the output coupler (which is anywhere from 90-99.99% reflective).

For our Ti:Sapph laser, the gain medium is, unsurprisingly, the Ti:Sapph crystal. With this medium, we have a broad range of energies that the electron can reside in for lasing, corresponding to an emission spectrum spanning 700-1000 nm, offering the potential of producing pulses with only a few femtoseconds of duration[74]. In the layout for our laser, shown in figure 3.4, the Ti:Sapph crystal (TS) is pumped with a 532 nm continuous wave (i.e. not pulsed) diode pumped solid state laser (Lighthouse Sprout G). This laser is focused into the TS crystal with a lens (F), and passes through a curved mirror which has a coating that passes the pump laser but highly reflects the generated laser pulses. A pair of curved mirrors encompass the TS crystal which guide and focus the generated pulses with the pump laser. The mirror shown on the right of TS sends the beam to a pair of prisms (P1 and P2) which act to control the dispersion that the pulses acquire through each pass in the cavity. After P2, an end mirror (EM) retro-reflects the pulse back through the cavity until it reaches the output coupler (OC), which has a partially reflective coating that allows a small portion of the pulse to exit the cavity.

Unfortunately, making short pulses is not quite as trivial as I have laid out so far. Unless designed carefully, the cavity will produce a narrow line width, despite TS having such a large emission range. To create the short pulses we desire, we must put the cavity in a geometry that is more favorable to short (hence, broadband) pulses. Techniques of this nature are known as "mode-locking", due to their ability to set millions of cavity modes in phase with each other. Our oscillator uses Ker-lens-modelocking (KLM), a technique that relies on the nonlinear Kerr effect[75;76]. Detailed explanation of KLM is beyond the context of this section, but I just want to point out that it relies of the fact that short pulses are

much more intense than continuous wave (CW) fields. Thus, when a cavity is arranged correctly, the Kerr effect gives a pulsed field much higher gain, which necessarily eliminates CW operation.

Finally, I want to point out that the intense pulses for KLM require that they are near FTL. Since the TS chirps the pulses as they pass through the crystal, there must be a way of removing this after every pass through the cavity. The prism pairs shown in figure 3.4 perform this operation in our laser. Because we are working with light in the near-infrared, longer wavelengths will propagate faster through the cavity than shorter wavelengths. The prisms reverses this by geometrically changing the path length for the individual colors. If you were to trace out the path for the yellow edge versus the red edge in figure 3.4, you would see that the yellow has a slightly shorter path length. Thus, after returning back through the prism pair on its way to the TS, the pulse has been shortened again.

At this point we have sufficiently (and succinctly) covered the generation of a short femtosecond pulse. While the description above is for a true laser, we will from here on refer to this component as the oscillator. In general, we consider this just the beginning stage of our system, and when I refer to laser throughout the rest of the thesis, I will also mean that to include the amplifier system as well.

3.1.3 Chirped-pulse amplification

For our purposes, the pulse duration of a Ti:Sapph oscillator is sufficient to perform the experiments we desire. However, it is lacking in pulse energy. Amplification techniques require focusing the pulse from the oscillator, referred to as the seed, into larger crystals for a set number of passes (this can vary from several tens of passes to a single pass depending on the amplifier design). This is overlapped with a pump laser delivering much higher average power than the pump for the oscillator.

If we attempted to directly amplify our laser to the terawatt peak power that we desire, every optical component inside the amplifier would suffer catastrophic failure, as the peak intensities they would receive are well beyond limits of any material. To bypass this, we use

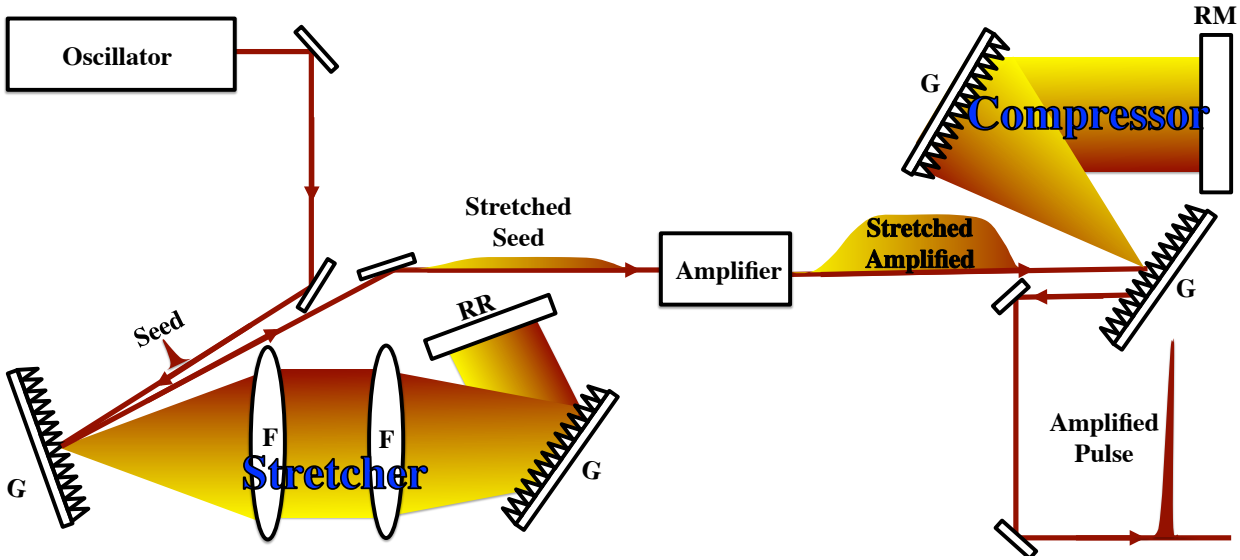

Figure 3.5: General layout of a chirped-pulse amplifier. G- grating, F - focal element, RR- retroreflector, RM - roof mirror.

a method known as chirped-pulse amplification (CPA)[64], which is shown in figure 3.5.

In figure 3.4, we saw that a prism pair can modify the chirp of a short pulse through geometric path differences to make a shorter pulse. We can do that exact same thing in reverse to temporally stretch an electric field. In this way, we can take the weak, femtosecond signal and make it several hundred picoseconds in duration. In this scenario, the pulse is chirped significantly so that, when amplified, the pulse can contain high pulse energies but still possess peak power and peak intensities below the damage threshold of the amplifier's components.

Afterwards, another grating pair forms a compressor, which will take the now amplified chirped pulse back to its FTL pulse duration. By using CPA, we have now taken a 12 fs, 5 nJ pulse and produced a 30 fs, 20 mJ, increasing the peak power by a factor of 10^6 in the process. Since its introduction, CPA has been the dominant method for producing high peak power laser fields, and is the technique used in producing our laser.

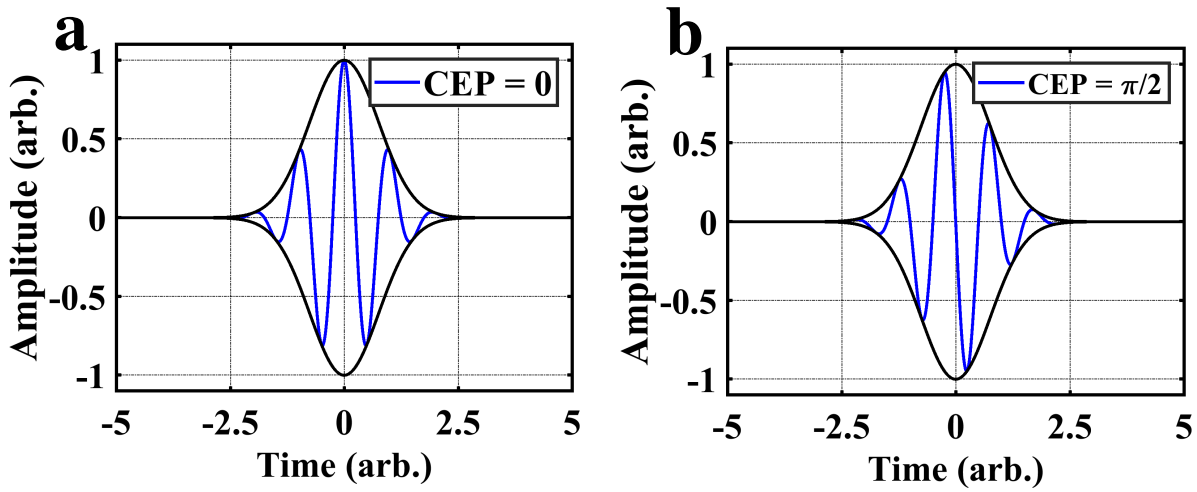

Figure 3.6: **a** An electric field in time with a carrier envelope phase (CEP) of 0. **b** An electric field in time with a CEP of $\pi/2$.

3.2 Carrier envelope phase

For a given electric field, there exist a phase offset between the group envelope and the wave packet. We refer to this as a phase slip between the carrier field and the envelope, or carrier envelope phase (CEP). When laser fields become very short, the electric field possesses only a few oscillations under the envelope and the peak of every half-cycle can experience a significant change in amplitude as a function of CEP.

An example of CEP effects is shown in figure 3.6. In figure 3.6a, we see a waveform corresponding to a CEP=0 rad., and this waveform has a single crest with a much larger field strength versus neighboring troughs and crests. In figure 3.6b, we see a waveform corresponding to a CEP= $\pi/2$ rad. This field has two half-cycles with the same peak field strength pointing in the opposite direction. Likewise, a field with CEP = π would be the same as 3.6a but pointing in the opposite direction.

In general, any physical effect relying on the instantaneous field strength will have a dependence on the CEP. These effects typically arise with the dynamics of a free electron under the influence of the laser field. In phenomena where this electron continues to behave with the atom/molecular system it arises from, rich CEP driven dynamics can occur. A few

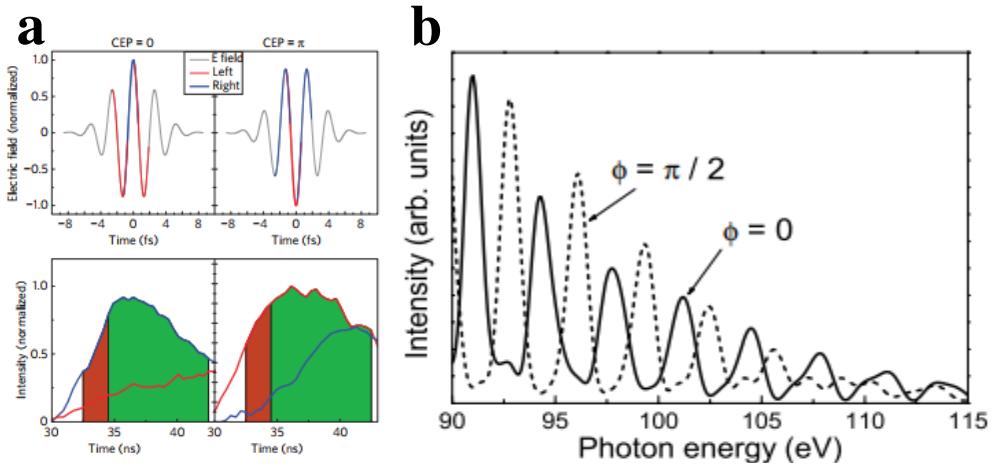

Figure 3.7: **a** Electron momenta controlled as the CEP changes the direction of the laser field from one direction to another. (Adapted from [77]). **b** The higher-order harmonic spectra shift as the CEP shifts from 0 to $\pi/2$. (Adapted from [78]).

examples where few-cycle laser fields control electron dynamics are shown in figure 3.7. In figure 3.7a, we see that the momentum of high energy ATI electrons along the left (down) and right (up) axis of the field can be more favorable for one direction versus another as the CEP is shifted from 0 to π [77]. This is a direct consequence of the electron being accelerated in the field. The favorability for up versus down is controlled by which direction the field's strongest half-cycle is aligned with. In figure 3.7b, we can see that the high harmonic spectra driven by a short laser field can shift to higher and lower energies depending on the CEP [78]. In this case, the CEP is shifted from 0 to $\pi/2$, which reduces the amplitude of the few-cycle field's strongest half-cycle, reducing the cut-off energy. In addition to these effects, CEP control is important in the production of isolated attosecond pulses [34], laser-induced electron diffraction [39], and non sequential double ionization [28].

3.3 Ultrafast pulse characterization

Because the generation short-pulsed electric fields requires very precise control over the bandwidth and its phase, we require techniques to accurately characterize these pulses. Unfortunately, even the fastest electronic devices on the market have response times many

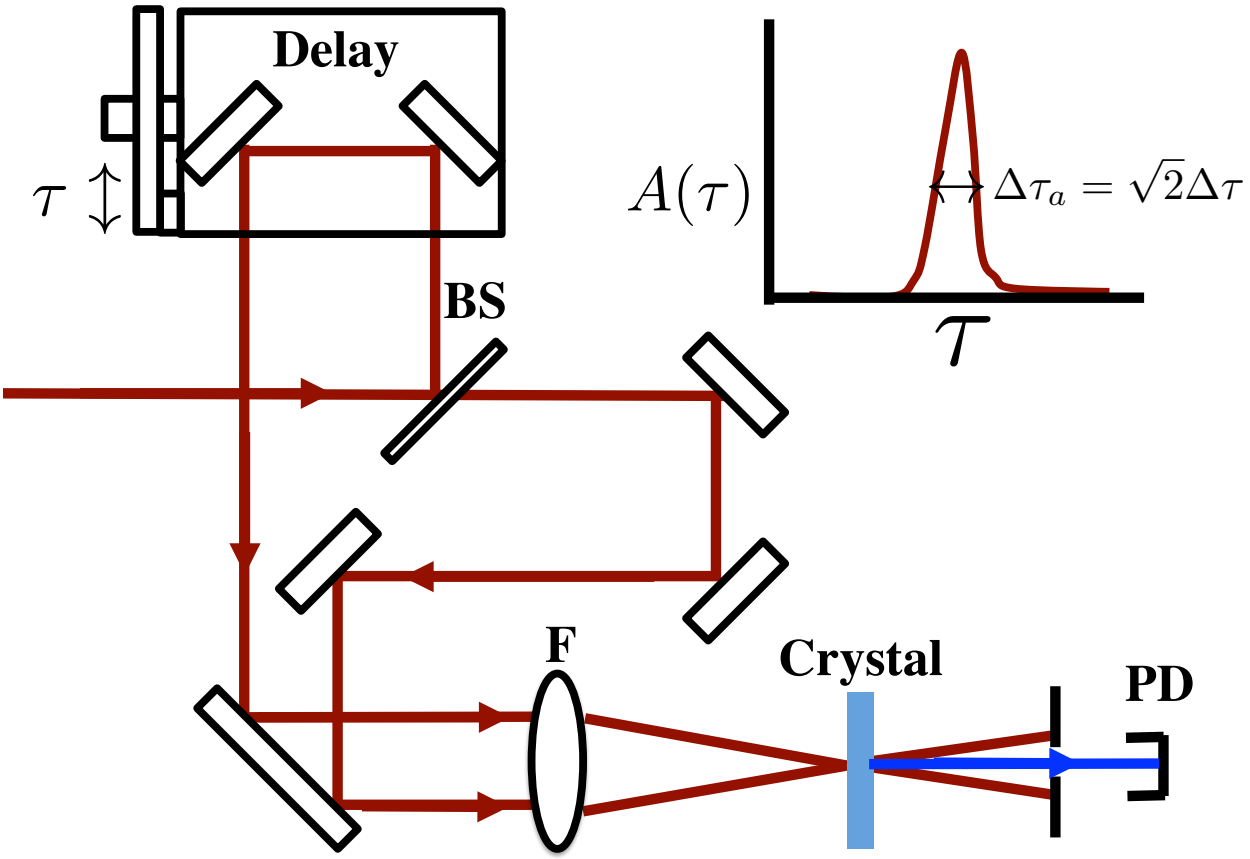

Figure 3.8: Example layout for an intensity autocorrelation measurement. BS - beam splitter, F - focusing element, PD - photodetector. The inset shows the measured signal, $A(\tau)$, as a function of delay, τ.

orders of magnitude slower than our femtosecond pulse durations. This necessitates an all optical measurement of the electric field.

There are dozens (and perhaps more) techniques that have been demonstrated over the last several decades for measuring pulses. The first in use is the intensity autocorrelator, which after 50 years, is still a widely used method for pulse width characterization[8]. The general layout is shown in figure 3.8.

An intensity autocorrelation measurement splits the incoming pulse into two identical "copies" using a beamsplitter. These two beams are sent through an interferometer that recombines them on a crystal using a focusing element, such as a lens or parabolic mirror. One arm is placed on a delay stage so that the time overlap can be controlled between the two

arms. The crystal will produce a signal that is dependent on the overlap of the two beams, and is shown in blue in figure 3.8. Details of how this signal is generated are explained in section 3.4.

The signal, which we can call $A(\tau)$, with τ being the delay between the two fields, is given by the following,

$$A(\tau) = \left| \int_{-\infty}^{\infty} \mathcal{E}(t)\mathcal{E}(t-\tau)dt \right|^2 . \tag{3.13}$$

We consider $\mathcal{E}(t)$ the field to be measured and $\mathcal{E}(t-\tau)$ the gate. The photodetector measures $A(\tau)$ in intensity, so the entire integrand is squared. After we substitute equation 3.1 into 3.13, we find

$$A(\tau) = \left| \int_{-\infty}^{\infty} \exp\left\{-\frac{2\ln(2)}{\Delta\tau^2}t^2\right\} \exp\left\{-\frac{2\ln(2)}{\Delta\tau^2}(t-\tau)^2\right\} dt \right|^2 , \tag{3.14}$$

$$= \left| \exp\left\{-\frac{2\ln(2)}{\Delta\tau^2}\tau^2\right\} \exp\left\{\frac{2\ln(2)}{\Delta\tau^2}\tau^2\right\} \right|^2 , \tag{3.15}$$

$$= \exp\left\{-\frac{4\ln(2)}{2\Delta\tau^2}\tau^2\right\} . \tag{3.16}$$

We can then define the FWHM of the autocorrelation signal, $\Delta\tau_a$ and, keeping in mind that we are now in intensity, we find that $\Delta\tau_a = \sqrt{2}\Delta\tau$. Thus, we can perform an intensity autocorrelation measurement on a Gaussian pulse and collect $A(\tau)$. We can then find $\Delta\tau_a$ and then the pulse duration of $\mathcal{E}(t)$ is found by dividing $\Delta\tau_a$ by $\sqrt{2}$.

In some applications, especially with picosecond pulses, intensity autocorrelation is a sufficient technique for measuring pulses. However, it comes with a number of drawbacks, the first of which is that it cannot retrieve the full electric field. That is, any of the phase profiles that can hamper the duration of a short femtosecond pulse cannot be extracted from an intensity autocorrelation measurement. If we want to know how to make our pulse shorter, we need a measurement technique that retrieves the full electric field. Perhaps an even bigger problem is that we do not have a priori information on the pulse shape, which can change the scaling factor for $\Delta\tau_a$ by an appreciable amount. For example, if we have a

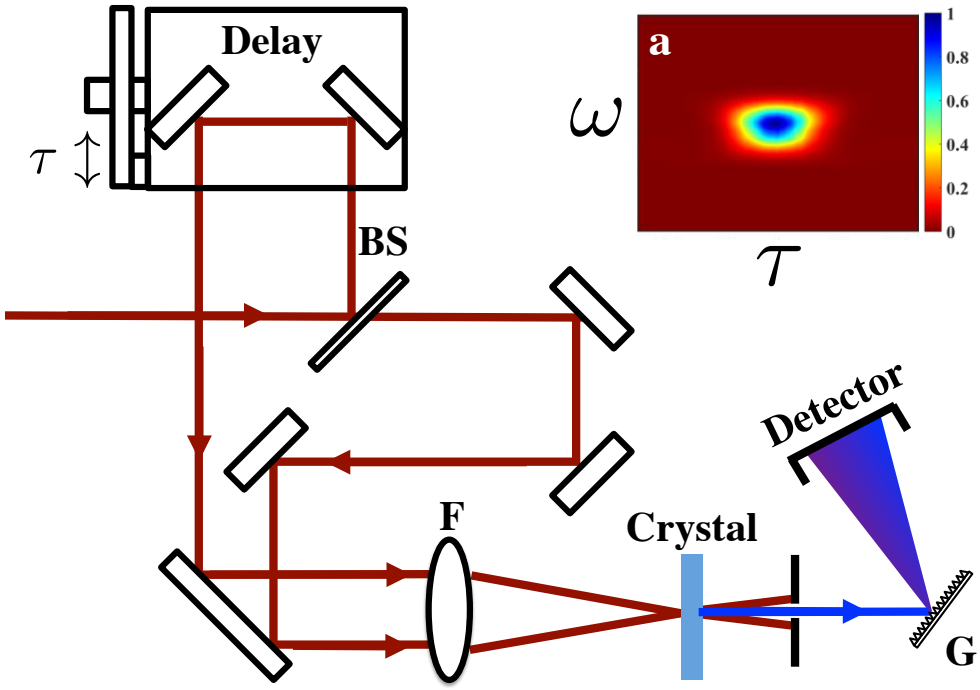

Figure 3.9: Example layout for a FROG measurement. BS - beam splitter, F - focusing element, G- grating. The inset shows the measured signal, $A^{(SHG)}(\omega, \tau)$.

sech^2 pulse shape rather than a Gaussian, the scaling factor goes from $\sqrt{2}$ to 1.55.

3.3.1 Frequency resolved optical gating

To measure the full electric field, we need a time resolved measurement that gives us spectral information. In this way, as we gate $E(t)$ with $E(t-\tau)$, we will see how the spectral content changes in the pulse over time. Thus, experimentally, the instrument for making this measurement is very similar to the intensity autocorrelator, except now the detector is placed after a grating to deliver spectral information, as shown in figure 3.9.

This method is called frequency resolved optical gating, and has the cute acronym, FROG[4] [79]. There are many variations to FROG, but I want to point out the two versions that I used extensively in my research. To start, I will cover the second-harmonic generation FROG (SHG-FROG). In this case, the measurement is again similar to an intensity

[4]Since FROG, it has become, to the bane of virtually everyone in ultrafast optics, a standard convention to name pulse characterization methods after animals.

autocorrelation except now we resolve the signal in frequency,

$$A^{(SHG)}(\omega,\tau) = \left| \int_{-\infty}^{\infty} \mathcal{E}(t)\mathcal{E}(t-\tau)\exp(-\mathrm{i}\omega t)dt \right|^2, \tag{3.17}$$

where $A^{(SHG)}(\omega,\tau)$ indicates that the measurement, called a spectrogram, is frequency resolved at each delay point, τ. An example of a spectrogram is shown in the inset of figure 3.9.

Unlike an intensity autocorrelation, which has a very simple method to analyze the signal, FROG requires a clever approach to interpreting the measurement. We cannot simply extract an electric field from the data. Instead, we use a sophisticated algorithm which starts with a guessed electric field, and proceeds to compare computed spectrograms with the measured spectrogram. After many iterations of guessing, it is hoped that the theoretical spectrogram delivered is very close to the measurement. We can reduce the guesswork in how well

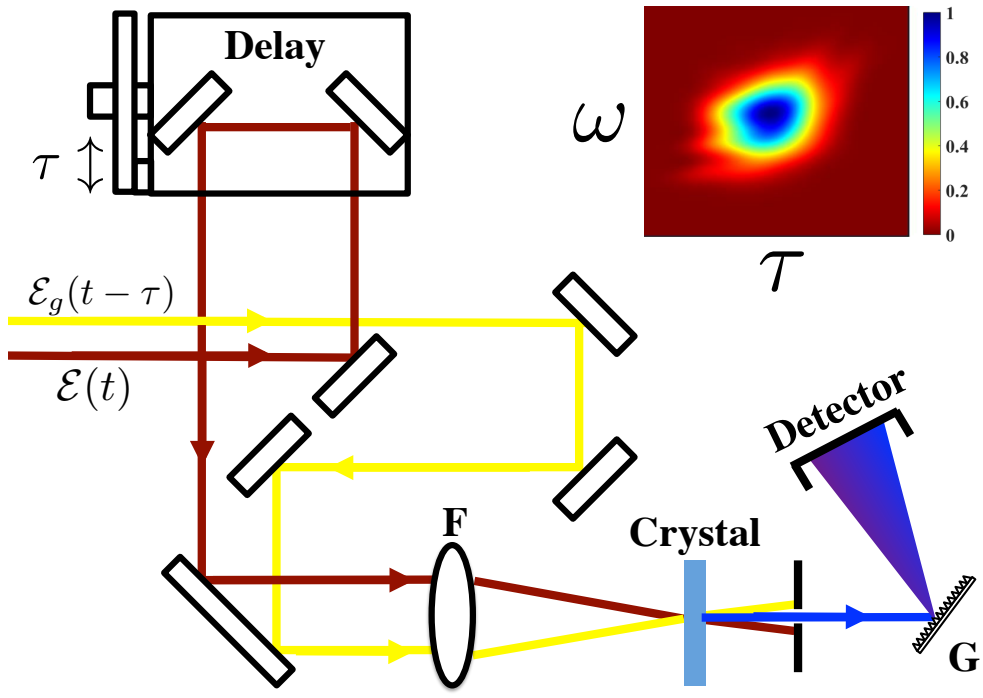

Figure 3.10: Example layout for a XFROG measurement. $\mathcal{E}_g(t-\tau)$- Gating field, $\mathcal{E}(t)$- Measured field, F - focusing element, G- grating. The inset shows the measured signal, $A^{(XFG)}(\omega,\tau)$.

our FROG retrieval algorithm performed with a quantity known as the FROG error, which essentially is a measurement of how close the theoretical and measured spectrograms compare with one another. In our lab, we use a commercially built algorithm called FROG V 3.2.2. from Femtosoft Technologies.

3.3.2 Cross-correlation frequency resolved optical gating

Most of the electric fields in our lab can be measured easily with the SHG-FROG technique. One exception is the long-wave infrared (LWIR, 5-10 μm) pulses from our results in chapter 6. For technical reason explained later, the signal $A^{(SHG)}(\omega,\tau)$, is very difficult to measure. While we could perform a simple autocorrelation, we prefer to still have the full electric field characterization made possible from the FROG method.

For this reason, we implemented a variation of the FROG method, known as cross-correlation FROG (XFROG) [80]. Besides giving full electric field characterization, the XFROG method has the added advantage of being easily measured in our lab. The technique, relies on a variation of the intensity autocorrelation, where the gate is no longer an identical copy of the pulse to be measured. This pulse, called the gate, $\mathcal{E}_g(t)$, can be any electric field, so long as it is fully characterized. In practice, it is best that the gating field is approximately the same duration as the field to be measured. The measurement then is quite similar to $A^{(SHG)}(\omega,\tau)$,

$$A^{(XFG)}(\omega,\tau) = \left| \int_{-\infty}^{\infty} \mathcal{E}(t)\mathcal{E}_g(t-\tau)\exp(-\mathrm{i}\omega t)dt \right|^2, \tag{3.18}$$

except $\mathcal{E}(t-\tau)$ is replaced with the gating field. In our lab, any available pulse that can be characterized with an SHG-FROG can be used as the gate. After obtaining $A^{(XFG)}(\omega,\tau)$, we can use the spectrogram along with the retrieved field, $\mathcal{E}_g(t)$ to find $\mathcal{E}(t)$ using a retrieval algorithm that is essentially a modification of the one for SHG-FROG. We use the FROG V 3.2.2. software from Femtosoft Technologies to retrieve $\mathcal{E}(t)$.

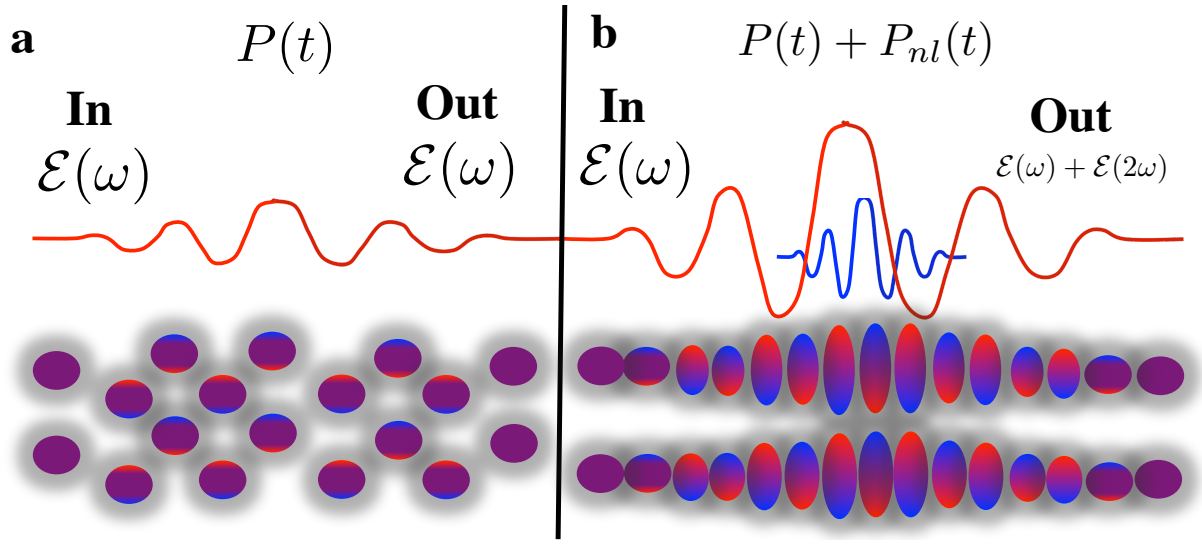

Figure 3.11: A physical explanation of nonlinear optics. **a** A weak AC field, $\mathcal{E}(\omega)$, produces a time dependent polarization, $P(t)$, which acts to propagate the field through the medium. **b** When $\mathcal{E}(\omega)$ is much stronger, the polarization field is no longer oscillates at just the driving frequency, but induces the term, $P_{nl}(t)$. This "nonlinear" polarization results in the production of new frequencies. In this examples, $P_{nl}(t)$ is a source for the field $\mathcal{E}(2\omega)$.

3.4 Introduction to nonlinear optics

We are now ready to discuss how we produce fields at arbitrary frequencies. For our purposes, the Ti:Sapph amplifier system is largely fixed in wavelength. Since we require it for the production of high peak power laser fields, we cannot simply get a new laser at a different wavelength if we desire something other than 800 nm.

To generate short, energetic electric fields, we use nonlinear optical effects. A pictogram in figure 3.11 gives a physical explanation for how this arises. When an electric field, $\mathcal{E}(t)$, is applied to a medium, the medium responds to the electric field with a net displacement of the electrons, resulting in a polarization field, $P(t)$, which we can describe as

$$P_l(t) = \epsilon_0 \chi^{(1)} \mathcal{E}(t). \tag{3.19}$$

Here, ϵ_0 is the permittivity of free space, and $\chi^{(1)}$ is the material's susceptibility, which describes how strongly it responds to electric field. Generally speaking, $\chi^{(1)}$ is a second-order

tensor because the media we are dealing with are not always isotropic in their susceptibility. However, if we limit ourselves to linear polarization so that field only propagates along a single orientation of the crystal, then $\chi^{(1)}$ can be treated as a scalar. We see in figure 3.11a that as the electric field (shown in red) passes through a medium, the individual atoms (purple) have displaced charge (indicated with red and blue on the poles). Because oscillating charges emit radiation, the medium in the weak field simply acts to continue propagating the field at the normal frequency ω.

In figure 3.11b, a much stronger field is applied to the medium. In this scenario, the polarization is no longer represented by just a linear field dependence but also has a response proportional to the square of the field

$$P(t) = P_l(t) + P_{nl}(t) = \epsilon_0(\chi^{(1)}\mathcal{E}(t) + \chi^{(2)}\mathcal{E}^2(t)), \tag{3.20}$$

where $\chi^{(2)}$ is the second order susceptibility. For the general case of second order nonlinearity, $\chi^{(2)}$ is in the form of a third rank tensor. As we did with $\chi^{(1)}$, shown earlier, we can again chose our initial conditions so that $\chi^{(2)}$ can be treated as a scalar[5]. In the particular scenario drawn in figure 3.11b, $P_{nl}(t)$ is driven such that the medium responds at twice the frequency of the fundamental, which generates a new electric field at twice the frequency, $\mathcal{E}(2\omega)$.

We can take a close look at this response by writing down the electric field as a composite of two CW fields.

$$\mathcal{E}(t) = E_1 \exp(-\mathrm{i}\omega_1 t) + E_2 \exp(-\mathrm{i}\omega_2 t) + c.c., \tag{3.21}$$

where E_1 and E_2 are the amplitudes to two frequency components of $\mathcal{E}(t)$ with frequencies ω_1 and ω_2, respectively, and *c.c.* indicates the complex conjugate of both terms. Up to now, this has not been written in the text but, because all electric fields are real (and the complex parts are just representations to make the math simpler), we can add these terms without changing $\mathcal{E}(t)$. They are useful to write in the next step, where we substitute equation 3.21

[5]See section 1.5.7. in Boyd *Nonlinear Optics* [76].

into $P_{nl}(t)$,

$$P_{nl}(t) = \epsilon_0 \chi^{(2)} \mathcal{E}(t) \mathcal{E}^*(t) \propto \tag{3.22}$$

$$\left[E_1 \exp\left(-\mathrm{i}\omega_1 t\right) + E_2 \exp\left(-\mathrm{i}\omega_2 t\right) + c.c.\right] \times \left[E_1 \exp\left(\mathrm{i}\omega_1 t\right) + E_2 \exp\left(\mathrm{i}\omega_2 t\right) + c.c.\right], \tag{3.23}$$

which, when factored out, becomes

$$P_{nl}(t) \propto \overbrace{E_1^2 + E_2^2}^{\text{OR}} + \overbrace{E_1^2 \exp\left(\mathrm{i}2\omega_1 t\right) + E_2^2 \exp\left(\mathrm{i}2\omega_2 t\right)}^{\text{SHG}} + \overbrace{E_1 E_2 \exp\left(\mathrm{i}(\omega_1 + \omega_2)t\right)}^{\text{SFG}} + \underbrace{E_1 E_2 \exp\left(\mathrm{i}(\omega_1 - \omega_2)t\right)}_{\text{DFG}} + c.c. \tag{3.24}$$

From here we see all the nonlinear mixing properties that can occur in a second order mixing process. Optical rectification (OR) is responsible for a DC field offset, which can produce fields in the single Terahertz range when driven by fields with large bandwidth. Second harmonic generation (SHG) is what we have already seen in figure 3.11, and produces a new field at twice the frequency. Sum frequency generation (SFG) is a more general analogue of SHG and is the addition of fields with arbitrary frequencies. Likewise, difference frequency generation (DFG) is something of a general analogue to OR with arbitrary frequencies, and yields a new field with a lower frequency than the inputs.

A nice demonstration of these mixing processes is shown in figure 3.12, which was generated in the HITS lab. Here we see two input fields, the pump (P, 800 nm) and the signal (S, 1340 nm). In this case the two fields are interacting in a nonlinear crystal called beta-barium borate (BBO). A variety of sum and difference frequency mixing processes are occurring in this figure. In this example the generated fields, labeled in green, are strong enough themselves to generate a sequential set of nonlinear mixing processes, shown in red, with another sequential set shown in blue.

Like all physical processes, nonlinear optics must satisfy the physical laws of conservation of energy and conservation of momentum. For this, it is easiest to use the photon description

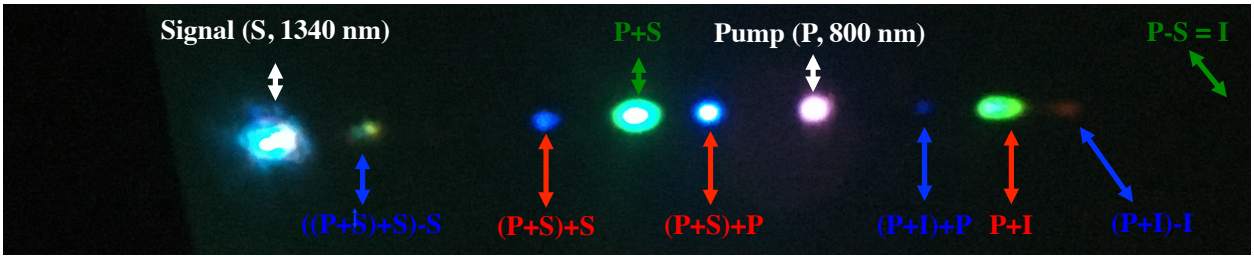

Figure 3.12: A demonstration of several sequential frequency mixing processes via nonlinear optics. The beams labeled white are the input pump (P) and signal (S) (which is actually invisible but propagates with stray light). Sum frequency and difference frequency (invisible since it is ~ 2000 nm) between these two fields are generated and labeled in green, including the idler (I) shown on the far right (I is also invisible but is approximately in the labeled location). Afterwards, additional sum frequency mixings occur, shown in red. Yet another series of sequential mixing processes occur that are labeled in blue. (picture was taken with my phone).

of light, where a photon has an energy $\hbar\omega$, with $\hbar$ being Planck's constant, and a momentum $\hbar k$, with k being the wave vector, $k = 2\pi/\lambda$. From conservation of energy, we find that photons can be split or combined, depending on the process, to form new photons. For example, in SHG and SFG, two photons are combined to yield a new photon with energy equal to the sum of both constiuents. In DFG, a higher energy photon is split into two photons, one with the same frequency as the second, and a third photon being their energy difference.

Conservation of momentum requires that the generated photon has a momentum that equals the sum of the initial photons in the process. For example, in SHG,

$$\mathbf{k} = k_1 + k_1 = 2\frac{2\pi}{\lambda_1} = \frac{2\pi}{\lambda_2} = k_2, \tag{3.25}$$

where $\lambda_2 = \lambda_1/2$ and corresponds to the wavelength of the second harmonic. In figure 3.12, the mixing fields enter at an angle with one another, causing the generated fields to propagate in different directions. For instance, the SFG $(P + S)$ between P and S, while the DFG (I) is to the right of P and S. We also see that $(P + S)$ is is closer to P than S, due to P's larger momentum contribution. We could go through every process shown in this image and verify that the conservation laws are verified. Personally, I find this image to be

one of the most beautiful illustrations of two of the most fundamental physical laws.

3.5 Difference frequency generation

Section 3.4 gave a simple person's overview of second order nonlinear optics. However, we should delve deeper into the derivations than what I have shown so far so we can gain additional insight into projects discussed in chapters 4-6 and 8. In all these chapters, our primary concern is with DFG. For that reason I will emphasize the peculiarities of DFG in this section. In several places, I will closely follow the work shown in Boyd *Nonlinear Optics*[76]. In section 3.5.2, I will continue with Boyd's notation but solve for a more general case of DFG.

3.5.1 General Solution

We start our derivation from the beginning using Maxwell's equations[6]

$$\nabla \cdot \mathbf{D} = 0 \qquad \nabla \cdot \mathbf{B} = 0 \tag{3.26}$$

$$\nabla \times \mathbf{E} = -\frac{\partial \mathbf{B}}{\partial t} \qquad \nabla \times \mathbf{H} = -\frac{\partial \mathbf{D}}{\partial t}. \tag{3.27}$$

Where I assume there are no free charges or current present, $\mathbf{B}$ is the magnetic field, $\mathbf{D} = \epsilon_0\mathbf{E} + \mathbf{P}$, and $\mathbf{H} = \mu_0\mathbf{B}$. ϵ_0 and μ_0 are the permittivity and permeability of free space, respectively.

If we take the curl of $\nabla \times \mathbf{E}$, we can can replace the right hand side of the equation with $-\mu_0 \frac{\partial \mathbf{D}}{\partial t}$ and use the identity

$$\nabla \times \nabla \times \mathbf{F} = \nabla(\nabla \cdot \mathbf{F}) - \nabla^2\mathbf{F}, \tag{3.28}$$

with $\mathbf{F}$ being any given vector. In particular, the relation between $\mathbf{D}$, $\mathbf{E}$, and $\mathbf{P}$ require us to

[6] I could try to start later in the derivation but it is much nicer for me to see where everything gets placed into the derivation.

take into account the consequence of the first term on the right of equation 3.28. In general, this term is usually very small and, in some simplifying cases, is identically zero. Thus, we will drop this term, giving us a nonlinearly driven wave equation:

$$\nabla^2\mathbf{E} - \frac{1}{c^2}\frac{\partial^2}{\partial t^2}\mathbf{E} = \frac{1}{\epsilon_0 c^2}\frac{\partial^2}{\partial t^2}\mathbf{P}, \tag{3.29}$$

where $\epsilon_0\mu_0 = 1/c^2$. Because $\mathbf{P}$ has both the linear and nonlinear polarization, as shown in equation 3.20, we can separate the terms to leave just $\mathbf{P}_{nl}$ on the right hand side.

$$\nabla^2\mathbf{E} - \frac{1}{c^2}\frac{\partial^2}{\partial t^2}\mathbf{D}_l = \frac{1}{\epsilon_0 c^2}\frac{\partial^2}{\partial t^2}\mathbf{P}_{nl}. \tag{3.30}$$

Here, we have defined $\mathbf{D}_l = \epsilon_0\mathbf{E}+\mathbf{P}_l$. If we take the nonlinearity susceptibility to be frequency independent then we can write the displacement field as $\mathbf{D}_l = \epsilon_0(1+\boldsymbol{\chi}^{(1)})\cdot\mathbf{E} = \boldsymbol{\epsilon}_r\cdot\mathbf{E}$, where $\boldsymbol{\epsilon}_r$ is a first rank tensor describing the material's permittivity. Then equation 3.30 becomes

$$\nabla^2\mathbf{E} - \frac{1}{c^2}\frac{\partial^2}{\partial t^2}\boldsymbol{\epsilon}_r\cdot\mathbf{E} = \frac{1}{\epsilon_0 c^2}\frac{\partial^2}{\partial t^2}\mathbf{P}_{nl}. \tag{3.31}$$

We see that this is the wave equation in a dispersionless, lossess medium with a source term given by the second time partial derivative of $\mathbf{P}_{nl}$. Thus, we can see now, for this simple derivation, that nonlinear optics can be described by a system of differential equations. Each equation in the system will be used to describe the evolution of the n^{th} field in the mixing process as they propagate through the medium. At this point, we can make some assumptions about the fields involved in the nonlinear mixing in order to give us some intuition into the DFG process. Let us say that the total field is described as a sum of n linearly polarized, plane-wave, monochromatic fields. This allows us to write $\mathbf{E}(t)$ as $\mathbf{E}(\mathbf{r},t) = \sum_n \mathbf{E}_n(\mathbf{r},t)$. Then the n^{th} field is given by

$$\mathbf{E}_n(\mathbf{r},t) = E_n(z,t) = A_n(z)\exp\left(\mathrm{i}(k_n z - \omega_n t)\right). \tag{3.32}$$

As E_n is linearly polarized, the field will have a fixed propagation through the nonlinear

medium, allowing us to reduce $\boldsymbol{\epsilon}_r$ to a scalar. Equation 3.31 takes the form,

$$\left[\frac{\partial^2}{\partial z^2}A_n + 2\mathrm{i}k_n\frac{\partial}{\partial z}A_n - k_n^2 A_n + \frac{\epsilon_r\omega_n^2}{c^2}A_n\right]\exp\left(\mathrm{i}(k_n z - \omega_n t)\right) = \frac{1}{\epsilon_0 c^2}\frac{\partial^2}{\partial t^2}P_{nl}; \tag{3.33}$$

and since $\omega_n\sqrt{\epsilon_r}/c = 2\pi n_r/\lambda_n = k_n$, the third and fourth terms on the left hand side cancel.

We are interested in DFG, lets start by solving for A_3[7]. The plane-wave approximation with three linearly polarized fields allows us to write,

$$P^{nl}(z,t) = \epsilon_o 4 d_{eff} A_1 A_2^* \exp\left[\mathrm{i}\left(k_1 - k_2\right)z - \mathrm{i}\omega_3 t\right]. \tag{3.34}$$

I substituted $\omega_3 = \omega_1 - \omega_2$ and $d_{eff} = 2\chi^{(2)}$, which is a scalar due to the simplifications made earlier. Then 3.33 becomes,

$$\left[\frac{\partial^2}{\partial z^2}A_3 + 2\mathrm{i}k_3\frac{\partial}{\partial z}A_3\right] = \frac{-\omega_3^2}{c^2}4 d_{eff} A_1 A_2^* \exp\left[\mathrm{i}\left(k_1 - k_2 - k_3\right)z\right]. \tag{3.35}$$

In general, the remaining term in the exponential is not always zero. We call this the phase matching condition and replace $k_1 - k_2 - k_3$ with Δk. Also, between the two terms on the left hand side, we will assume that the second derivative evolves on a much slower scale than the first derivative. This holds well when the medium is not driven too strongly, and is called the slowly varying envelope approximation. We are then left with the rather simple relation

$$\frac{\partial}{\partial z}A_3 = \frac{2\mathrm{i}\omega_3^2}{k_3 c^2} d_{eff} A_1 A_2^* \exp\left[\mathrm{i}\Delta k z\right]. \tag{3.36}$$

We can go through this same derivation for A_1 and A_2:

$$\frac{\partial}{\partial z}A_1 = \frac{2\mathrm{i}\omega_1^2}{k_1 c^2} d_{eff} A_2 A_3 \exp\left[-\mathrm{i}\Delta k z\right], \tag{3.37}$$

$$\frac{\partial}{\partial z}A_2 = \frac{2\mathrm{i}\omega_2^2}{k_2 c^2} d_{eff} A_1 A_3^* \exp\left[\mathrm{i}\Delta k z\right]. \tag{3.38}$$

[7]We will take the convention that $\omega_1 \geq \omega_2 \geq \omega_3$. We will refer to these three as the pump, signal, and idler, respectively.

And that completes the system of equations for DFG.

We can gain some insight into the physical processes of DFG, and nonlinear optics in general, by considering the consequences of the system of equations shown in 3.36, 3.37, and 3.38. Regardless of the initial amplitude of the three fields, if $d_{eff} = 0$ then there is no nonlinear mixing between the fields. In that scenario, they would continue to propagate without any conversion between one another. However, if $d_{eff} \neq 0$, then given a medium of suitable length, nonlinear conversion will take place. The magnitude of d_{eff} for a given medium is one of the critical considerations for designing a nonlinear amplifier because it dictates how efficiently the conversion takes place during the process.

3.5.2 Weak signal limit: optical parametric amplification

DFG starts with two high frequency fields, $\mathcal{E}_1$ and $\mathcal{E}_2$, which mix to either generate $\mathcal{E}_3$, or amplify $\mathcal{E}_2$ and generate $\mathcal{E}_3$ simultaneously. These are limiting cases of two regimes of DFG, the latter of which we refer to as optical parametric amplification (OPA). Because OPA starts with $\mathcal{E}_2$ being much weaker than the pump, $\mathcal{E}_1$, the extraction of energy from the pump field does not change its amplitude much with propagation through the crystal. For this reason, we can make an approximation and assume that equation 3.37 is zero, and A_1 is a constant. At this point, if only the phase matching, Δk, were zero then we could give this to our undergraduate for homework in differential equations.

Instead, we can go ahead and give it to our undergrad anyway, and make them guess a solution. Since the solution with $\Delta k = 0$ clearly has the form of hyperbolic sine and cosine, we can try to guess something of the following form

$$A_3(z) = \left\{Be^{gz} + Ce^{-gz}\right\} \exp(\mathrm{i}\Delta k z/2) \tag{3.39}$$

$$A_2(z) = \left\{De^{gz} + He^{-gz}\right\} \exp(\mathrm{i}\Delta k z/2) \tag{3.40}$$

where B, C, D, H, and g remain undetermined. We can use these solutions in equations

3.38 and 3.36:

$$g(Be^{gz} - Ce^{-gz})\exp(\mathrm{i}\Delta kz/2) + \frac{\mathrm{i}\Delta k}{2}(Be^{gz} + Ce^{-gz})\exp(\mathrm{i}\Delta kz/2)$$
$$= \Phi_3\left\{De^{gz} + He^{-gz}\right\}\exp(\mathrm{i}\Delta kz/2),$$

$$g(De^{gz} - He^{-gz})\exp(\mathrm{i}\Delta kz/2) + \frac{\mathrm{i}\Delta k}{2}(De^{gz} + He^{-gz})\exp(\mathrm{i}\Delta kz/2)$$
$$= \Phi_2\left\{Be^{gz} + Ce^{-gz}\right\}\exp(\mathrm{i}\Delta kz/2). \quad (3.41)$$

Our clever manipulation of the complex term allows us to drop it from both equations. Φ_3 and Φ_2 are the z independent coefficients on the right hand side of equations 3.38 and 3.36, respectively. At this point we consider that both these equations must hold for all z, and the terms in each equation involving e^{gz} and e^{-gz} must satisfy this condition separately. This leaves us with four equations:

$$B\left(g + \frac{\mathrm{i}\Delta k}{2}\right) = D\Phi_3, \quad (3.42)$$
$$C\left(-g + \frac{\mathrm{i}\Delta k}{2}\right) = H\Phi_3, \quad (3.43)$$
$$D\left(g + \frac{\mathrm{i}\Delta k}{2}\right) = B\Phi_2, \quad (3.44)$$
$$H\left(-g + \frac{\mathrm{i}\Delta k}{2}\right) = C\Phi_2. \quad (3.45)$$

The first and third equations can be placed in matrix form, as well as the second and fourth:

$$\begin{bmatrix} \left(g + \frac{\mathrm{i}\Delta k}{2}\right) & -\Phi_3 \\ -\Phi_2 & \left(g + \frac{\mathrm{i}\Delta k}{2}\right) \end{bmatrix} \begin{bmatrix} B \\ D \end{bmatrix} = \begin{bmatrix} 0 \\ 0 \end{bmatrix}, \quad (3.46)$$

$$\begin{bmatrix} \left(-g + \frac{\mathrm{i}\Delta k}{2}\right) & -\Phi_3 \\ -\Phi_2 & \left(-g + \frac{\mathrm{i}\Delta k}{2}\right) \end{bmatrix} \begin{bmatrix} C \\ H \end{bmatrix} = \begin{bmatrix} 0 \\ 0 \end{bmatrix}. \quad (3.47)$$

Now we just take the determinant to find the solutions for g. After rearranging we find

the following

$$g = \sqrt{\Phi_2 \Phi_3} + \frac{\mathrm{i}\Delta k}{2}. \tag{3.48}$$

We have taken only one root because our guessed solution in equation 3.40 already accounts for both roots. Now we can assume some typical boundary conditions. Since we seed with the signal, the idler is initially zero, so $A_3(0) = 0$. So $B = -C$ and we find that

$$\begin{aligned} A_3(z) = 2B \sinh(gz) \exp(\mathrm{i}\Delta k z/2) &= 2B \sinh\left(\left(\kappa + \frac{\mathrm{i}\Delta k}{2}\right) z\right) \exp(\mathrm{i}\Delta k z/2) \\ &= 2B \left[\sinh(\kappa z)\cos(\Delta k z/2) + \cosh(\kappa z)\sin(\Delta k z/2)\right] \exp(\mathrm{i}\Delta k z/2), \end{aligned} \tag{3.49}$$

where $\kappa = -\sqrt{\Phi_2 \Phi_3}$. Likewise, we can say that the signal starts with a given amplitude $A_2(0) = A_{20}$. Then $H = A_{20} - D$ and we get

$$A_2(z) = 2D \left[\sinh(\kappa z)\cos(\Delta k z/2) + \cosh(\kappa z)\sin(\Delta k z/2)\right] \exp(\mathrm{i}\Delta k z/2) - A_{20} e^{-\kappa z}. \tag{3.50}$$

We can then use equations 3.38 and 3.36 to find B and D. We find that

$$B = \frac{-\Phi_3 A_{20}}{2(\kappa + \Delta k/2)}, \tag{3.51}$$

$$D = \frac{-\kappa A_{20}}{2(\kappa + \Delta k/2)}. \tag{3.52}$$

If we take the limiting case that $\Delta k = 0$ then we see that

$$A_2(z) = A_{20} \cosh(\kappa z), \tag{3.53}$$

$$A_3(z) = \sqrt{\frac{\Phi_3}{\Phi_2}} A_{20} \sinh(\kappa z), \tag{3.54}$$

and we get the nice simple result we expected if we assumed this in equations 3.38 and 3.36.

Results for DFG amplification with propagation distance are shown in figure 3.13 for a BBO crystal. The process is set to phase match a weak (1 MW/cm^2) signal (A_2) at 1400 nm

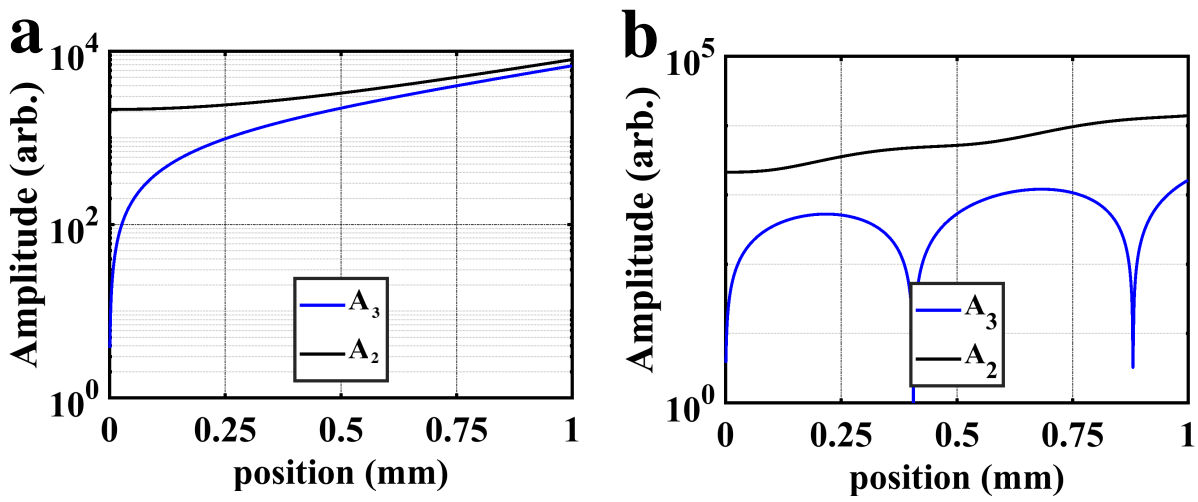

Figure 3.13: Effects of phase matching on DFG amplification. **a** When $\Delta k = 0$. **b** When $\Delta k \neq 0$.

with $\sim$ TW/cm^2 level pump at 790 nm, and produce a field, A_3 with a wavelength near 1810 nm. For small z in figure 3.13a, we see that A_3 receives exponential gain. This is unique to DFG among the $\chi^{(2)}$ processes, as other processes receive only quadratic gain, and therefore, can be much less efficient in their amplification. About half-way through the crystal, A_3 approaches the field strength of A_2 and both fields continue to amplify as they propagate through the crystal. When $\Delta k \neq 0$, as shown in figure 3.13b, we see that the amplification of A_3 can oscillate in strength as it propagates through the crystal.

This behavior is extremely important for our considerations, as the pulses we deal with have broad-bandwidth. Given that Δk depends on the value of the k-vectors for all fields involved in the DFG interaction, we see from this figure that it is important to keep Δk as close to zero as possible. This is very tricky because k depends on both the wavelength and the refractive index of the material at that wavelength.

To maximize the efficiency of DFG across a large bandwidth range, we seek to keep the crystal thin, as the unwanted effects from $\Delta k \neq 0$ arise when the beam propagates a large distance in the crystal. However, we see that for well phase-matched processes, we receive more gain when the beams have a longer interaction length. It is our desire to have both of these results! To combat this requires careful planning for the DFG process, including beam

diameter, crystal choice, and crystal dimensions. In some cases, it can be possible to find crystals where d_{eff} is very high, and because d_{eff} and Δk are independent, one can design a DFG amplification with high gain in a short propagation length, maintaining the broad bandwidth.

3.5.3 Other approximations for DFG

Our derivation for DFG in the previous section makes many assumptions. For instance, we assume that the beams are monochromatic, plane waves, and that the pump (A_1) does not deplete with propagation in the crystal. There are many cases where some, or all, of these approximations are no longer valid. For instance, if we take our DFG to occur at the focus of a beam (which is typical for the initial amplifier stage), the wave-front radius-of-curvature can be large enough that the system deviates far from the plane-wave approximation. As we discussed at the end of the previous section, our broadband pulses require us to consider the effects of bandwidth and pulse duration on the nonlinear mixing process.

In this section, I will briefly cover solutions to DFG amplification that do not make these approximations. For the sake of saving pages of derivation, I will only show the solutions and discuss their implications.

A_1 depletion

In the case that $\frac{d}{dz}A_1 \neq 0$ (with plane-wave and monochromatic assumptions still in place), we are simply left with a system of three equations for 3.36, 3.37, and 3.38. While we can solve this analytically[81], we can also implement a much less painful solution computationally with software such as Matlab.[8]

Figure 3.14 shows the effects from when the depletion of A_1 is included. Up until the position $z = 0.5$ mm, we see that the full solution follows our depleted pump approximation. Unlike our previous derivation, we see energy conservation in the form of A_1 decreasing significantly when A_2 and A_3 reach their maximum. We also see that, despite $\Delta k = 0$, after

[8] In fact, this was much easier than the derivation in the previous section.

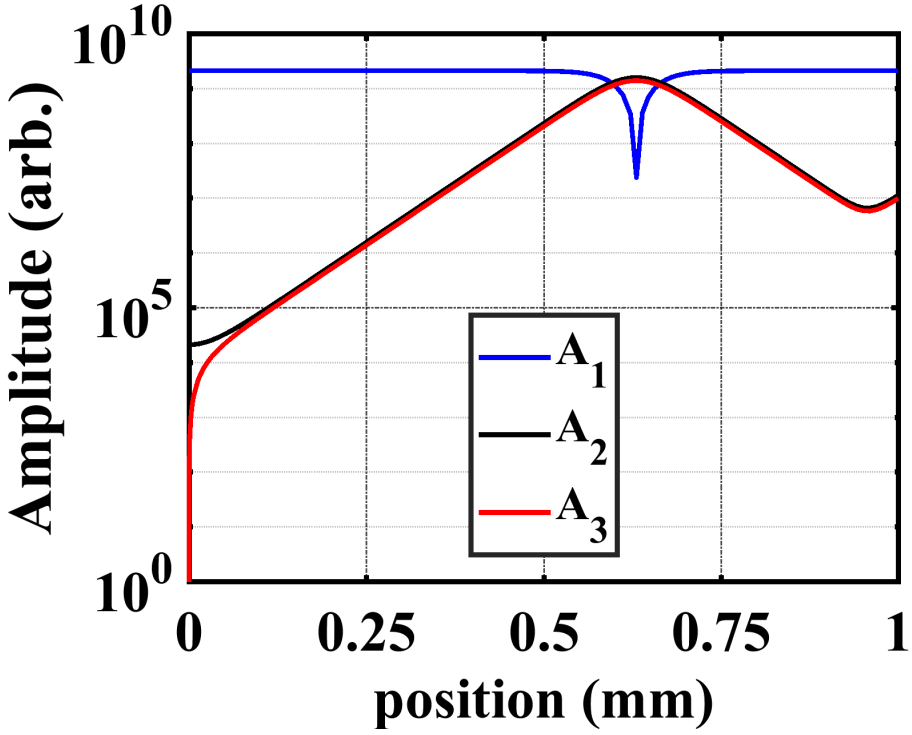

Figure 3.14: Effects of pump (A_1) depletion on DFG amplification.

the interaction has optimized A_2 and A_3, the process reverses and A_1 begins to increase again. This process, known as back-conversion, is yet another limitation on nonlinear amplification that we need to be mindful of.

Transverse beam propagation

In general, a beam must be expressed with an amplitude that depends on transverse (r) and longitudinal (z) coordinates. A common description of the profile of a mode through a focus can be represented as

$$A(r,z) = A_0 \frac{w_0}{w(z)} \exp\left[-\frac{r^2}{w(z)^2} + \frac{\mathrm{i}kr}{2R(z)} + \mathrm{i}\Phi(z)\right], \tag{3.55}$$

where w_0 is the $1/\mathrm{e}^2$ beam radius at the focus (beam waist), $w(z)$ is the $1/\mathrm{e}^2$ beam radius at position z, $R(z)$ is the radius of curvature of the beam at position z, and $\Phi(z)$ indicates how the phase varies in space.

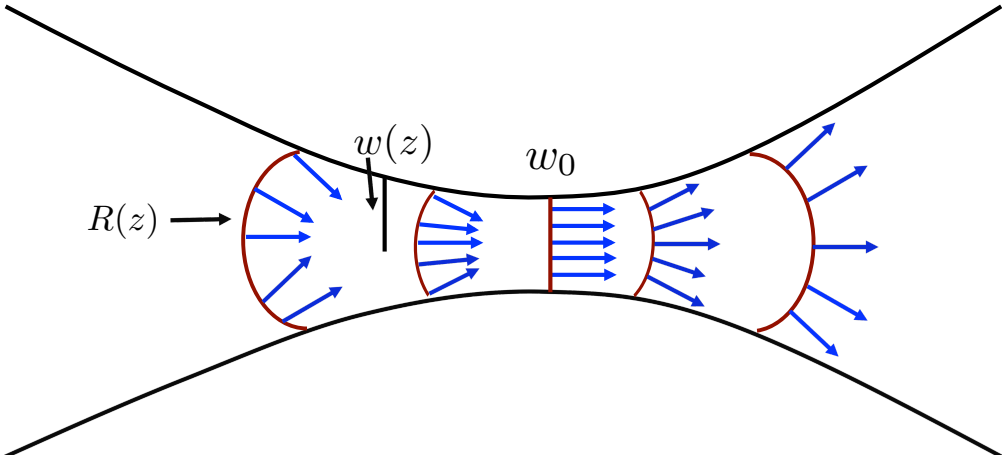

Figure 3.15: Profile of Gaussian beam through a focus. $R(z)$-radius of curvature (red line), $w(z)$-$1/e^2$ beam radius at position z, w_0 $1/e^2$ beam radius at focus (beam waist), blue arrows indicate direction of k vectors at position $A(r, z)$.

These effects are illustrated in figure 3.15 where the black curves indicate the variation of the beam diameter through the focus, the red lines indicate the radius of curvature at z, and the blue arrows indicate the directionality of k at position r and z.

With tight focusing, we see that the k-vectors can change dramatically through the focus. This implies that the phase matching constraints we made before with $\Delta k = k_1 - k_2 - k_3$ need to be modified when the spatial profile of a beam changes dramatically with propagation. In situations where the nonlinear process occurs at the focus of the beam, we need to make special emphasis on the modification of the k-vectors. There exists solutions for this in the literature[76] but I believe that the physical explanation given through figure 3.15 is sufficient for understanding the work of chapter 8.

Ultrafast pulses

The final approximation we should discuss is that of the monochromatic field. As we have discussed in the earlier parts of this chapter, we are working with fields that are far from being a single frequency. If we want a model that gives a true representation of our nonlinear amplification, we must include the effects due to the nature of broad-bandwidth fields. While this description is essential for representing our nonlinear interactions, the derivation is

tedious, so I only want to highlight essential points.

Starting with equation 3.30, we can modify the representation of the fields by including their bandwidth,

$$\mathcal{E}(t) = \frac{1}{\sqrt{2\pi}} \int \tilde{\mathcal{E}}(\omega) \exp(\mathrm{i}\omega t) d\omega, \tag{3.56}$$

$$\mathcal{D}_l(t) = \frac{1}{\sqrt{2\pi}} \int \tilde{\mathcal{D}}_l(\omega) \exp(\mathrm{i}\omega t) d\omega, \tag{3.57}$$

$$\mathcal{P}(t) = \frac{1}{\sqrt{2\pi}} \int \tilde{\mathcal{P}}(\omega) \exp(\mathrm{i}\omega t) d\omega, \tag{3.58}$$

where $\tilde{\mathcal{E}}(\omega)$, $\tilde{\mathcal{D}}_l(\omega)$, and $\tilde{\mathcal{E}}(\omega)$ are the field, linear displacement field (including linear susceptibility), and the nonlinear polarization field, respectively. If we assume plane wave, and the slowly varying envelope approximation are valid, then we can arrive at the following representation of the wave equation,

$$\left[2\mathrm{i}k_3^{(0)}\left(\frac{\partial}{\partial z} + k_3^{(1)}\frac{\partial}{\partial t}\right) + 2\mathrm{i}k_3^{(1)} D\frac{\partial}{\partial t} + 2k_3^{(0)} D - k_3^{(1)}\frac{\partial^2}{\partial t^2}\right] A_3(z,t) = \frac{1}{\epsilon_0 c^2}\frac{\partial^2 \mathcal{P}}{\partial t^2} \exp(-\mathrm{i}(k_3^{(0)} z - \omega_3^{(0)} t)), \tag{3.59}$$

where $\omega_3^{(0)}$ is the central frequency of field $A_3(z,t)$, and we now describe $k_3(\omega)$ as a power series,

$$k_3(\omega) = \sum_{n=0}^{\infty} \frac{1}{n!} k_3^{(n)} (\omega - \omega_0)^n, \tag{3.60}$$

where D is

$$D = \sum_{n=2}^{\infty} \frac{1}{n} k_3^{(n)} \left(\mathrm{i}\frac{\partial}{\partial t}\right)^n, \tag{3.61}$$

and $\mathcal{P}$ is

$$\mathcal{P}(z,t) = 4\epsilon_0 d_{eff} A_1(z,t) A_2^*(z,t) \exp\left[\mathrm{i}(k_1^{(0)} - k_2^{(0)})z - \mathrm{i}(\omega_1^{(0)} - \omega_2^{(0)})t\right]. \tag{3.62}$$

We then find that

$$\left[2\mathrm{i}k_3^{(0)}\left(\frac{\partial}{\partial z}+k_3^{(1)}\frac{\partial}{\partial t}\right)+2\mathrm{i}k_3^{(1)}D\frac{\partial}{\partial t}+2k_3^{(0)}D-k_3^{(1)}\frac{\partial^2}{\partial t^2}\right]A_3(z,t)$$
$$=\frac{4d_{eff}}{c^2}\frac{\partial^2}{\partial t^2}A_1(z,t)A_2^*(z,t)\exp\left[\mathrm{i}\Delta k^{(0)}z\right], \quad (3.63)$$

with $\Delta k^{(0)}$ being the phase matching condition for the central k vectors. As before, similar derivations can be made for the fields $A_1(z,t)$ and $A_2(z,t)$.

While this derivation contains many terms, we can see a few important features pertaining to ultrafast pulses not present in the monochromatic case. For instance, the power series expansion of $k(\omega)$ allows us to separate out the effects of phase velocity ($k_3^{(0)}$), group velocity ($k_3^{(1)}$), GDD and other higher order dispersions (D).

When the pulses are short, the group velocity, v_g, places a limitation on the interaction length in the medium. While we must choose $k_i^{(0)}$ so that $\Delta k^{(0)}=0$, we have to live with corresponding values for $k_i^{(1)}$ which, in general, are different for the three interacting fields. Thus, the three envelopes travel at different speeds in the medium and after sometime, cease to overlap with one another. This is illustrated in figure 3.16a. In most situations, the index for v_g decreases with wavelength, meaning that the pump field envelope (shown in blue) propagates at a slower speed than the signal (green) and idler (red).

One way around this affect is to choose a phase matching type that gives the pump an intermediate group velocity, as illustrated in figure 3.16b [82;83]. This is possible under certain phase matching types because of the choice of which field is polarized along which axis. Most crystals (that I use) are negative uniaxial, which means that there is only one extraordinary axis and that it has a lower refractive index than the ordinary plane. We achieve phase matching when the pump is polarized along this axis. This allows it to have a faster group velocity than the signal. which is still polarized along the ordinary axis. Thus, by placing the idler along the same axis as the pump, we can ensure that the pump is always slower than the idler and faster than the pump. In this scenario, even though the signal lags the pump, the idler will continue to pass through the pump and receive amplification, which

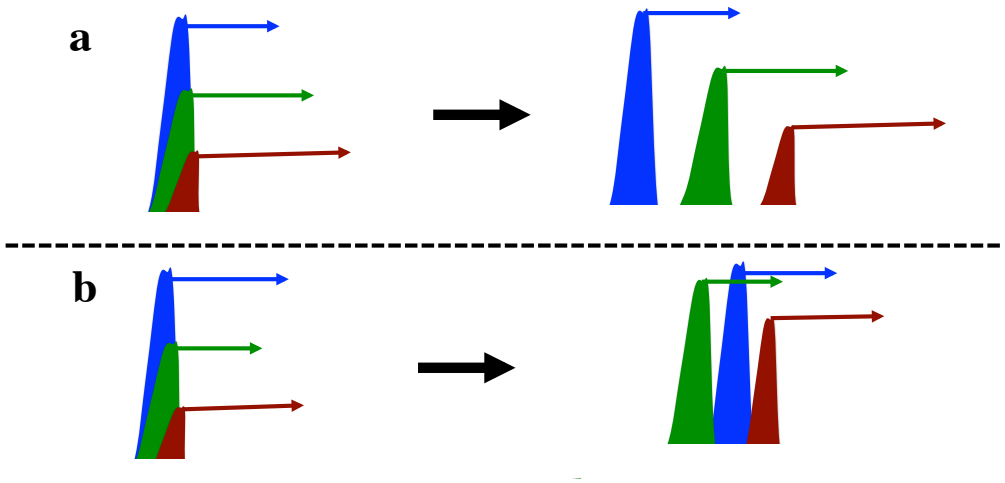

Figure 3.16: **a** Illustration of the effects due to group velocity, v_g on a three wave interaction. Pump is shown in blue, signal is shown in green, and idler is shown in red. The length of the arrows indicate the magnitude of v_g. **b** Alternate construction of a three wave interaction so that the pump field has an intermediate v_g with respect to the signal and idler.

maintains amplification of the signal. Thus the three-wave mixing can be maintained for a much longer distance.

3.6 $\chi^{(3)}$ processes, self phase modulation

So far, we have limited our discussion for nonlinear optics to processes involving $\chi^{(2)}$ interactions. While these are very useful for changing the wavelength of our laser, there are interactions involving higher order nonlinearities that can deliver electric fields not possible from a laser or $\chi^{(2)}$ alone. As a final section to this chapter, I will include a derivation for $\chi^{(3)}$ interactions, and describe their consequences which are relevant for the work in this thesis. This derivation mixes elements from solutions in Boyd *Nonlinear Optics*[76] and Agrawal *Nonlinear Fiber Optics*[75].

For our basic level of understanding, we can use the work derived for 3.35. Specifically, we are interested in a $\chi^{(3)}$ effect which is proportional to $|\mathcal{E}(t)|^2 \mathcal{E}(t) = I(t)\mathcal{E}(t)$, where $I(t)$

is the pulse intensity profile in time. Thus, we represent $P^{nl}(z,t)$ as

$$P^{nl}(z,t) = \epsilon_o \frac{3}{2} d_{eff} \left|A_1\right|^2 A_1 \exp\left[\mathrm{i}k_1 z - \mathrm{i}\omega_1 t\right], \tag{3.64}$$

where, in this case, $d_{eff} = \chi^{(3)}/2$. We can now substitute this into equation 3.35 and find the following

$$\frac{\partial}{\partial z} A_1 = \mathrm{i}\frac{3\omega_1^2}{4k_1 c^2} d_{eff} \left|A_1\right|^2 A_1. \tag{3.65}$$

We can make the following substitutions for the coefficients that allow us to better interpret the result:

$$\left|A_1\right|^2 = \frac{2}{n^{(1)}\epsilon_0 c} I(t), \tag{3.66}$$

$$\frac{c}{n^{(1)}} = \frac{\omega_1}{k_1}, \tag{3.67}$$

where $n^{(1)}$ is the linear refractive index for ω_1. We then find,

$$\frac{\partial}{\partial z} A_1 = \mathrm{i}\frac{3\omega_1}{n^{(1)2} 2c^2} d_{eff} I(t) A_1, \tag{3.68}$$

and finally, we substitute the nonlinear refractive index,

$$n_2 = \frac{3}{2}\frac{d_{eff}}{n^{(1)2}\epsilon_0 c}, \tag{3.69}$$

and we are left with

$$\frac{\partial}{\partial z} A_1 = \mathrm{i}\frac{\omega_1 n_2}{c} I(t) A_1. \tag{3.70}$$

To solve this, let's write A_1 in a form of a complex field in polar coordinates:

$$A_1 = V_0 \exp(\mathrm{i}\Phi_{nl}). \tag{3.71}$$

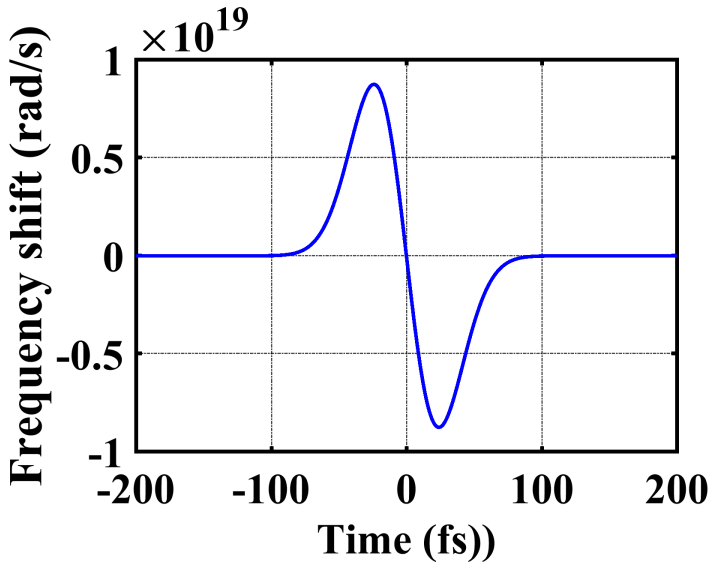

Figure 3.17: The frequency shift in time for a pulse undergoing self phase modulation (SPM).

Here, V_0 is the amplitude and we will call Φ_{nl} the nonlinear phase.

This can be solved without any trouble if we take the assumption that $\frac{d}{dz}V_0 = 0$,

$$\frac{d}{dz}\Phi_{nl} = \frac{\omega_1 n_2 I(t)}{c}, \tag{3.72}$$

and after the simple integration,

$$\Phi_{nl} = \frac{\omega_1 n_2 I(t)}{c} L, \tag{3.73}$$

where L is the length of the medium of propagation.

To gain a little insight into this result, we can find the instantaneous frequency $\delta\omega(t)$ by taking a time derivative on Φ_{nl}. To do that, we need some information about our pulse, $I(t)$. We can simply leave this as a Gaussian, which is represented in intensity as

$$I(t) = I_0 \exp\left(-4\ln(2)\frac{t^2}{\Delta\tau^2}\right), \tag{3.74}$$

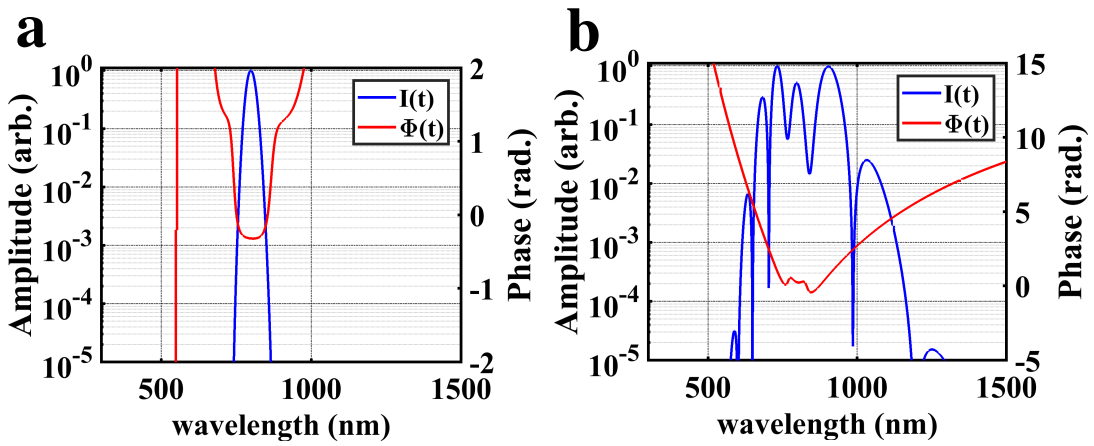

Figure 3.18: **a** When a field is weak and propagating through a medium with an n_2, it has the ability maintain its initial electric field characteristics. **b** A much stronger laser field has the ability to produce a spectral plateau due to the frequencies added with the phase shift.

which tells us that the frequency shift in time goes as

$$\delta\omega(t) = -\frac{\omega_1 n_2}{c} L \frac{8\ln(2)t}{\Delta\tau^2} I(t). \tag{3.75}$$

We conclude that, when the intensity is high and the envelope changes quickly in time, the frequency components of the electric field can substantially increase. This is further illustrated in figure 3.17, where the frequency shift is shown in time. Furthermore, figure 3.17 shows us that the pulse undergoes a shift towards lower frequencies at the front of the pulse ($t \geq 0$) and a corresponding shift to higher frequencies at the back of the pulse.

This process, known as self phase modulation (SPM), is responsible for producing laser fields with bandwidth supporting few-cycle laser fields at the milli-Joule level. This is illustrated in figure 3.18 by comparing the frequency broadening of a weak laser field (3.18a) and a strong field (3.18b) under the influence of the same material. In this case, the fields propagate through a 3 mm thick, fused silica window. The weak field experiences virtually no frequency broadening and has a correspondingly minimal phase shift across the spectrum. Meanwhile, the strong field produces a broad bandwidth which extends toward an octave spanning spectrum.

The generation of broadband, strong laser fields will be discussed in chapters 4 and 5. However, I would like to give a basic overview of the process. Since we start with strong laser fields, we need a method that allows us to perform SPM that can manage the power without damage. For this reason, solid materials are a poor choice because of their low damage thresholds. Instead, we can use a gas, as the damage threshold (ionization probability) is much higher and we can easily replace it. The drawback is that the n_2 of gases is pretty low, so we need to propagate on the order of a meter or more for effective SPM. For this reason, we use a hollow fiber[9] which guides the pulse in a confined, gas filled center. The light is delivered so that it goes through the fiber at a high ($\lesssim$90 degree) angle of incidence so that losses are minimized. With this configuration, virtually no light couples into the capillary's cladding, allowing for very high pulse energies and average powers to be propagated without damage. Then, it is a simple matter of delivering gas to the hollow core. The capillary is usually placed in a vacuum chamber which allows for removing atmospheric gas from the system and delivering pure gas samples ($\sim$ 99%). This allows for tunability in SPM by controlling the species of gas and the pressure.

[9]They are more properly referred to as capillaries, because fibers guide light through a material with a higher index than the cladding. However, this is the name we are stuck with.

Chapter 4

A CEP stable terawatt class laser with wavelength tunability

Much of the work in this chapter was shown in a previous publication[84].

This chapter will go through the details of the High Intensity Tunable Source (HITS) laser at Kansas State University. HITS was installed during the second year of my PhD and is the backbone for much of my research. The laser has some features which were designed in collaboration with the company who built the laser, Kapteyn-Murnane Laboratories, and were published in the journal, Optics Express[84]. This chapter serves to highlight the work that went into making the laser while providing a background on its capabilities we utilize in work shown in later chapters.

Much effort has been put into the pursuit of shorter and more energetic laser pulses with an ultimate goal of measuring, studying and controlling electronic dynamics, which naturally occur on the attosecond time scale[85]. Seminal work in the last two decades boosted pulse energies to milijoule (mJ) or even joule level while achieving pulse durations as short as a few fs. The former was achieved using the chirped-pulse-amplification (CPA) technique[64], and the latter was realized through nonlinear optical processes such as self-

Figure 4.1: The HITS laser after installation in the James Macdonald Laboratory.

phase-modulation (SPM) in a gas filled hollow-core fiber (HCF)[86] or via filamentation[65]. Owing to development in both areas, terawatt[87], or even petawatt[88] class lasers are now available.

However, further accessing even shorter, non-sinusoidal, light transient waveforms in the optical regime with a high energy has been quite challenging due to experimental difficulties in coherently generating multi-octave bandwidths, as well as compensating for the resulting dispersion. Recently, the technique of synthesizing laser pulses covering different spectral regions[89–92] has shown promise for generating energetic non-sinusoidal, light transient waveforms. This technique also provides the ability to tailor light transient waveforms for potential applications such as arbitrary waveform generation[92], quantum control[93], etc. Nevertheless, the key ingredient for a light field synthesizer, a carrier-envelope-phase (CEP) stable laser system, has been technically challenging and, so far, mostly restricted to systems with a few mJ energy, thus limiting the synthesized pulse energy to the μJ level[90;91]. To

date, only a few CEP stable lasers with tens of mJ have been reported with < 300 mrad single-shot CEP stability[94;95].

Accessing even shorter time scales requires the use of high-harmonic generation (HHG)[12;33], which has enabled laser pulses in the extreme ultraviolet (XUV) region with attosecond pulse durations. Attosecond pulses can be created as part of an attosecond pulse train (APT)[34] or as isolated attosecond pulses (IAPs)[96], depending on the number of electron collisions with the parent atom. Since HHG is intrinsically a sub-cycle phenomenon, it is ideal to have a light transient waveform to enable the generation of IAPs. However, due to the lack of laser sources that provide non sinusoidal, light transient waveforms, IAPs are often generated by using ionization gating to select part of the XUV spectrum driven by a CEP stable few-cycle laser[97] or by using optical gating to reduce the number of collisions in a CEP stable few-cycle or multi-cycle laser[98]. Both methods sacrifice either the usable XUV energy or the driving laser energy, thus limiting the generated IAPs to nJ energies or smaller.

It is intuitive to link the inefficient use of energy of the two methods. Both point to the need for a CEP stable high energy laser source. In this chapter, I will present our achievement of a CEP stable, terawatt level, Ti:Sapphire laser system, which is a vital first step towards generating energetic, synthesized, light transient waveforms and the creation of more energetic IAPs. We start with a detailed description of the construction of the laser, then focus on a critical part of this realization, vibrational damping of the stretcher and compressor. We then present the resulting single-shot CEP noise values of 250 mrad over 1 hour and 300 mrad over 9 hours. Also, we briefly discuss the use of this laser source to pump an optical parametric amplifier (OPA) as well as the possibilities of generating mJ level non sinusoidal light transient waveforms.

4.1 Layout of the High Intensity Tunable Source Laser

A schematic of the laser system is shown in Fig. 4.2. The oscillator operates at 78 MHz and consists of the traditional soft-aperture Kerr lens modelocking design[99], utilizing a prism pair for intracavity dispersion compensation. The oscillator is pumped by a frequency

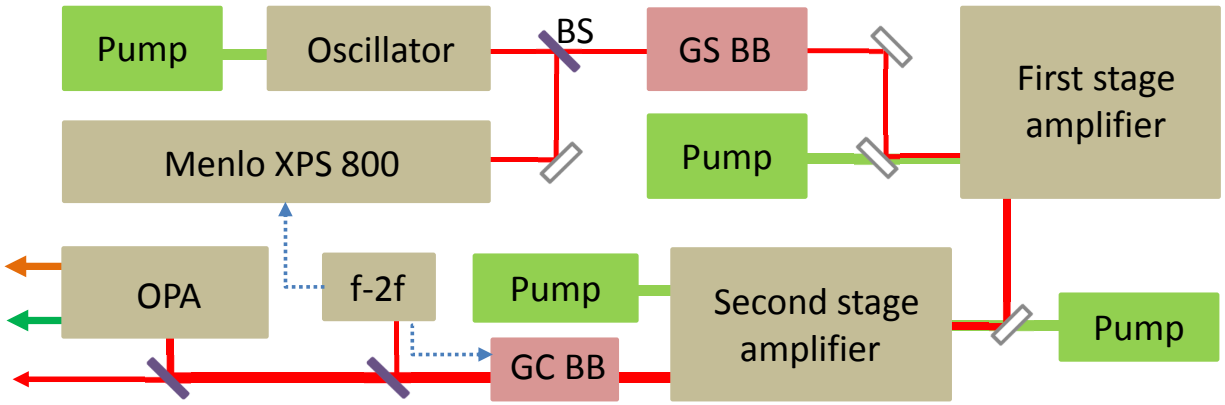

Figure 4.2: Layout of the 1 kHz, 20 mJ, 26 fs laser system. BS: beam splitter; GS BB: grating stretcher breadboard; GC BB: grating compressor breadboard. See text for design details. (Adapted from [84]).

doubled diode-pumped-solid-state (DPSS) laser (Lighthouse Sprout G). A portion of the oscillator output is used to stabilize the oscillator CEP with a Menlo Systems XPS800 f-2f interferometer (discussed in section 4.2.1) with the SYNCRO electronics package. The CEP noise correction is provided by moving the high reflector in the dispersed arm of the oscillator. In order to make the system more stable, the pump laser, oscillator, and the XPS800 are integrated into a single box.

The output of the oscillator, or seed laser, passes through two Faraday rotators to prevent back propagation of the seed or amplified light into the oscillator. The seed then propagates into a grating-based stretcher and is stretched to around 200 ps for CPA. Since the CEP noise accumulated in the amplification stages mainly originates from the stretcher and compressor [100;101], both are mounted on separate breadboards for noise reduction (discussed in section 4.2.3). The seed laser out of the stretcher is sent to a Pockels cell, in which a 1 kHz pulse train is picked off and sent to the first multipass amplification stage.

The first stage consists of a total of twelve passes in a "ring" amplifier. The gain medium is a Brewster cut Ti:Sapphire crystal optically pumped by a frequency doubled, 35 W, Q-switched, DPSS pump laser (Photonics Industries DM35). The first five passes go through a gain flattening filter to reduce gain around the central wavelength (~790nm). Upon amplification this configuration produces a super Gaussian output spectrum with a FWHM in

excess of 60 nm and tail to tail width of 120 nm. The crystal is cooled to below -200 °C with a cold helium cryogenic cooling system (CryoMech) to avoid thermal lensing. The first amplification stage produces a 1 kHz, 2.7 mJ pulse train which is then sent to a second Pockels cell to attenuate pre/post-pulses and amplified spontaneous emission.

The second amplification stage consists of a five-pass amplifier in a "bow tie" configuration optically pumped by two frequency doubled, 50 W, Q-switched, DPSS pump lasers (Photonics Industries DM50). The gain medium is a normal cut Ti:Sapphire crystal rod with anti-reflection coatings on both ends. The crystal is cooled by the same cooling system used in the first stage crystal. The mode size of the seed laser and the pump lasers is carefully matched to increase the efficiency of the amplification (∼30%), resulting in a 1 kHz, 29 mJ output. The laser beam is expanded to a $1/e^2$ diameter of about 3 cm before being sent to the grating-based compressor. An overall transmission efficiency of ∼70% is achieved through the compressor and gives a 1 kHz, 20 mJ, 26 fs output.

A second-harmonic frequency-resolved optical gating (SHG FROG)[79] measurement is shown in figure 4.3a to indicate the achieved pulse duration. To demonstrate the stability of the laser pulse energy, the power of the third harmonic of the amplifier output was measured for 9 hours, resulting in a standard deviation of 1.6%, as shown in figure 4.3b. The focused beam profile is also shown in the inset of figure 4.3b with an M^2 value of 1.36 along the X axis and 1.27 along the Y axis.

4.2 Demonstrating long term CEP stability in a high peak power laser.

One of the more interesting features of the HITS laser system is the improved method for stabilizing the CEP. Specifically, the HITS laser significantly suppresses the introduction of phase noise in the amplifier by mechanically stabilizing key optical components[84;100;101]. Before getting into the details of this, it is important to note just how the CEP is measured.

Once the importance of the CEP was realized, a conceptual technique for its measure-

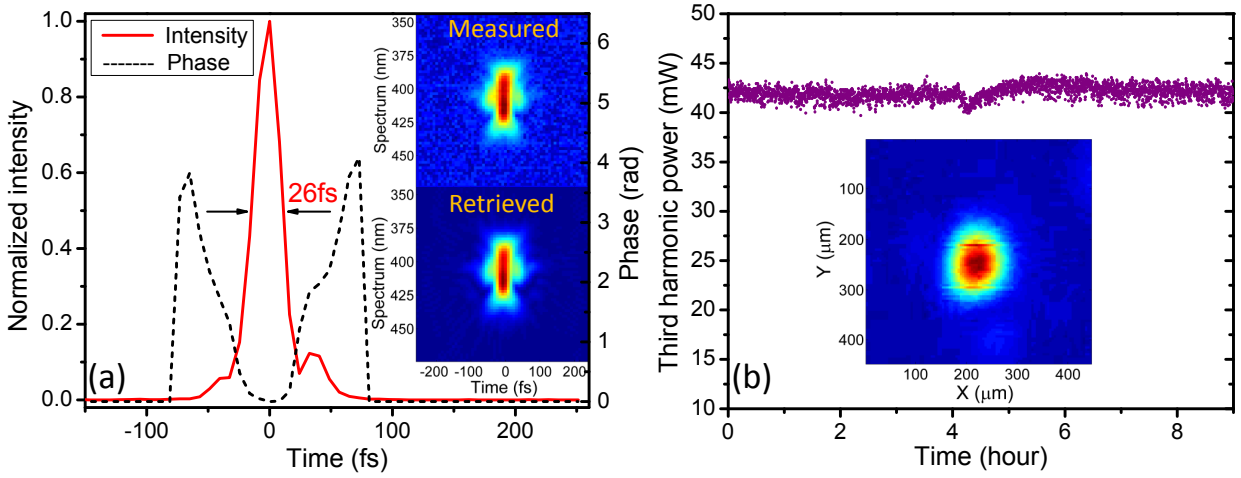

Figure 4.3: **a)** The retrieved laser electric field amplitude and the temporal phase as measured by SHG FROG. The measured and retrieved FROG traces are plotted in the inset. **b)** The power stability measurement of the third harmonic power of the laser output for 9 hours. The inset shows the focus of the laser using a 3m lens. (Adapted from[84]).

ment was proposed[102] and then demonstrated a few years later[103;104]. Even though newer methods, such as the feed-forward technique[105], offer higher performance, the original designs are still powerful and benefit from nearly two decades of engineering. This section will focus exclusively on the methods of stabilizing the CEP of the HITS laser system. If you require more information, Eric Moon wrote an entire PhD thesis on locking the CEP of an amplified laser system; many of the topics in this section will reference his work[106].

4.2.1 Design of a f-2f interferometer for the oscillator

Because a shift in CEP in the time domain corresponds to a shift in f_0 in the frequency domain, stabilizing f_0 of our oscillator gives us a method of locking the CEP. Since we can choose the frequency of f_0 to be in the MHz range, it is advantageous for us to perform a direct measurement of f_0 on the oscillator. Once that has been established, a feedback method on the oscillator can be utilized to control CEP fluctuations.

To measure f_0 consider a pulse with an octave spanning bandwidth, that is, $f_{max} = 2f_{min}$ where f_{min} is the lowest frequency in the pulse and f_{max} is the highest. In terms of f_0 these

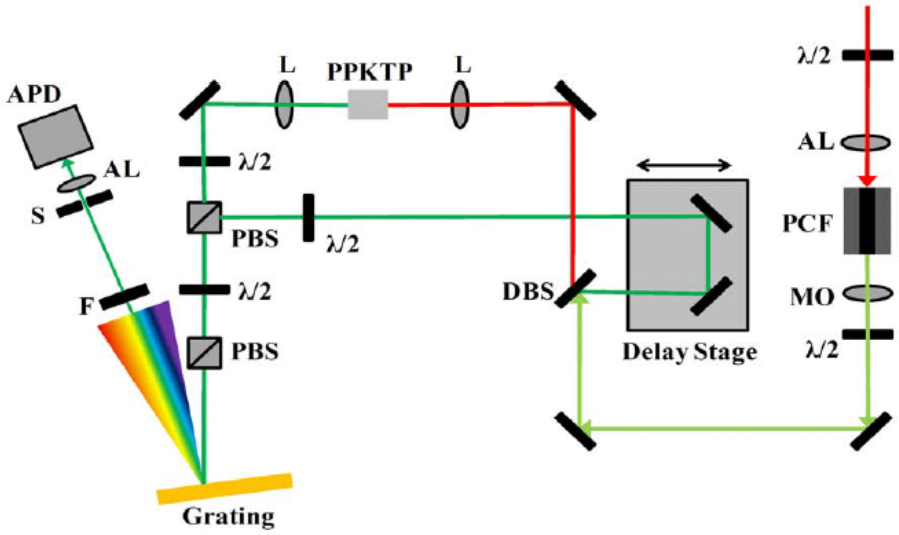

Figure 4.4: Layout for an f-2f interferometer designed to stabilize f_0. $\lambda/2$- half-wave plate, AL - aspheric lens, PCF- photonics crystal fiber, MO- microscope objective, DBS- dichoric beam splitter, L- lens, PPKTP- periodically-poled potassium titanyl phosphate, PBS- polarization beamcube splitter, F- narrow linewidth filter, S- slit, APD- avalanche photodiode. (Adapted from [106]).

frequencies are,

$$f_{min} = m f_{rep} + f_0 \tag{4.1}$$

$$f_{max} = 2m f_{rep} + f_0, \tag{4.2}$$

where f_{rep} is the repetition rate of the laser ($\sim$78 MHz for HITS) and m is the comb order. If we use nonlinear optical property of second harmonic generation to frequency double f_{min}, then the generated frequency will be $2f_{min} = 2(mf_{rep} + f_0)$. Overlapping this with f_{max} produces an interference pattern with a beat frequency, f_{beat} of

$$f_{beat} = 2f_{min} - f_{max} = 2(mf_{rep} + f_0) - (2mf_{rep} + f_0) = f_0, \tag{4.3}$$

and so a measurement of the beat signal is a direct measurement of f_0.

An apparatus capable of this measurement is known as an f-2f interferometer. An example of one is shown in figure 4.4. In the case of HITS, the oscillator does not support an octave

spanning pulse and so the bandwidth is broadened in a photonic crystal fiber (PCF). A PCF allows for the oscillator to be directly broadened via self-phase modulation (discussed in section 3.6) before amplification, giving us f_{min} and f_{max}. f_{max} and f_{min} are then split via a dichoric beam splitter (DBS) so that their spatiotemporal overlap can be optimized later on. Next, f_{min} is focused in a frequency doubling crystal to create $2f_{min}$. Since the strength of the signal at f_{min} is typically very weak, it is important that a well optimized nonlinear crystal is used to generate $2f_{min}$. In this example, the crystal PPKTP was chosen.

Now that f_{max} and $2f_{min}$ are generated, they can be recombined for the measurement of f_{beat}. Keep in mind now that f_{max} and $2f_{min}$ are the same frequency so dichoric optics are no longer a suitable option. In this example, a polarizing beam cube splitter (PBS) is used along with a pair of half wave plates ($\lambda/2$) to completely reflect f_{max} and transmit $2f_{min}$. This necessitates that the two signals are orthogonally polarized and so another $\lambda/2$-PBS pair is used to rotate their polarizations and select a horizontal component from both. This attenuation technique can be used to control the contrast of f_{beat} later on.

Only a few nanometers of bandwidth, around the 530 nm range, out of the octave spanning bandwidth are required for measuring f_{beat}. Since the rest of this light will only obfuscate the measurement, the final optics in the setup are used for isolating the desired region. A grating paired with a slit (S) provides most of the filtering while another narrow line width filter (F) provides a finer control over the frequencies neighboring the desired signal.

With this, f_{beat} (and hence, f_0) can be measured using an avalanche photodiode (APD). When the light is incident on the APD, the rf signals from the pulse train are converted into an electronic signal which are measured with an rf spectrum analyzer. Such a spectrum is shown in 4.5 and shows not only f_0, but the repetition rate of the laser, f_{rep} as well as a mixing frequency between the two.

f_0 is given by the following expression

$$f_0 = -\frac{\Delta\phi_{CEP} f_{rep}}{2\pi}, \tag{4.4}$$

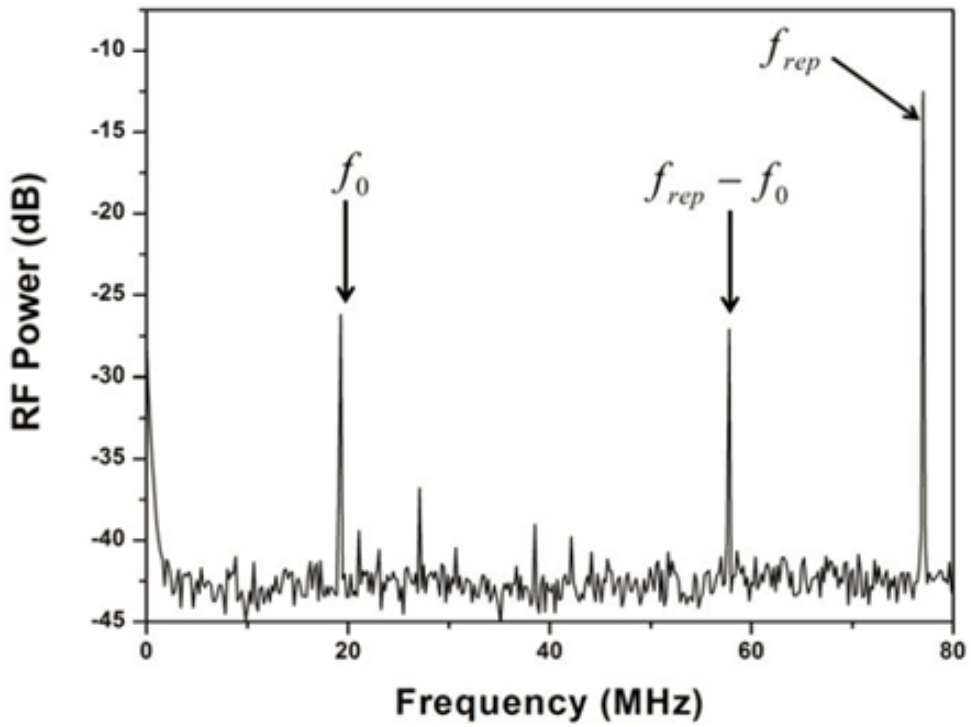

Figure 4.5: Example of an RF spectrum measured on the APD in figure 4.4. f_{rep}- repetition frequency, f_0- offset frequency. (Adapted from [106]).

and its derivation can be found elsewhere [106]. What is important to know from this is that f_0 can be chosen to be any number of values, based on the cavity length (f_{rep}) and the cavity dispersion ($\Delta\phi_{CEP}$). Thus, depending on what frequency we stabilize f_0 to, every subsequent pulse can have either the same CEP ($f_0 = 0$) or a CEP shifted by a value $\Delta\phi_{CEP}$. We choose $f_0 = f_{rep}/4$ because 1) a 20 MHz signal is easy to measure and control and 2) $\Delta\phi_{CEP} = \pi/2$, so every fourth pulse has an identical CEP. Later, when we reduce the repetition rate to 1 kHz for amplification, every pulse will have the same CEP.

In the case of the HITS laser, the acquisition and locking of f_0 is performed by the XPS800 from Menlo Systems. This system is contains an f-2f interferometer enclosed in a compact housing, as shown in figure 4.6a. This allows everything for CEP control to sit in a single $\sim$0.5 m^2 enclosure and ensures limited environmental influence. Once the signal is obtained, we can then produce an error signal with the SYNCRO electronics package shown in figure 4.6b, which consists of a Proportional Integral Derivative (PID) controller. This controls the angle of the oscillator's end mirror via a piezoelectric transducer (PZT). The end mirror is

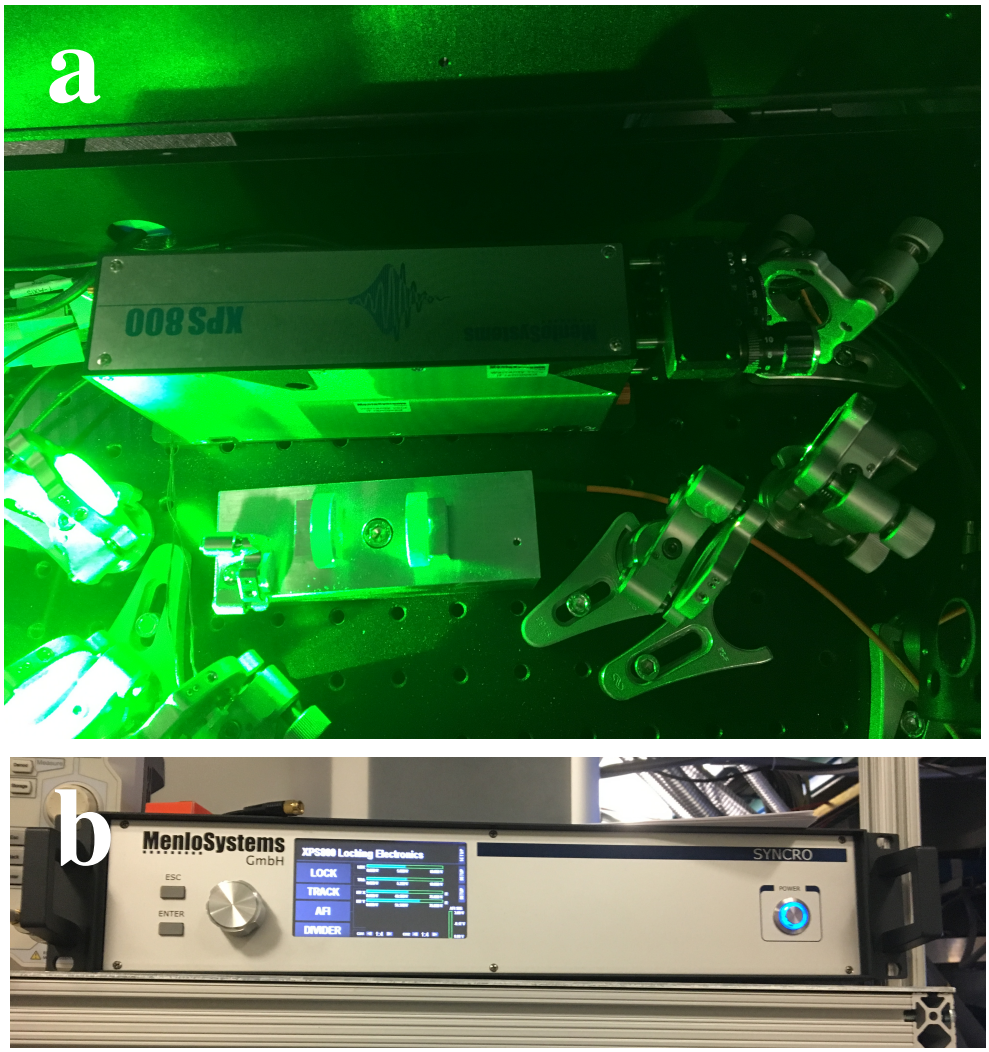

Figure 4.6: **a)** The Menlo XPS800 system as installed inside the HITS oscillator box. This contains the full optical system for the generation and measurement of f_{beat}. **b)** The SYNCRO electronics package, shown here, produces the error signal that is sent to the end mirror of the oscillator. This mirror is just visible on the lower left area of figure 4.6a.

placed after a prism pair located in the oscillator so it receives a spectrally dispersed beam. Thus, the angle of the mirror can be used to offset the cavity dispersion. Every fourth pulse of the resulting pulse train carries CEP noise of 110 mrad in the integration range from 1 Hz to 2 MHz.

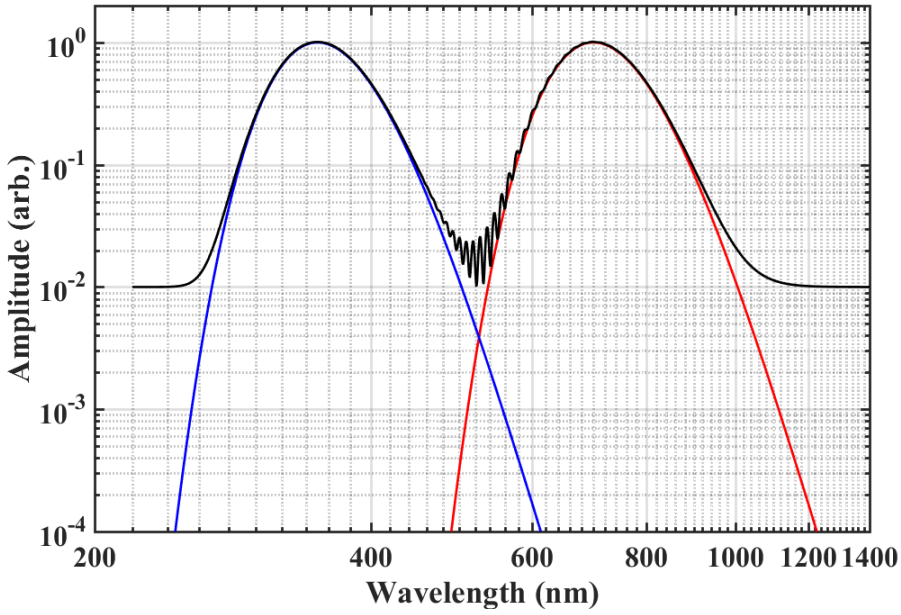

h

Figure 4.7: Example of an octave spanning spectrum (red), its' second harmonic (blue), and their total measured intensity (black). In the last spectrum, a fringe pattern is observed due to interference between the beam.

4.2.2 Design f-2f interferometer for the amplifier

The CEP of the amplifier is also stabilized with an f-2f interferometer. However, there are several differences in how f-2f measurements are made in the amplifier versus the oscillator. For one, the amplifier system does not benefit from a MHz repetition rate, and so an rf signal cannot be used. At the same time, the amplifier benefits from having over 10^6 times more energy per pulse, so even a minuscule level of leaked pulse energy from the amplifier is orders of magnitude stronger than what is available from the oscillator. Our amplifier f-2f takes advantage of this available light and, in the case of the HITS laser, performs CEP measurements on individual laser shots by measuring spectral fringes [104].

Just as in the last section, the amplifier f-2f performs a measurement on the spectral overlap of an octave spanning fundamental field and its second harmonic. When combined,

their full electric field can be written as

$$E(\omega) = E_f \exp\left[-2\ln 2\frac{(\omega-\omega_0)^2}{\Delta\omega^2} - \mathrm{i}(\omega t_f + \phi_{CEP})\right] + E_{2f} \exp\left[-2\ln 2\frac{(\omega-2\omega_0)^2}{\Delta\omega^2} - \mathrm{i}(2\omega t_{2f} + 2\phi_{CEP})\right], \tag{4.5}$$

where E is the full electric field in frequency, ω. E_f and E_{2f} are the amplitude of the fundamental field and its second harmonic, respectively, and ω_0 is the central frequency of the fundamental field. $\Delta\omega$ gives the FWHM of the field's bandwidth and the phase is given by ϕ_{CEP}. t_f and t_{2f} are the time for E_f and E_{2f}, respectively, and are distinct because the fields are not necessarily overlapped in time. Because E_{2f} is generated from E_f, its phase is simply twice that of the fundamental.

An important point to make here is that what I am calling ϕ_{CEP} is not entirely made up of the CEP. Rather, it is a conglomerate of several effects introducing an overall phase shift. In other words, one never measures the *absolute* phase, but some offset from the *absolute* value. That being said, we will later see how the amplifier f-2f is designed so that the phase slippage between individual laser shots is ϕ_{CEP}. Because we are more interested in a stable CEP versus an absolute measurement of the CEP, we can for now on ignore the constant offset.

We always measure the intensity whenever we measure the spectral content, so $I(\omega)$ for $E(\omega)$ is

$$I(\omega) = E(\omega)E^*(\omega) = I_f(\omega) + I_{2f}(\omega) + E_f(\omega)E_{2f}(\omega)\cos(\omega\tau + \phi_{CEP}), \tag{4.6}$$

where $E_f(\omega)$ and $E_{2f}(\omega)$ are the real parts of the fields for the fundamental and second harmonic, respectively. $I_f(\omega)$ and $I_{2f}(\omega)$ are the spectral intensities for the fundamental and second harmonic, respectively. $\tau = 2t_1 - t_2$ and gives the relationship between the delay of the two fields.

An example of the full spectrum for equation 4.6 is shown in figure 4.7. $I_f(\omega)$ is shown in red, while $I_{2f}(\omega)$ is shown in blue. $I(\omega)$ is in black with a small vertical offset so all

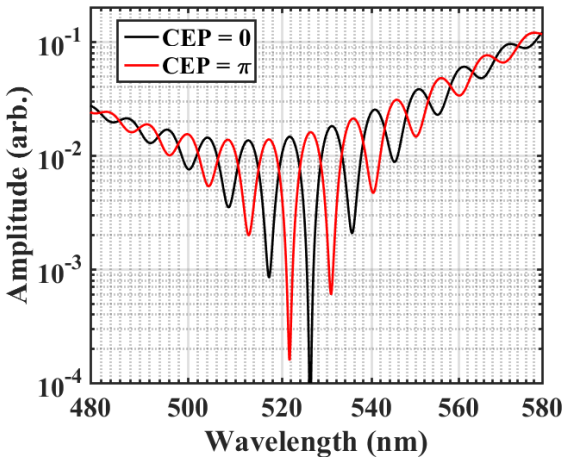

Figure 4.8: Expanded view of the fringe region from figure 4.7. When the CEP shifts from 0 to π the peak of the fringe shifts in frequency. This effect provides us a signal that we can measure and control CEP with.

spectra can be clearly shown. As expected from equation 4.6, when the bandwidth of the two fields is broad enough that they overlap, an interference pattern is produced. Looking at the argument of the cosine, we observe that the fringe separation is determined by the delay τ and the fringe position is determined by the phase, ϕ_{CEP}.

Figure 4.8 is an expanded view on the fringes in figure 4.7. We see that for a shift in ϕ_{CEP} from 0 to π, the fringes can shift from minima to maxima, and vice versa. Thus, a measurement of the spectral fringes in an f-2f interferometer is a method of measuring the shift in CEP. There are two methods of extracting the CEP. A simple method is to record the full fringe spectrum, like what is shown in figure 4.8, and perform a Fourier transformation. The frequency of the CEP fringe will produce a peak in the reciprocal domain. The change in the phase associated with that peak corresponds to a shift in the CEP. Another, more direct approach, uses a pair of closely spaced photodiodes in the Fourier plane of a diffraction grating-lens pair and measures the difference in the signal strengths on the individual diode. When a fringe moves spectrally, the difference in signals changes. This direct approach is much faster for recording every single laser shot and we use this method for the feedback on the HITS laser. Because there is ample supply of light available in our f-2f, we simultaneously record the fringes with a spectrometer to be used in data analysis.

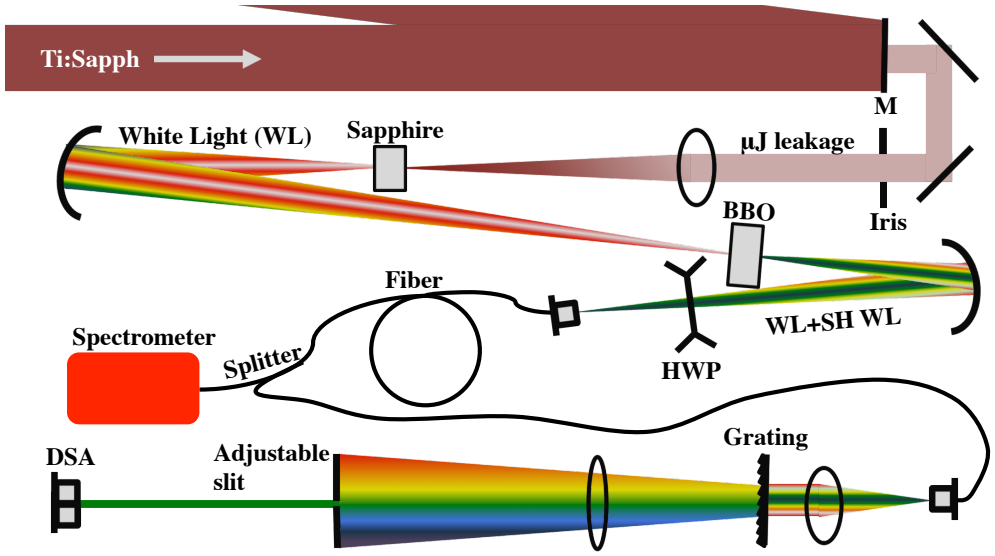

Figure 4.9: Amplifier f-2f layout.

The amplifier f-2f for the HITS laser is setup as shown in figure 4.9. The 20 mJ Ti:Sapph laser is incident on a 50 mm diameter dielectric mirror with a 99.5% anti-reflective coating for a zero degree reflection (Alpine Research Optics, MR6260) . This allows approximately 50-100 μJ of light to pass through the mirror, which is nearly 10,000 times the pulse energy available from the oscillator. Just as before, we need to produce an octave spanning spectrum from the fundamental field; this is accomplished by focusing the leakage into a sapphire plate. Afterwards, a silver coated concave mirror focuses the octave spanning fundamental field into a beta-barium borate (BBO) crystal to produce the second harmonic field. Because the SHG is a type I process, the second harmonic field is perpendicular to the fundamental and needs to be rotated with a half wave plate (HWP).

We now have the optical signal and are ready to measure the fringe patten. The two most common methods for performing this measurement are with a spectrometer or a difference signal amplifier (DSA). The HITS laser utilizes both techniques because the DSA is the best method for providing an electronic feedback signal while it is much simpler to optimize an f-2f signal using a spectrometer. In addition, the spectrometer provides an out-of-loop CEP measurement, which can record data without influencing the in-loop feedback. The optical signal is focused into a fiber optic cable with a silver coated spherical concave mirror. The

fiber guides the signal to a splitter to simultaneously send the signal to both the DSA and the spectrometer. Before the DSA, a grating lens pair spectrally disperse and then focus the beam to create a Fourier plane. This gives us the required spectral contrast for measuring the fringes. We want to record an individual fringe, so an adjustable slit blocks most of the light allowing only a small region to pass onto the photodiode pair. The signal from the DSA is integrated to give an analog error signal with a bandwidth up to the repetition rate of the amplifier, in this case, 1 kHz. This analog error signal is then processed in a proportional-integral-derivative (PID) controller and used as feedback to both the oscillator and compressor gratings. The oscillator is fed with the higher frequency signals (1 Hz to 500 Hz). It pre-compensates the fast drifts of the CEP by modulating the same high reflector used for oscillator CEP locking. The feedback to the compressor grating is termed slow-loop (DC to 1 Hz). It drives the piezo stage under one of the gratings using a PID program to correct for long-term CEP drifts.

4.2.3 Mitigating vibrational noise in the amplifier's stretcher and compressor

Using the instruments described in detail in section 4.2 allows us to control the CEP of the HITS laser. However, it was later determined that the vibrational noise on the laser's breadboard was significant enough that the feedback signals alone were not enough to control the CEP output to a reasonable level. For our purposes, the CEP noise we wanted to reach was 300 milli-radians (mrad) single shot (no average) rms error. The effect of the initial vibration mitigation technique on amplifier CEP stability is shown in figure 4.10a with a single-shot CEP error of 880 mrad, which was impractically large for our purposes. Since the oscillator CEP was controlled to a sub-100 mrad level, it was determined that the source of the noise must be from vibrational coupling into the stretcher and compressor components of the amplifer, which are known to be the main source of amplifier CEP noise[100;101]. Note that the cryogenic cooling system is located in a separate room to reduce vibrations. Also, both the stretcher and compressor sub-breadboards were mounted with a vibration absorb-

ing mat (Rathburn Associates ISODAMP C-1000) underneath to reduce vibrational energy transmitted through the optical table. The sub-breadboards are secured to the amplifier breadboard with vertical clamps. We determined that the CEP noise could be reduced if we could improve the vibrational isolation into these components.

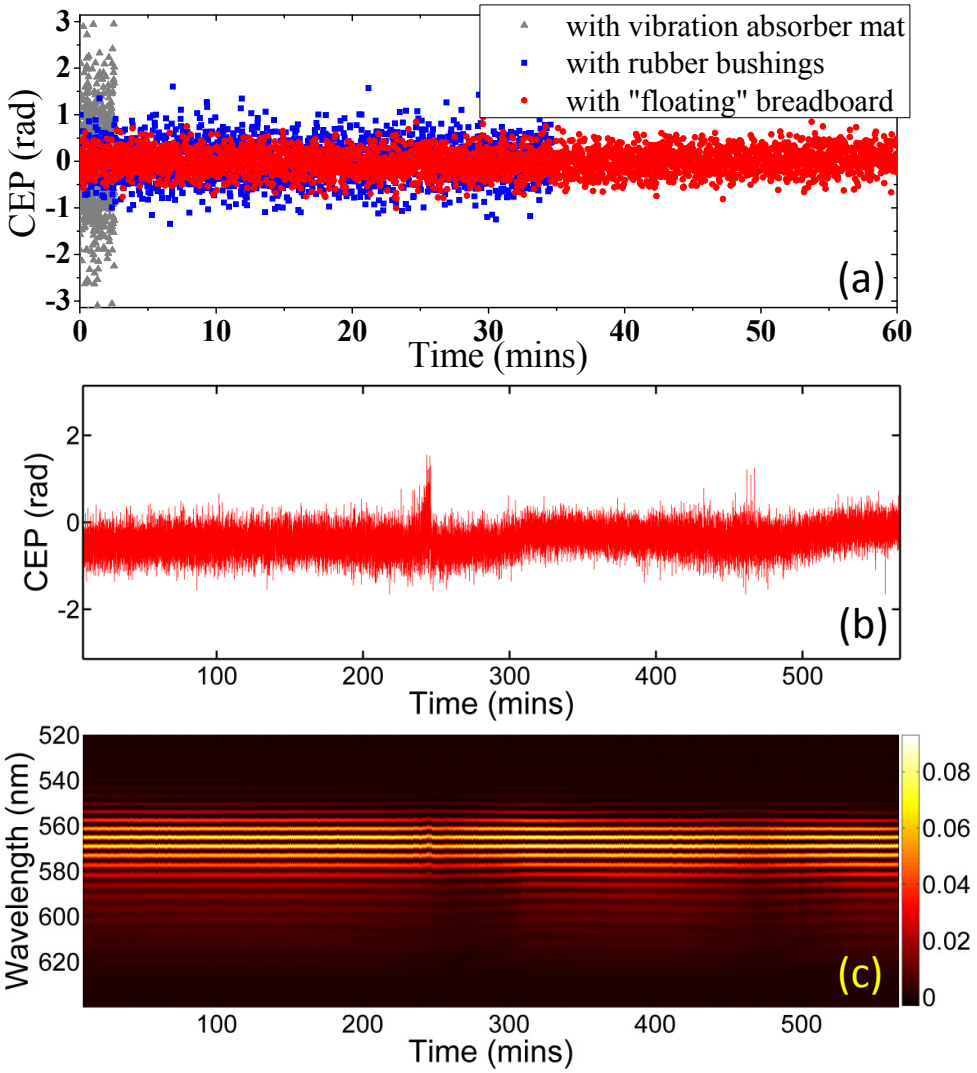

Figure 4.10: **a** Short-term single-shot CEP error as measured in the three different vibrational damping schemes. **b** Long-term single shot CEP error with the "floated" stretcher and compressor. **c** The spectral fringes for the long-term CEP stabilization using the floating and compressor and stretcher. All measurements performed with an f-2f interferometer. (Adapted from[84]).

A modified vibrational damping method is sketched in figure 4.11a. Four rubber bushings were installed underneath each breadboard (the rubber bushings are squeezed severely in

practice) to reduce contact of the breadboard with the optical table. Lateral and vertical clamps are used to "squeeze" the breadboard in place instead of using bolts. The clamps were found to transmit less vibrational energy from the optical table to the sub-breadboard. In this design, the breadboard is less susceptible to lateral and vertical vibrational energy transfer than in the initial design.

The vibrational frequencies present on the breadboard were measured with an accelerometer and characterized with a vector signal analyzer. The results with the vibration absorber mat and the rubber bushings are compared in figure 4.11c. Considerable reduction of vibrational frequencies above 50 Hz is achieved with the new damping method, although the 30 Hz noise is enhanced by almost a factor of 2 compared to the absorbing mat, and the 60 Hz noise remains prominent.

The CEP noise in this case was measured to have single-shot error of 425 mrad, as shown in figure 4.10a. This was more than a two-fold improvement of the CEP stability over the initial design. One of the main drawbacks of this mounting scheme is that since the breadboard is less constrained, it takes much longer for the laser pointing out of the stretcher and compressor to be stabilized and the whole system is more sensitive to room temperature fluctuations. Note that, in our case, the laser room temperature is controlled to within ± 1 ^{o}C, making the effect of the temperature fluctuation less significant.

To further improve the CEP stability, the vibrational energies at 30 and 60 Hz needed to be attenuated. This was achieved by "floating" both breadboards. This floating scheme is different from optical table floating, in which high pressure air is used to push the optical table above the supporting legs. In our case, a special mount is utilized, as sketched in figure 4.11b. It includes two parts. The first is bolted on the optical table and has a container for a thick piece of polyurethane (Sorbothane®). The second part is bolted to the breadboard and has a bolt threaded through one side. This bolt is coupled to a movable rod which sits on the polyurethane cylinder held by the first part. Four of these mounts are placed at the corner of each breadboard. By tightening the bolt above the removable rod, the breadboard can be lifted off the optical table and carefully balanced and leveled. The force of the breadboard pushing onto the polyurethane pieces produces a cone shaped pocket around each rod. These

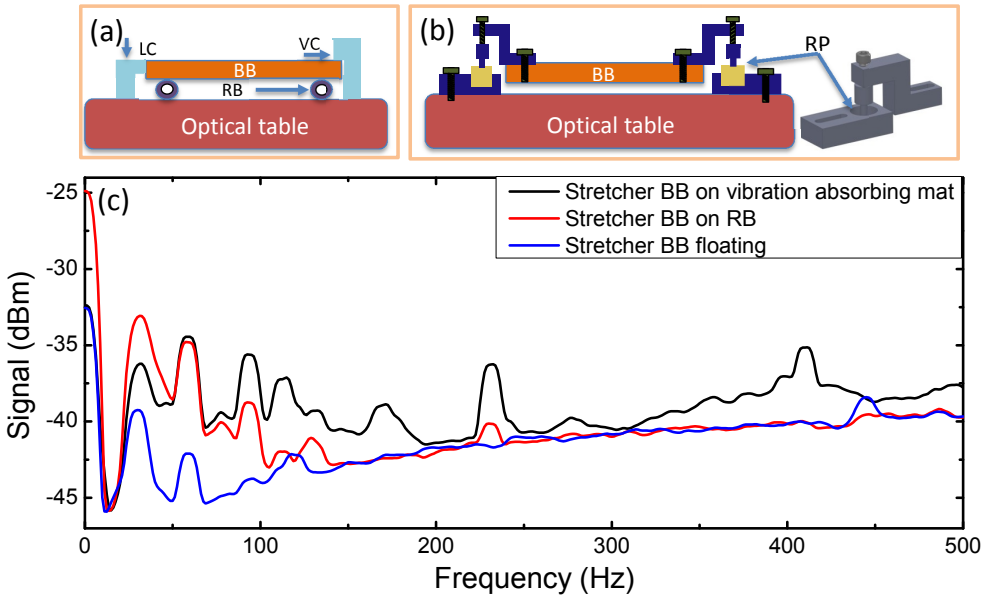

Figure 4.11: **a** The mounting scheme for the vibrational damping method using rubber bushings. LC: lateral clamp; VC: vertical clamp; BB: breadboard; RB: rubber bushing **b** The mounting scheme for the vibrational damping method using "floating" breadboards. RP: rubber plug **c** The vibrational energy spectrum with three different methods, measured on the stretcher breadboard. (Adapted from [84]).

cones allow for lateral constraint of the breadboard while still maintaining isolation from the table itself. The only way that any vibrational energy from the table can couple into the breadboard is through the polyurethane piece and the rod.

Using this mounting method for the breadboards on both the stretcher and compressor, vibrations are attenuated even further, as illustrated in figure 4.11c. The 30 and 60 Hz vibrational energies and the overall vibrations below 100 Hz are attenuated by as much as -10 dB. Under this condition, the single-shot CEP variation is locked to within 250 mrad for an hour as shown in figure 4.10a. Since the breadboards are much less constrained in this case, it takes a few days for the polyurethane pieces and the breadboards to reach equilibrium.

To determine long term stability, an overnight CEP locking was performed after the system stabilized and resulted in a 300 mrad single-shot CEP error over a 9 hour period. To the best of our knowledge, these values are among the best short- and long-term CEP noise values reported for a terawatt class laser system. The result is shown in figure 4.10b

along with the spectral fringe pattern (figure 4.10c). The spike around the 250 minute mark occurred when the fast-loop PID reached the locking limit, but was driven back by the slow-loop. A temperature fluctuation caused the slightly dimmer spectral fringe at around 300 and 500 minutes, but did not seem to affect the CEP locking.

Recently, a CEP stabilized amplifier system producing 0.8 mJ of energy per 25 fs pulse at a 10 kHz was reported[107]. The phase noise for this amplifier was reported to be 98 mrad measured in-loop and 140 mrad measured out-of-loop for periods of 50 s. While similar methodology (separate high and low frequency feedback) for active phase stabilization was used in that amplifier, more attention was needed to address the mechanical sources of phase noise stemming from the reflection grating based stretcher and compressor. In order to avoid optical component damage at pulse energies above 10 mJ it is more practical to use the grating approach for chirped pulse amplification. In addition, a ten-fold lower repetition rate is required to reach TW peak powers producing a ten-fold decrease in the available feedback bandwidth. This severe feedback bandwidth limitation further necessitates effective mechanical decoupling of the stretcher and compressor. Furthermore, production of IAPs and their ultimate experimental applications necessitates the use of vacuum pumping machinery. These can couple vibrational energy into the laser amplifier which will contribute additional phase noise through the grating based stretcher and compressor[100;101]. Finally, we should stress that the very impressive values of 98 mrad and 140 mrad in the CEP rms noise reported in[107] were only sustained for 50s. On the other hand, our goal was to make CEP control experimentally usable by extending the lock time to several hours.

4.3 The High Energy optical parametric amplifier

The HITS laser includes a high energy OPA from Light Conversion. Combined with the Ti:Sapph laser, this allows us to produce mJ level laser fields with central wavelengths spanning the NIR.

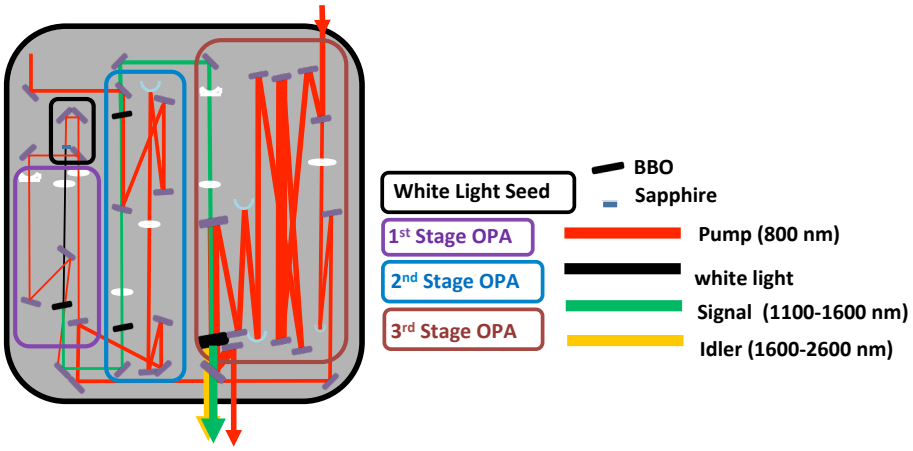

Figure 4.12: Layout of the high energy OPA. 18 mJ enters the setup from the top right of the figure and is split into four different arms using a series of beam splitters. A few microJ is used to generate a white light signal via SPM in a sapphire plate in the area circled in black. This produces a weak signal in the NIR (1100-1600 nm) which is then amplified to the 1 μJ level in the first stage, circled in purple, using a BBO crystal. A second amplification stage, circled in blue, amplifies the signal to the 100 μJ level with another BBO. The final amplification stage, circled in red, pumps the resulting signal with approximately 16 mJ of energy, scaling the signal to the mJ level and simultaneously producing an idler field a the mJ level.

4.3.1 Layout

Out of the 20 mJ of total energy, we split the laser output into two arms (see figure 4.2), one with 2 mJ pulse energy and the other with 18 mJ pulse energy. The 18 mJ arm pumps a white-light-seeded OPA system (Light Conversion HE-TOPAS-Prime-Plus). As shown in figure 4.12, the OPA consists of three amplification stages. In the first stage, 3 μJ pulse energy is used for generating a signal in the wavelength range of 1100-1600 nm using SPM in a sapphire crystal. The signal is then preamplified by mixing it with $\sim$35 μJ of 800 nm light in a type II β-barium borate (BBO) crystal. A second stage amplification further enhances the signal energy to the 100 μJ level by pumping it with $\sim$700 μJ of 800 nm light in a second type II BBO crystal. In the final stage, a $\sim$17.2 mJ pump laser boosts the total energy of the signal (S) and idler (I) to 6 mJ with a 60/40 S/I ratio when the signal is tuned to 1320 nm. By tuning the angle of the BBO crystals, the wavelength of the signal (idler) can be tuned from 1150 nm to 1600 nm (2600 nm to 1600 nm). The achieved pulse energy at different

wavelengths is shown in figure 4.13b.

The wavelength of the OPA is entirely tunable with computer software. The program, called WinTopas 4, controls the crystal angle and a delay stage for each amplification stage in order to correctly phase match and supply the light for amplification. These six stages can be calibrated, allowing for instant "turn key" control of the OPA's wavelength. Another actuator based mirror mount controls the input light into the OPA for maximum precision on controlling the beam position inside the OPA. The OPA is also equipped with a glass plate-based delay stage on the signal's path (green) between the second and third amplification stage for controlling the CEP of the idler, as discussed in the next section.

4.3.2 CEP stability of the idler

Our OPA offers us three individual beams at unique central wavelengths. These are the signal (1180 nm - 1600 nm), idler (1600 nm - 2400 nm) and the depleted pump (800 nm). It is possible to generate few-cycle pulses in each of these beams and preserve their CEP stability, paving a path towards generating high energy light transients, as done in [90;92;108]. Due to the fact that SPM preserves CEP, the OPA signal will ideally inherit the same CEP as the pump [109]. Any small CEP drifts due to path difference fluctuations between the arms of the OPA can be corrected by rotating a pair of glass plates in the OPA using a piezo motor. Furthermore, the idler output is known to have passive CEP stability [109], and spectral broadening in HCFs has also been shown to maintain CEP stability [69;110]. Therefore, if the time separation of all three pulses is precisely stabilized and delayed [111], ∼mJ level light transients could be realized. Details on this technique, known as multi-pulse synthesis, will be discussed chapter 5.

To demonstrate the major steps towards achieving this, we performed SPM on the signal, idler, and the remaining 2 mJ pump. Since the three beams support anywhere from 30-100 nm of bandwidth FWHM at their respective central wavelengths, they are far from possessing spectral overlap. These gaps are filled by performing SPM. This is achieved by coupling the pump and signal fields into a 1 m long, 250 μm diameter hollow core fiber (HCF) filed with

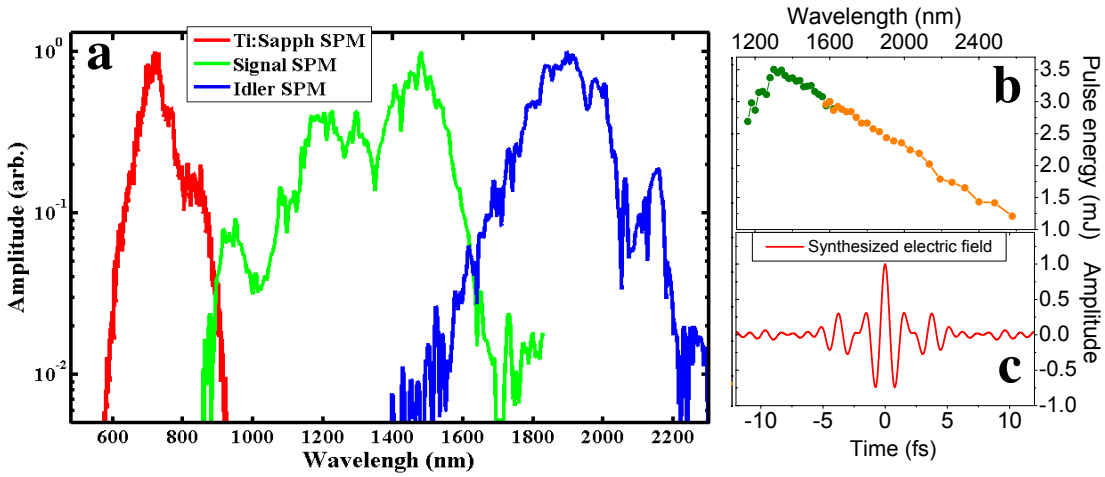

Figure 4.13: **a** The broadened spectrum of pump, signal and idler. **b** OPA output energies as a function of wavelength. **c** Theoretically calculated synthesized electric field using spectrum from **a** and assuming a flat phase across the whole spectrum. (Adapted from [84]).

argon gas an absolute pressure of 30 PSI and a 1.5 m spherical concave mirror. The idler field is coupled in the same HCF, but filled with 45 PSI argon gas and focused with a 0.75 m CaF_2 lens. These allows for sufficient filling of the spectral gaps, as shown in figure 4.13a. In our case, we were able to obtain more than a combined 2.5 mJ of energy per pulse in the broadened pump, signal and idler.

Both the energy per pulse and the broadening represent lower limits of what is achievable, yet demonstrates over 2 octaves of bandwidth and multi-mJ energies. Such achievements emphasize the strength of our method, as synthesis has yet to be demonstrated with such parameters. We need to point out that at this stage we haven't compressed the broadened pulses, nor recombined them. A theoretical calculation of the time-domain synthesized laser pulse is shown in figure 4.13c. This calculation is simply a Fourier transform of a transform limited pulse using the full spectrum shown in figure 4.13a.

To conclude this chapter, we demonstrated a 0.77 TW Ti:Sapphire laser system that is CEP stable for extended periods of time. The laser delivers 20 mJ, 26 fs pulses at 1 kHz repetition rate with central wavelength of 790 nm. We measured CEP single-shot RMS noise of 250 mrad over one hour and 300 mrad over 9 hours. In our opinion, these measurements represent some of the best CEP noise levels for a terawatt class laser. Our emphasis is on

the long-term stability of very intense laser pulses. The low CEP RMS noise obtained over such long timeframes makes CEP-controlled experiments, with intense femtosecond pulses, a possibility. Such research is still considered quite challenging and is mostly performed in a CEP-tagged fashion[77;112].

To achieve such low noise, we developed a new mounting scheme, in which both stretcher and compressor are "floating" and, therefore, isolated from vibrational noise on the optical table. The noise sources and frequencies were obtained by Fourier analysis of the f-2f feedback signal and the mounts were tuned to mitigate such frequencies. With this approach the resulting short- and long-term CEP stabilities are both significantly improved. With the excellent short- and long-term CEP stabilities at such high energy and repetition rates, stable and energetic ($>$ 2 mJ energy per pulse) light transients are feasible by synthesizing spectrally-broadened fundamental and OPA outputs. Energetic optical synthesis promises the generation of high energy-per-pulse, high flux (1 kHz repetition rate), and high photon-energy XUV sources and opens a new door for the generation of bright isolated attosecond pulses and strong-field coherent control.

Chapter 5

Simultaneous few-cycle pulse generation in a single hollow core fiber as an approach for optical synthesis

Much of the work in this chapter was demonstrated in a previous publications[113;114]

This chapter picks up where chapter 4 left off to propose a new technique for performing synthesis. The aim is to demonstrate the feasibility of this design and discuss how it can improve upon previously established methods. We also discuss how incorporating this into the HITS laser system can produce highly energetic light transients that are useful for isolated attosecond pulse generation.

Since the development of the first lasers, techniques for generating larger bandwidths of coherent light have been pursued in the quest for shorter pulses and arbitrary control over their temporal characteristics. In the past decade, light sources with octave spanning bandwidths and peak intensities in the strong-field regime ($>10^{14}$ W/cm^2) have been realized[65;86]. The recent push for extending these techniques utilize the general principle of multi-pulse synthesis. In this technique, two or more pulses with different central wave-

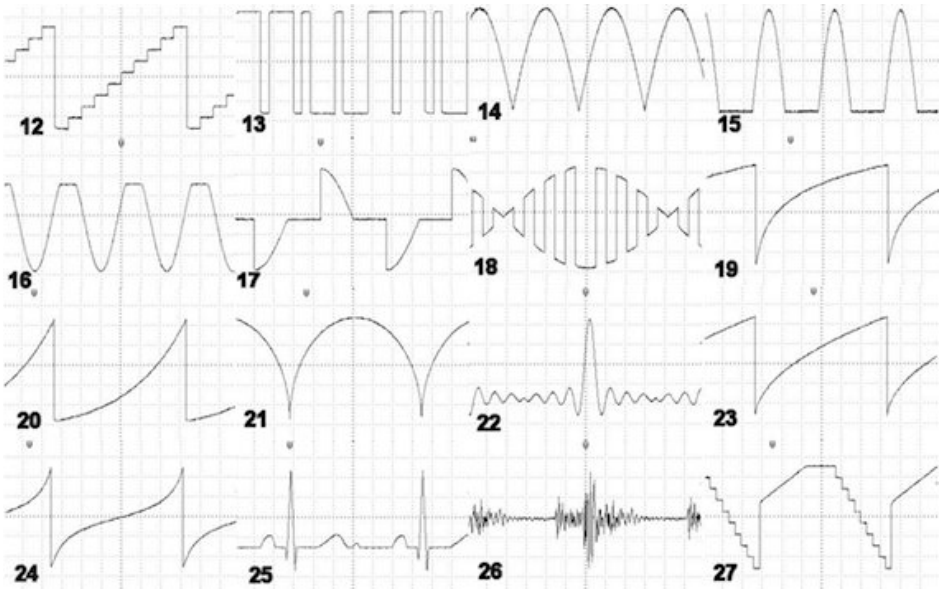

Figure 5.1: Several examples of arbitrary electric field waveforms at the radio frequency range. Of the listed waveforms, number 22 is of valuable interest in the optical frequency range. Adapted from the web page of BK Precision[117].

lengths are spatio-temporally combined to generate a new pulse comprising the sum of all inputs. Techniques of this nature have utilized self-phase modulation (SPM) of Ti:Sapph lasers[90;108], optical parametric amplifiers (OPA)[115;116], optical parametric chirped-pulse amplifier (OPCPA)[91], and coherent modulation[89].

5.1 Introduction to optical synthesis

Synthesis is a method for generating waveforms that can support a single oscillation of the electric field. It relies on superposition of two or more laser fields possessing different central wavelengths, which is achieved by overlapping them in time and space. Their fields constructively *and* de-constructively interfere to produce a new waveform, which can possess a very different profile than its constituents. Since any pulsed electric field can be thought of as the superposition of many "fields" across a given bandwidth, this is not a new concept for us. However, synthesis expands this principle to producing waveforms with a single oscillation, and are no longer "sine-like".

If we look at figure 5.1, we see various examples of arbitrary waveforms generated in

the radio-frequency (RF) region. In this region, the generation of arbitrary waveforms has been available in the 1 kHz - 1 MHz for decades. However, the development of such waveforms in the infrared and optical regimes (10-1000 THz) has only been demonstrated since 2011 [89–91;108;115;116]. Whereas producing such waveforms in the RF regime requires only basic electronics setups and can even be made by hobbyist, coherent optical frequencies require lasers, which are limited in bandwidth. The commonality of synthesis techniques is in producing the necessary bandwidth via nonlinear optics by utilizing two or more bandwidth channels. These can then be recombined to yield the desired waveform.

Producing such waveforms in the optical regime would open new areas of research on the control of ultrafast dynamics in atoms, molecules, and solids [118]. The light transients produced via optical synthesis are ideal tools for the producing higher order harmonic generation (HHG) and, in particular, the production of isolated attosecond pulses. Theory suggests that a properly tailored waveform can enhance HHG electron recombination and significantly increase the harmonic yield [119].

Attosecond pulse production is only the immediate goal of synthesized light transients. Much of the dynamics occurring in the ultrafast regime is controlled by the waveform. While the field of pulse shaping has been around for decades [120;121], the control is limited to shaping the field envelope or governing the higher order chirp of the laser field. With non-sinusoidal fields, pulse shaping could be extended to the the waveform and allow for the arbitrary control of ultrafast dynamics on the sub-cycle timescale [92;118].

5.1.1 State-of-the-art in optical synthesis

The exciting possibilities for light transients mentioned in section 5.1 have made their synthesis a major field in ultrafast optics development. Currently, the field is still in its infancy, as many approaches have been proposed and/or demonstrated. Here, I will go through three general paths towards light transient generation and explain their benefits and flaws.

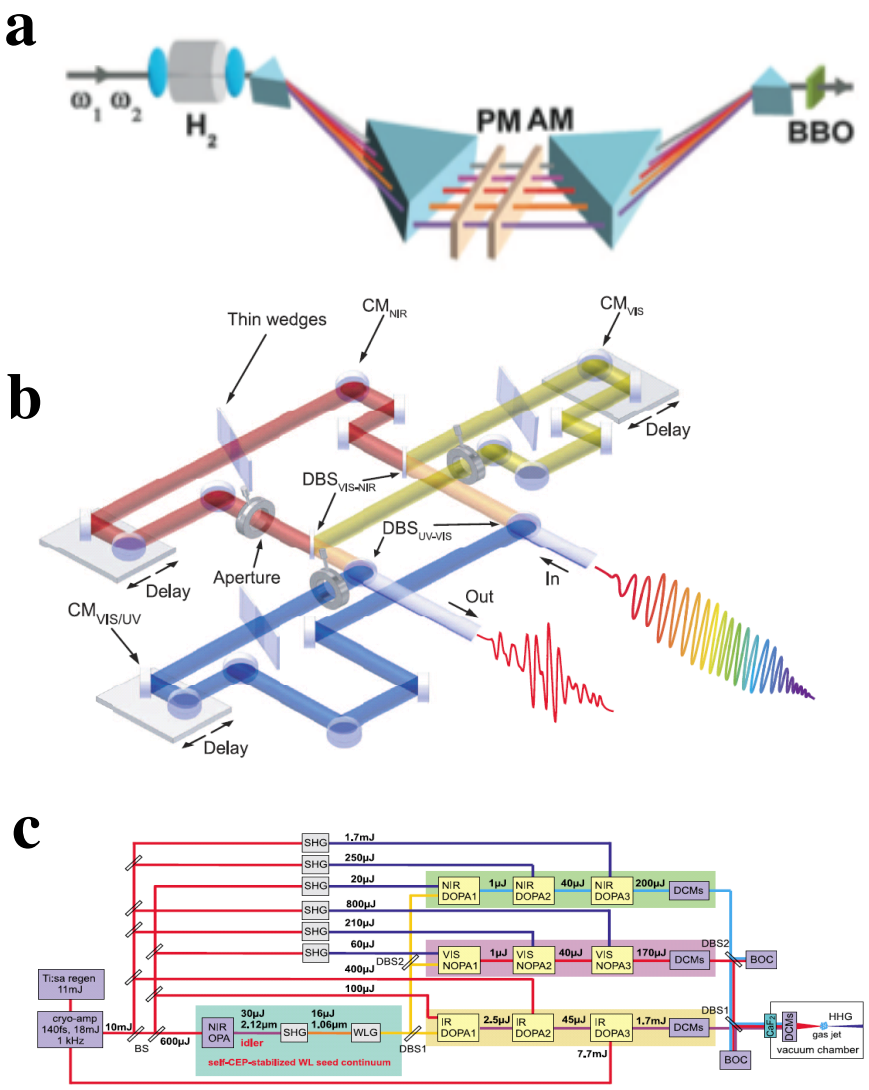

Figure 5.2: Three techniques for generating arbitrary electric field waveforms in the optical frequency range. **a** Molecular modulation (figure adapted from [89]). **b** Multichannel Hollow Core Fiber (figure adapted from [92]). **c** Parallel amplifiers (figure adapted from [115]).

Molecular Modulation

One of the first methods proposed for arbitrary waveforms was molecular modulation [89;122], shown in figure 5.2a. In this technique, two lasers with a frequency difference equal to a ro-vibrational transition in a molecule coherently drive the system. This produces an ensemble of ro-vibrational states, which can then emit discreet optical frequencies. Under optimum

performance, such a technique can produce many octaves of bandwidth. It was demonstrated that by simply controlling the CEP and phase difference between the driving lasers, the resulting waveforms could be changed from sawtooth, ramp, and square waves[89]. This technique has demonstrated by far the most control in terms of optical waveform generation but nonetheless presents many limitations in terms of applications in ultrafast optics. In particular, these waveforms are produced with a > 100 THz repetition rate under a single, nanosecond envelope. Ideally, each waveform would be separated much further in time so that each shot would interact with a fresh sample. This usually limits us to sources with much lower repetition rates, typically under 1 MHz. Another consequence is that each waveform contains roughly 1 nJ of pulse energy. Most experiments of interest in waveform control, would require pulse energies on the 100 μJ or even mJ level. While the technique of molecular modulation has demonstrated ground breaking work in the control of optical waveforms, these limitations in its performance are inherent to the technique and will not be discussed further.

Multichannel Hollow Core Fiber

Another method exercises the use of self phase modulation (SPM) in a hollow core fiber (HCF)[90;108], shown in figure 5.2b. While SPM in HCF's has been a popular method for generating "sine-like" few-cycle fields for over two decades[86], the difficulty in controlling the outgoing waveform into a light transient limited its demonstration until only recently. In this method, a single pulse from a Ti:Sapph laser at the mJ level is used to create 1.5 - 2 octaves of bandwidth extending from the NIR to the UV. The outgoing field from a HCF is usually much longer than the input and supports a spectral phase that is difficult to correct with most optical systems. Because of this, the bandwidth is separated into several channels, where appropriately designed chirped mirrors, so named because of their ability to add (remove) chirp to (from) a laser field, are used to cancel out these higher order phases. Afterwards, the individual channels can be recombined to yield a light transient. The channels provide a crude method of pulse shaping by controlling their individual CEP's

and time overlaps. Also, the geometry of the synthesis setup can be made very compact, which reduces environmental noise that can couple into the setup.

Parallel Amplifiers

Yet another technique relies on amplifying spectral channels in a parallel configuration, as shown in figure 5.2c. In this method, two or more optical setups, such as optical parametric amplifiers (OPA) or optical parametric chirped-pulse amplifiers (OPCPA), are seeded with the same laser source in order to output coherent waveforms. Each OPA (or OPCPA) can then be tuned to amplify a distinct spectral channel so that the sum of all the amplifiers yields the desired bandwidth for the outgoing waveform. Afterwards, each channel can be compressed and combined to yield the resulting waveform. This technique is very flexible, allowing for wavelength tunability and high output energies. For this reason, much of the research effort in future synthesis designs has been focused on using parallel amplifiers [91;115;116].

5.1.2 Drawbacks of synthesis techniques

One of the main drawbacks in the construction of modern synthesis setups is the presence of relative timing jitters among the synthesizer's different channels. A useful synthesizer maintains the control of the waveform from one laser shot to the next, which requires the timing jitter to be stable on the order of several tens to hundreds of attoseconds for fields in the NIR. This requires arm length variations, due to vibrational noise, to be suppressed to the level of 10-100 nm.

All multi-channel synthesizers require some sort of active electronic feedback to suppress these variations. The most common method is balanced cross correlation (BCC) [123], which is an all optical method of measuring the timing jitter. First, a sampling of the recombined channels is split into two arms. Each arm generates a signal, such as sum frequency generation, that requires the time overlap of both bandwidth channels. One arm has an additional optical window to provide a known group delay offset with respect to the first arm. At this point, a pair of photodetectors measures the amplitude of the signal in each arm and

measures the difference between these signals for each laser shot. The timing jitter shows up as positive or negative voltage out of the BCC, providing an error signal which can feed a piezo-driven delay stage on one of the arms.

While this technique has been demonstrated as an effective tool in suppressing jitter, it still requires passive stability in the input fields. As demonstrated with CEP in chapter 4, passive methods are essential in removing as much environmental noise as possible so that active feedback can perform adequately. The main issue arising in the parallel amplifiers described in section 5.1.1 is that they typically introduce large path lengths differences. Each amplifier can comprise of multiple amplification stages in order to achieve the required pulse energy for the seed. Additionally, each amplifier introduces noise due to fluctuations in thermal load on the crystals. Because the repetition rate of these amplifiers is limited in order to achieve large pulse energies (100 μJ- mJ), the sampling rate on vibrational noise limits the frequency detection of the synchronization instrument.

Sources such as the ones described in section 5.1.1 and in [90;92;108] have a proven track record of day-to-day performance which can be attributed to the minimal path differences ($\sim$0.5 m) of their individual channels. Because the entire synthesizer fits on a single, $\sim$1m^2 breadboard, the entire instrument can be passively stabilized from vibrations by choosing the appropriate mounting on the breadboard and baseplate, while the thermal variations are suppressed with a temperature stabilized water flow system through the breadboard [92]. This passive system allows the active stabilization method, in this case spectral interferometry between the individual channels, to primarily concentrate on mHz-DC noise. Such passive control would be extremely difficult with the systems described in section 5.1.1.

As powerful as the stabilization scheme for sources in section 5.1.1 is, there is a major drawback in that they are limited in output bandwidth. In the case of the sources demonstrated so far, they work in the UV-visible regime [90;92;108]. For HHG, this limits the maximum frequency cutoff, which scales with λ^2 where λ is the central wavelength of the driving field. Also, scaling the system to larger bandwidth and pulse energies is difficult when SPM is only driven by a single field. For this reason, introducing a technique of passive stabilization for multiple beams at different wavelengths is desired.

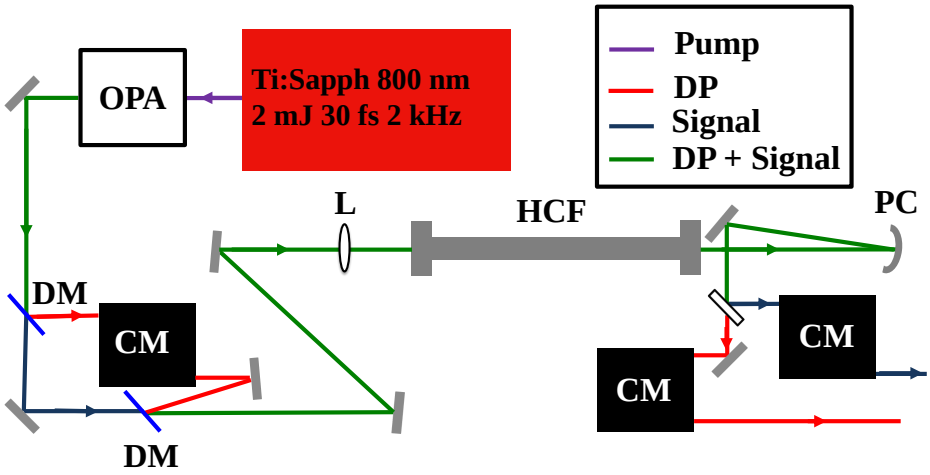

Figure 5.3: The experimental setup for simultaneous few cycle pulse generation. The legend identifies the paths traveled for both beams. DP - depleted pump, OPA- Optical parametric amplifier, DM- dichoric mirror reflecting DP and transmitting signal, CM- chirp mirrors.

5.2 Using the output of an OPA in a single HCF, including the depleted pump

We propose a new take on synthesis by generating few-cycle pulses from the multiple beams exiting an OPA in a single hollow core fiber (HCF). In an OPA, the central wavelengths of the signal, idler, and depleted pump (DP) span over an octave. Thus, as demonstrated in section 4.3.2, it is possible to use spectral broadening to fill the gaps and yield more than 2 octaves of bandwidth[84]. Using the DP instead of an additional beam that bypasses the OPA offers us a couple of notable advantages. First, since the DP exits the OPA with the signal and idler, it starts with comparatively minimal timing jitter. In addition, in section 5.3, we demonstrate that the DP is capable of few-cycle pulse generation. This recycling of the DP enhances the overall efficiency, thus lowering the energy requirements of the pump laser.

Though OPA modes are inherently poor in spatial quality, the use of a HCF has been shown to act as a spatial filter when properly aligned[124]. This is especially useful for the DP as it acquires spatially dependent energy depletion when optimizing the OPA output. Using the same HCF for all beams offers another stage with passive stability on the timing

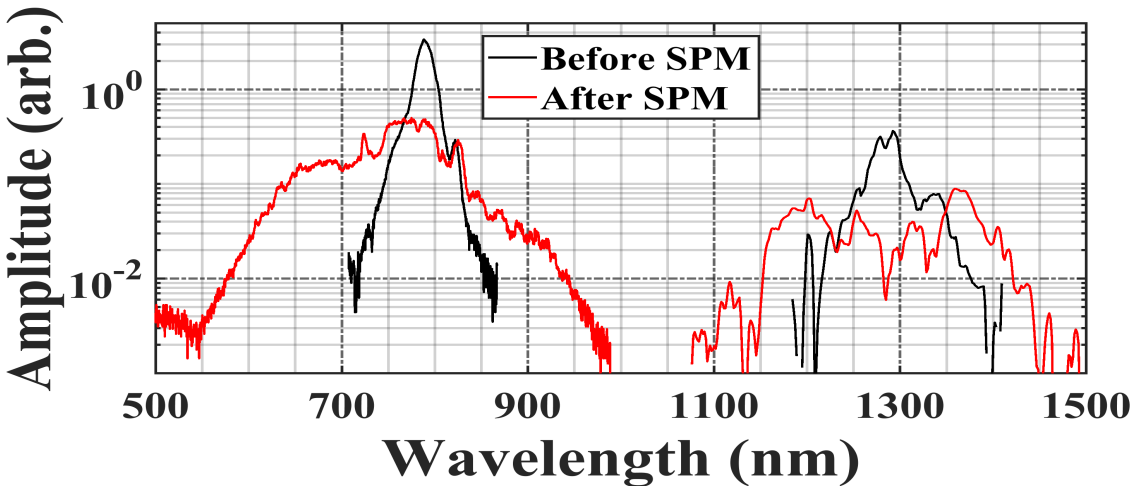

Figure 5.4: Spectra of the DP and Signal before and after the HCF.

jitter as HCF setups are usually several meters long. This significant reduction in separate path lengths improves the performance of synchronization tools. Because a single HCF is less sensitive to environmental noise than using multiple fibers, we believe our method to be more robust than the multi-channel techniques[115;116] described earlier. Thus, what we are essentially proposing is to include multiple laser fields into a single HCF and tuning their central wavelengths to cover the maximum bandwidth while maintaining overlap. With this, we can extend the capabilities of sources describe in section 5.1.1 to larger bandwidth and larger pulse energies while maintaining their impressive stability.

We demonstrate steps required to perform synthesis of the DP and signal and show they can be simultaneously broadened to spectra supporting few-cycle pulses. We further compress both outputs to few-cycle duration using the appropriate chirped mirrors and measure these pulses with the second harmonic generation frequency resolved optical gating (SHG-FROG)[79] technique. We perform a calculation on the synthesis of these pulses and discuss the practical implications of this apparatus. We also discuss how a future generation of the instrument can utilize the benefits demonstrated in this paper while overcoming several of the present limitations.

The experimental setup is shown in figure 5.3. The system starts with an 800 nm, Ti:Sapph laser operating at 2 mJ energy per pulse with an intensity FWHM pulse duration

of 30 fs and a 2 kHz repetition rate. The laser pumps a parametric superflouresence (PSF) seeded OPA from Light Conversion (TOPAS 800). The OPA generates a 410 μJ signal centered near 1300 nm with a FWHM intensity pulse duration of 40 fs, along with a residual 850 μJ depleted pump (DP).

The output of the OPA is separated with a dichroic mirror that reflects the DP but transmits the signal. Since the laser chirp is optimized for the OPA, the DP would be approximately 60 fs upon entering the HCF. To bring the DP closer to transform limited, a set of chirped mirrors (CM) is used to compress the pulse to 40 fs before entering the HCF. Note that, the need for separating out the DP for chirp compensation mostly originates from the 3 mm thick beta-Barium Borate (BBO) crystal used for amplification in this particular OPA system. The separation also adds about a nanosecond of delay between the two pulses which eliminates the possibility of four-wave mixing. This spatial separation and chirp compensation step during SPM in an HCF can be avoided by using a thinner ($\approx$ 1mm) BBO crystal at the last stage of the OPA[84]. In that configuration, the effect of four-wave mixing should be minimal as the DP and signal are cross polarized and would have 50-80 fs of delay due to transmissive optics.

The signal and DP are recombined with another dichroic mirror and aligned into the HCF. The spatial mode quality of the OPA necessitates strong focusing into the fiber, we used an uncoated CaF_2 plano-convex 75 cm lens. The HCF is one meter long with a 250 μm diameter core filled with argon gas at an absolute pressure of 1.04 kTorr. The output efficiency for both the depleted pump and signal is around 33%, leaving 230 μJ for the DP and 100 μJ for the signal.

After the fiber, the beams are collimated using a silver coated plano-concave mirror. We do not currently possess a dichroic mirror capable of separating these two broadband spectra so the entire output is sent in either of two sets of chirped mirrors. One is for compressing the DP, while the other is for the signal[66]. The compressed pulse can then be sent to a FROG for electric field characterization.

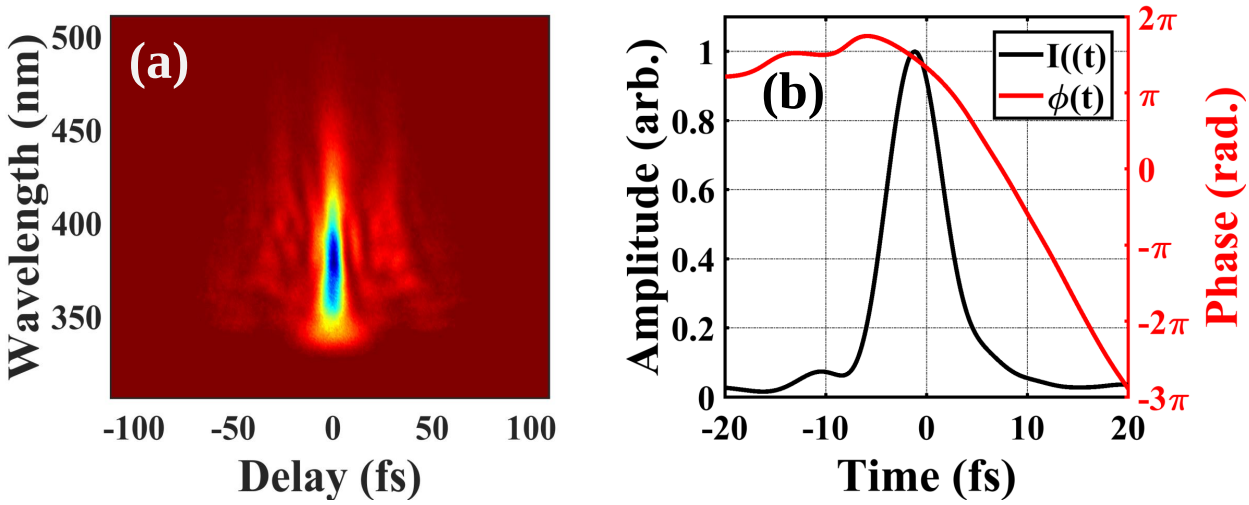

Figure 5.5: **a** Spectrogram for the broadened DP using a single shot SHG FROG. **b** Retrieved time domain electric field and phase for the DP.

5.3 Few-cycle pulses from the depleted pump and signal in a single HCF

The spectra shown in figure 5.4 are generated simultaneously using the same HCF, as laid out in figure 5.3. The spectra span nearly 1.5 octaves while maintaining a high spectral amplitude for most of the region. The combined energy of 330 μJ gives enough energy to, if synthesized, perform strong-field science experiments. To take a step closer to realizing synthesis, we measure the electric field characteristics using SHG-FROG for the DP and the signal.

Figure 5.5a shows the SHG FROG spectrogram for the DP using a home-built single-shot SHG-FROG. To determine the pulse characteristics we use the xFROG 3.2.2. program from Femtosoft Technologies to perform a pulse retrieval algorithm. The retrieval was found with a FROG error of 0.45%. The retrieved time-domain intensity envelope and phase in time is shown in figure 5.5b. The DP is found to have a duration of less than 7 fs, which is a few-cycle pulse containing about 2.5 electric field cycles for a center wavelength near 750 nm. This is achieved even with the presence of the higher order phase. The spectral bandwidth is capable of supporting a 4.3 fs pulse, assuming no higher order dispersion is

present. This demonstrates that despite the poor spatial and temporal qualities of the DP, it is still capable of strong SPM in an HCF and can generate few-cycle pulses with Bessel mode properties.

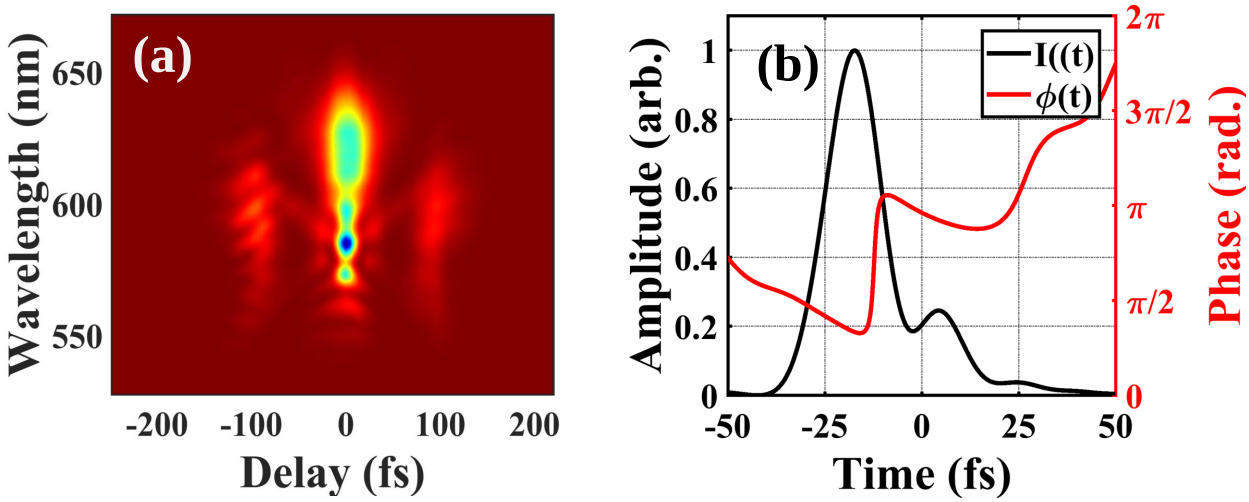

Figure 5.6: **a** Spectrogram for the broadened signal using a scanning SHG FROG. **b** Retrieved time domain electric field and phase for the signal.

To characterize the signal, we use a home-built scanning SHG-FROG designed for broadband long wavelength pulses. The same retrieval program was used to characterize the pulse for the signal as was done for the DP. The spectrogram and electric field in time are shown in figure 5.6a and 5.6b, respectively. The retrieval was found with a FROG error of 0.25%. The phase in 5.6b indicates that, apart from some third order dispersion, the pulse is largely transform limited. The retrieved pulse duration of 16.5 fs, corresponding to a 3.8 cycle pulse, is close to the transform limited duration of 14 fs. We note that the signal at these wavelengths experiences very little dispersion in standard transmissive optical material such as fused silica (-2.3 fs^2/mm) and CaF_2 (9.1 fs^2/mm). For this reason, the beam is nearly transform limited entering the HCF which allows the pulse to be compressed with the high quality shown in figure 5.6b.

Figure 5.7 is a calculated synthesized field based on an ideal recombination (no jitter) of the experimentally retrieved fields shown in figures 5.5b and 5.6b. We find a central wavelength of 1020 nm, corresponding to a 3.4 fs field cycle. The FWHM of the synthesized

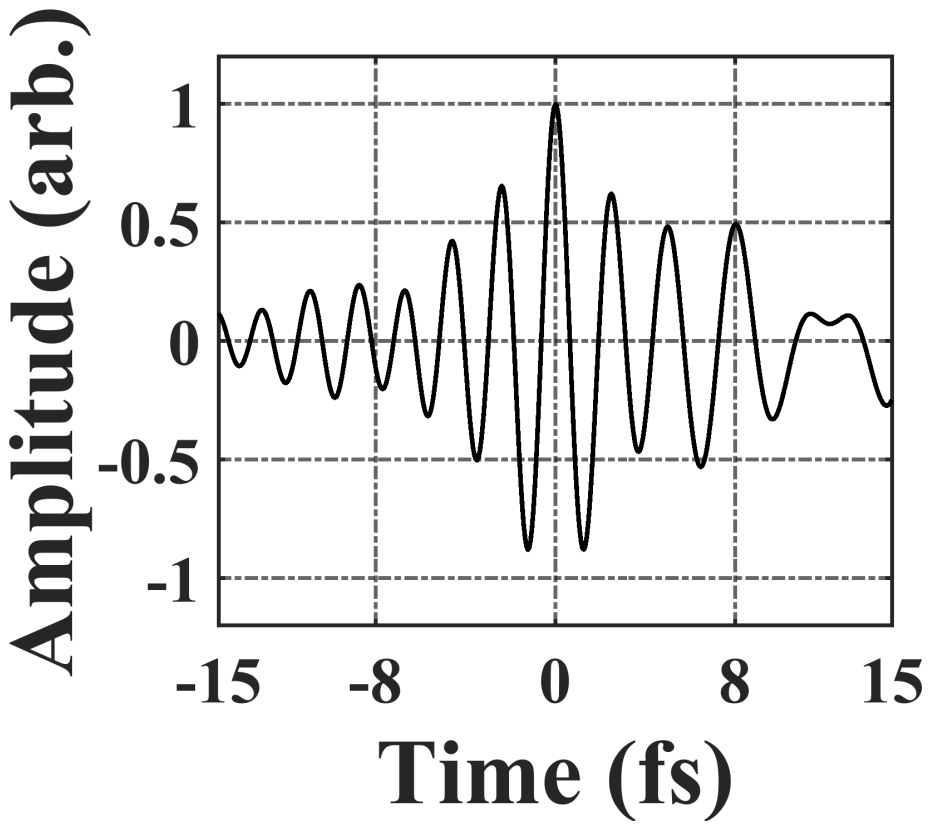

Figure 5.7: Simulation of a synthesized field in using the pulses shown in figures 5.5b and 5.6b.

pulse is 4.3 fs, resulting in a 1.25 cycle field. Better control of higher order phase could reduce the intensity FWHM pulse duration to under one carrier cycle. Moreover, while setups for synthesis employing HCF's tend to generate center wavelengths in the visible range[90;92], this setup yields a central wavelength in the NIR.

The results of our approach demonstrate significant steps towards a future waveform synthesizer with passively suppressed timing jitter. Our current design presents a few limitations that can be easily handled in a future generation of the source. One current drawback is the use of a PSF seeded OPA which does not preserve the carrier envelope phase (CEP) of the pump to the signal. In addition to the relative phase stabilization, the overall CEP should be stable in order to provide a consistent synthesized pulse for each laser shot. Fortunately, our next generation source can utilize a CEP stable Ti:Sapph laser[84]. This, along with a white-light seeded OPA, which preserves the CEP of the pump in the signal[109], can yield

phase stable pulses in both the DP and the signal.

In our current setup, the low peak intensity of the DP required us to separate the beams before the HCF in order to decrease the pulse duration with chirped mirrors. As stated earlier, we believe this step can be eliminated as our future source will utilize a thinner BBO, a DP with pulse energy >10 mJ, and a HCF capable of handling the total fluence[125;126]. This would allow for a single, short path length, stage of separation after the HCF for pulse compression, much like that in[90;108]. Since systems like the one discussed in[84] possesses a mJ level idler which is passively CEP stable[109], a three pulse synthesizer with a single HCF could be realized using our new system as the pump. Again, because the beams co-propagate for most of the optical setup, we could produce mJ-level synthesized waveforms with bandwidth spanning from the UV to the mid-IR with optimum passive control of the time jitter.

5.4 Broad bandwidth pulses from signal and idler in a single HCF

In another step towards demonstrating transients from multi-octave, mJ level fields in the NIR, we demonstrated the simultaneous generation of bandwidth supporting few-cycle fields for both the signal and the idler of an OPA. In the setup, described in sections 5.2 and 5.3, we were required to separate the two fields before SPM in the HCF. In this section, we demonstrate the feasibility of bypassing this step by maintaining co-propagation of the signal and idler from their generation from the BBO and through the HCF.

In the final amplification stage of our OPA (see section 4.3), the pump and seed (100 μJ signal) are co-linearly overlapped, using a dichoric mirror (DM) in a large diameter beta-barium borate (BBO) crystal, and the amplified signal and idler are separated from the now depleted pump using another DM. When this stage is well aligned, the signal and idler can follow one another for a large distance ($\approx$10 m) after the OPA.

However, this is not precise enough for coupling both beams into a fiber. As shown in

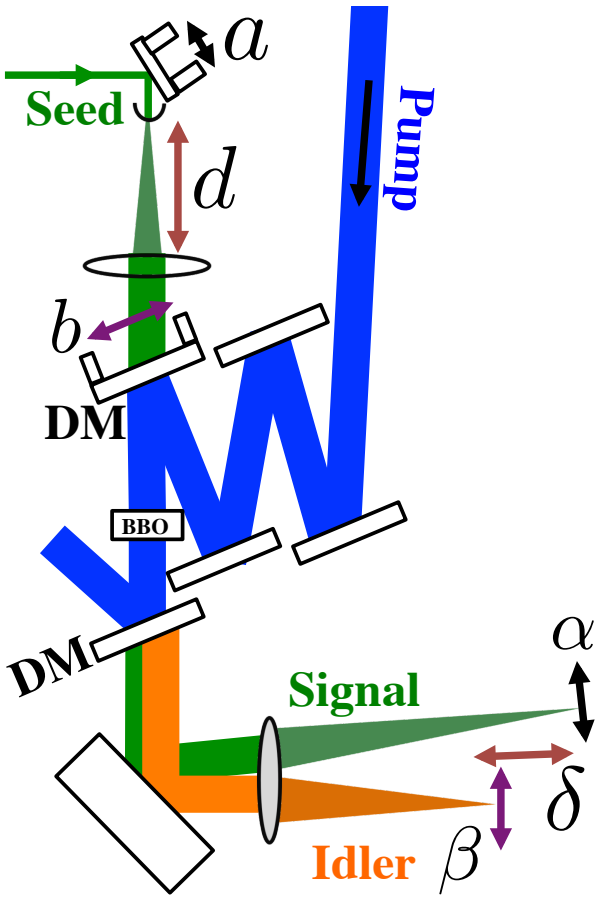

Figure 5.8: Method for creating co-propagating fields using the final amplification stage of the HE-OPA (see section 4.3). The seed (green) is incident on mirror a and passes through a beam-expanding telescope with a separation distance d. The pump (blue) is incident on the dichoric mirror (DM), b, where the seed and the pump both pass collinearly through the BBO to generate OPA. Afterwards, the pump is removed with an additional DM. The now amplified seed (signal, green) and idler (orange) exit the OPA. For the two fields to be coupled into an HCF simultaneously without separation, the positions α and β must be identical as well as the relative divergence, δ. The primary control knob for α is mirror a, the primary control knob for β is b, while the primary control for δ is d.

figure 5.8, the transverse position of signal (labeled α) and the idler (β) can still be several beam diameters apart when focused in a collinear arrangement. In addition, they can have significant deviations in their divergence, shown by δ. To efficiently couple both beams into an HCF, all of these parameters need to be controlled. To do so, we perform small adjustments on the beams before the amplification stage.

The divergence mismatch of the signal and idler arises from the alignment of the telescope separation in figure 5.8. Both the signal and the pump have a small divergence mismatch,

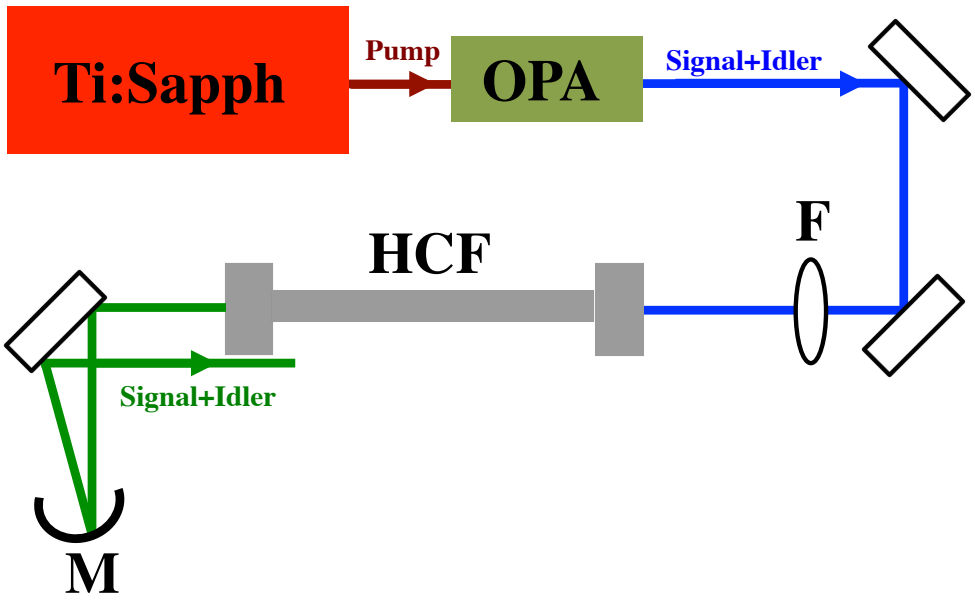

Figure 5.9: Layout for co-propagating the signal and idler into an HCF. Ti:Sapph- Titanium Sapphire laser (HITS), OPA- Optical Parametric Amplifier, F- 75 cm CaF_2 lens, HCF- hollow core fiber, M- 1 meter spherical concave Ag:coated mirror.

which causes a small momentum mismatch that is made up for by the idler. For example, if the pump is collimated, but the signal is slightly converging, then the idler will slightly diverge, and vice versa. We can control the divergence of both the signal and the idler using the telescope separation, d. This effectively matches the divergence of the signal to the pump, so that not only the signal and idler can focus into fiber at the same longitudinal position, but also the depleted pump could be coupled in later on.

After the beams have been matched to focus at the same place on the table, we can control their transverse positions. The mirror labeled a controls the transverse position of the signal, α. However, due to conservation of momentum, this will simultaneously shift the position of the idler β. A better method would be to efficiently couple the signal into the HCF and then optimize the idler without influencing the signal. Because the pump position has little influence on the signal when we perform small alignment deviations, we can tune mirror b to control the coupling of the idler. In practice, two mirrors on the pump path are required to get the angle into the HCF, as well as the position, for the idler follows signal. Once this alignment has been performed, the coupling of both the signal and the idler can

be greater than 50 %, and is stable so long as the laser/OPA system requires no realignment.

The layout for simultaneous SPM of the signal and idler is shown in figure 5.9. We used the HITS laser (operating at 8 mJ mode) to pump our OPA, which can be done when the OPA is equipped with an alternate telescope and beam splitter option for the final amplification stage. We co-propagate 1 mJ of the signal and 0.8 mJ of the idler and focus them into an HCF using a 75 cm CaF_2 lens (F). In this experiment, the HCF was a 60 cm long, 450 μm diameter fiber filled with argon gas at an absolute pressure of 1.5 ktorr. The output is then collimated using 1 m spherical concave silver-coated mirror.

The broadening is shown in figure 5.10. We see that the spectra before the fiber (red) are relatively narrow and have a spectral gap; while afterwards (black), the spectral gaps are filled and show extension of the overall supported bandwidth. We also retrieved roughly 50 % transmission for both beams, maintaining a total pulse energy at the milli-Joule level. Up to now, this experiment has only been attempted on preliminary runs, so we have yet to perform FROG measurements on these fields. For the time being, we can use a quick calculation of the FTL pulse duration, shown in figure 5.11. The calculation shows that we clearly have enough bandwidth to support few-cycle fields in both pulses.

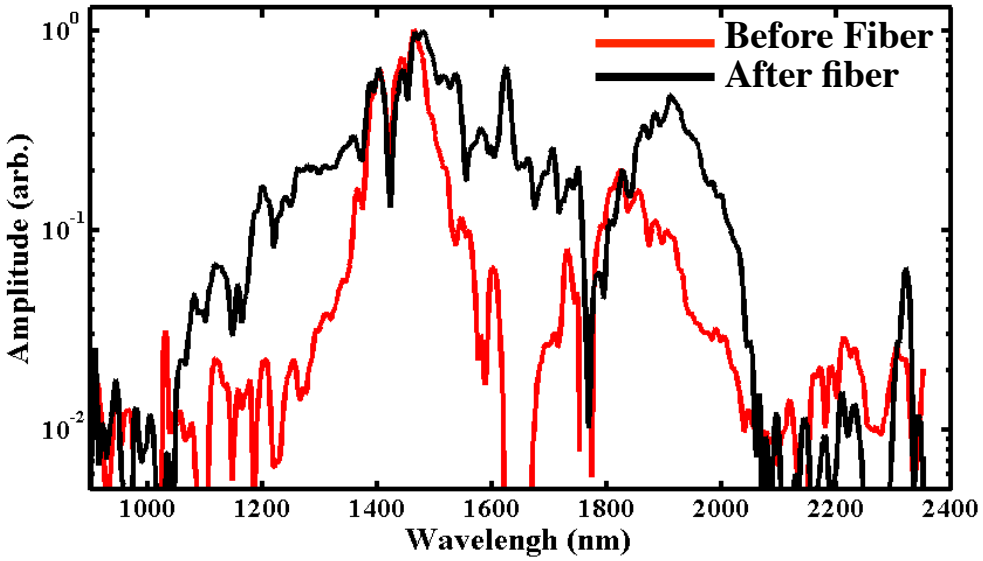

Figure 5.10: Spectra for the signal and idler before the HCF (red) and after (black).

It is possible to improve these results in the future with some simple modifications.

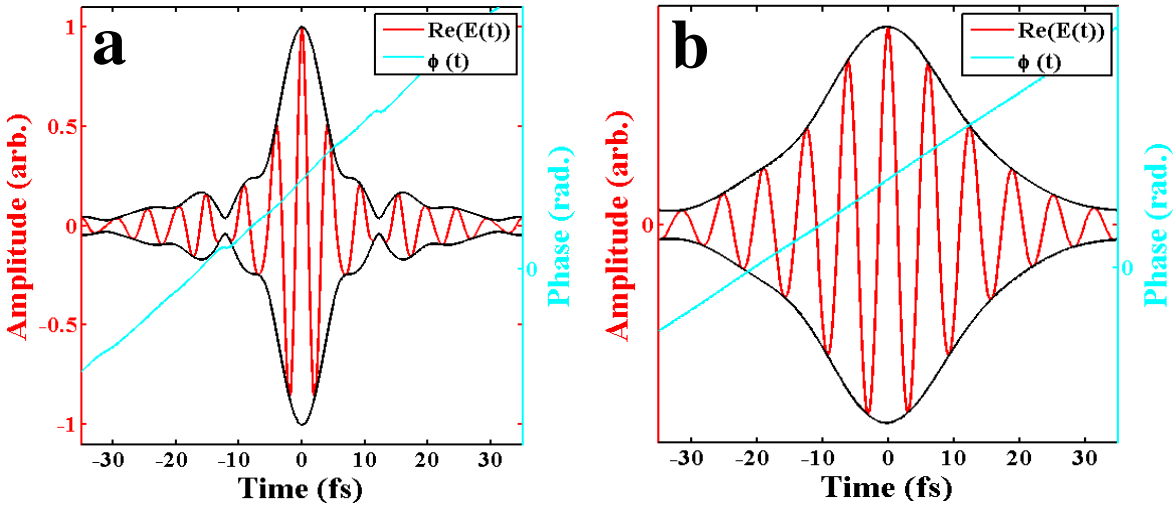

Figure 5.11: Calculated transform limited fields.

A better fiber design from few-cycle inc.[125;126] would allow for improved broadening and transmission. For technical reasons, the HITS laser was running in a truncated mode for these experiments, and it is possible to increase the overall energy for better broadening.

In addition, the depleted pump could be included. At the time, we were unable to efficiently couple the DP from the HITS OPA due to astigmatism, which is most likely due to poor alignment of one of the telescopes for the DP inside the HITS OPA. Recent observations of the focused DP show no sign of astigmatism.

In principle, once the signal and idler are co-propagating into the HCF, it should be a simple matter of removing the final dichoric mirror (DM) in the OPA, shown in figure 5.8, to couple the DP with the other two beams. However, the very high pulse energy of the DP ($>$ 10 mJ) could easily damage the fiber with any misalignment, as well as more than doubling the average power coupling into the HCF. There are ways to mitigate this. For one, a specially designed coating could be manufactured to reduce the power of the DP but also transmit the signal and idler. Due to the special nature of this request, we could expect it to be limited in quality and expensive to produce. Another option is to exploit the beam diameters of the three beams. The nonlinear process of OPA effectively reduces the beam diameter of the signal and idler with respect to the DP. Perhaps a simple iris can both decrease the power and better match the DP's spot size with the signal and idler, produce

a better coupling.

In summary, we have demonstrated several significant steps for a new approach of generating mJ level, multi-octave fields for arbitrary waveform generation. In particular, our variation of the synthesis technique relies on a passive system where vibrational noise is minimally coupled into the system by minimizing path length separation. To be effective, this technique requires, 1) a OPA depleted pump which can generate few-cycle laser fields 2) multiple laser fields to be simultaneously coupled into a single HCF and 3) multiple laser fields to co-propagate without separation before an HCF. We have demonstrated these three critical steps. In the future, a laser equipped with the same level of CEP stability as shown for HITS in chapter 4 but with longer term reliability can demonstrate the generation of arbitrary waveforms.

Chapter 6

A light source for strong-field physics in the long wave infrared

Much of the work in this chapter will be presented in an upcoming publication[127].

In this chapter, we will shift our focus on another development project utilizing the HITS laser. In this case, we are interested in creating short (few-cycle) laser fields in the long-wave infrared (LWIR, 8-15 μm) that are capable of reaching peak intensities greater than 10 TW/cm^2.

6.1 The physics of going to longer wavelengths

Intense fields in the long-wave infrared (LWIR, 8-15 μm) have the potential to create new areas of research in strong-field science. Sources in this range can utilize the λ^2 scaling of the ponderomotive energy to accelerate electrons to kilo electron-volt (keV) energies while still having the peak intensity to perform ionization unassisted[128;129]. In particular, few-cycle fields are interesting because they can create isolated attosecond pulses via higher order harmonic generation[35]. Theory also suggests that short, intense fields ($\approx 10^{14}$ W/cm^2) in

the LWIR may be capable of molecular dissociation via multi-photon transitions between vibronic levels[130] and observation of the breakdown of the dipole approximation[131]. We demonstrate a simple technique capable of generating few-cycle pulsed fields with carrier wavelengths tunable from 5.3 μm to 8.9 μm. The 80 femtosecond pulse duration, combined with pulse energies ranging 80-120 μJ, yield peak powers at the Gigawatt level. Evidence of reaching peak intensities of 100 TW/cm^2 is demonstrated by ionizing xenon.

Highly energetic electrons are responsible for the first demonstration of a table-top coherent X-ray source[132], isolated attosecond pulses with a center frequency of 300 eV[133], and the first attosecond-resolved measurements of a chemical bond with ångström resolution[39;40]. Such breakthroughs are possible thanks to the extension of femtosecond sources into the 3-5 μm range of the mid-wave infrared (MWIR, 3-8 μm)[134–137]. These studies have motivated the development of intense ultrafast sources at even longer wavelengths. While a variety of techniques for producing strong fields in the LWIR have existed for decades, they have yet to satisfy all the requirements for harnessing the capabilities available in the MWIR.

The most intense sources currently available in the LWIR are based on CO_2 laser technology, which is limited to picosecond ($>$ 30 field cycles) durations[138]. A standard method for generating femtosecond pulses in this region employs difference frequency generation (DFG), where two high frequency fields are mixed in a suitable nonlinear medium for DFG to produce a new field which can possess a much longer wavelength[67;68;139;140]. Recently, a new source based on optical parametric chirped-pulse amplification has demonstrated 200 μJ, $\approx$8-cycle pulses with a MWIR wavelength of 7 μm[141], while another based on DFG has achieved sub-cycle fields at 30 μJ, spanning 2-9 μm, but with a central wavelength of 4.2 μm[142]. None of these sources have performed strong-field science experiments due to the difficulty of their achieving the required peak intensities.

An exciting prospect for strong-field, few-cycle sources in the LWIR is the possibility of uncovering phenomena not present at shorter wavelengths. In particular, they can have a dramatic influence on molecular dynamics because the photon energy approaches, or falls below, the energy spacing of vibronic levels in many molecules. It has been proposed that

strong, few-cycle fields in the LWIR could dissociate molecules at a higher rate than sources in the NIR and MWIR due to multi-photon transitions between individual vibronic levels[130]. Other possibilities are the observation of dynamics due to the breakdown of the dipole approximation at modest intensities[14;131] and extreme modification of optical waveforms via shock formation[143]. Despite the value these studies have in strong-field, ultrafast science, no light source has been demonstrated with the required specifications for performing them.

6.2 Technical considerations for the LWIR

Before discussing the method for our setup, it is important to consider the available options for generating strong laser fields in the LWIR. Each method has notable advantages and disadvantages. We ultimately select the method of difference frequency generation due to its ease of incorporating into our available light source, the HITS laser, and its ease of use in strong-field laser experiments.

6.2.1 Criteria for choosing an LWIR generation technique

To achieve strong laser fields in the LWIR we need to overcome a few major obstacles. Because no lasing media exists in the LWIR for direct femtosecond pulse production, we require the use of nonlinear optics. In the case of some of the earliest pioneering work in strong-field physics, this was resolved by starting with CO_2 lasers, operating at 10.6 μm, and using appropriate compression techniques to produce picosecond (> 30 field cycle) laser fields[128;129]. Thirty years have passed since this was demonstrated, and while the technique has improved in peak power, the challenge of producing femtosecond, tabletop compatible, sources is ongoing[138].

The standard approach for femtosecond fields is via difference frequency down-conversion of high frequency laser fields. Because this technique amounts to splitting photon energies,

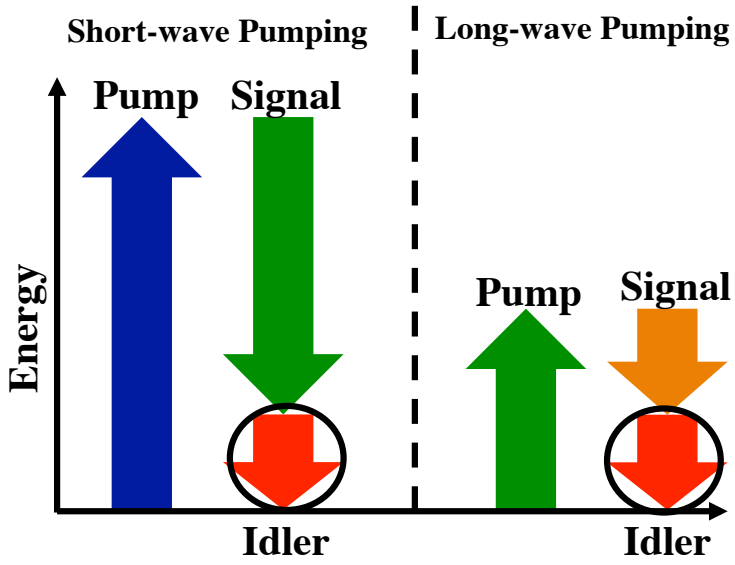

Figure 6.1: Explanation of quantum efficiency. On the left, a high photon energy pump is mixed with a high photon energy signal, producing an idler photon with much lower energy. On the right, the same idler photon is produced but using a pump and signal that are much lower in energy. Typically, the process on the right will be much more efficient since a larger fraction of the energy will be yielded to the idler.

it can be severely limited by the quantum conversion efficiency, $Q.E.$, which goes as,

$$Q.E = \frac{E_i \lambda_i}{E_p \lambda_p}, \tag{6.1}$$

where E_i and E_p are the pulse energies of the idler and pump for the mixing process, respectively, and λ_i and λ_p are the wavelengths of the idler and pump, respectively. When $Q.E. = 1$, all available photons have been used. So, if we start with an 800 nm laser, and seek to produce an 8 μm field with a perfect $Q.E.$, we would suffer an order of magnitude drop in pulse energy. However, if we had a pump laser starting at a much longer wavelength, say 2.4 μm we could potentially retrieve three times more pulse energy into the idler simply because the photon energy is more commensurate. A visual explanation of this process is demonstrated in figure 6.1.

In general, the situation is even worse because of other physical limitations. For example, our laser fields are typically Gaussian in space and time, meaning that the instantaneous electric field strength varies widely in all three dimensions. Because nonlinear mixing is very

sensitive to the field strength, we cannot expect the process to be perfectly efficient in all these dimensions. Thus, even a good beam geometry can expect a $Q.E.$ of only 0.4. Another way to think of this is that it is very difficult to construct a nonlinear amplification such that every single pump photon participates. Thus, we can think of $Q.E.$ as a measurement of the number of pump photons that participate in nonlinear amplification.

With this in mind, we can consider two options. The most logical is to have a pump laser operating at longer wavelengths, as shown on the right hand side of figure 6.1. In this way, one can reduce the limitations of $Q.E.$ via a large splitting ratio of the photon energy. Eventually (and even as I write this) the field is moving to this scheme. However, these sources are still far in the developmental stage and have practical limitations. Specifically, effort is being placed into solid-state Holmium:YLF and Holmium:YAG lasers operating at 2 μm wavelengths. To pump these media requires appropriate high average power lasers in the 1900 nm-2000 nm range, with the most successful being cw unpolarized Tm:fiber lasers[144–147]. These are difficult to manufacture at the present time, and systems utilizing these suffer from the engineering constraints[141]. So, while the future of LWIR femtosecond production is mostly likely with 2 μm, or even 4 μm pump lasers[141;148], for the time being, an apparatus with the task of performing experiments requires time-proven technology.

A reliable method for LWIR generation is DFG on an OPA, as shown in figure 6.2. The OPA first splits the photons of the pump laser, and because it is tunable, we can control the ratio of the photon energy between the resulting signal and idler laser fields. Thus, their difference frequency is also tunable. The second step of the process then involves another frequency down-conversion in a suitable nonlinear crystal.

There are a couple of limitations in this method, the first of which is overall efficiency. As mentioned earlier, we expect nonlinear amplification to be limited in its $Q.E.$, and because this requires two amplification steps, the process is necessarily inefficient. Another issue is that, while the signal and idler wavelengths are tunable, there is a unique solution for a desired DFG wavelength. Thus, we cannot arbitrarily choose which wavelength to pump with in this scheme, which limits us in our choice of nonlinear crystal. There exists an alternate method, commonly known as dual-OPA, which can mitigate this issue.

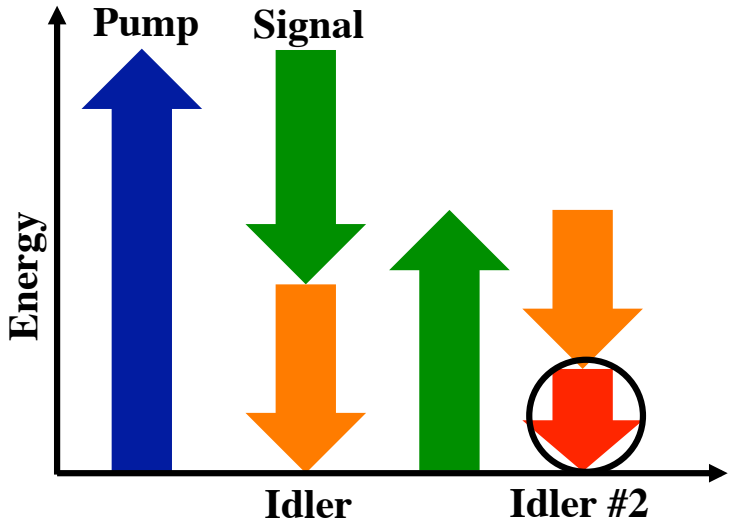

Figure 6.2: Pictogram of the two-step process for generating LWIR pulses. First, a laser (blue arrow) pumps an OPA to generate a signal (green) and idler (orange). The signal and idler and then mixed in an additional DFG process, shown on the right, to create the LWIR beam (red).

Due to the technical constraints of going to longer pump laser wavelengths, and the fact that we posses a 20 mJ laser with a 6 mJ OPA, our choice for generating LWIR wavelengths will utilize DFG of our OPA. Now we need to consider our choice of crystal.

6.2.2 Choosing the best crystal

The UV-Visible-NIR ranges are spoiled with the beta-barium borate (BBO) crystal, which has possibly some of the most well-rounded properties one can ask for in high energy nonlinear amplifiers. Someone must have made a terribly large sacrifice to Lh'Asor, the lord of lasers (see the dedication page), for this crystal to exist. Besides its suitable birefringence, with appropriate phase matching bandwidth throughout this range, its d_{eff} of 2.2 pm/V[149], while quite modest, allows for strong frequency conversion. The crystal's main advantage is its ability to withstand intense laser fields of several hundred GW/cm^2 when pumped with NIR, femtosecond fields without inducing higher order nonlinearities, such as SPM.

While BBO has revolutionized strong field laser sources, there is no such crystal in the LWIR that is available in large supply. So when selecting which crystal is most appropriate

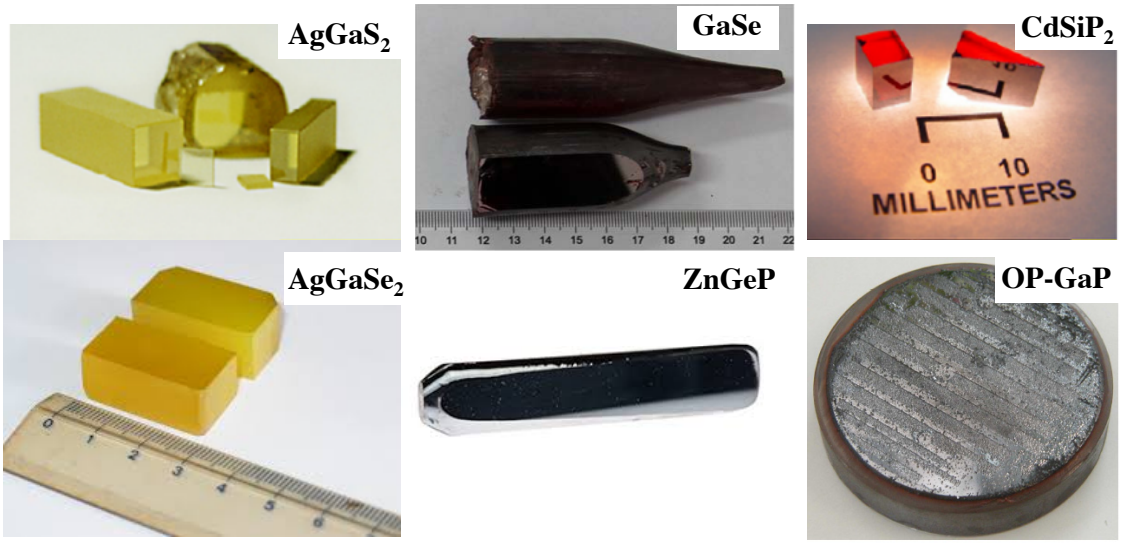

Figure 6.3: Various crystals for generating light in the LWIR.

for our application, we are required to weigh a multitude of criteria. For one, it must be transparent to both the pumping wavelengths (1-2 μm range for us) and the LWIR. It must also be birefringent, and phase-match large enough bandwidth for femtosecond pulses. An appropriate d_{eff} allows us to use a thinner crystal, improving our bandwidth limitations. Other practical limitations are the growth dimensions, which, combined with damage threshold, provide an upper bound on our available pumping energies. Finally, availability is essential, as it is impossible to use a crystal if no one is willing to grow it for us.

A list of crystals we consider as candidates for LWIR generation are shown in table 6.1, with accompanying photographs in figure 6.3. As we can see, there are varying pros and cons to each. For instance, ZGP is a clear winner if only we could pump with wavelengths 2 μm and up, while $CdSiP_2$ and Orientation Patterned (OP)-GaP are an excellent choice if you can have the crystal manufactured for your system. GaSe is severely limited by its weak crystalline structure and $AgGaSe_2$ is somewhat limited by its absorption edge.

We are left to consider $AgGaS_2$ (AGS). This crystal can be grown to diameters that allow us to use most of the OPA light ($\approx$ 4.2 mJ) without immediate damage. We found its properties to be the best compromise for our system.

Crystal	transparency range (μm)	d_{eff} (pm/V)	radius (mm)	damage threshold (GW/cm^2)	availability
$AgGaS_2$	1.05-12[150]	13[151]	10	25[152]	common
$AgGaSe_2$	1.4-18[153]	33[154]	10	20[152]	common
GaSe	1.3-18[155]	54[156]	7 (only z cut)	700[157]	common
$CdSiP_2$	1-10[158]	84[159]	20	20[160]	rare
OP-GaP	1-12	75[161]	20	55[162]	rare
$ZnGeP_2$	1.9-12[155]	75.4[163]	25	1000[164]	poor

Table 6.1: A list of candidate crystals for use as a nonlinear medium for DFG in our setup. The dimensions of GaSe are only available in z-cut, which severely limits the actual area of the crystal when rotated for nonlinear amplification. $CdSiP_2$ is currently grown by one laboratory in the world. Damage thresholds are reported for 100 fs pulse durations at a wavelength of 1 μm.

6.3 Layout for LWIR generation

The DFG scheme allows us a few advantages. First and foremost, the technique is simple, requiring only one nonlinear crystal after an optical parametric amplifier (OPA). Secondly, the short path length and minimal number of transmissive optics allows for near transform-limited pulses. Finally, with a front-end based on Ti:Sapphire and an OPA, technology present in most strong-field science laboratories, this method can be immediately extended to other facilities.

As shown in figure 6.4, the system uses an 800 nm, Ti:Sapphire laser to pump an OPA generating up to 6 mJ of signal (1300 nm-1450 nm) and idler (2000nm - 1735 nm) in the NIR. Additional information about the laser and OPA system can be found in[84] and chapter 4. DFG between the signal and idler of the OPA is performed in an interferometer-based setup. Co-linear overlap is ensured by observing the spatial chirp of the LWIR mode in the far field. This allows the beam to be focused to the smallest possible area and, thus, produce the highest peak intensities.

For DFG, we use a 1x1x0.1 cm, anti-reflective (AR) coated $AgGaS_2$(I) crystal (AGS, Altechna). With such a large surface area, up to 4.2 mJ of the OPA can be used in the DFG process. Incident energies greater than 4.2 mJ accelerate degradation of the crystal and show

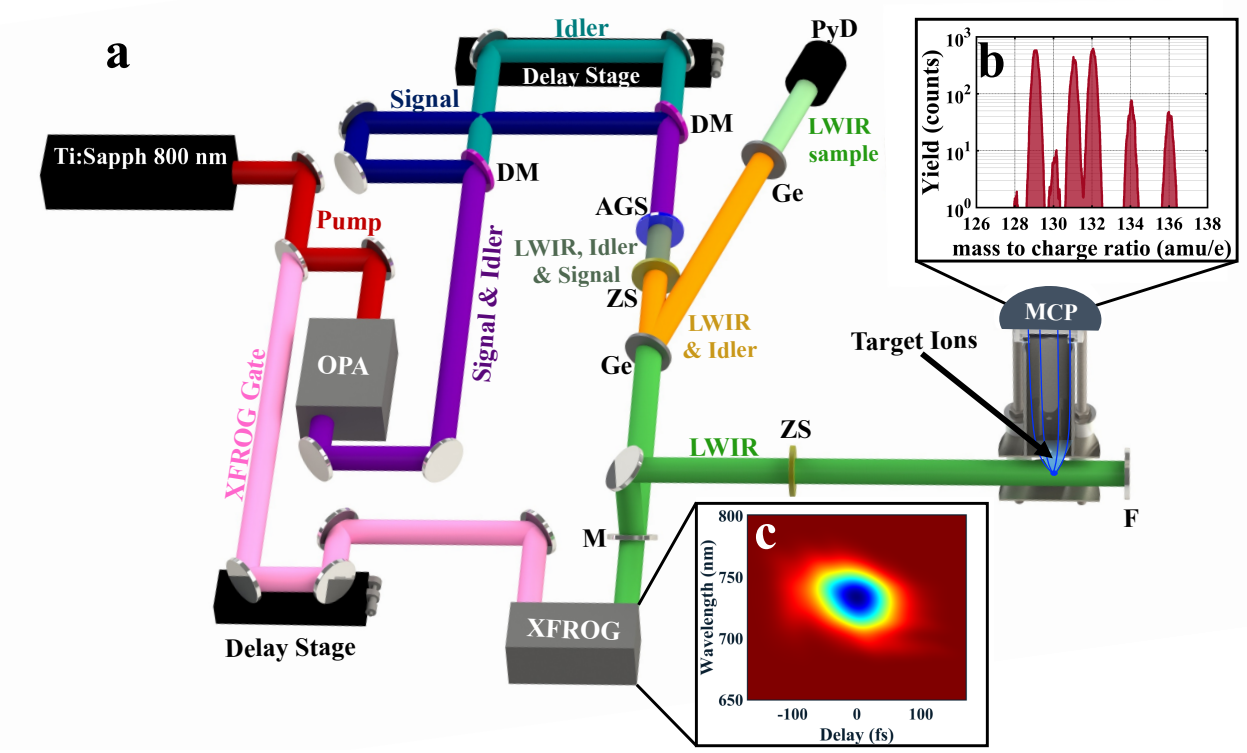

Figure 6.4: **Layout for the LWIR generation, a:** The output of a 20 mJ Ti:Sapph 800 nm laser is separated with a beam splitter (BS) to pump an optical parametric amplifier (OPA) with 18 mJ, 26 fs pulses at 1kHz. The OPA generates 6 mJ of signal+idler, up to 4.2 mJ of this beam are used in a dichroic mirror (DM) based interferometer to generate LWIR pulses via difference frequency generation in a $AgGaS_2$(I) crystal (AGS). The OPA is filtered using a pair of anti-reflective coated Zinc Selenide (ZS) and Germanium (Ge) windows. The Fresnel reflection off the Ge window is filtered with an additional Ge window so residual leakage from the LWIR beam can be recorded on a pyroelectric detector (PyD) for single-shot power tagging. A periscope sends the remaining pulse energy ($> 95\%$) into an experimental chamber with a ZS window and a -25 mm spherical concave mirror (F) to back focus the few-cycle LWIR pulse in Xenon (Xe) gas. A pair of electrostatic lenses guide the Xe ions onto a micro-channel plate (MCP) detector for time-of-flight measurements. A small portion of the remaining 2 mJ beam (pink), split prior to the OPA, is used as a gating field in the XFROG. Mirror M is removed from the periscope to couple the LWIR pulse into the XFROG for full electric field characterization. **Ion Time of Flight (iTOF), b:** A typical time of flight spectrum for Xe^+ when ionized with 8.9 μm pulse (see section 6.6). **XFROG, c:** A retrieved XFROG spectrogram for an 8.9 μm laser field (see section 6.4).

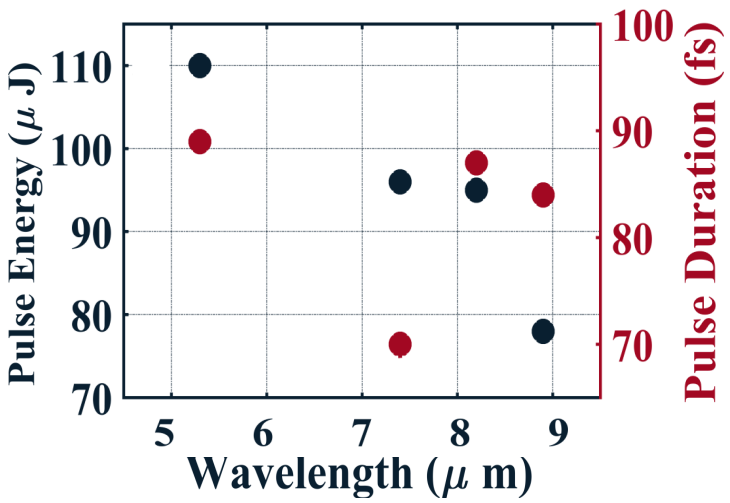

Figure 6.5: Pulse energy (μJ, black) and pulse duration (fs, red) across the tuning range of the LWIR source.

signs of nonlinear back-conversion and self-focusing. By tuning the central wavelength of the signal from 1300 to 1450nm, with the corresponding idler changing from 2000 to 1730nm, we can tune the center wavelength of the DFG process from 3.8 μm to 8.9 μm.

To filter the OPA from the LWIR, we use a pair of Zinc Selenide (ZS) and Germanium (Ge) windows, each possessing a 3-12 μm AR coating. Ge windows are commonly used as low pass filters for the MWIR and LWIR by absorbing all light below 2 μm. Because of the OPA's high incident fluence, we observe free carrier absorption (FCA) in Ge high enough to attenuate the LWIR by as much as 55 %. We eliminate FCA by incorporating the ZS window before the Ge filter, which blocks 90 % of the OPA signal. This increases the usable peak power in the LWIR by as much at a factor of 2.2 at wavelengths greater than 8 μm. Further discussion on the role of FCA in our setup is found in section 6.5.2. Figure 6.5 shows the measured pulse energy in micro-Joules and the quantum conversion efficiency (defined in [165]) across the tuning range. With this filtering configuration, the setup generates a maximum of 120 μJ at wavelengths of 5.3 μm and up to 80 μJ at wavelengths as long as 8.9 μm.

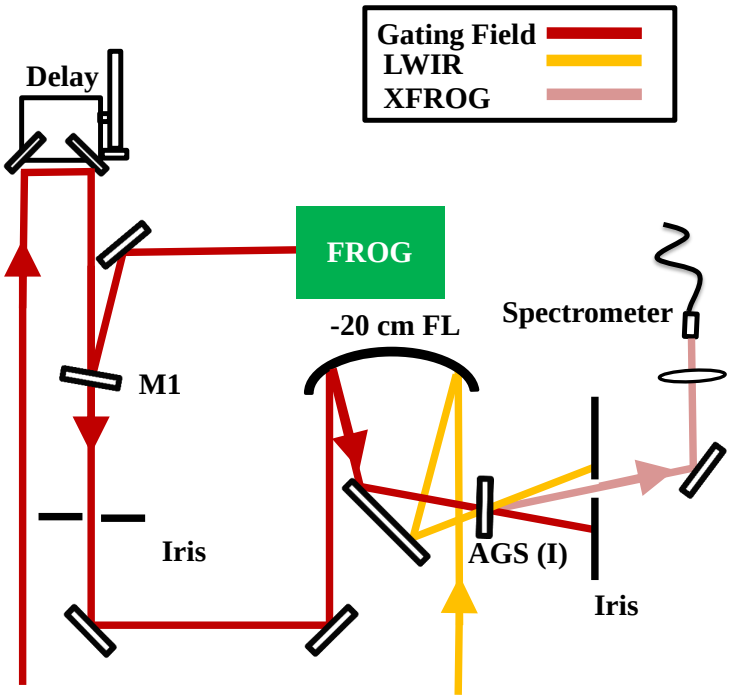

Figure 6.6: Layout for the XFROG. The LWIR and the gating field are sent to a 50 mm diameter, -20 cm focal length Ag coated mirror to non-colinearly overlap the beam on a 8X8X0.4 mm $AgGaS_2$(I) crystal for sum frequency mixing. The XFROG signal is then spatially filtered with an iris and collected with a fiber to be measured with an Stellernet NIR-Vis spectrometer. The spectrogram is taken by recording spectra versus delay using an automated stage on the gating field. A measurement of the gating field can be performed with a FROG when mirror M1 is inserted into the beam line.

6.4 Pulse characterization

XFROG is a cross correlation optical measurement technique which is favorable when an autocorrelation signal is difficult to measure or produce[80]. In the case with LWIR generation, a frequency resolved measurement of the second harmonic field requires a HgCdTe or pyroelectric based spectrometer, which are expensive, time consuming, and/or sensitive to thermal noise. On the other hand, an XFROG employing the sum frequency of 800 nm Ti:Sapph laser + LWIR, results in a signal that is not only measured with a readily available, silicon ccd based spectrometer, but is visible by eye and easily optimized in the laboratory setting.

The XFROG setup is shown in figure 6.6. The gating field and the LWIR are incident on

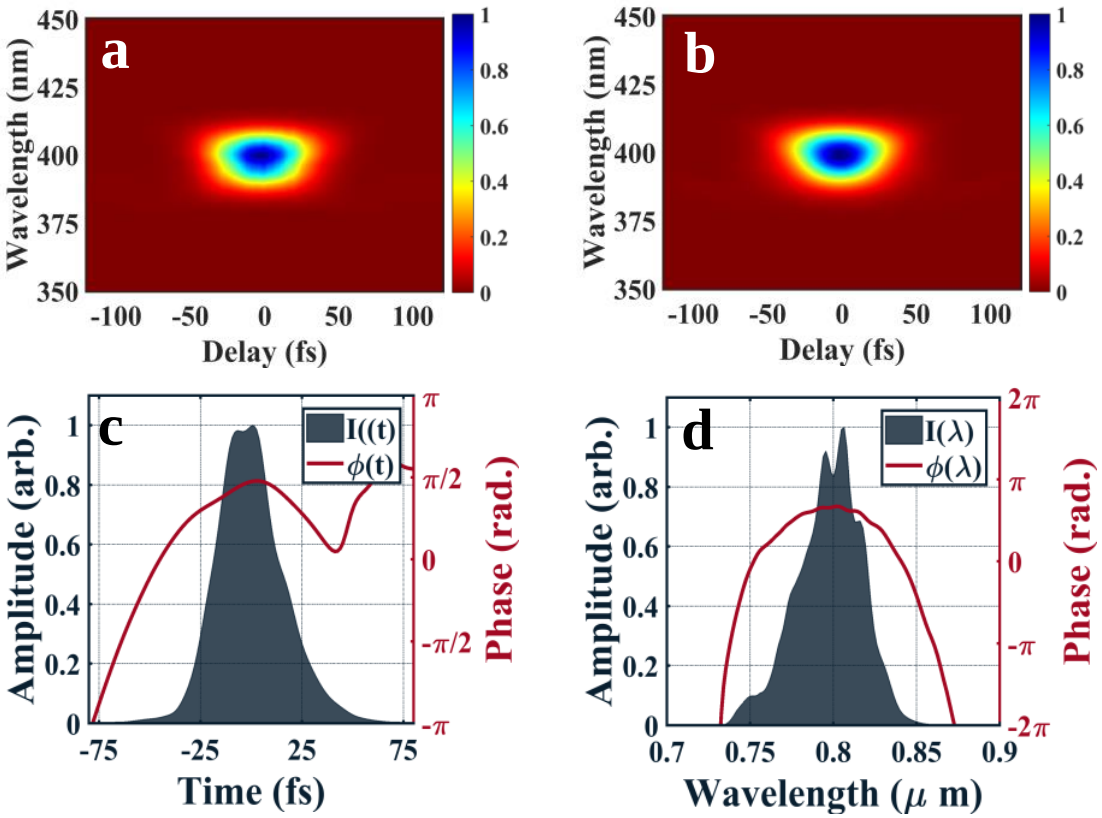

Figure 6.7: Results for the FROG of the gating field.**a** Measured spectrogram. **b** Retrieved Spectrogram. **c** Retrieved pulse in intensity, with phase. **d** Measured and retrieved spectra with the spectral phase.

a 50 mm diameter, 20 cm focal length Ag coated spherical mirror. The beams are placed on opposite sides of the mirror so that they non-co-linearly overlap in a 8x8x0.4mm $AgGaS_2$(I) crystal. This allows the weak sum frequency beam to be spatially separated from the much stronger gating field using an iris. After collecting the signal in a spectrometer, a spectrogram can be collected using a delay stage. Afterwards, software, such as the FROG 3.2.2. from Femtosoft Technologies, can be used to analyze the measurement and determine the electric field characteristics.

Since the XFROG retrieval algorithm is sensitive to errors introduced in more complex pulses, it is best that the gating field is near transform-limited at the position of the nonlinear crystal within the XFROG. Since the grating based compressor of the Ti:Sapph laser is

optimized for the final BBO crystal inside the OPA, we must match the dispersion acquired in this path in the gating field. This is achieved by minimizing the amount of transmissive optics in the gating field's beam line, while the compactness of the setup requires only an additional 1.5 meters of propagation compared to the OPA's final BBO.

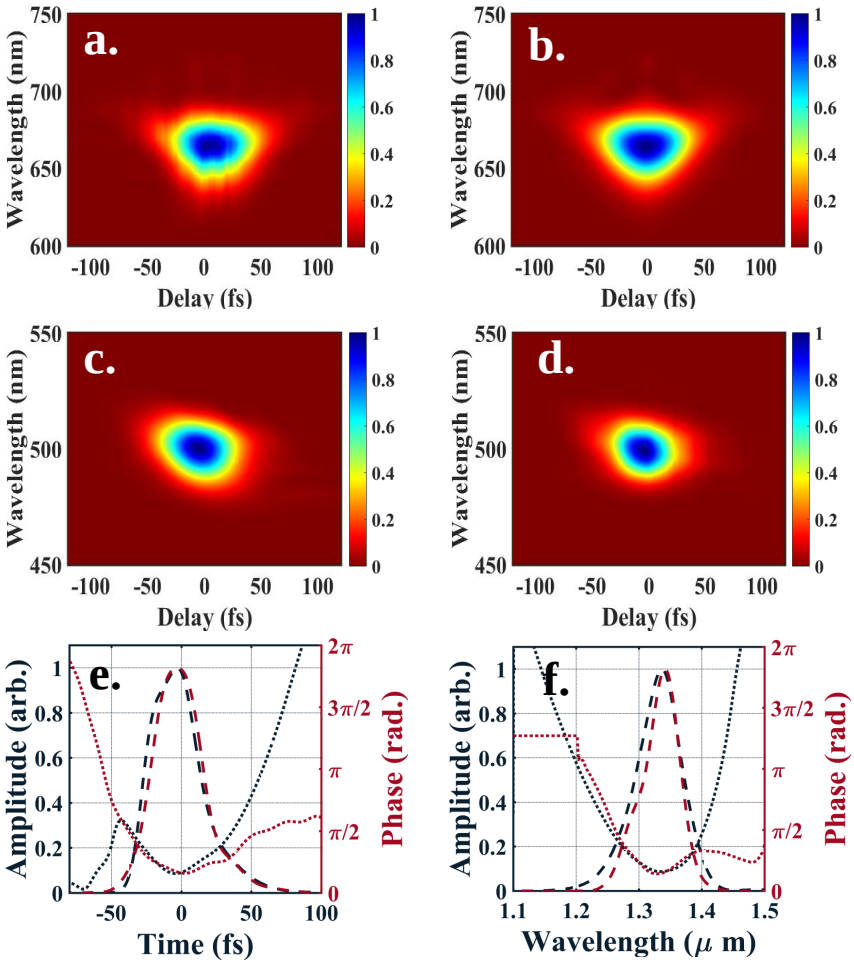

Figure 6.8: Comparing XFROG and FROG on the OPA signal (1340 nm). **a** Measured FROG spectrogram. **b** Retrieved FROG Spectrogram. **c** Measured XFROG spectrogram. **d** Retrieved XFROG spectrogram. **e** Retrieved time domain intensity envelope (dashed lines) and phase (dotted lines). Lines colored black are for the FROG and red lines are for the XFROG. **f** Retrieved spectra in intensity (dashed lines) with phase (dotted lines). Lines colored black are for the FROG and red lines are for the XFROG.

Mirror (M1) is insertable into the gating field beam line so that it can be sent to a FROG for characterizing. The path length from the laser output to the nonlinear crystal is within

1 cm as that of the XFROG's AGS crystal. Paths for both FROG and XFROG also use the same transmissive optics (e.g. neural density filter, iris with same inner diameter and position). An example of the results for the FROG of the gating field are shown in figure 6.7. The measured and retrieved spectrograms show a high level of agreement with a FROG error of only 0.15%. The laser experiences small drifts from day-to-day and, though negligible in terms of pulse duration and characteristics of the OPA/LWIR, FROG's were continuously acquired to ensure that a properly characterized gating field was used for a specific data set.

As an additional confirmation of our XFROG's accuracy, we demonstrate the technique's precision by comparing it to FROG. Referring to figure 6.4, we see that by blocking the OPA idler and removing AGS, ZS, and Ge in the initial path of LWIR generation, we can perform XFROG on the OPA signal, a field that we can easily FROG. The comparison of the FROG versus XFROG on the OPA signal is shown in figure 6.8. The same BBO crystal used in our FROG was also used in place of the AGS crystal shown in the XFROG setup in figure 6.6. Figures 6.8a and 6.8b are the measured and retrieved spectrograms for the OPA signal using FROG, respectively. Figures 6.8c and 6.8d are the measured and retrieved spectrograms using XFROG.

The comparison of the time domain of the field is shown as intensity in figure 6.8e. The dashed lines represent amplitude and the dotted lines represent phase; the lines are colored black for FROG and lines colored red are for XFROG. First, we see that the overall shape of the intensity envelope has the same duration, about 40 femtoseconds for XFROG versus 42 femtoseconds for FROG. The phase in the region of the FWHM of the amplitude is comparable, showing mostly a second order chirp present in both retrievals.

Figures 6.8f shows the retrieved spectral intensity. As before, the dashed lines are amplitude while dotted are phase, and XFROG is shown in red while FROG is in black. The blue solid line is the measured spectra using an InGaAs based spectrometer.

More XFROG results for the LWIR apparatus are shown in figure 6.9. The first column on the left shows the retrieved XFROG spectrograms and the measured XFROG spectrograms are shown in the second column. The next column shows the retrieved spectra in intensity (black) with their phase (red) and the last column shows the time domain electric field

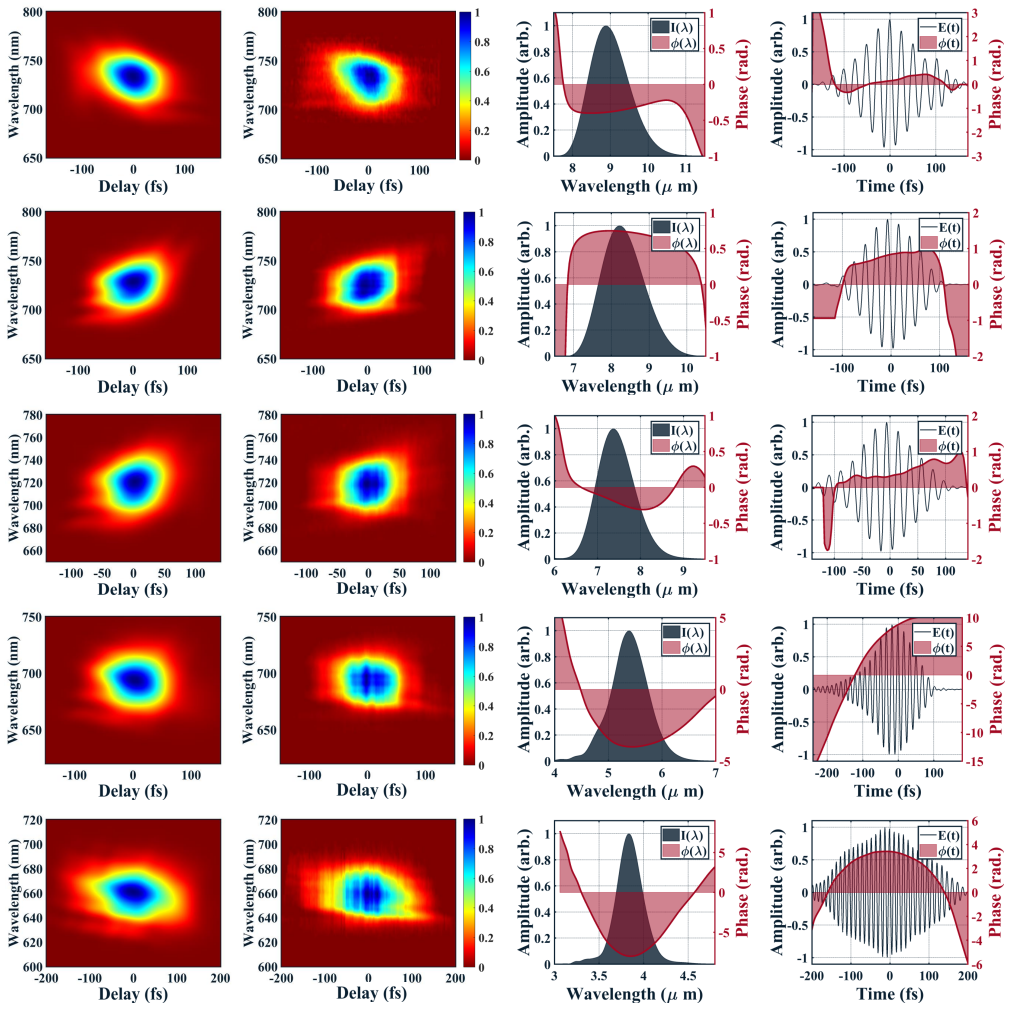

Figure 6.9: XFROG results across the tunable range of the source. Each row represents one individual wavelength. Starting with the first column on the left: (1) retrieved XFROG spectrogram, (2) measured XFROG spectrogram, (3) retrieved spectra in intensity (black) with phase, (red) (4) time domain electric field (black) and phase (red). Starting from the top row: central wavelength (1) 8.9 μm, (2) 8 μm, (3) 7.2 μm, (4) 5.3 μm, (5) 3.8 μm.

(black) and phase (red). Each row is for a different wavelength, starting with 8.8 μm on the top row and down to 3.8 μm on the final row.

6.5 Maximizing the peak intensity of the laser field

To ensure that the source permits the maximum available peak intensity, we require that every measure is taken to optimize the quality of the light source. This includes maximiz-

ing the permissible peak intensity, while maintaining the shortest pulses and a tight focus. Section 6.4 already shows that our setup is capable of transform limited, few-cycle laser fields in the LWIR. In addition to this, we require our DFG to be performed in a collinear arrangement to eliminate angular dispersion of the LWIR, which can quickly increase the focal spot size. This is explained in section 6.5.1. A co-linear geometry then requires the use of long-pass filters to efficiently separate the LWIR from the OPA fields. Because of the high fluence involved in the experiment, special consideration of the material properties of our filters was required, as explain in section 6.5.2.

6.5.1 Design of a tight focusing arrangement

A laser's peak intensity is inversely proportional to the beam area at the focus, so a two-fold increase in w_0 corresponds to a four-fold decrease in the peak intensity. For this reason, maintaining a tight focusing beam is more critical than the pulse energy and duration, which only linearly decrease peak intensity.

There are several resources in the literature to understand how a laser beam focuses [166;167]. For this reason, I will just write down the result for a focused Gaussian beam,

$$w_0 = \frac{2\lambda}{\pi}\frac{f}{D}, \tag{6.2}$$

where w_0 is the $1/e^2$ radius at the focus (i.e. the beam waist), λ is the central wavelength, f is the focal length of the lens, and D is the $1/e^2$ diameter of the beam before the focal element. f/D, also known together as the f number, cannot be less than one, so the minimum permissible beam waist, w_0^{min}, is

$$w_0^{min} = \frac{2\lambda}{\pi}, \tag{6.3}$$

which we can approach under certain conditions. In our case, we are attempting to achieve our focus inside a vacuum chamber possessing an ion time-of-flight (iTOF) (see figure 6.4). The experimental apparatus consists of a pair of electrostatic lenses with a 50 mm diameter,

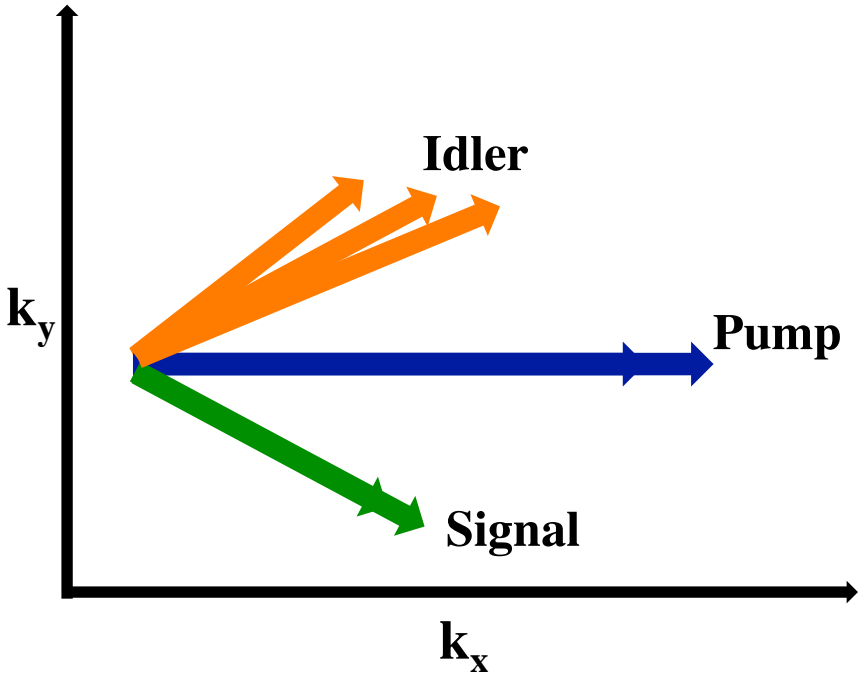

Figure 6.10: Example of angular dispersion for a broadband, non-colinear DFG scheme. The length of the vectors corresponds to the energy of the photon while the direction corresponds to its two dimensional momentum.

approximately 25 mm apart, and at voltages in the ±2 kV range.

We use a back focusing arrangement, where the beam first propagates through the iTOF and then retro-reflects off a spherical concave mirror. This is because a Ag-coated mirror is better suited for our short laser pulses than a lens. Also, this allows us to approach the smallest possible f number and allow for maximum peak intensity. We want to focus in the center of the iTOF, so the closest our back focusing element can approach is 25 mm before it will have an adverse effect on the field generated by the electrostatic lens system. While in principle, we could have a beam of roughly the same diameter, in practice this is difficult because we require sending the beam through a window to enter vacuum. We use a 25 mm diameter, 2mm thick, zinc selenide (ZS) window, which would be difficult to adjust precisely in line with the iTOF if the beam diameter was the same. A 50 mm window would make this much easier, but would require our window to be increased to 8 mm thick, which would stretch our 9 μm laser pulse to approximately 250 fs. Another issue with larger diameter

beams is they require telescoping, which is difficult to align correctly when a camera is not available for correcting astigmatism.

With these considerations on the various constraints of the system, we settled with a 25 mm spherical concave Ag coated mirror as our back focusing element, while leaving our LWIR input diameter, D, at 10 mm, which is the diameter it possesses when it exits the crystal. A quick calculation for these parameters suggest that we could achieve $w_0 = 8.5$ μm for a $\lambda = 5.2$ μm central wavelengths and $w_0 = 14.5$ μm for our $\lambda = 8.9$ μm field. However, this calculation should only be considered a guide for our setup, as we do not have a simple method for characterizing the focus inside the experimental apparatus.

Another important consideration is the level of spatial chirp present in the mode due to angular dispersion. A pictogram for angular dispersion is shown in figure 6.10. When the three wave mixing process is initiated by two fields interacting at an angle, their $\vec{k}$-vectors mismatch so that different frequencies of the generated field have a unique output angle. In our case, the LWIR fields have much lower photon energy than the OPA signal and OPA idler, which means that even a slightly non-co-linear arrangement can have a dramatic influence on the angular dispersion.

This angular dispersion has a negative impact on the focus, as not all frequencies will be sent to the exact same location. This can not only increase w_0, but also temporally stretch the pulse because the bandwidth is not uniformly distributed. For these reasons, we must maintain a collinear geometry with enough precision that no angular dispersion is present in our generated field. This is done by observing the unfocused, LWIR mode with a FLIR One® thermal imagining camera. While we cannot directly image our laser mode with this camera due to its low damage threshold, we can observe the mode on a surface with highly dissipative thermal properties. An example of a well aligned mode is shown in figure 6.11. We can observe angular dispersion by scanning the OPA idler delay stage (see figure 6.4) and observe the transverse distribution of the generated field. A poorly aligned setup will have a mode that shifts vertically or horizontally with a change in delay. These can be corrected for by walking the appropriate axis' on the mounts for the input mirrors. When properly aligned, the generated mode will stay still, only increasing or decreasing in fluence as delay

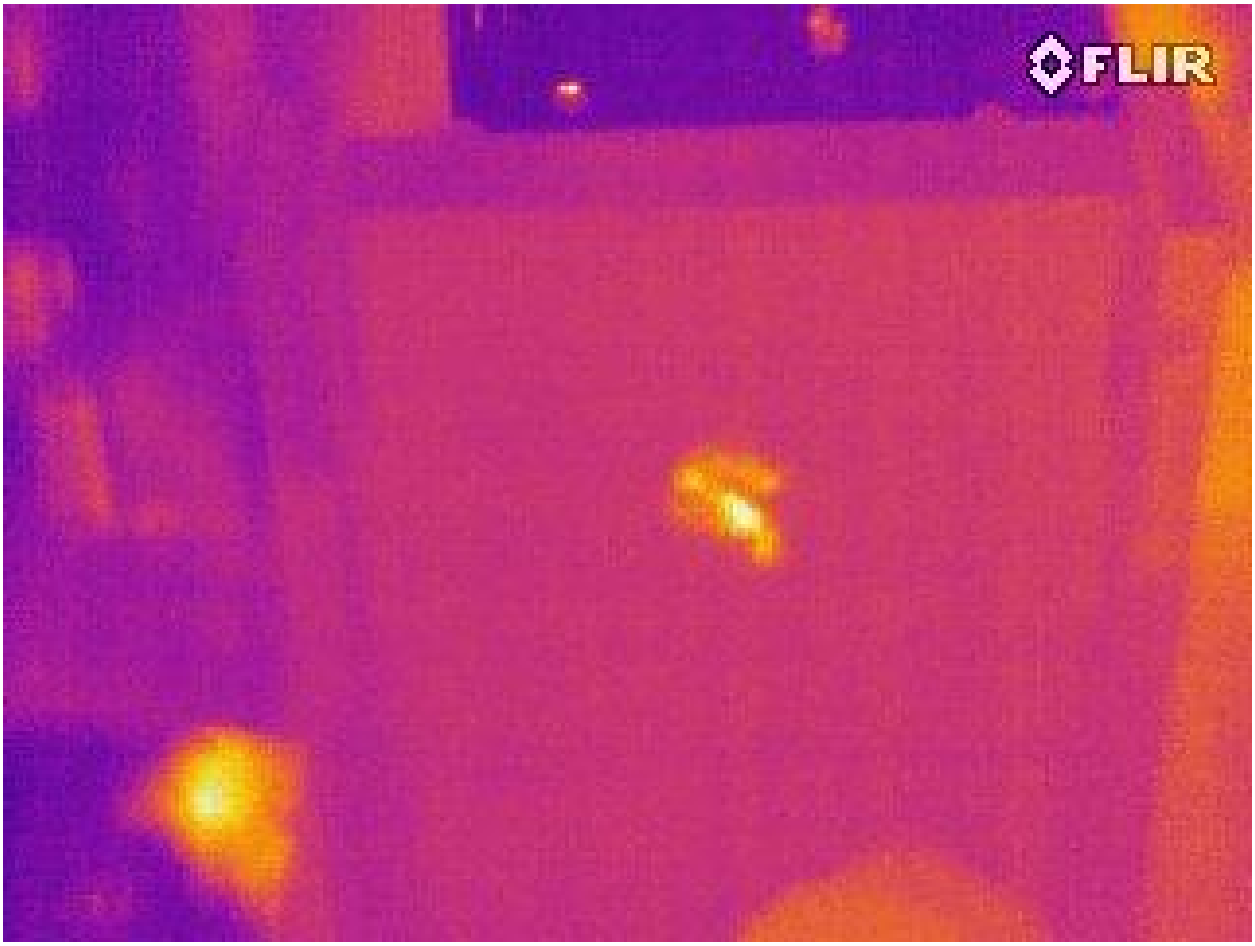

Figure 6.11: Image of our mode in the LWIR using a FLIR One® camera, shown as a bright yellow region in the center of the image. To allow the camera to see only scattering of the light (versus dissipated heat), the mode is incident on a material with a low heat conductivity (pink).

is scanned.

6.5.2 Bypassing free carrier absorption in Germanium

As discussed in section 6.3, it was observed that inserting a zinc selenide (ZS) filter before the germanium (Ge) filter increased the measured pulse energy, while inserting ZS after Ge yields a 3-5 % drop in the measured value. Though XFROG determines that our LWIR is near transform-limited, it was important to consider the presence nonlinear effects such as self-phase modulation or filamentation in Ge, which could be reduced with ZS since it has a

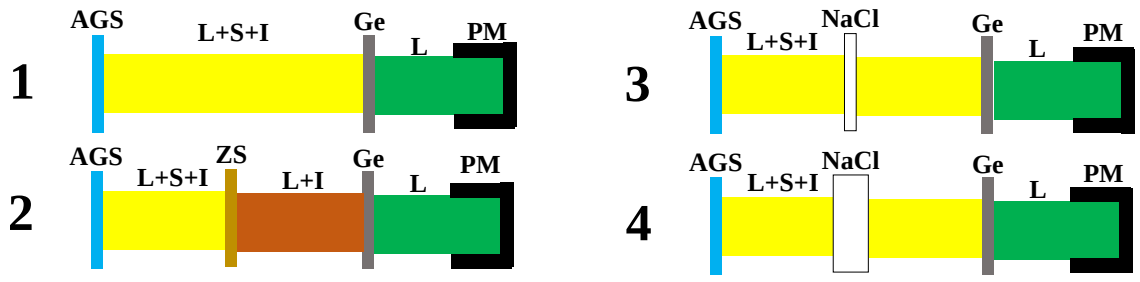

Figure 6.12: Four combinations of filtering were used to determine the physical effects behind the observed enhancement in setup 2. AGS - $AgGaS_2$(I) crystal, ZS- zinc selenide window, Ge- germanium window, NaCl - sodium chloride window, PM - power meter, L- LWIR beam, S- OPA signal, I- OPA idler.

negative group velocity dispersion (- 17 fs^2/mm at 5 μm, -519 fs^2/mm at 8 μm). If this were the case, then another material with similar negative GVD, such as sodium chloride (NaCl) (- 130 fs^2/mm at 5 μm, -630 fs^2/mm at 8 μm) would achieve the same effect.

Figure 6.12 shows the layout for determining the role of chirp in our pulses. We generate LWIR in our $AgGaS_2$ (AGS) crystal and tried four combinations of filtering the beam from the OPA signal and idler, and measured the pulse energy with a thermopile sensor. The first combination is a single, 1 mm thick, Ge window with a 3-12 μm anti-reflective (AR) coating. The second combination includes a 1 mm thick, ZS window, also with a 3-12 μm AR coating, before Ge. The third and fourth combinations replace ZS with a 2 mm and 5 mm thick NaCl window, respectively.

Table 6.2 shows the results for two different LWIR wavelengths. While the second arrangement shows a clear enhancement, both NaCl windows show loss, mostly due to Fresnel losses and possibly some degradation of the window's surface from humidity. Additionally, the enhancement at 5 μm is roughly 20 %, whereas the enhancement at 8 μm is much larger at 220 %.

Since the ZS window blocks over 90 % of the OPA signal, and the NaCl windows pass most of the OPA light, it was suspected that the signal of the OPA causes the absorption of LWIR to occur inside Ge. We further investigated the role of the OPA signal by measuring the effect of fluence using the setup in figure 6.13. A -50 mm uncoated CaF_2 lens expands

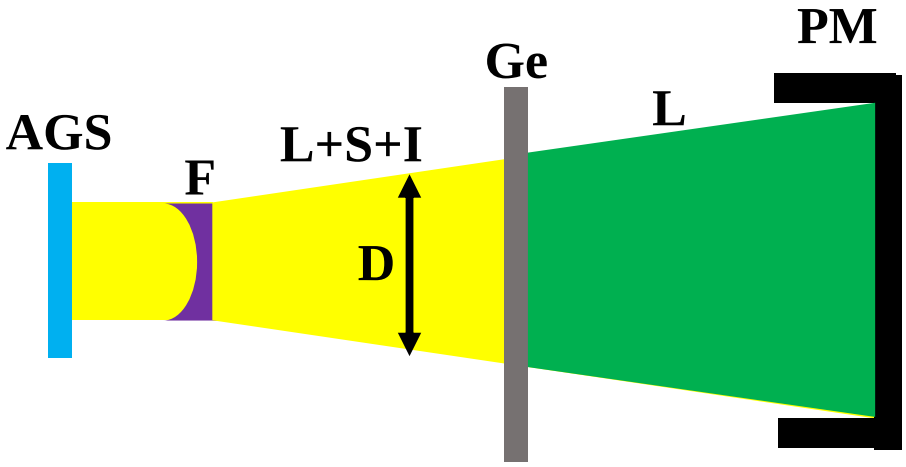

Figure 6.13: Setup for measuring the effect of fluence on the germanium (Ge) window. AGS - $AgGaS_2$ crystal, F- uncoated -50 mm CaF_2 lens, Ge- AR coated 50 mm diameter germanium window, PM- large area thermopile based sensor, L- LWIR, S- OPA signal, I- OPA idler.

the three beams exiting the AGS crystal. This is measured on a large area thermopile sensor. The Ge window can be scanned in the direction of laser propagation to decrease the fluence.

Table 6.3 shows the results for this scan performed at the same wavelengths as table 6.2. Due to the large area of the thermopile, the measured pulse energies are to the nearest 10-20 μJ level and should only be considered an estimate. Nonetheless, the results indicate that a larger area beam diameter on the Ge window surface increases LWIR transmission.

Combined, the results of tables 6.2 and 6.3 indicate that LWIR can be attenuated with a high fluence of the OPA on the Ge window. Ge has a direct band gap of 0.8 eV and an indirect band gap at the L point of 0.66 eV, allowing it to strongly absorb all light from the

Configuration	5 μm energy (μJ)	8 μm energy (μJ)
1	90	37
2	106	80
3	75	28
4	63	30

Table 6.2: Measured pulse energy for the four filtering combinations shown in figure 6.12.

OPA.

Using the band model, an electron in a semiconductor's conduction band can more readily absorb lower energy photons, as there are no forbidden energy regions limiting the electron from being absorbed. When the electron density (also called carrier density) in the conduction band is high enough, absorption from these "free carriers" can be significant. We can estimate the carrier density required to produce the results seen in table 6.2 using the Drude model for free carrier absorption (FCA)[168;169].

The FCA rate, α, in a single band gap (intravalley), can be described by the Drude model as

$$\alpha = \frac{\lambda^2 e^3 N_c}{4\pi^2 c^3 \epsilon_0 n_r m_e^2 \mu_c}, \tag{6.4}$$

where λ is the wavelength of light being absorbed, e is the electron charge, N_c is the carrier density, c is the speed of light, ϵ_0 is the permittivity of free space, n_r is the refractive index, m_e is the electron mass, and μ_c is the carrier mobility. Notice that the carrier rate goes as λ^2 which is consistent with our findings in table 6.2.

It should be noted that Ge possesses a complex band structure, where both intravalley FCA and intervalley FCA can participate in absorption[169]. This, combined with the limitations of the Drude model and the complex spatial profile of the OPA modes would require significant detail to provide a reliable simulation. Our purpose here is to have an estimate on the physical processes behind the filtering technique used in the setup shown in figure 6.4. For this reason, we only focus on the main behavior by considering a simple, one band

Beam diamater (cm)	5 μm energy (μJ)	8 μm energy (μJ)
1	60	30
1.5	70	40
2	90	50
2.5	110	60
3.5	120	70

Table 6.3: Measured pulse energy for two wavelengths as a function of beam diameter on Ge window surface as shown in the setup in figure 6.13.

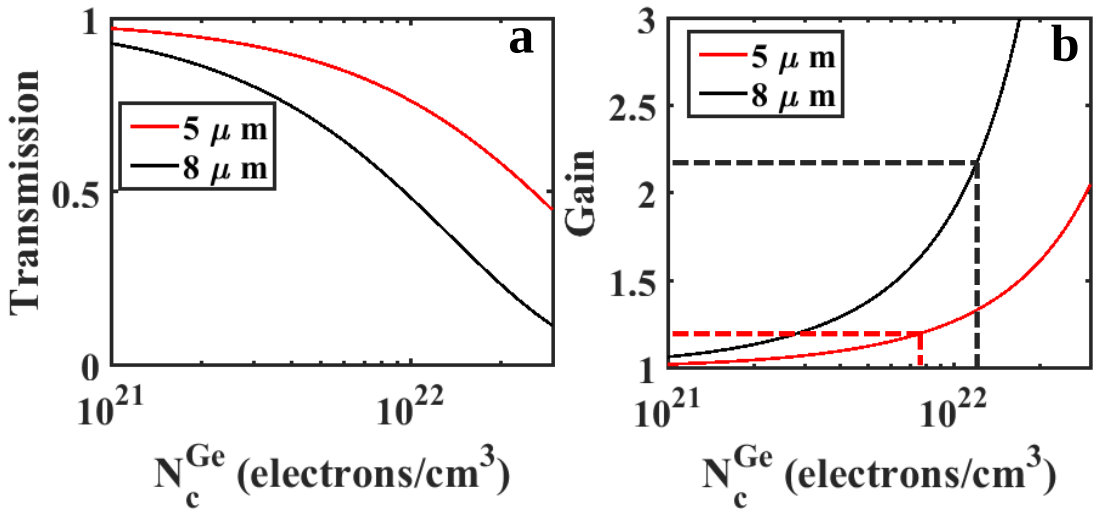

Figure 6.14: Calculations of FCA in germanium. **a** Transmission, T, versus N_c^{Ge} for 5 μm (red) and 8 μm (black). **b** Gain, G, versus N_c^{Ge} for 5 μm (red) and 8 μm (black). The dashed lines indicate the measured value of G on each curve, obtained from the data in table 6.2.

gap model of Ge and an approximation on the distribution of the carrier density, N_c.

If we consider that FCA occurs in the direct band gap (0.8 eV), then the OPA signal is the dominant contributor of free carriers. In that case, adding the ZS window amounts to reducing the carrier density by a factor of 10, and so $N_c^{Ge} = 10N_c^{ZS}$ where N_c^{Ge} is the carrier density in Ge without the ZS window and N_c^{ZS} is the carrier density in Ge when ZS is included. An estimate for the gain, G, made when including the ZS window is then given by

$$G = \frac{T_{ZS}}{T_{Ge}} = \exp[-z(\alpha_{ZS} - \alpha_{Ge})] = \exp[9z\alpha_{ZS}], \tag{6.5}$$

where T_{ZS} and α_{ZS} are, respectively, the transmission and FCA rate with ZS included, T_{Ge} and α_{Ge} are the transmission and FCA rate without ZS, respectively, and z is the depth of propagation. Because the absorption rate of the OPA signal is on the order of ≈ 1 μm^{-1} [170] we can assume that the carriers occur predominately on the window's surface. Assuming $z = 2$ μm, we can find T and G as a function of N_c^{Ge}, as shown in figure 6.14.

Figure 6.14b shows the predicted values of N_c^{Ge} for values of G obtained from data in

table 6.2. The measurements at 8 μm predict $N_c^{Ge} = 1.2 \cdot 10^{22}$ cm^{-3} while the measurements for 5 μm predict $N_c^{Ge} = 8 \cdot 10^{21}$ cm^{-3}, which are less than a factor of two apart and correspond to roughly 20-25 % of the available electrons in the Ge lattice.

6.6 Demonstration of high peak intensities in the LWIR via strong-field ionization

As proof of this source's ability to study strong field science across a large wavelength range, we measure strong field ionization of Xenon (Xe) at three wavelengths in the range of 5.3 μm to 8.9 μm. Figure 6.4 shows the experimental setup. The Fresnel reflection from the Ge window is filtered with another set of Ge windows to record a small ($< \mu$J) amount of LWIR leakage on a pyroelectric detector (PyD). This allows for single shot monitoring of the LWIR by recording the peak of the electronic signal with an analogue to digital converter (ADC). A periscope steers the LWIR into an ion time-of-flight (iTOF) apparatus. The beam is back focused inside the chamber with a spherical concave mirror of -25 mm focal length in order to provide the maximum permissible peak intensity. An electrostatic lens system was designed so that the optical mirror could focus at the center of the electrostatic lenses without distorting their field. The ion yield is detected with a micro-channel plate (MCP) and recorded with time-digital converter (TDC) ion counting electronics. Figure 6.15a shows a time-of-flight measurement for Xe at $\lambda = 8.9$ μm in blue with a fit on the yield in red determined by the known isotopic abundances.

All ionization experiments were performed using an ion time-of-flight (iTOF) mass spectrometer. With a background pressure of $\sim 1 \cdot 10^{-7}$ torr, gas samples were introduced to the vacuum system as an effusive jet with pressures on the order of 10^{-5} torr. A constant extraction potential was maintained for all data in this figure with a 2 kV voltage applied to the repeller and -2.2 kV applied to the electrostatic lens system. Ions generated in the interaction region of the laser are guided to a micro-channel plate (MCP) detector where ion detections are converted into a time-dependent voltage. A time to digital converter

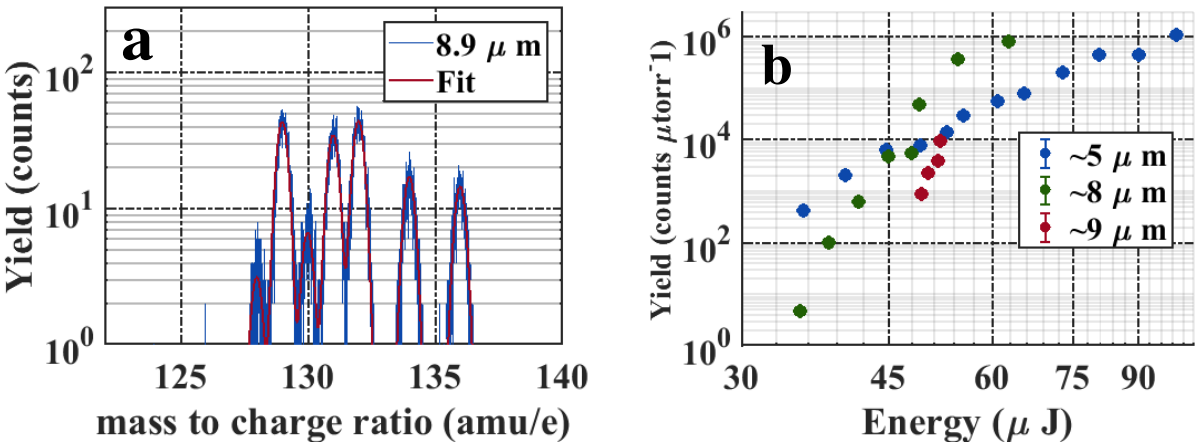

Figure 6.15: **Ionization of noble gases.** **a** Example iTOF spectrum for Xe using the 8.9 μm field from the setup in figure 6.4. The fit is described in main text. **b** Measured yield of Xe^+ versus input pulse energy for $\lambda = 8.9$ μm (red), 8 μm (green), and 5.3 μm (blue).

records individual hits on the MCP and are recorded for each laser shot. Meanwhile, an analogue to digital converter records the energy of each laser pulse, which is saved for each hit in the iTOF. Each intensity point was recorded for a 20 minute span for consistency and satisfactory yields across the scanned range.

Figure 6.15a shows an example iTOF spectrum for Xe. We clearly distinguish seven of the nine Xe isotopes (the other 2 are rare enough that more statistics are required to resolve them). The fit on figure 6.15a is described by the following equation:

$$F(m_q) = A \sum_i^n C_i \exp\left[-\left(\frac{m_q - m_{q_i}}{w_0}\right)^2\right], \tag{6.6}$$

where F is the fitting function, m_q is the charge to mass ratio value, A is an overall amplitude coefficient, C_i is the relative abundance for the i^{th} isotope, m_{q_i} is the m_q value for the i^{th} isotope, and w_0 is the gaussian $1/e$ width. For the case of Xe, there are nine isotopes to be fit. Since C_i and m_{q_i} are known for all species, fitting requires minimizing the error of F with the measured yield, Y, using only A and w_0. The fit is determined minimizing the

error function, E,

$$E(A, w_0) = \sqrt{\sum_i (F(m_{q_i}) - Y(m_{q_i}))^2}, \tag{6.7}$$

where the fit is given by the values of A and w_0 when E is minimized. For figure 6.15a, $A = 1.65$ and $w_0 = 0.285$. We can transform w_0 into w_{FWHM} and find that $w_{FWHM} \approx 0.4$ which is small enough to detect individual isotopes, as shown in figure 6.15a.

As stated earlier, there are nine Xe isotopes, but the fit is only shown for seven in figure 6.15a. This is because ^{124}Xe and ^{126}Xe have coefficients $(A \cdot C_i)$ less than one, due to their low abundance. Tests on the apparatus using the OPA idler give significantly higher yields, where these species show the same behavior as the rest of the isotopes.

Because we are in the counting regime, i.e. where the probability of counting an isotope per laser shot is much less than one, we can determine our error bars on the number of counts received at each intensity position. This amounts to a standard error of $1/\sqrt{n}$, where n is the total number of Xe counts (for all isotopes) at each intensity and wavelength.

Figure 6.15b shows the measured ion yield of Xe^+ as a function of pulse energy in log-log scale for $\lambda = 5.3$, 8, and 8.9 μm. Because we do not have a method for calibrating the intensity, the x-axis is left in terms of the pulse energy coupled into the iTOF apparatus with the relative energy spacing between points determined with the ADC measurements of the PyD. Error bars are determined through the normal convention in the counting regime and are found to be smaller than the marker size in figure 6.15b. The intensity scan is performed by employing a fused-silica based, variable neutral density filter in the arm of the OPA signal in the LWIR interferometer. Between the scan at 5.3 μm and 8 μm we see a large increase in the slope of the yield. Our energy recording was constrained at the 8.9 μm scan because of insufficient leakage onto the PyD, but if more intensity points could be taken we could expect the trend to continue. At this point in time, the cause of this change in slope with wavelength is still under investigation.

In conclusion, we have demonstrated the generation of intense, few-cycle pulses in the LWIR that are tunable from 5.3 μm to 8.9 μm. Our DFG scheme maintains broadband

transform-limited pulses in this wavelength range. We experimentally measured the pulse durations to be 70 - 90 fs, depending on the wavelength, delivering a 5.8 cycle field at 5.3 μm and 2.8 cycles at 8.9 μm. In this wavelength range, the source can be focused on target to peak intensities high enough to induce strong field ionization in Xe. To the best of our knowledge, these are the longest wavelengths that a femtosecond pulse has been used to ionize neutral atomic targets.

Chapter 7

Strong-field photoexcitation in solids

Much of the work in this chapter will be presented in an upcoming publication[171] or was partially demonstrated in a conference proceeding[172].

Interest in the interaction of strong laser fields with solid state materials has increased rapidly since the discovery of high harmonic generation (HHG) in these systems[45]. One of the several exciting prospects for this phenomenon is the promise of an all optical technique for recovering the band structure across the first Brillouin zone[60;61;173–175]. These methods benefit from the significant theoretical work that has been placed in calculating the photoexcitation rate (i.e. promotion of electrons from the valence to conduction band) for cosine-band materials[58;176–180]. Models incorporating the cosine band have included the deformation of the band due to Bloch oscillations[58;177], channel closing due to the Stark effect[180], and ionization dynamics within a laser field cycle[178;180]. Our understanding of photoexcitation with intense fields has progressed significantly in materials that are well represented by the cosine band, which are typically dielectric materials. Because the first step of HHG is photoexcitation, our understanding of HHG in dielectrics has improved significantly due to these advances.

In the case for semiconductors, two-photon absorption (2PA) and three-photon absorption (3PA) measurements have been performed across a large range of laser parameters for

decades, with the goal of extracting absorption coefficients based on empirical fitting[181–184]. At intensities where the field is no longer a perturbation, it has been suggested that semiconductors are well represented by Keldysh's original theory[59;180;185] which utilizes the Kane-band model[17;55]. These claims are based on measurements and calculations for the case of 2PA with either octave spanning spectra[180;185], or with limited intensities[59]. Other work with semiconductors has dealt with materials that can still be represented with the cosine band[174], or have provided alternate theoretical interpretations[60;186;187].

Using all-optical band structure reconstruction techniques for semiconductors could allow for quickly determining their dispersion properties without damaging them, providing better diagnostics for their fabrication. As these materials represent the cornerstone of modern electronics and the future of nano-photonics, the use strong-field interactions, such as photoexcitation and subsequent HHG, could be a promising avenue for fast material characterization. If HHG-based techniques are to be used for these materials, it must be ensured that our understanding of how the laser field interacts with the material is correct. Since HHG is considered a multi-step process, measuring the first step, the photoexcitation rate, by itself can offer us insight into the effectiveness of the Keldysh formulation.

7.1 Strong-field photoexcitation in Gallium Arsenide

In this chapter, we measure the dependence of the photoexcitation rate on intensity and m^* (discussed in sections 2.2.1 and 2.2.2) at four wavelengths spanning the near-infrared window (1180 nm- 2400 nm) for Gallium Arsenide (GaAs). These conditions cover 2PA and 3PA and cover both the multi-photon and tunneling regimes with an adiabatic parametric of $\gamma = 0.3 - 3$. Because the photoionzation rate is linked to the number of photons absorbed in the sample, we can extract this information by measuring the absorbance[44;59]. We utilize a normalization scheme for comparing the response of all intensities and wavelengths to the change in m^*. The experimental results show that, for 2PA, the response of the laser field to varying m^* follows that of Keldysh's Kane-band model, as has been suggested by previous studies[180;185]. However, the results for 3PA do not follow this pattern. We suspect that

this arises from a physical response similar to that of strong laser fields with a cosine-band material. The results suggests that photoexcitation rates in semiconductors deviate from the Keldysh's Kane-band model for longer wavelengths because the electron is driven to higher momenta in the conduction band, which is not well represented by the Kane-band description.

7.2 Setup

The experimental setup is shown in figure 7.1. An 800 nm, 20 mJ, 28 fs Ti:Sapph laser with a 1 kHz repetition rate pumps an optical parametric amplifier (OPA) with up to 18 mJ of pulse energy[84]. The OPA has a tunable range from 1180 nm - 2400 nm using either the signal (1180 nm- 1600 nm) or the idler (1600 nm - 2400 nm). We choose either the signal or the idler by spatially separating them approximately 5 meters from the OPA output with an iris. The beam then enters an intensity attenuator consisting of an achromatic half-wave plate (HWP) and a pair of Germanium windows at Brewster's angle. Afterwards, a beam splitter produces two arms. One arm, the reference, monitors both the single-shot and average power. Single-shot measurements are made with a photodiode mounted in an integration sphere and recorded with an oscilloscope. The average power is measured on a thermopile based sensor. Since the experiment for one wavelength usually runs for 18 hours, the reference allows for constant laser stability monitoring over the course of the data acquisition.

The signal is generated in the remaining arm by focusing the laser onto the GaAs sample. The GaAs sample (MTI Corporation) used in the experiment is grown via the vertical gradient freeze method, intrinsic, c-cut (i.e. [001] is normal to the surface), and 500 μm thick. The focusing element provides a 40-90 μm $1/e^2$ radius at the beam waist, depending on its focal length and set wavelength. The Rayleigh range was kept at least an order of magnitude large than the 0.5 μm thick GaAs sample. Another achromatic HWP rotates the polarization of the light incident on the sample surface.

The transmission through the sample was detected with a photodiode and measured

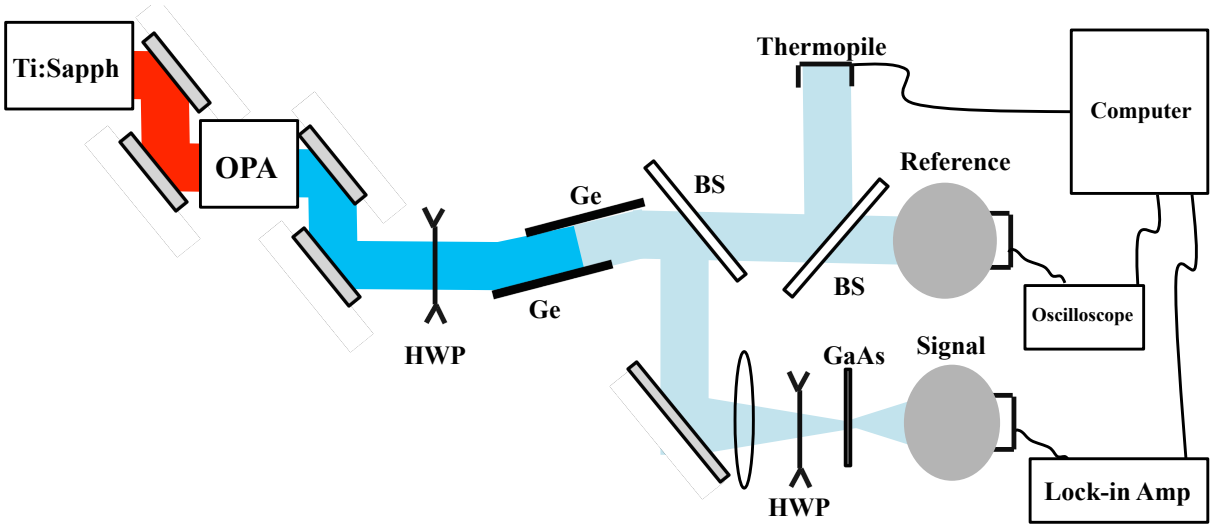

Figure 7.1: Experimental Setup for measuring the strong field excitation in Gallium Arsenide. OPA - optical parametric amplifier, HWP- half-wave plate, Ge- Germanium window, BS- beam splitter, GaAs- Gallium Arsenide.

with a lock-in amplifier. Measuring the absolute transmission requires knowing both the amount of light passing through the sample as well as the amount incident on the sample surface. To measure the latter, the sample is mounted on an automatic stage so that it can be periodically removed from the laser path. This provides us a fully calibrated measurement which, along with monitoring of the reference arm, allows for a precise measurement of the transmission at each data point.

Each wavelength (1180 nm, 1580 nm, 2000 nm, 2400 nm) dataset spans an intensities range of 0.1-1 TW/cm^2 or greater. For each intensity, we sample a full 2π rotation of the laser polarization in 2 degree steps, for a total of 180 points. After the experiment has accumulated multiple averages, we observe a transmission signal, $T(\theta)$, that repeats every $\pi/2$ of rotation, corresponding to the rotational symmetry for GaAs as shown in previous studies[59]. Noise in the signal largely shows up as high frequencies which are easily removed with a nearest neighbor averaging. This is only performed between the two nearest neighbors of a given point to eliminate errors due to smoothing ratios.

Small misalignments of the crystalline axis with respect to the laser's propagation axis

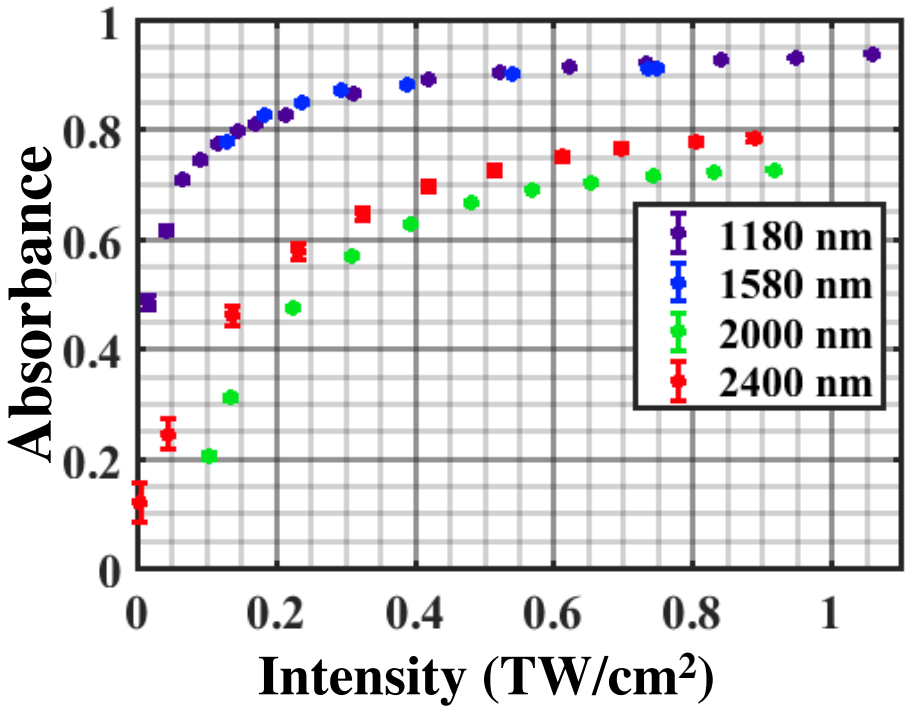

Figure 7.2: Absorbance along the [100] axis for all wavelengths and intensities.

can induce an additional π modulation, corresponding to a change in the Fresnel reflection. Similarly, the HWP just before the sample is checked to ensure that the surface is normal to the laser axis by observing the back reflection. Acquiring a 2π scan allows us to determine that the data corresponds to a properly aligned sample by comparing the error bars on points between the different quadrants of the crystalline axis. After determining that the experiment is properly aligned for a given data set, we exploit the four-fold symmetry of GaAs by averaging over all quadrants.

Finally, it is important that our intensity is measured carefully. Since the experiment is done in atmosphere, we are permitted to carefully measure the spot size, pulse duration, and pulse energy at the site of the sample. Our spot size is measured with a 40 μm wide scanning slit in 5 μm step sizes at several z positions within the Rayleigh range. The light passing through the slit is detected with the same photodiode and lock-in detection as the experiment. A software extracts the beam profile based on a minimization of a convolution of the measured data with a Gaussian profile. The pulse duration is measured with a second

harmonic generation frequency resolved optical gating (SHG-FROG) measurement while the pulse energy is measured with a thermopile sensor.

7.3 Scaling with intensity

We consider the absorbance, A, as a function of intensity for each wavelength when the laser is polarized along the [100] ($\Gamma \leftrightarrow X$) axis. This is shown in figure 7.2. Given that GaAs has a band gap of 1.3 eV, we find that the wavelength sets of 1180 nm (1.05 eV) and 1580 nm (0.78 eV) correspond to 2PA while 2000 nm (0.62 eV) and 2400 nm (0.52 eV) require 3PA

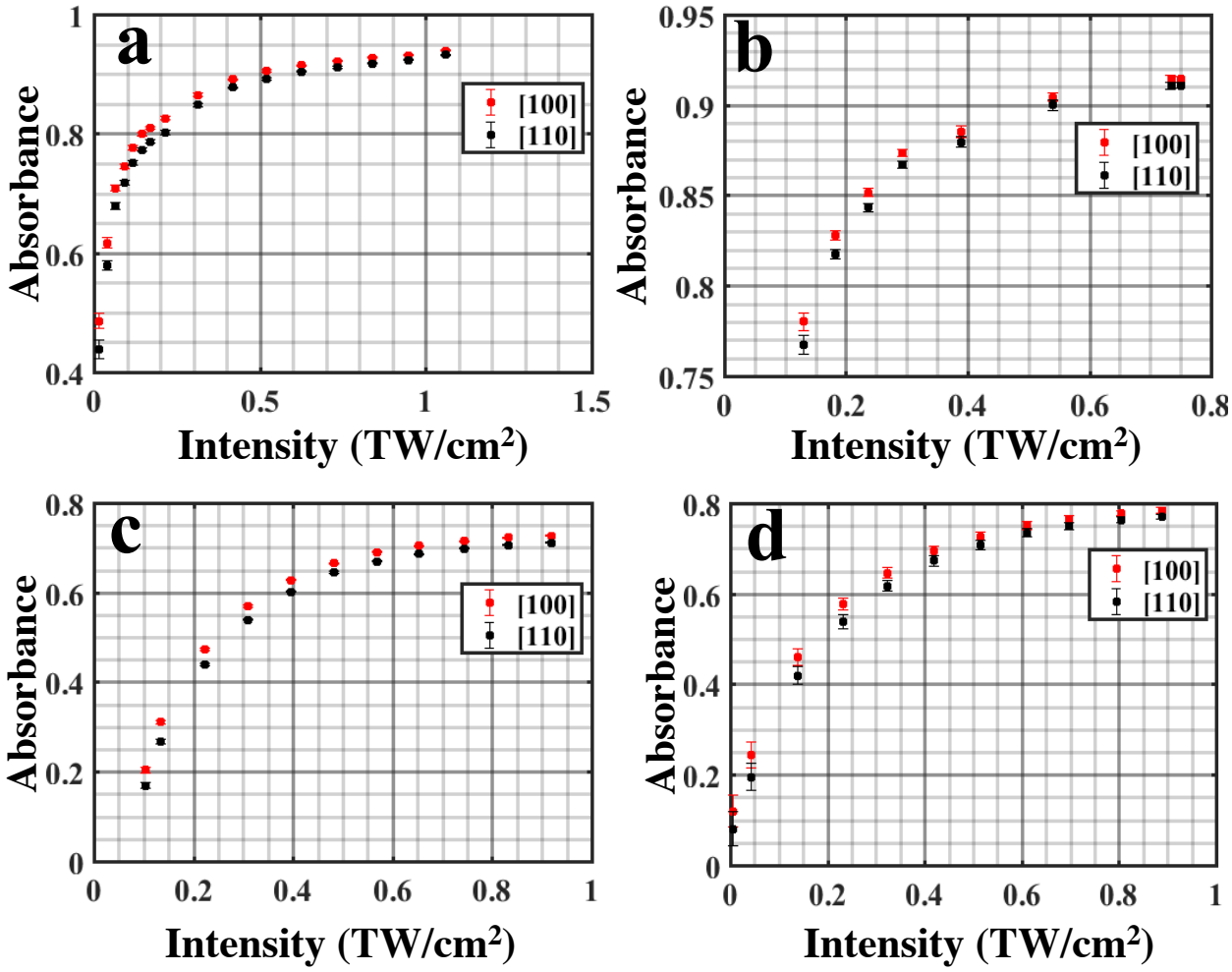

Figure 7.3: Absorbance along the [100] and [110] axes for all wavelengths and intensities. **a** 1180 nm. **b** 1580 nm. **c** 2000 nm. **d** 2400 nm.

to reach the GaAs conduction band. Thus, we expect that the lower two wavelengths and the longer two wavelengths to posses similar absorbance characteristics with intensity. This is clearly demonstrated in figure 7.2.

We can also observe the role of m^* by observing how A changes when the polarization is rotated from the [100] direction to [110] ($\Gamma \leftrightarrow K$). By doing this, we decrease m^* from $0.091m_e$ to $0.068m_e$, where m_e is the rest mass of the electron. This is shown in figure 7.3. Each subfigure in 7.3 shows A along the [100] (red) and [110] (black) axes for 1180 nm (7.3a), 1580 nm (7.3b), 2000 nm (7.3c), and 2400 nm (7.3d). From here, we can see a clear change in A as a result of the change in m^*.

We can also directly observe this change in contrast, $C = A([100]) - A([110])$, by plotting C for all wavelengths and intensities, as shows in figure 7.4. Instead of using the physical data point at [100] and [110], we utilize a fit to include all sampled points, $F(\theta)$, where

$$F(\theta) = C\cos(4\theta) + \delta, \tag{7.1}$$

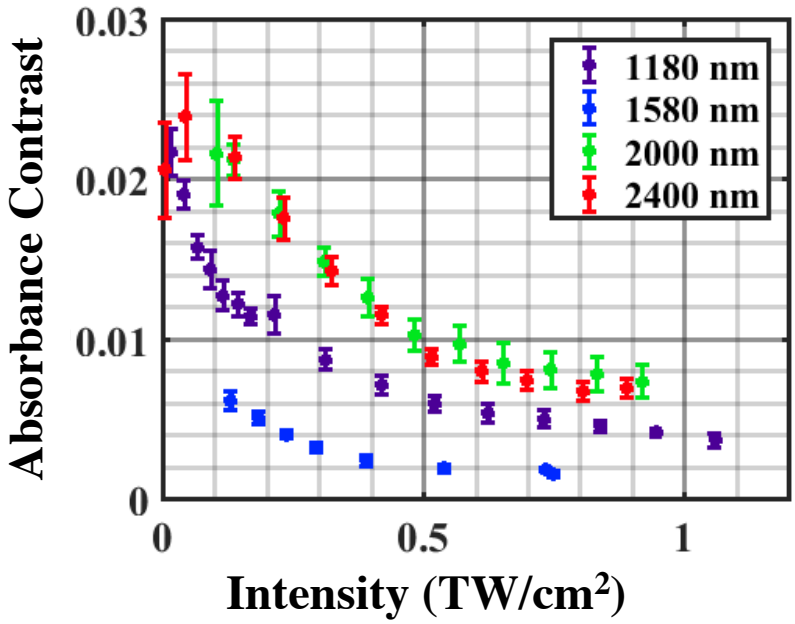

Figure 7.4: Absorbance contrast, $C = A([100]) - A([110])$, for all wavelengths and intensities.

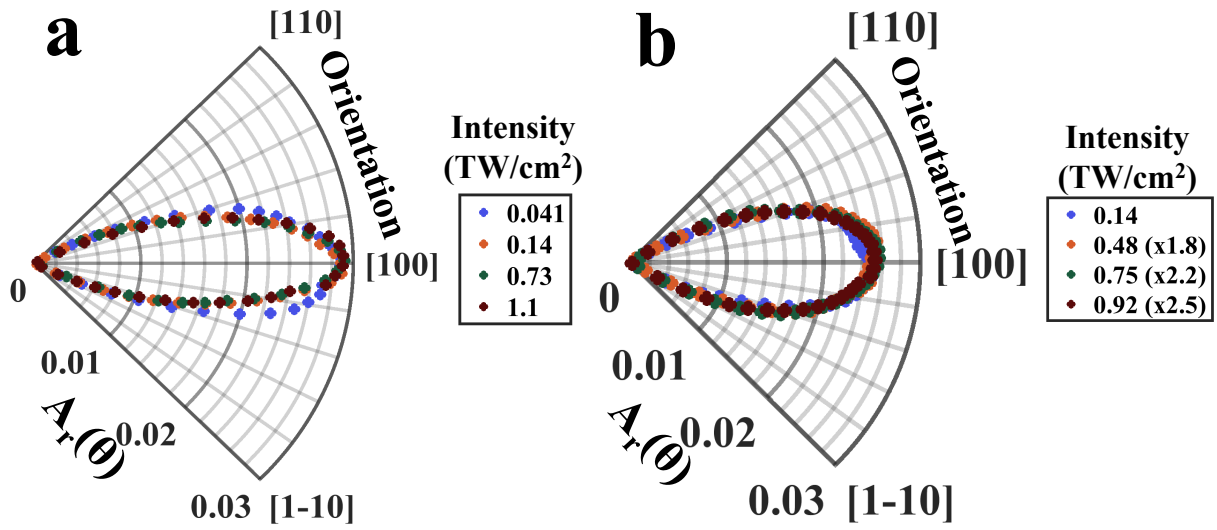

Figure 7.5: Reduced absorbance, $A_r(\theta) = A(\theta) - \delta + C/2$ for 1180 nm (**a**) and 2000 nm (**b**).

with θ as the angle of polarization and δ is the amplitude offset (i.e. the average of A for all θ). Later, it will be shown that there exists deviations from a sine wave that vary with intensity and wavelength, but for the simple task of finding C, the sine wave is appropriate. The error bars are the error of the fit for all data points. From figure 7.4 we see that C always decreases with increasing intensity, regardless of the wavelength. Higher absorbances experience a lower contrast due to A approaching its asymptotic limit of 1. For this reason, C is not a relevant quantity for understanding the role of m^* on excitation rates. Instead, we examine the reduced absorbance, $A_r(\theta) = A(\theta) - \delta + C/2$, which lowers $A([110]) = 0$. This is shown in figure 7.5. By doing this, we can compare the change in A with m^* as we vary both the intensity and wavelength.

Figure 7.5 shows $A_r(\theta)$ for several intensities at 1180 nm (7.5a) and 2000 nm (7.5b). Because C changes with intensity, we multiply $A_r(\theta)$ by a scaling factor to compare various scans. We see from figures 7.5a and 7.5b that there is only minimal change between the measurements; this is true for the other wavelengths measured. However, by comparing the scans between 7.5a and 7.5b, we see that $A_r(\theta)$ for the longer wavelengths shows a much broader feature, while $A_r(\theta)$ is narrower. We will further examine this in the next section.

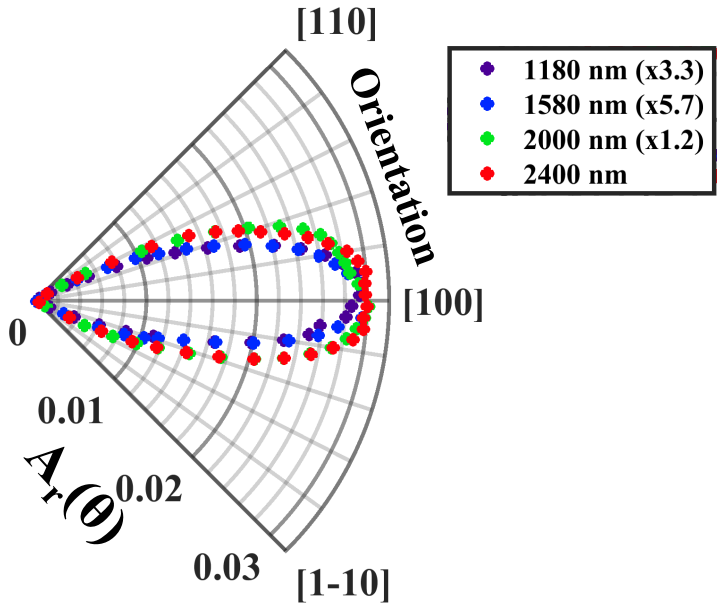

Figure 7.6: $A_r(\theta)$ for all wavelengths with γ fixed. For 1180 nm (violet) and 2000 nm (green) $\gamma \sim 1.15$ along the [100] axis and $\gamma \sim 1$ along the [110] axis. For 1580 nm (blue) and 2400 nm (red), $\gamma \sim 1.2$ along the [100] axis and $\gamma \sim 1.05$ along the [110] axis.

7.4 Scaling with wavelength

Figure 7.6 shows $A_r(\theta)$ for all wavelengths where we keep γ fixed. For 1180 nm (violet) and 2000 nm (green) $\gamma \sim 1.15$ along the [100] axis and $\gamma \sim 1$ along the [110] axis. Whereas, for 1580 nm (blue) and 2400 nm (red) in figure 7.6, $\gamma \sim 1.2$ along the [100] axis and $\gamma \sim 1.05$ along the [110] axis. The reason γ is not identical for all wavelengths along a given axis is due to the minimal number of intensity points acquired.

From the comparison shown in figure 7.6, we see that the response of $A_r(\theta)$ is largely influenced by the wavelength, with 3PA transitions maintaining a broader feature for $A_r(\theta)$ than that of 2PA. We also notice that scans of the same photon order are similar with one another in terms of their structure. Finally, while we hold γ close to fixed for this figure for the sake of comparing it with Keldysh photoexcitation theory, we see from the results in figure 7.5 that, regardless of the intensity, these effects are primarily dependent on the wavelength.

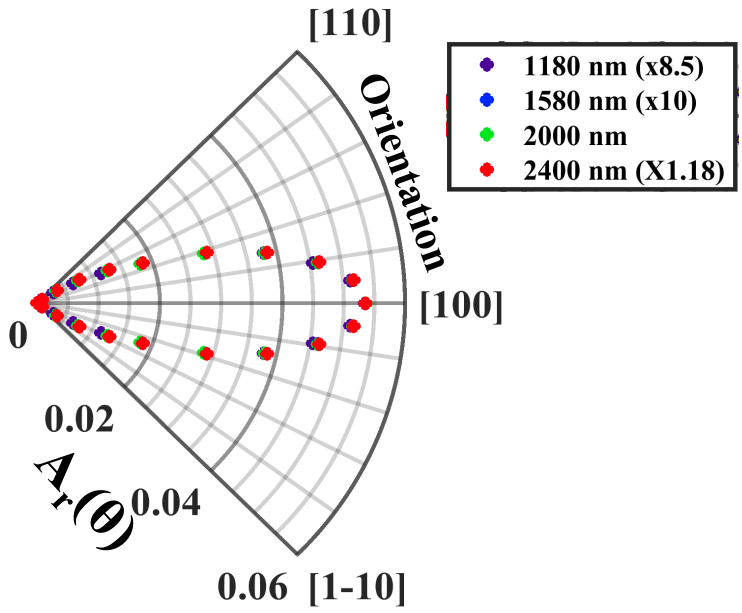

Figure 7.7: Simulation of $A_r(\theta)$ using a Kane-band simulation for the wavelengths and intensities examined in figure 7.6.

7.5 Comparison to Kane-band Theory

From the data presented in sections 7.3 and 7.4, we have an indication that strong-field photoexcitation in semiconductors has a wavelength dependence differing from what the Kane-band theory would predict. To demonstrate this, figures 7.7 and 7.8 show a full simulation on the results of figures 7.5 and 7.6 using the Kane-band model[17]. Details on the simulations are explained in a previous study[59] and the code is shown in appendix B. As expected, the Kane-band's dependence on γ causes virtually no influence on the shape $A_r(\theta)$, as demonstrated in figure 7.7. If we compare the 2PA scans in figure 7.6 to the results of 7.7, there is a strong correlation. However, the 3PA scans show a clear broadening that is not present in figure 7.7.

We can also cross examine $A_r(\theta)$ with intensity, shown in figure 7.5 with the Kane-band simulation, shown in figure 7.8. Here we see that, when scans are scaled so that $A_r(\theta)$ overlaps, Kane-band theory suggests that the shape of the feature is constant. In other words, the Kane-model expects that $A_r(\theta)$ is a constant quantity regardless of the wavelength or

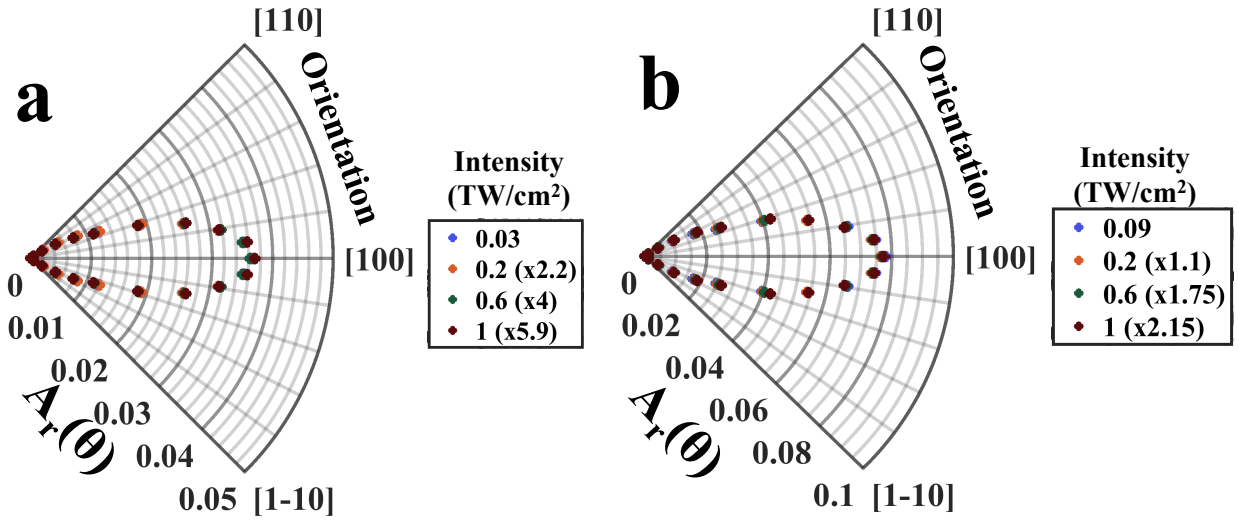

Figure 7.8: Simulation of $A_r(\theta)$ using a Kane-band simulation for the wavelengths and intensities examined in figure 7.5. **a** 1180 nm. **b** 2000 nm.

intensity used in the measurement.

This is in contradiction to the measurements in figures 7.5 and 7.6. However, our examination has shown us that for 2PA, the Kane-band largely agrees with the experiment and that the main deviations only show in 3PA where $A_r(\theta)$ develops a broader feature than was expected. One possible explanation for this discrepancy is the contribution of the conduction band's dispersion relation for larger momenta. While a parabolic dependence is acceptable for small momenta in semiconductors, such as GaAs, the conduction band energy has a complicated dependence with larger momentum. Longer wavelengths will drive the electron to higher momenta in the conduction band for the same intensity range. Thus, we can expect that, as the wavelength of the driving field increases[1], the electron will see a larger portion of the conduction band and hence, be more effected by regions of the band that deviate further from the Kane-band representation.

For instance, in figure 3 of Golin, et al.[59], we see for small momenta that the electron's dispersion is largely parabolic and well described by the conduction band's effective mass. However, for larger momenta, the dispersion relation oscillates before reaching the Brillouin edge. As these oscillations in the band energy change dramatically from $\Gamma \leftrightarrow X$ to $\Gamma \leftrightarrow W$,

[1]Equivalently, as the photon order required for the electron to be excited to the conduction band increases.

their influence on the photoexcitation rate becomes more prominent when the momentum is large (i.e. for large F and small ω). Moreover, the complicated dependence of the band structure on orientation can account for the fact that intense fields at longer wavelengths experience a deviation in $A_r(\theta)$ from the Kane-band theory. For these reasons, we suspect that intense, longer wavelengths fields require the inclusion of a larger portion of the conduction band into the calculation of photoexcitation rate.

For large band gap materials (e.g. alkali halide crystals) the cosine band model for excitation has been demonstrated as a suitable representation of the band structure to the Brillouin edge[45;58;178]. Theoretical results suggest that when the full Brillouin zone is incorporated in such models, excitation rates at high intensities are better represented because they include the full modification of the electron's dispersion relations in the conduction band. As explained in sections 2.2.2 and 2.3, intense fields can accelerate electrons across the Brillouin zone and induce Bloch oscillations[58;177], which are more prominent with increasing F and decreasing ω. Thus, we expect that as the wavelength increases, Bloch oscillations become more important, despite holding γ fixed. Theoretical results explain how Bloch oscillations modify the band structure and tend to increase the density of states for the medium[58;177]. Consequently, the rate is no longer related to γ.

While the cosine band delivers an acceptable representation of the entire Brillouin zone for dielectric materials, no analogue has been formed for semiconductors. This is partly because a generalized description of these bands is difficult; and the calculations required for such a band are not trivial to produce. However, it is possible that by including this description, the effects on $A_r(\theta)$ shown in this chapter could be reproduced, as the modified dispersion relations could be described accurately. Including these dependencies into photoexictation rates would also allow for better simulations of the dynamics of electrons in the conduction band and accurate prediction of effects such as HHG in these materials.

Chapter 8

The next generation of short mid infrared laser fields

Much of the work in this chapter will be presented in an upcoming publication[188].

Up to this point, I have shown a variety of projects undertaken during my graduate studies at Kansas State University. The projects can be broadly classified as 1) interaction of solid state materials with strong laser fields, and 2) development of novel laser sources for applications in strong-field science. Everything that has been presented up until this chapter was determined by my co-advisors to be satisfactory in fulfilling the requirements of a doctorate of philosophy. At this point, the thesis could conclude.

Instead, I want to include a brief chapter describing a project I have been working on in my free time. The results of the last few chapters have spawned ideas for the next generation of projects. In the future, I plan to continue working in developing long wavelength, few-cycle laser fields for applications in HHG and physics requiring highly energetic electrons.

First, I will briefly discuss optical parametric chirped-pulse amplification, which has become the standard technique for producing this kind of light. Then I will go into the principle of Fourier domain optical parametric amplification (FOPA) and discuss some of

the advantages of this method. Later, I will show my work in performing simulations on FOPA using a the mlSNLO nonlinear optics package.

8.1 Overview of optical parametric chirped-pulse amplification

Soon after the demonstration of chirped pulse amplification in lasers, it was realized that nonlinear amplification could benefit from the same principle[190], since the main limitation of transform limited OPA's is damage threshold due to peak intensity. With optical parametric chirped-pulse amplification (OPCPA), one can keep the peak intensity the same as an OPA and deliver orders of magnitude more pulse energy simply because it is delivered in a much longer pulse[191;192]. This allows the seed to acquire much more energy in an OPCPA as compared to OPA. Afterwards, compressing the pulse allows us to retrieved nearly the same pulse duration as an OPA, as long as the input and output bandwidth are comparable.

The OPCPA technique is shown in figure 8.1, a seed with a pulse duration anywhere between a few femtoseconds to several tens of femtoseconds is temporally stretched using either a grating based stretcher or chirped mirrors. The amount the seed is stretched depends on the pulse duration of the pump beam, which is usually in the picosecond to tens of picoseconds regime. The stretched seed is then spatio-temporally overlapped in a nonlinear crystal which optimizes their nonlinear interaction. Afterwards, the seed is brought back to

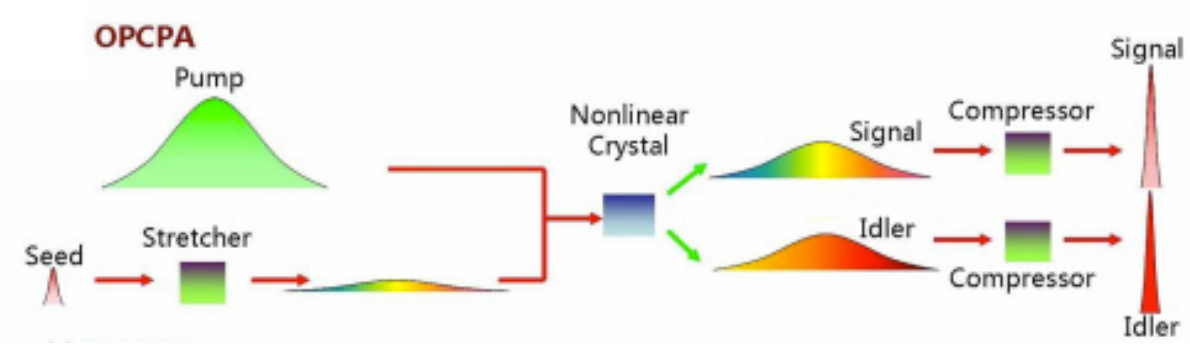

Figure 8.1: General construction of an OPCPA. (Adapted from[189]).

transform limited duration using a compressor, but now with a much higher pulse energy.

OPCPA has allowed for high peak power pulses[193], short, high repetition rate pulses[194], and the extension of intense fields to much longer wavelengths[141]. At this point in time, OPCPA has promised to be a "go-to" tool for extending strong-field light sources to longer wavelengths. However, as we will see in the next section, a new technology has been proposed which could replace OPCPA for several applications.

8.2 Introduction to Fourier domain OPA (FOPA)

While OPCPA is an established technique, it has some limitations. For one, the use of chirped pulses for amplification means that different frequencies of the seed pulse receive a different pump amplitude. Combined with the use of a single nonlinear crystal, gain narrowing is a prevalent issue in OPCPA that can limit its overall performance.

Recently, a new approach to amplifying few-cycle fields was demonstrated, called Fourier domain optical parametric amplification (FOPA)[195]. The layout of FOPA is shown in figure 8.2. The technique starts by spectrally dispersing the seed with a grating (G1). After propagating for a specified distance from G1, a curved mirror (M1) collimates the dispersing

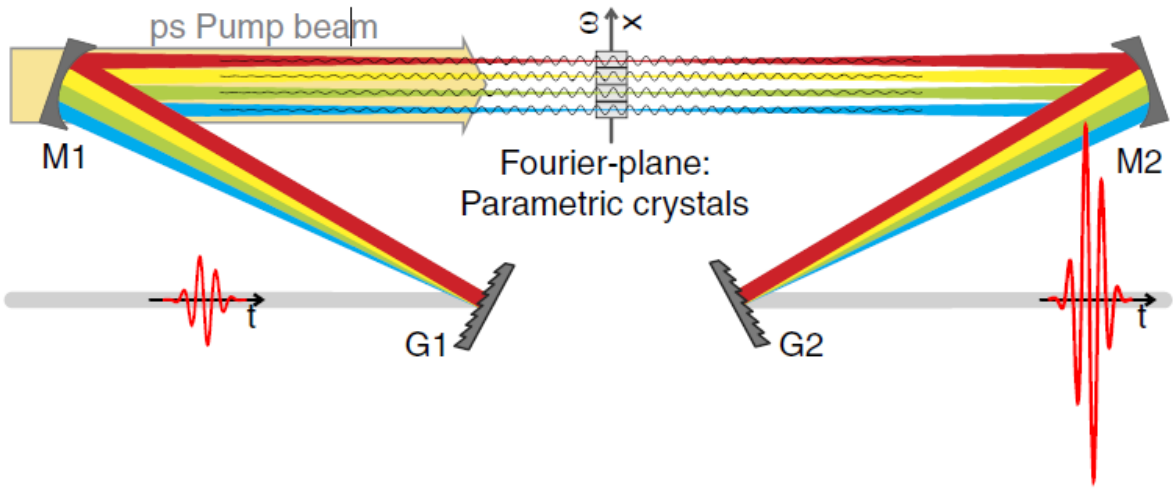

Figure 8.2: General construction of a FOPA. (Adapted from[195]).

seed. After a distance f from M1, with f being M1's focal length, the seed is now in what is called the Fourier plane (FP). At this point, each frequency is highly confined in the horizontal plane, as demonstrated by the blue, green, yellow, and red "beamlets" shown in figure 8.2. This implies that the bandwidth at any position in the horizontal plane is much lower than that of the seed as a whole. Thus, even though the field is transform limited, the pulse duration increases. This is demonstrated in figure 8.3, where the OPCPA amplifies a highly chirped field compared to FOPA. In section 8.3.1, I will derive an approximate calculation of the pulse duration in the FP that explains how it can be controlled in a FOPA.

Next, nonlinear crystals are placed in the FP. A pump pulse with a commensurate pulse duration is delivered into the FP such that it has a constant fluence across the entire FP. This can be achieved using a Powell lens[195;196]. The FP can be made wide enough to introduce multiple nonlinear crystals. After amplification, the the spectral dispersion is removed by focusing the beamlets back with another curved mirror (M2) and collimating them with a grating (G2).

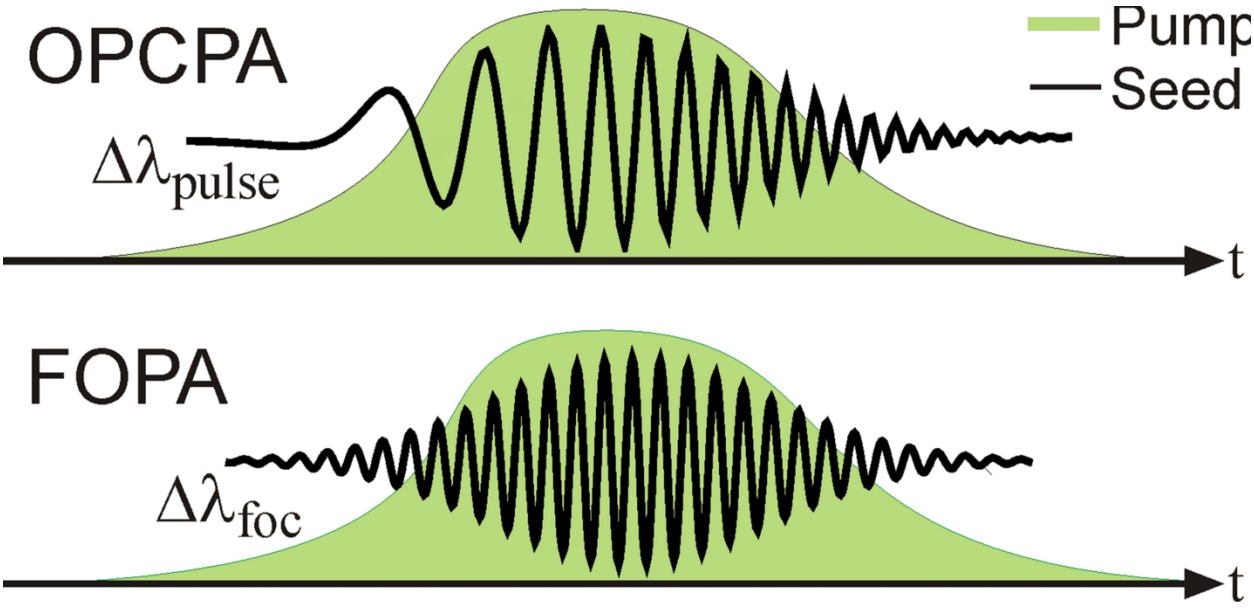

Figure 8.3: Comparison of the pulse at the amplification site for OPCPA and FOPA. (Adapted from[196]).

Performing amplification in the FP has two immediate advantages over OPCPA. Because the temporal stretching happens by separating the frequencies in space instead of time, we can deliver adequate pump energy to all spectral components. We also are not limited to the phase matching limitations of a single crystal. When multiple crystals are introduced into the FP, each can be set up to minimize phase mismatch for a smaller bandwidth channel. This gives FOPA the ability to simultaneously eliminate gain narrowing effects while also increasing the potential of overall amplification. Additionally, because we have more crystals, a larger surface area for amplification is available. This can allow for much larger pump energies in the FP compared to an OPCPA.

8.3 Computationally designing a FOPA

FOPA has the potential to scale amplification to higher energies than OPCPA, due to its allowance of multiple crystals in a parallel configuration, while also preventing gain narrowing since each crystal can be tailored to an individual frequency channel. On a more practical note, the entire setup requires less optical components on the table than OPCPA, allowing for a stabler, more compact system.

These benefits come at an expense; constructing a FOPA is difficult. For instance, the pulse duration in the Fourier plane (FP) depends upon the choice of mirror, grating, and input beam diameter, in addition to the alignment. Poor alignment of the setup can result in spatial chirp at the FP[197] changing the optimum temporal overlap for different frequency channels. Finally, the arrangement and choice of crystal parameters for nonlinear amplification is a difficult task.

We can remove much of the "trial and error" from the construction aspect of FOPA by performing simulations. FOPA requires expensive lasers and expensive optical components, and knowing how your design will perform before constructing it can save a lot of time and money. For instance, instead of guessing what crystal parameters to use based on a calculation of Δk, we can run simulations on dozens of designs based on crystal type, bandwidth across each crystal, crystal thickness, pump energy etc. This is especially useful

for scaling FOPA to new wavelength regions. Additionally, we can gain insight into ways to improve FOPA. For instance, all FOPA's to date have used a constant pump fluence across the FP, which can limit the conversion efficiency. By spatially varying the pump fluence across the FP, we can maximize the gain and increase the performance of the design. A full model of the FOPA's nonlinear amplification could allow us to design a phase mask appropriate for this.

In the original paper on FOPA, calculations were made that demonstrated how the pulse duration can be tuned with grating groove density and focal length[195]. I will go through a more detailed derivation that includes the beam diameter, in section 8.3.1.

What has yet to be demonstrated is how the nonlinear amplification occur in the FP. This may seem trivial at first, but complexities arise due to the fact that the FP is at a focus, implying that the plane-wave approximation could be invalid. In section 8.4, I will describe two techniques for simulating the nonlinear amplification in a FOPA using the Matlab package of the SNLO software and in section 8.5, I will compare the results of these two techniques to the experimental results of[195]. Throughout the next two sections I will present examples for particular design criteria, for consistency, all numbers and calculations will be based on this paper. This is useful for verifying theory against the experimental outcomes.

8.3.1 Construction of the Fourier plane

There are multiple ways to approach the construction of the FP and others may have their own restrictions that would lead them to run this simulation in a different manner. My initial conditions for the problem are the central wavelength of the seed, λ_0, the bandwidth of that seed, $\Delta\omega$, the spectrum, $A(\lambda)$, and the width of the FP, W. The last criteria is mostly from a financial perspective as it determines how many crystals are required. From here, other parameters, such as the input beam diameter, D, grating ruling width, d, and focal length, f, can be chosen such that the desired pulse duration at the FP is reached.

Since we do not want spatial chirp at the FP, we use our grating in the Littrow configu-

ration,

$$2\sin(B) = m\lambda_i/d, \tag{8.1}$$

where m is the grating order, and B is the grating's blaze angle. This is only valid for one wavelength, λ_i, which should be chosen to be as close to λ_0 as possible. More generally, each wavelength has an angular dispersion off the grating described as

$$\theta(\lambda) = \arcsin(m\lambda/d - \sin(B)). \tag{8.2}$$

Because we know $\Delta\omega$, we can find the total angular spread, $\Delta\Theta$,

$$\Delta\Theta = \theta(\lambda_{max}) - \theta(\lambda_{min}), \tag{8.3}$$

where λ_{max} and λ_{min} are the longest and shortest wavelengths of $A(\lambda)$, respectively. Another condition for properly setting up the FP is that the focal element (i.e. spherical concave mirror) is exactly a distance f from the grating, where f is the focal length. When properly aligned, the separation between λ_{max} and λ_{min} on the curved mirror's surface is W. From here we can easily find a relation for the focal length of the plano-concave mirror, f, using some basic trigonometry

$$f = \sqrt{\frac{W^2}{2(1-\cos(\Delta\Theta))}}. \tag{8.4}$$

Because there are engineering limitations to these parameters, it is probably useful to go to a grating company's web page, such as Richardson's gratings, and look through their catalogue[198]. As an example for this chapter, I want to amplify a seed with λ_{min}=1300 nm and λ_{max}=2300 nm in a FP where W= 58 mm. Richardson has a grating with a B=3.6 degrees and d=13.3 μm, corresponding to a λ_0=1600 nm, which is pretty close to the central frequency. When I use this grating, I find that $\Delta\Theta \approx$4 degrees and that I need a curved mirror with f= 800 mm, which is a good length to have (in general, it is good for $f >> W$).

Choosing these parameters was the easy part, the next step, calculating the pulse duration, is a little trickier. To do this, we consider that the FP under these conditions is

transform limited, but that the spectral overlap has decreased. We need a way to calculate what the spectral overlap at a given position, x, is in the FP, which we will refer to as $A^{(x)}(\lambda)$. Each x can be associated with a given λ

$$x(\lambda) = f\tan(\theta(\lambda)) = f\tan(\arcsin(m\lambda/d - \sin(B))), \tag{8.5}$$

which we can equally write λ in terms of x,

$$\lambda(x) = d/m(\sin(\arctan(x/f)) + \sin(B)). \tag{8.6}$$

This spectrally overlaps with neighboring x due to its spot size, w_o,

$$w_o(x) = 2\lambda(x)f/(\pi D), \tag{8.7}$$

where we define w_o as the $1/e^2$ radius. So the spectrum at a given point, x_0, in the FP will be the sum of the amplitudes of all wavelengths at that particular position,

$$A^{(x_0)}(\lambda) = A(\lambda(x))G(x(\lambda) - x_0), \tag{8.8}$$

where $A^{(x_0)}(\lambda)$ is the full spectrum at position x, $A(\lambda(x))$ is the amplitude of $\lambda(x)$, and

$$G(x(\lambda) - x_0) = \exp\left[-2(x(\lambda) - x_0)^2/w_o(\lambda(x))^2\right]. \tag{8.9}$$

This equation can be computationally solved for each wavelength in the FP. A visual explanation of this equation is shown in figure 8.4. While each position in the FP can be associated with a wavelength, neighboring positions overlap in accordance with their focusing parameters. As a result, neighboring positions contribute to the bandwidth with an amplitude largely associated with the difference in their positions. We can think of $G(x(\lambda) - x_0)$ as a convolution between a δ function and a Gaussian, except in this case the Gaussian is capable of having a changing width since $w_0 \to w_0(x)$. Once this calculation is

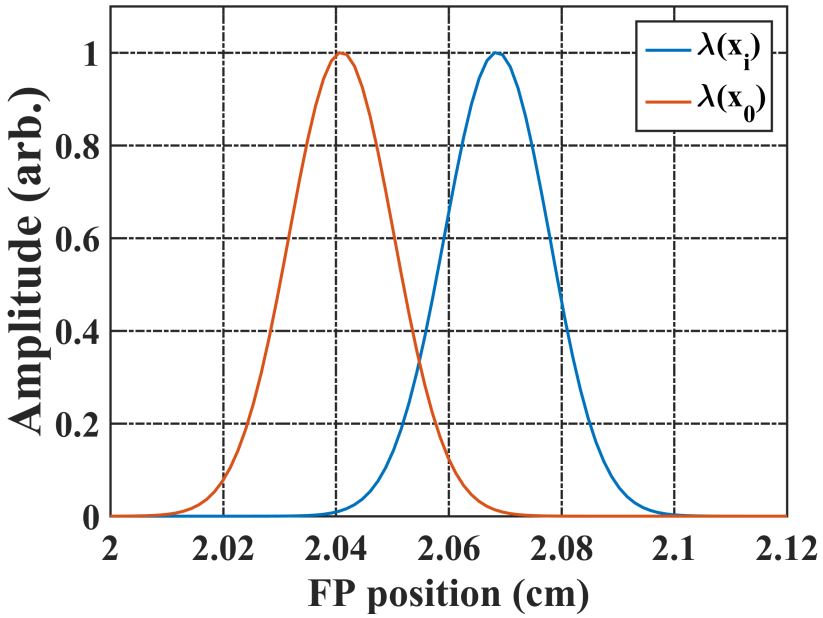

Figure 8.4: Visual explanation of how the bandwidth at each spot in the FP is calculated. Position x_0 has an associated wavelength $\lambda(x_0)$ which has a focus profile dictated by Gaussian optics, shown in red. Meanwhile, the wavelength at an adjacent position, $\lambda(x_1)$, overlaps at x_0 with a much lower amplitude.

performed, we have information about the bandwidth at each position in the FP, which can then tell us the pulse duration with a simple Fourier transform.

While equation 8.8 is the full derivation, it is worthwhile to find an analytical solution so we can understand how the various parameters in a FOPA design affect the pulse duration. We start with the obvious assumption that $w_o(\lambda) << W$, implying that $A(\lambda(x))$ is slowly varying with respect to $G(x(\lambda) - x_0)$. We can also, to a decent approximation, assume that $w_o(\lambda) \to w_o$. Finally, since $G(x(\lambda) - x_0)$ is only large for a small region of the FP, we can drop the complicated form of $x(\lambda)$ and assume that the wavelength changes linearly for each step in x. However, for the ease of simplifying the calculation later, I will change this to frequency, ω.

Out of these approximations, the last one is the least accurate, especially for large $\Delta\omega$, which is what we are most interested in using in FOPA. Nonetheless, the final result makes it worthwhile to pursue, and turns out to be within a factor of two of the actual value. To

start, let's write x in terms of ω,

$$x(\omega) = s(\omega - \omega_{min}). \tag{8.10}$$

To find s, we solve for $x(\omega_{max})$,

$$x(\omega_{max}) = W = s(\omega_{max} - \omega_{min}) = s\Delta\omega \tag{8.11}$$

$$s = \frac{W}{\Delta\omega}. \tag{8.12}$$

$A^{(x_0)}(\lambda)$ now takes the form (recall that $A(\lambda(x))$ =constant)

$$A^{(x_0)}(\omega) = G(x(\omega) - x_0) = \exp\left[-2(s(\omega - \omega_{min}) - x_0)^2/w_o^2\right]. \tag{8.13}$$

We can now take a Fourier transform and find

$$A^{(x_0)}(t) = F.T.\left\{A^{(x_0)}(\omega)\right\} = \tag{8.14}$$

$$\frac{1}{\sqrt{2\pi}}\int_{-\infty}^{\infty} \exp\left(-\frac{2s^2}{w_0^2}\omega^2 + \frac{2s\alpha}{w_0^2}\omega - \frac{2\alpha^2}{w_0^2}\right)\exp\left(\mathrm{i}\omega t\right)d\omega, \tag{8.15}$$

where $\alpha = s\omega_{min} + x_0$. After consulting a handy integral table, and ignoring the complex terms and factors independent of t (since they do not affect the pulse duration), we arrive at

$$A^{(x_0)}(t) = \exp\left[\frac{-w_0^2\Delta\omega^2}{32W^2}t^2\right], \tag{8.16}$$

which we can quickly use to solve for the FWHM of the pulse duration, τ, by equating the exponential term to

$$2\log(2)\left(\frac{t}{\tau}\right)^2 = \frac{-w_0^2\Delta\omega^2}{32W^2}t^2. \tag{8.17}$$

We are left with the result

$$\tau = 8\sqrt{\log(2)}\frac{W}{w_0}\frac{1}{\Delta\omega}. \tag{8.18}$$

When I plug in the numbers for the FP design I presented earlier in this section, and

use w_0 corresponding to the central frequency, I get $\tau = 3.6$ ps. This is about a factor of 2 higher than what the full calculation gives (which has been experimentally verified in [195]). Moreover, we get a nice sense of how we can change τ, as it clearly increases linearly with W, and inversely with w_0 and $\Delta\omega$.

At this point, we have geometrically configured the FOPA. By considering parameters such as seed bandwidth, peak intensity, pump pulse duration, as well as manufacturing constraints, we can find an optimal setup for performing FOPA. The next step is to choose the crystals, which is described in section 8.3.2.

8.3.2 Nonlinear Optics in the FP

Now that we have our laser parameters determined, we can start determining some of the parameters for the crystals. To do so, we will continue with the example FOPA parameters we began with in section 8.3.1. We will be pumping this seed with an 800 nm Ti:Sapph laser that is chirped so that it delivers a pulse duration of about 2 ps. In this section, we are interested in determining $\Delta k(x)$, which is the phase mismatch across the FP. In addition to the wavelength of the pump and seed, this depends on the number of crystals. As the work in Bruno S. et al. used four BBO crystals, I will just stick with using that for this section [195].

From the last section, we know the distribution of the seed across the FP, $\lambda(x)$. The phase mismatch as position x is

$$\Delta k = k_p(x) - k_s(x) - k_i(x), \tag{8.19}$$

where $k_n = \omega_n / v_n$ and v_n is the phase velocity. The phase velocity can be easily calculated if we have the Sellmeier equation for the refractive index. In this example, we are using type I phase matching, so only the pump has a component along the extraordinary axis of the crystal. We also need to know the group velocity, $v_g = \frac{d\omega}{dk}$ and the group velocity dispersion, $GVD = \frac{d^2\omega}{dk^2}$.

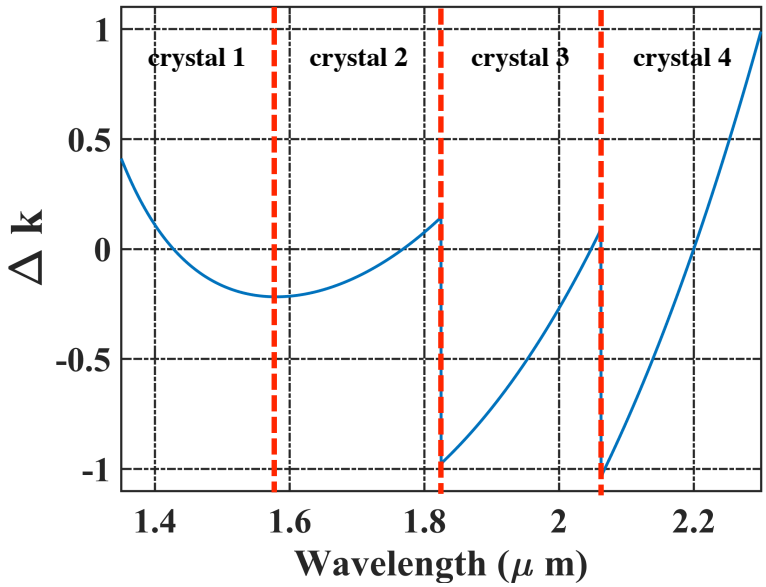

Figure 8.5: The calculation of Δk with wavelength in the FP. Due to having 4 crystals, we can select our phase matching to reduce the mismatch across the FP.

To utilize these calculations in the Fourier plane, we can start by generating bandwidth channels. Since we know $\lambda(x)$, this can be done by simply binning the wavelengths in each quarter of the FP. Afterwards, we can choose a crystal angle, θ_c, that gives $\Delta k = 0$ for the central wavelength of each channel. With θ_c known, we can quickly calculate Δk for all wavelengths. The result for our ongoing example is shown in figure 8.5. You can clearly see that the two channels on the left hand side have a continuous phase-matching distribution while the two channels on the right have discreet steps in Δk from the boundary of one crystal to the next. These jumps are due to correcting the crystal angle between each channel.

If you look closely, you will notice that $\Delta k \neq 0$ at the center for some channels. This is especially true for channel (crystal) 3. Later I will be using a software called SNLO to input all this data. SNLO rounds input data, and in the case of θ_c, to the nearest 0.1 degrees. We are working with BBO near the degeneracy point, i.e. $\lambda_s = 1600$ nm $= 2\lambda_p$, which typically has broader phase matching bandwidth[199] and, hence, Δk does not change so dramatically. This all goes to say that this discrepancy isn't a mistake.

At this point I want to make something clear. As I just mentioned, channels 1-3 in figure

8.5 have relatively low phase mismatch across their entire domain. In principle you could probably amplify these three channels one crystal, it would just need to be 2 inches wide in this example! The power of FOPA comes in with channel 4. We can see that the slope of Δk is much larger in channel four than the other three. To include this spectral channel in an OPCPA would have required sacrificing the overall gain of the other three channels. FOPA gives us the opportunity to generate a broader bandwidth pulse without hampering amplification.

8.4 SNLO software for modeling FOPA

At this point, we have gone over the details of various input parameters that go into the FOPA simulations. As you can read in appendices C and D, there are various applications in the SNLO package, of which only four or five are really used for FOPA or OPA based calculations. I will leave details of this to the appendix, so in this section, I will focus more on how we actually "fit" a FP into SNLO.

There are two models in SNLO that I will use, each has a different set of input require-

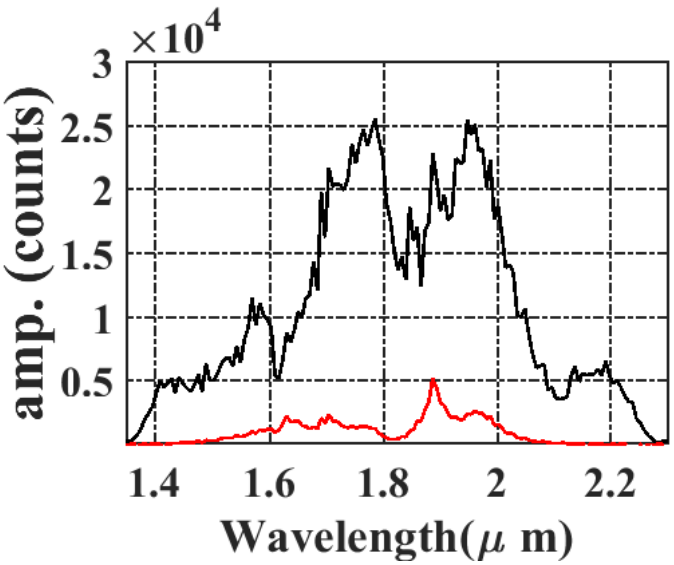

Figure 8.6: Seed measured before (red) and after (black) amplification. Made using data produced in[195].

ments that requires me to give special attention to them. If you want to know more about these functions in general before reading on, consult appendix C.

The underlying problem of using SNLO is that it is designed for fairly specific fields. That is, you cannot specify things like the spatial chirp, the number of crystals, and characteristics such as mode profile are assumed to be Gaussian. Thus, if we want to model a FOPA, we have to be a little clever.

To start with, lets consider what we want our calculation to give us. We could say the resulting output pulse energy, but this is underspecified because it does not tell us how our calculation worked across the seed spectrum. Therefore, a better metric from our simulation would tell us how it performed at each wavelength. If we look at figure 8.6, we can see the seed input spectrum (in red) along side the amplified spectrum (black) taken under the same conditions so we can see the amplification.

A good way then to monitor the performance of our simulation is to consider the spectral gain, $G(\lambda)$

$$G(\lambda) = \frac{A^{(f)}(\lambda)}{A^{(i)}(\lambda)}, \tag{8.20}$$

where $A^{(i)}(\lambda)$ is the initial energy of wavelength λ, and $A^{(f)}(\lambda)$ is the amplified energy. Not

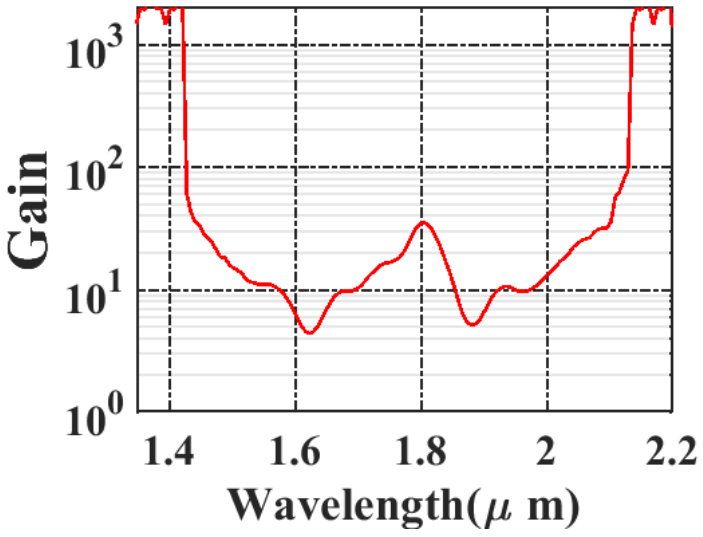

Figure 8.7: Measured gain in FP, shown in log scale. Made using data produced in[195].

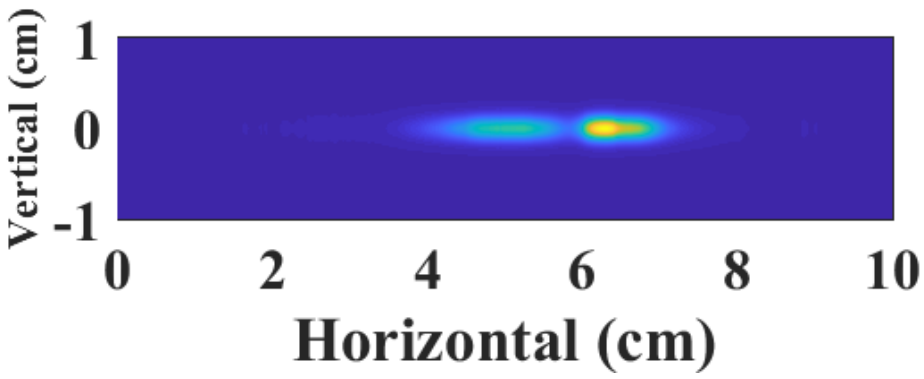

Figure 8.8: Distribution of mode in the FP. Made using data produced in [195].

only is this a useful metric for determining the performance of our model, we also have data from a recent publication, shown in figure 8.7, on FOPA to use as a guide for our simulations. From figure 8.7, we see a general trend that regions with higher G have an initially lower fluence. This makes sense from our limiting cases we considered way back in section 3.5.

Now that we have determined what we need from SNLO, we need to figure out how to correctly treat each wavelength when programming it in. Since we cannot run the entire FP in one go, we must treat each step of the FP individually. SNLO wants to have the pulse energy and a FWHM of a Gaussian mode as an input. If we look at figure 8.8, we can get a sense of what the FP looks like in terms of its mode profile. While the transverse axis largely corresponds to change in spectral energy density, the traverse axis is still Gaussian.

To exploit this, consider a very thin "strip of the FP", as shown as a purple line figure 8.9. This strip has a central wavelength, with a calculated pulse duration, phase matching characteristics, and fluence. While the mode distribution is overlapping with neighboring beamlets in the horizontal axis, (e.g. see figure 8.4) it has a well defined Gaussian distribution in the transverse axis, with a FWHM of w_f. When the strip is made much smaller than this mode profile, then we can say to a good approximation that the change in fluence in the horizontal is approximately constant.

Doing this allows us to create a new mode profile with the same characteristics as the strip. In a way, this is sort of the reverse job of what we were doing in section 8.3.1 for finding the pulse duration. There, the distribution of the beamlets was important in finding

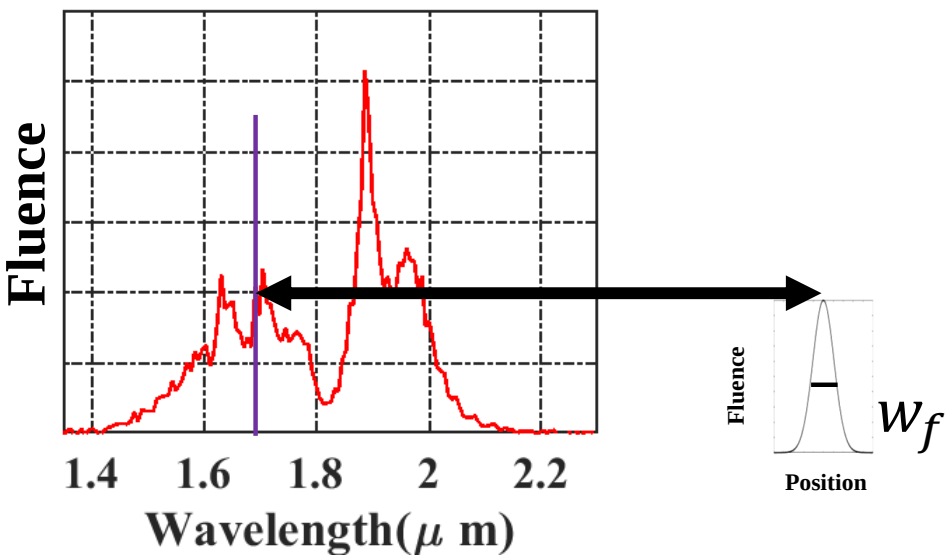

Figure 8.9: Visual for how the FP is sent into SNLO. Made using data produced in [195].

the spectral overlap. Here, we want to pull an individual beamlet out of the distribution. This new mode is shown on the right hand side of figure 8.9. We see that it has the same peak fluence, but a different mode profile that can be easily run in any of the nonlinear amplification codes of SNLO. After this beam has been operated on, we can simply reverse the process and find the total energy in the same strip of the mode that we started with. This amplified strip will contain $A^{(f)}(\lambda)$ and can be used to find $G(\lambda)$. We can choose to run this for every step of the FP if we wish, but since each individual strip is very small (approximately 10 % of the $1/e^2$ radius, or < 20 μm), we can usually skip a chunk of steps and assume that $G(\lambda)$ is the same for that group of strips.

At this point we have made enough suppositions that we can at least try to run SNLO and see how well is reproduces experimental results. But before we jump into that, we should discuss the different functions available from SNLO. In particular, we should consider the "Plane-wave mix short-pulse" (PW-SP) and the "Two-dimensional mix short pulse" (2D-SP). Short pulse programs are required because, even for a picosecond pulse, we have to consider the influence of group velocity and group velocity dispersion. The main difference between the two is pretty clear, PW-SP assumes the plane wave approximation is adequate

while 2D-SP takes into account the mode propagation affects (e.g. the change in radius of curvature while going through a focus). We might assume that, being in the FP, we would have to use 2D-SP. However, the plane-wave approximation is quite common in nonlinear optics (due to its simplicity), and we are not guaranteed that a complex simulation such as 2D-SP sufficiently replicates the complexities of the FP. For this reason, it is best to try both and determine whether or not the full 2D-SP calculation is necessary.

8.5 Results and comparison to experiment

At this point, we simply run a software, which is described more explicitly in appendices C and D. The goal in this section is to use the input parameters that we have described in sections 8.3 and 8.4 and see if we can accurately reproduce corresponding results in the literature. Our ongoing example has a measurement of $G(\lambda)$ for a series of pump energies ranging from 3 mJ to 12.8 mJ.

Figure 8.10 shows the results for the FOPA simulations as compared to the experimental results of the total output pulse energy. If we only considered this metric, we could easily be inclined to believe that the 2D-SP model is extremely accurate in representing FOPA, while the PW-SP is consistently optimistic in the output energy by 50-70% across the entire range.

The output energy is the sum of the spectral gain times the spectral fluence. Before we can conclude that either model is working, we need to compare them to the results in figure 8.7. This is shown in figure 8.11 for a pump laser energy in the FOPA of 3 mJ (8.11a) and 12.8 mJ (8.11b). Here we see that the 2D-SP model tends to overshoot the spectral gain on the wings and underestimate the gain in the regions with higher fluence. So while it rarely yields the correct spectral gain, the model tends to use the good ol' trick of "two wrongs make a right".

On the other hand, the PW-SP model tends to, more or less, get the regions with higher initial fluence correct, while continuing to overestimate the gain for the wings. Because of this, the PW-SP model retrieves a consistently higher pulse energy in figure 8.10 than what

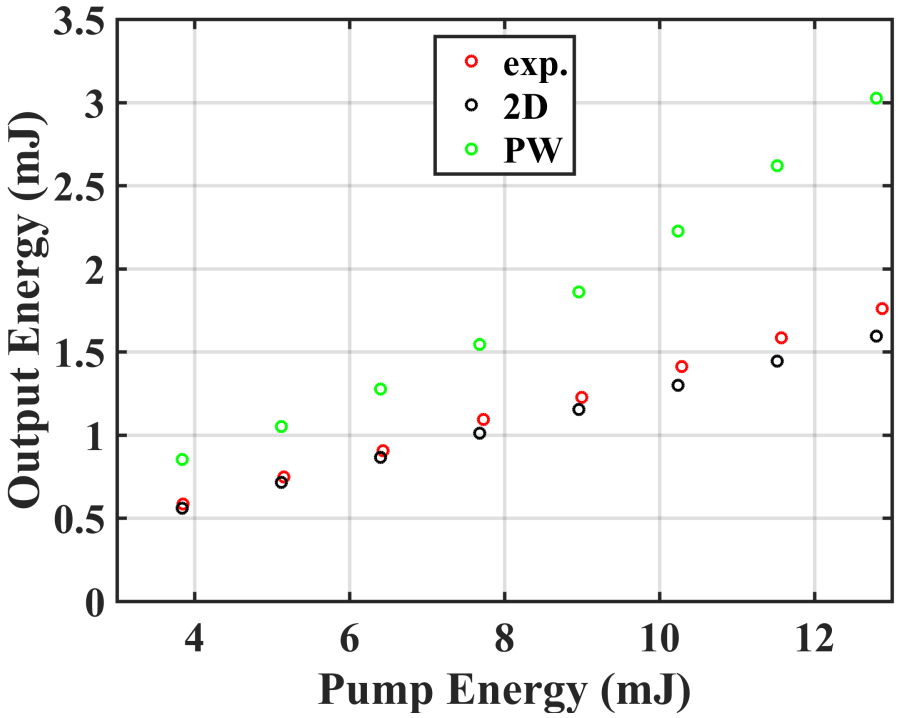

Figure 8.10: Results for retrieved pulse energy from FOPA under the conditions described in [195]. Experimental points are shown in red, with the PW-SP model in green and 2D-SP in black. Made using data produced in [195].

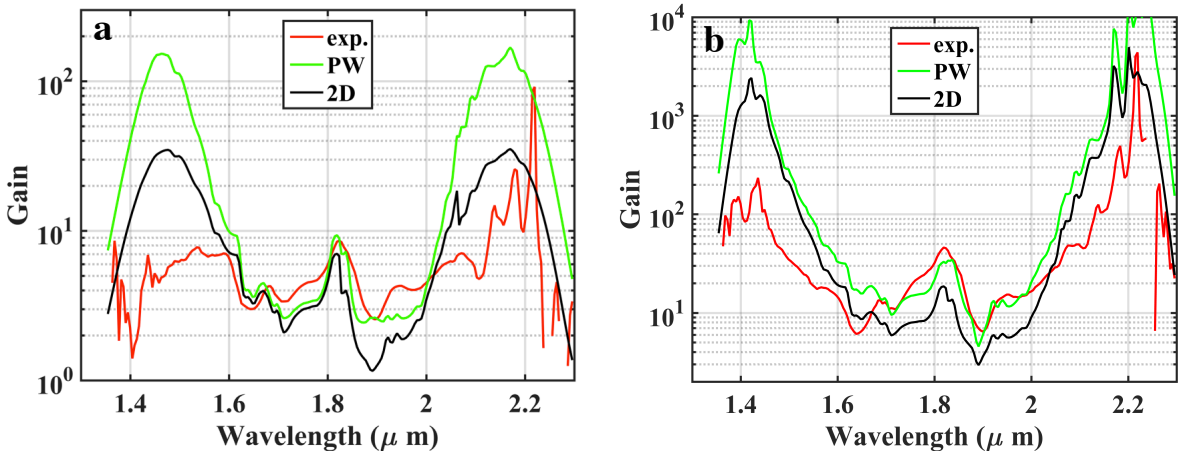

Figure 8.11: Results for spectral gain from FOPA under the conditions described in [195]. Figure **a** corresponds to a FOPA pumped with 3 mJ, while in figure **b**, the FOPA is pumped at 12.8 mJ. Experimental points are shown in red, with the PW-SP model in green and 2D-SP in black. Made using data produced in [195].

was experimentally verified.

Thus far, the results for simulating a FOPA are fairly optimistic. If I were to choose one based on the results of figures 8.10 and 8.11, I would go with the PW for two reasons. First, I prefer a simulation that is right some of the time, versus almost none of the time. Second, the PW code can run an entire simulation in roughly 2-3 minutes on my desktop computer, while the 2D model requires approximately 2 hours.

Nonlinear optics is complicated, and the fact that we can run a plane-wave approximation for the entire FP and be off by 50 % is actually impressive. What is not so impressive is the large sensitivity that FOPA has to the seed's initial spectral fluence. One of the major advantages of the FOPA geometry is the ability to tailer a pump so that we can enhance regions with lower fluence. If we want to simulate this, we need to have, in the very least, a simulation that yields consistent behavior across a large range of initial seeding fluences.

In this iteration of the FOPA simulator, I have relegated myself to using the nonlinear optics packages from SNLO. These are met with some limitations. One step towards improving these simulations in the future could focus on designing a custom nonlinear propagation function. Using this, we may be able to include the propagation effects that are unique to FOPA into a nonlinear model. This could produce more reliable results on the spectral edges, allowing us to extend the design capabilities of FOPA design.

Nonetheless, we can still treat certain FOPA designs with our model. Perhaps we can monitor the spectral gain and know that when the model yields gain on the order of 500 or greater, that we should be cautious not to put too much trust in the results.

8.6 Outlook on improving FOPA with simulations

A difficult problem in nonlinear optics applications is the correct choice of crystal. In the scenario for our ongoing example, the four BBO crystals have been demonstrated to work well, but the choice of crystal thickness is not as simple because of the variation in the seed energy density across the FP, as shown in figure 8.8. Crystals are routinely the most expensive component in a light source, and custom designs can easily take months or up to

a year to have delivered. Therefore, it is essential that when we buy a crystal, we get it right the first time. A FOPA simulation allows us to correctly choose the number of crystals, and crystal dimensions for a FOPA with relative ease.

In addition to being dependent on the initial seed fluence, FOPA performance is also correlated to the pump fluence and the crystal thickness. A common nonlinear effect that we haven't discussed directly[1] up to this point is back-conversion. That is, once a pump laser has been depleted, the nonlinear optical interaction continues, but now in reverse! Thus, while you may want a thick crystal to enhance the wings of a FOPA seed, you can easily begin back-converting the regions with high seed fluence. There are hints that this effect is occurring in the FOPA example provided in this chapter.

Unfortunately, it is pretty hard to vary the crystal thickness in the FP and still expect to retrieve a good pulse out of the FOPA. Instead, we can try varying the pump laser fluence in the FP. There exists etch-able phase masks from Silios Technologies which can be used in series with the pump delivery system to produce a pump laser profile tailored to the seed's fluence in the FP. Unfortunately, we cannot use an active phase mask (such as a spatial light modulator) with intense pump lasers due to their low damage thresholds. Therefore, we require a priori information about the required pump laser distribution. One route to doing this is with a FOPA simulation that allows us to tests various pump profiles generated via a mask.

Finally, FOPA has so far been demonstrated in the NIR/MWIR (1-3 μm) region. In this range, the choice of nonlinear crystal is the standard BBO. However, strong-field, ultrafast science is pushing for longer wavelengths (>4 μm), and FOPA can be expected to be a major technique in producing sources in this region. Before designing new FOPA's from scratch and buying crystals based solely off of the nonlinear phase matching curves, it would be useful to have a simulation we can run to get an idea of the performance of the system.

[1] But was hinted at in section 3.5.3.

Chapter 9

Conclusion and outlook

In summary, this thesis comprised of several studies centered on the goal of understanding wavelength scaling of matter's interaction with strong laser fields. To do this, we collaborated with a company to produce a Terawatt class peak power, Ti:Sapph laser delivering unprecedented CEP performance, as demonstrated in chapter 4. With this laser, we can realize a new technique for producing milli-Joule level, non-sinusoidal light transient waveforms in the NIR. To date, the most successful development for these sources has occurred in the visible-UV regime, which has limited applicability in strong-field science. Chapter 5 shows work demonstrating two major steps for a technique that utilizing the output of a high energy OPA which would be capable of low noise, stable, waveforms due to its centralized design on minimizing the length of parallel paths for separate channels.

Perhaps the most exciting work of this thesis is the extension of strong-field, few-cycle, light studies to the LWIR region, shown in chapter 6. As no light source was readily available in this region that could produce the necessary peak intensity and pulse duration, we designed our own system based on difference frequency generation of our high-energy OPA. We measured the pulses with a custom designed cross-correlation FROG, and demonstrated Gigawatt level peak powers from 5 μm to 9 μm. We supplied evidence that this source could reach high ($\geq 10^{13}$ TW/cm^2) intensities by measuring strong-field ionization in Xenon gas across this wavelength range.

We then moved into applications of strong laser fields by considering the wavelength scaling of strong-field photo-excitation in semiconductors in chapter 7. As the photo-excitation rate depends on the density of states in the system, we observed a change in the absorbance by rotating the sample with respect to the laser's polarization, and measured the laser's transmittance. We used the large wavelength tunability of our OPA to study four wavelengths covering both two-photon and three-photon absorption in gallium arsenide. The results show that absorbance has a strong dependence on photon order. We believe this could indicate something about the dynamics of the electron in the conduction band.

Finally, chapter 8 addresses some of the issues that arise in the generation of LWIR pulses, such as the limitations in scalability and pulse duration. We covered a new amplification technique, known as FOPA, and its many advantages. However, the design of a FOPA is tricky and could be expensive in both time and money if not designed correctly the first time. For this reason, I have been setting out a method of modeling FOPA in Matlab using the mlSNLO package. While primitive in design, the code shows promise in replicating experimental results that will most likely lead to more advanced computational techniques in the future.

Up to chapter 8 is where my research currently stands; I am happy to see that this is not where it finishes. Several projects have inspired new experiments or source designs that will be carried out by the next generation of the Carlos Trallero group. Notably, methods for improving the LWIR have been made on several fronts. The first has already been discussed and centers on FOPA. A proposal written by me and Carlos has been submitted to the Defense University Research Instrumentation Program (DURIP) for a source based on work from this project.

From chapter 6, the characterization and reduction of the free carrier absorption in Ge for effective filtering of the LWIR is something we believe should be presented in the literature. We plan to make careful measurements of this for a journal.

While we are interested in using FOPA for new sources in the LWIR, we have been improving the design of our DFG by considering a method utilizing a dual-OPA system. If properly designed, this system may be capable of scaling LWIR to the milli-Joule level. With

this setup, we could continue the work we have been perform in chapter 7 by conducting experiments on HHG in solids and material damage studies. Because of the low band gap energies of semiconductors, there remains many experiments to be performed with the LWIR source in chapter 6 or future generations of the source. Carlos Trallero and I have written a proposal to the Office of Naval Research (ONR) and a grant has been award to the Carlos Trallero group for carrying out this development and studies.

To conclude this thesis, we saw that several areas of strong-field science were lacking in light-based technology due to the known wavelength-scaling nature of the interaction. We found means of producing sources that can be of a large benefit to our understanding of strong-field science by allowing studies to access previously unexplored wavelength regimes. I was also able to apply our OPA to understanding the role of photon order in strong-field absorbance in gallium arsenide. Finally, the development of strong-field setups in the long-wave infrared continues by means of new amplification technologies.

Bibliography

[1] Max Herzberger. Optics from Euclid to Huygens. *Applied Optics*, 5(9):1383–1393, sep 1966.

[2] Harry Edwin Burton. The Optics of Euclid. *Journal of the Optical Society of America*, 35(5):357–372, 1945.

[3] Ibn (Alhazen) Al-Haitham. *Opticae Thesaurus Alhazeni*. 1015.

[4] S L Campbell, R B Hutson, G E Marti, A Goban, N Darkwah Oppong, R L McNally, L Sonderhouse, J M Robinson, W Zhang, B J Bloom, and J Ye. A Fermi-degenerate three-dimensional optical lattice clock. *Science*, 358(6359):90 – 94, 2017.

[5] J W Beams. A review of the use of Kerr cells for the measurement of time intervals and the production of flashes of light. *Review of Scientific Instruments*, 1(12):780–793, 1930.

[6] H Abraham and J Lemoine. Disparition instantanée du phénomène de Kerr. *Comptes Rendus (Paris)*, 129(206):206–208, 1899.

[7] T H Maiman. Stimulated Optical Radiation in Ruby. *Nature*, 187:493, 1960.

[8] J A Armstrong. Measurement of picosecond pulse widths. *Applied Physics Letters*, 10(1):16–18, 1967.

[9] C V Shank and E P Ippen. Subpicosecond kilowatt pulses from a mode-locked cw dye laser. *Applied Physics Letters*, 24(8):373–375, 1974.

[10] Zewail Ahmed H. Nobel Prize in Chemistry, 1999.

[11] Central Intelligence Agency USA. The world factbook: Electricity - installed generating capacity, 2014.

[12] P B Corkum. Plasma perspective on strong field multiphoton ionization. *Physical Review Letters*, 71(13):1994–1997, 1993.

[13] Maria Göppert-Mayer. Über elementarakte mit zwei quantensprüngen. *Annalen der Physik*, 401(3):273–294, 1931.

[14] A Ludwig, J Maurer, B. W. Mayer, C. R. Phillips, L Gallmann, and U Keller. Breakdown of the Dipole Approximation in Strong-Field Ionization. *Physical Review Letters*, 113(24):243001, 2014.

[15] L. D. Landau and E. M. Lifshitz. *Quantum Mechanics*. Pergamon Press, 1963.

[16] B. M. Smirnov and Chibisov M. I. The breaking up of atomic particles by an electric field and by electron collision. *Soviet Physics: Journal of Experimental and Theoretical Physics*, 22(3):585, 1966.

[17] L. V. Keldysh. Ionization in the Field of a Strong Electromagnetic Wave. *Soviet Physics: Journal of Experimental and Theoretical Physics*, 20(5):1307–1314, 1965.

[18] A. M. Perelomov, V. S. Popov, and M. V. Terent'ev. Ionization of atoms in an alternating electric field. *Soviet Physics: Journal of Experimental and Theoretical Physics*, 23(5):924, 1966.

[19] F H M Faisal. Multiple absorption of laser photons by atoms. *Journal of Physics B: Atomic and Molecular Physics*, 6(4):L89, 1973.

[20] Gennady L. Yudin and Misha Yu. Ivanov. Nonadiabatic tunnel ionization: Looking inside a laser cycle. *Physical Review A*, 64:013409, 2001.

[21] S V Popruzhenko. Keldysh theory of strong field ionization: history, applications, difficulties and perspectives. *Journal of Physics B: Atomic, Molecular and Optical Physics*, 47(20):204001, 2014.

[22] P. Agostini, F. Fabre, G. Mainfray, G. Petite, and N. K. Rahman. Free-free transitions following six-photon ionization of xenon atoms. *Phys. Rev. Lett.*, 42:1127–1130, 1979.

[23] Y Gontier Trahin, M Poirier, and M. Multiphoton absorptions above the ionisation threshold. *Journal of Physics B: Atomic and Molecular Physics*, 13(7):1381, 1980.

[24] P Kruit, J Kimman, H G Muller, and M J van der Wiel. Electron spectra from multiphoton ionization of xenon at 1064, 532, and 355 nm. *Physical Review A*, 28(1):248–255, 1983.

[25] A. Lohr, M. Kleber, R. Kopold, and W. Becker. Above-threshold ionization in the tunneling regime. *Physical Review A*, 55:R4003–R4006, 1997.

[26] Klaus Ergenzinger. Multiphoton ionization as time-dependent tunneling. *Physical Review A*, 55:577–588, 1997.

[27] M F Kling, Ch. Siedschlag, A J Verhoef, J I Khan, M Schultze, Th. Uphues, Y Ni, M Uiberacker, M Drescher, F Krausz, and M J J Vrakking. Control of Electron Localization in Molecular Dissociation. *Science*, 312(5771):246–248, 2006.

[28] M Kübel, K J Betsch, Nora G Kling, A S Alnaser, J Schmidt, U Kleineberg, Y Deng, I Ben-Itzhak, G G Paulus, T Pfeifer, J Ullrich, R Moshammer, M F Kling, and B Bergues. Non-sequential double ionization of Ar: from the single- to the many-cycle regime. *New Journal of Physics*, 16(3):33008, 2014.

[29] G G Paulus, W Nicklich, Huale Xu, P Lambropoulos, and H Walther. Plateau in above threshold ionization spectra. *Physical Review Letters*, 72(18):2851–2854, 1994.

[30] D. N. Fittinghoff, P. R. Bolton, B. Chang, and K. C. Kulander. Observation of nonsequential double ionization of helium with optical tunneling. *Physical Review Letters*, 69:2642–2645, 1992.

[31] P. Dietrich, N. H. Burnett, M. Ivanov, and P. B. Corkum. High-harmonic generation

and correlated two-electron multiphoton ionization with elliptically polarized light. *Physical Review A*, 50:R3585–R3588, 1994.

[32] Dimitar Popmintchev, Benjamin R. Galloway, Ming-Chang Chen, Franklin Dollar, Christopher A. Mancuso, Amelia Hankla, Luis Miaja-Avila, Galen O'Neil, Justin M. Shaw, Guangyu Fan, Skirmantas Ališauskas, Giedrius Andriukaitis, Tadas Balčiunas, Oliver D. Mücke, Audrius Pugzlys, Andrius Baltuška, Henry C. Kapteyn, Tenio Popmintchev, and Margaret M. Murnane. Near- and extended-edge X-ray-absorption fine-structure spectroscopy using ultrafast coherent high-order harmonic supercontinua. *Physical Review Letters*, 120:093002, 2018.

[33] Jeffrey L Krause, Kenneth J Schafer, and Kenneth C Kulander. High-order harmonic generation from atoms and ions in the high intensity regime. *Physical Review Letters*, 68(24):3535–3538, 1992.

[34] P M Paul, E S Toma, P Breger, G Mullot, F Augé, Ph. Balcou, H G Muller, and P Agostini. Observation of a Train of Attosecond Pulses from High Harmonic Generation. *Science*, 292(5522):1689–1692, 2001.

[35] M Hentschel, R Kienberger, Ch. Spielmann, G A Reider, N Milosevic, T Brabec, P Corkum, U Heinzmann, M Drescher, and F Krausz. Attosecond metrology. *Nature*, 414:509, 2001.

[36] Eleftherios Goulielmakis, Zhi-Heng Loh, Adrian Wirth, Robin Santra, Nina Rohringer, Vladislav S Yakovlev, Sergey Zherebtsov, Thomas Pfeifer, Abdallah M Azzeer, Matthias F Kling, Stephen R Leone, and Ferenc Krausz. Real-time observation of valence electron motion. *Nature*, 466:739, 2010.

[37] M. Von Ardenne and D. Beischer. Untersuchung von metalloxyd-rauchen mit dem universal-elektronenmikroskop. *Zeitschrift für Elektrochemie und angewandte physikalische Chemie*, 46(4):270–277, 1940.

[38] Debbie J. Stokes. *Principles and Practice of Variable Pressure/Environmental Scanning Electron Microscopy (VP?ESEM).* John Wiley & Sons, 2008.

[39] Cosmin I Blaga, Junliang Xu, Anthony D DiChiara, Emily Sistrunk, Kaikai Zhang, Pierre Agostini, Terry A Miller, Louis F DiMauro, and C D Lin. Imaging ultrafast molecular dynamics with laser-induced electron diffraction. *Nature*, 483(7388):194–197, 2012.

[40] Michael G. Pullen, Benjamin Wolter, Anh-Thu Le, Matthias Baudisch, Michaël Hemmer, Arne Senftleben, Claus Dieter Schröter, Joachim Ullrich, Robert Moshammer, C. D. Lin, and Jens Biegert. Imaging an aligned polyatomic molecule with laser-induced electron diffraction. *Nature Communications*, 6:7262, 2015.

[41] S V Bulanov, N M Naumova, and F Pegoraro. Interaction of an ultrashort, relativistically strong laser pulse with an overdense plasma. *Physics of Plasmas*, 1(3):745–757, 1994.

[42] Paul Gibbon. Harmonic Generation by Femtosecond Laser-Solid Interaction: A Coherent "Water-Window" Light Source? *Physical Review Letters*, 76(1):50–53, 1996.

[43] B Dromey, M Zepf, A Gopal, K Lancaster, M S Wei, K Krushelnick, M Tatarakis, N Vakakis, S Moustaizis, R Kodama, M Tampo, C Stoeckl, R Clarke, H Habara, D Neely, S Karsch, and P Norreys. High harmonic generation in the relativistic limit. *Nature Physics*, 2:456, 2006.

[44] M. Gertsvolf, H. Jean-Ruel, P. P. Rajeev, D. D. Klug, D. M. Rayner, and P. B. Corkum. Orientation-dependent multiphoton ionization in wide band gap crystals. *Physical Review Letters*, 101:243001, 2008.

[45] Shambhu Ghimire, Anthony D DiChiara, Emily Sistrunk, Pierre Agostini, Louis F DiMauro, and David A Reis. Observation of high-order harmonic generation in a bulk crystal. *Nature Physics*, 7:138, 2010.

[46] Neil W. Ashcroft and N. David Mermin. *Solid State Physics*. Saunders College, 1976.

[47] Charles Kittel. *Introduction to Solid State Physics: Eighth Edition*. Wiley & Sons, 2004.

[48] Felix Bloch. Über die Quantenmechanik der Elektronen in Kristallgittern. *Zeitschrift für Physik*, 52(7):555–600, 1929.

[49] R. Kronig and W. G. Penney. Quantum Mechanics of Electrons in Crystal Lattices. *Proceedings of the Royal Society of London A*, 130:499, 1931.

[50] David J. Griffiths. *Introduction to Quantum Mechanics*. Pearson Education, Inc., Upper Saddle River, NJ, 2nd edition, 2005.

[51] Vitali E Gruzdev. Laser-induced ionization of solids: back to Keldysh. volume 5647, pages 5613–5647, 2005.

[52] V E Gruzdev and J K Chen. Photo-ionization of wide band-gap materials by high-intensity laser radiation. volume 6261, pages 62610J–6261–12, 2006.

[53] Peter A Roos, Qudsia Quraishi, Steven T Cundiff, Ravi D R Bhat, and J E Sipe. Characterization of quantum interference control of injected currents in LT-GaAs for carrier-envelope phase measurements. *Optics Express*, 11(17):2081–2090, 2003.

[54] T. M. Fortier, P. A. Roos, D. J. Jones, S. T. Cundiff, R. D. R. Bhat, and J. E. Sipe. Carrier-envelope phase-controlled quantum interference of injected photocurrents in semiconductors. *Physical Review Letters*, 92:147403, 2004.

[55] E. O. Kane. Band structure of indium antimonide. *Journal of Physics and Chemistry of Solids*, 1(4):249–261, 1957.

[56] A. Vaidyanathan, T. Walker, A. H. Guenther, S. S. Mitra, and L. M. Narducci. Two-photon absorption in several direct-gap crystals. *Physical Review B*, 21:743–748, 1980.

[57] V. E. Gruzdev. Laser-induced ionization of solids: back to keldysh. In *Laser-Induced Damage in Optical Materials: 2004*, volume 5647 of *Proceedings of SPIE*. SPIE, 2005.

[58] V. E. Gruzdev. Photoionization rate in wide band-gap crystals. *Physical Review B*, 75:205106, 2007.

[59] S M Golin, S E Kirkwood, D D Klug, D M Villeneuve, D M Rayner, C A Trallero Herrero, and P B Corkum. Strong field processes inside gallium arsenide. *Journal of Physics B: Atomic, Molecular and Optical Physics*, 47(20):204025, 2014.

[60] M Hohenleutner, F Langer, O Schubert, M Knorr, U Huttner, S W Koch, M Kira, and R Huber. Real-time observation of interfering crystal electrons in high-harmonic generation. *Nature*, 523:572, 2015.

[61] Yong Sing You, DavidA. Reis, and Shambhu Ghimire. Anisotropic high-harmonic generation in bulkcrystals. *Nature Physics*, 13:345, 2016.

[62] D Normand, L A Lompre, and C Cornaggia. Laser-induced molecular alignment probed by a double-pulse experiment. *Journal of Physics B: Atomic, Molecular and Optical Physics*, 25(20):L497, 1992.

[63] Xiaoming Ren, Varun Makhija, and Vinod Kumarappan. Multipulse three-dimensional alignment of asymmetric top molecules. *Physical Review Letters*, 112:173602, 2014.

[64] Donna Strickland and Gerard Mourou. Compression of amplified chirped optical pulses. *Optics Communications*, 56(3):219–221, 1985.

[65] C P Hauri, W Kornelis, F W Helbing, A Heinrich, A Couairon, A Mysyrowicz, J Biegert, and U Keller. Generation of intense, carrier-envelope phase-locked few-cycle laser pulses through filamentation. *Applied Physics B*, 79(6):673–677, 2004.

[66] Mathieu Giguère, Bruno E Schmidt, Andrew D Shiner, Marie-Andrée Houle, Heidi C Bandulet, Gabriel Tempea, David M Villeneuve, Jean-Claude Kieffer, and François

Légaré. Pulse compression of submillijoule few-optical-cycle infrared laser pulses using chirped mirrors. *Optics Letters*, 34(12):1894–1896, 2009.

[67] A A Lanin, A A Voronin, E A Stepanov, A B Fedotov, and A M Zheltikov. Frequency-tunable sub-two-cycle 60-MW-peak-power free-space waveforms in the mid-infrared. *Optics Letters*, 39(22):6430–6433, 2014.

[68] A A Lanin, A A Voronin, E A Stepanov, A B Fedotov, and A M Zheltikov. Multi-octave, 3-18 μm sub-two-cycle supercontinua from self-compressing, self-focusing soliton transients in a solid. *Optics Letters*, 40(6):974–977, 2015.

[69] Bruno E Schmidt, Andrew D Shiner, Mathieu Giguère, Philippe Lassonde, Carlos A Trallero-Herrero, J-C Kieffer, P B Corkum, D M Villeneuve, and François Légaré. High harmonic generation with long-wavelength few-cycle laser pulses. *Journal of Physics B: Atomic, Molecular and Optical Physics*, 45(7), 2012.

[70] Melanie T Asaki, Chung-Po Huang, Dennis Garvey, Jianping Zhou, Henry C Kapteyn, and Margaret M Murnane. Generation of 11-fs pulses from a self-mode-locked Ti:sapphire laser. *Optics Letters*, 18(12):977–979, 1993.

[71] Huang, Chung-Po and Asaki, Melanie T. and Backus, Sterling and Murnane, Margaret M. and Kapteyn, Henry C. and Nathel, Howard. 17-fs pulses from a self-mode-locked Ti:sapphire laser. *Optics Letters*, 17(18):1289–1291, 1992.

[72] Anthony Siegman. *Lasers*. University Science Books, Sausalito, Ca, 1 edition, 1986.

[73] Peter Milonni and Joseph Eberly. *Laser Physics*. John Wiley & Sons, 2010.

[74] K. F. Wall and A. Sanchez. Titanium Sapphire Lasers. *The Lincoln Laboratory Journal*, 3(3):447, 1990.

[75] Govind Agrawal. *Nonlinear Fiber Optics*. Elsevier, 2008.

[76] Robert Boyd. *Nonlinear Optics*. Elsevier, third edition, 2008.

[77] T Wittmann, B Horvath, W Helml, M G Schätzel, X Gu, A L Cavalieri, G G Paulus, and R Kienberger. Single-shot carrier–envelope phase measurement of few-cycle laser pulses. *Nature Physics*, 5, 2009.

[78] G. Nisoli, M. and Sansone, G. and Stagira, S. and De Silvestri, S. and Vozzi, C. and Pascolini, M. and Poletto, L. and Villoresi, P. and Tondello. Effects of Carrier-Envelope Phase Differences of Few-Optical-Cycle Light Pulses in Single-Shot High-Order-Harmonic Spectra. *Physical Review Letters*, 91(21):213905, 2003.

[79] D J Kane and R Trebino. Characterization of arbitrary femtosecond pulses using frequency-resolved optical gating. *IEEE Journal of Quantum Electronics*, 29(2):571–579, 1993.

[80] S Linden, J Kuhl, and H Giessen. Amplitude and phase characterization of weak blue ultrashort pulses by downconversion. *Optics Letters*, 24(8):569–571, 1999.

[81] Xueming Liu, Hanyi Zhang, and Mingde Zhang. Exact analytical solutions and their applications for interacting waves in quadratic nonlinear medium. *Optics Express*, 10(1):83–97, 2002.

[82] P Di Trapani, A Andreoni, C Solcia, P Foggi, R Danielius, A Dubietis, and A Piskarskas. Matching of group velocities in three-wave parametric interaction with femtosecond pulses and application to traveling-wave generators. *Journal of the Optical Society of America B*, 12(11):2237–2244, 1995.

[83] Barry Luther-Davies and Yi Yu. Efficient Generation of Ultra-short Pulses in the Infrared from a Simple PPLN Optical Parametric Amplifier. In *Nonlinear Optics*, OSA Technical Digest (online), page NTu2A.4, Waikoloa, Hawaii, 2017. Optical Society of America.

[84] B Langdon, J Garlick, X Ren, D J Wilson, A M Summers, S Zigo, M F Kling, S Lei, C G Elles, E Wells, E D Poliakoff, K D Carnes, V Kumarappan, I Ben-Itzhak, and

C A Trallero-Herrero. Carrier-envelope-phase stabilized terawatt class laser at 1 kHz with a wavelength tunable option. *Optics Express*, 23(4):4563–4572, 2015.

[85] Ferenc Krausz and Misha Ivanov. Attosecond physics. *Reviews of Modern Physics*, 81(1):163–234, 2009.

[86] M Nisoli, S De Silvestri, and O Svelto. Generation of high energy 10 fs pulses by a new pulse compression technique. *Applied Physics Letters*, 68(20):2793–2795, 1996.

[87] C P J Barty, C L Gordon, and B E Lemoff. Multiterawatt 30-fs Ti:sapphire laser system. *Optics Letters*, 19(18):1442–1444, 1994.

[88] M D Perry, D Pennington, B C Stuart, G Tietbohl, J A Britten, C Brown, S Herman, B Golick, M Kartz, J Miller, H T Powell, M Vergino, and V Yanovsky. Petawatt laser pulses. *Optics Letters*, 24(3):160–162, 1999.

[89] Han-Sung Chan, Zhi-Ming Hsieh, Wei-Hong Liang, A H Kung, Chao-Kuei Lee, Chien-Jen Lai, Ru-Pin Pan, and Lung-Han Peng. Synthesis and measurement of ultrafast waveforms from five discrete optical harmonics. *Science*, 331(6021):1165–1168, 2011.

[90] A Wirth, M Th. Hassan, I Grguraš, J Gagnon, A Moulet, T T Luu, S Pabst, R Santra, Z A Alahmed, A M Azzeer, V S Yakovlev, V Pervak, F Krausz, and E Goulielmakis. Synthesized light transients. *Science*, 334(6053):195–200, 2011.

[91] Shu-Wei Huang, Giovanni Cirmi, Jeffrey Moses, Kyung-Han Hong, Siddharth Bhardwaj, Jonathan R Birge, Li-Jin Chen, Enbang Li, Benjamin J Eggleton, Giulio Cerullo, and Franz X Kärtner. High-energy pulse synthesis with sub-cycle waveform control for strong-field physics. *Nature Photonics*, 5(8):475–479, 2011.

[92] M Th. Hassan, A Wirth, I Grguraš, A Moulet, T T Luu, J Gagnon, V Pervak, and E Goulielmakis. Invited Article: Attosecond photonics: Synthesis and control of light transients. *Review of Scientific Instruments*, 83(11):111301, 2012.

[93] Warren S Warren, Herschel Rabitz, and Mohammed Dahleh. Coherent Control of Quantum Dynamics: The Dream Is Alive. *Science*, 259(5101):1581–1589, 1993.

[94] Georg Gademann, Fabien Plé, Pierre-Mary Paul, and Marc J J Vrakking. Carrier-envelope phase stabilization of a terawatt level chirped pulse amplifier for generation of intense isolated attosecond pulses. *Optics Express*, 19(25):24922–24932, 2011.

[95] J.-F. Hergott, O Tcherbakoff, P.-M. Paul, Ph. Demengeot, M Perdrix, F Lepetit, D Garzella, D Guillaumet, M Comte, P D' Oliveira, and O Gobert. Carrier-Envelope Phase stabilization of a 20 W, grating based, chirped-pulse amplified laser, using Electro-Optic effect in a LiNbO3 crystal. *Optics Express*, 19(21):19935–19941, 2011.

[96] G Sansone, E Benedetti, F Calegari, C Vozzi, L Avaldi, R Flammini, L Poletto, P Villoresi, C Altucci, R Velotta, S Stagira, S De Silvestri, and M Nisoli. Isolated Single-Cycle Attosecond Pulses. *Science*, 314(5798), 2006.

[97] E Goulielmakis, M Schultze, M Hofstetter, V S Yakovlev, J Gagnon, M Uiberacker, A L Aquila, E M Gullikson, D T Attwood, R Kienberger, F Krausz, and U Kleineberg. Single-Cycle Nonlinear Optics. *Science*, 320(5883), 2008.

[98] Kun Zhao, Qi Zhang, Michael Chini, Yi Wu, Xiaowei Wang, and Zenghu Chang. Tailoring a 67 attosecond pulse through advantageous phase-mismatch. *Optics Letters*, 37(18):3891–3893, 2012.

[99] D E Spence, P N Kean, and W Sibbett. 60-fsec pulse generation from a self-mode-locked Ti:sapphire laser. *Optics Letters*, 16(1):42–44, 1991.

[100] Chengquan Li, Eric Moon, and Zenghu Chang. Carrier-envelope phase shift caused by variation of grating separation. *Optics Letters*, 31(21):3113–3115, 2006.

[101] Zenghu Chang. Carrier-envelope phase shift caused by grating-based stretchers and compressors. *Applied Optics*, 45(32):8350–8353, 2006.

[102] L Xu, Ch. Spielmann, A Poppe, T Brabec, F Krausz, and T W Hänsch. Route to phase control of ultrashort light pulses. *Optics Letters*, 21(24):2008–2010, 1996.

[103] Scott A. Diddams, David J. Jones, Jun Ye, Steven T. Cundiff, John L. Hall, Jinendra K. Ranka, Robert S. Windeler, Ronald Holzwarth, Thomas Udem, and T. W. Hänsch. Direct link between microwave and optical frequencies with a 300 Thz femtosecond laser comb. *Physical Review Letters*, 84:5102–5105, 2000.

[104] Masayuki Kakehata, Hideyuki Takada, Yohei Kobayashi, Kenji Torizuka, Yoshihiko Fujihira, Tetsuya Homma, and Hideo Takahashi. Single-shot measurement of carrier-envelope phase changes by spectral interferometry. *Optics Letters*, 26(18):1436–1438, 2001.

[105] Fabian Lücking, Andreas Assion, Alexander Apolonski, Ferenc Krausz, and Günter Steinmeyer. Long-term carrier-envelope-phase-stable few-cycle pulses by use of the feed-forward method. *Optics Letters*, 37(11):2076–2078, 2012.

[106] Eric Wayne Moon. *Carrier-envelope phase stabilization of grating-based chirped-pulse amplifiers*. PhD thesis, Kansas State University, 2009.

[107] Fabian Lücking, Vincent Crozatier, Nicolas Forget, Andreas Assion, and Ferenc Krausz. Approaching the limits of carrier-envelope phase stability in a millijoule-class amplifier. *Optics Letters*, 39(13):3884–3887, 2014.

[108] M Th. Hassan, T T Luu, A Moulet, O Raskazovskaya, P Zhokhov, M Garg, N Karpowicz, A M Zheltikov, V Pervak, F Krausz, and E Goulielmakis. Optical attosecond pulses and tracking the nonlinear response of bound electrons. *Nature*, 530(7588):66–70, 2016.

[109] Andrius Baltušfika, Takao Fuji, and Takayoshi Kobayashi. Controlling the Carrier-Envelope Phase of Ultrashort Light Pulses with Optical Parametric Amplifiers. *Physical Review Letters*, 88(13):133901, 2002.

[110] William A Okell, Tobias Witting, Davide Fabris, Dane Austin, Maïmouna Bocoum, Felix Frank, Aurélien Ricci, Aurélie Jullien, Daniel Walke, Jonathan P Marangos, Rodrigo Lopez-Martens, and John W G Tisch. Carrier-envelope phase stability of hollow fibers used for high-energy few-cycle pulse generation. *Optics Letters*, 38(19):3918–3921, 2013.

[111] Shu-Wei Huang, Giovanni Cirmi, Jeffrey Moses, Kyung-Han Hong, Siddharth Bhardwaj, Jonathan R Birge, Li-Jin Chen, Irina V Kabakova, Enbang Li, Benjamin J Eggleton, Giulio Cerullo, and Franz X Kärtner. Optical waveform synthesizer and its application to high-harmonic generation. *Journal of Physics B: Atomic, Molecular and Optical Physics*, 45(7), 2012.

[112] T Rathje, Nora G Johnson, M Möller, F Süßmann, D Adolph, M Kübel, R Kienberger, M F Kling, G G Paulus, and A M Sayler. Review of attosecond resolved measurement and control via carrier–envelope phase tagging with above-threshold ionization. *Journal of Physics B: Atomic, Molecular and Optical Physics*, 45(7), 2012.

[113] Derrek J Wilson, Xiaoming Ren, Stefan Zigo, François Légaré, and Carlos Trallero-Herrero. Simultaneous few-cycle pulse generation of the depleted pump and signal from an optical parametric amplifier. *Journal of the Optical Society of America B*, 35(4):A45–A48, 2018.

[114] Derrek Wilson, Carlos Trallero-Herrero, and Xiaoming Ren. Simultaneous broadening of the depleted pump and signal from an optical parametric amplifier. In *CLEO: 2014*, page STh4E.5. Optical Society of America, 2014.

[115] O D Mücke, S Fang, G Cirmi, G M Rossi, S H Chia, H Ye, Y Yang, R Mainz, C Manzoni, P Farinello, G Cerullo, and F X Kärtner. Toward Waveform Nonlinear Optics Using Multimillijoule Sub-Cycle Waveform Synthesizers. *IEEE Journal of Selected Topics in Quantum Electronics*, 21(5):1–12, 2015.

[116] Bing Xue, Eiji J Takahashi, Yuxi Fu, and Katsumi Midorikawa. Intense attosecond

soft x-ray pulse by a high-energy three-channel waveform synthesizer. In *Conference on Lasers and Electro-Optics*, page FM2D.4. Optical Society of America, 2017.

[117] B & K Precision Corporation ©, 2017.

[118] Steven T Cundiff and Andrew M Weiner. Optical arbitrary waveform generation. *Nature Photonics*, 4:760, 2010.

[119] L E Chipperfield, J S Robinson, J W G Tisch, and J P Marangos. Ideal Waveform to Generate the Maximum Possible Electron Recollision Energy for Any Given Oscillation Period. *Physical Review Letters*, 102(6):63003, 2009.

[120] A M Weiner, D E Leaird, J S Patel, and J R Wullert. Programmable shaping of femtosecond optical pulses by use of 128-element liquid crystal phase modulator. *IEEE Journal of Quantum Electronics*, 28(4):908–920, 1992.

[121] Andrew M Weiner. *Ultrafast Optics*. John Wiley & Sons, Hoboken, 1 edition, 2009.

[122] S E Harris and A V Sokolov. Subfemtosecond Pulse Generation by Molecular Modulation. *Physical Review Letters*, 81(14):2894–2897, 1998.

[123] T R Schibli, J Kim, O Kuzucu, J T Gopinath, S N Tandon, G S Petrich, L A Kolodziejski, J G Fujimoto, E P Ippen, and F X Kaertner. Attosecond active synchronization of passively mode-locked lasers by balanced cross correlation. *Optics Letters*, 28(11):947–949, 2003.

[124] H-C Bandulet, D Comtois, A D Shiner, C Trallero-Herrero, N Kajumba, T Ozaki, P B Corkum, D M Villeneuve, J-C Kieffer, and F Légaré. High harmonic generation with a spatially filtered optical parametric amplifier. *Journal of Physics B: Atomic, Molecular and Optical Physics*, 41(24):245602, 2008.

[125] Nicolas Thiré, Samuel Beaulieu, Vincent Cardin, Antoine Laramée, Vincent Wanie, Bruno E Schmidt, and François Légaré. 10 mJ 5-cycle pulses at 1.8 μm through optical parametric amplification. *Applied Physics Letters*, 106(9):91110, 2015.

[126] Vincent Cardin, Nicolas Thiré, Samuel Beaulieu, Vincent Wanie, François Légaré, and Bruno E Schmidt. 0.42 TW 2-cycle pulses at 1.8 μm via hollow-core fiber compression. *Applied Physics Letters*, 107(18):181101, 2015.

[127] Derrek J. Wilson, Adam M. Summers, Stefan Zigo, Brandin Davis, Seyyed Robatjazi, Daniel Rolles, Artem Rudenko, and Carlos Trallero-Herrero. An intense, few-cycle source in the long-wave infrared. *in preparation*, 2018.

[128] F Yergeau, S L Chin, and P Lavigne. Multiple ionisation of rare-gas atoms by an intense CO_2 laser (10^{14} W cm^{-2}). *Journal of Physics B: Atomic and Molecular Physics*, 20(4):723, 1987.

[129] P B Corkum, N H Burnett, and F Brunel. Above-threshold ionization in the long-wavelength limit. *Physical Review Letters*, 62(11):1259–1262, 1989.

[130] A. Picón, A. Jaroń-Becker, and A. Becker. Enhancement of vibrational excitation and dissociation of H_2^+ in infrared laser pulses. *Physical Review Letters*, 109:163002, 2012.

[131] H. R. Reiss. Limits on tunneling theories of strong-field ionization. *Physical Review Letters*, 101:043002, 2008.

[132] Tenio Popmintchev, Ming-Chang Chen, Alon Bahabad, Michael Gerrity, Pavel Sidorenko, Oren Cohen, Ivan P Christov, Margaret M Murnane, and Henry C Kapteyn. Phase matching of high harmonic generation in the soft and hard X-ray regions of the spectrum. *Proceedings of the National Academy of Sciences*, 106(26):10516–10521, 2009.

[133] Francisco Silva, Stephan M Teichmann, Seth L Cousi, Michael Hemmer, and Jens Biegert. Spatiotemporal isolation of attosecond soft X-ray pulses in the water window. *Nature Communications*, 6(1):6611, 2015.

[134] B Sheehy, J D D Martin, T O Clatterbuck, D W Kim, L F DiMauro, P Agostini, K J Schafer, M B Gaarde, and K C Kulander. Strong field atomic physics in the mid-infrared. *AIP Conference Proceedings*, 525(1):59–69, 2000.

[135] P Colosimo, G Doumy, C I Blaga, J Wheeler, C Hauri, F Catoire, J Tate, R Chirla, A M March, G G Paulus, H G Muller, P Agostini, and L F DiMauro. Scaling strong-field interactions towards the classical limit. *Nature Physics*, 4(5):386, 2008.

[136] C. I. Blaga, F. Catoire, P. Colosimo, G. G. Paulus, H. G. Muller, P. Agostini, and L. F. DiMauro. Strong-field photoionization revisited. *Nature Physics*, 5:335, 2009.

[137] J Tate, T Auguste, H G Muller, P Salières, P Agostini, and L F DiMauro. Scaling of wave-packet dynamics in an intense mid-infrared field. *Physical Review Letters*, 98(1):13901, 2007.

[138] D Haberberger, S Tochitsky, and C Joshi. Fifteen terawatt picosecond CO_2 laser system. *Optics Express*, 18(17):17865–17875, 2010.

[139] F Seifert, V Petrov, and M Woerner. Solid-state laser system for the generation of midinfrared femtosecond pulses tunable from 3.3 to 10 μm. *Optics Letters*, 19(23):2009–2011, 1994.

[140] Alexander Sell, Alfred Leitenstorfer, and Rupert Huber. Phase-locked generation and field-resolved detection of widely tunable terahertz pulses with amplitudes exceeding 100 MV/cm. *Optics Letters*, 33(23):2767–2769, 2008.

[141] D Sanchez, M Hemmer, M Baudisch, S L Cousin, K Zawilski, P Schunemann, O Chalus, C Simon-Boisson, and J Biegert. High Energy Mid-IR OPCPA at 7 μm with 2 μm Pump. *Optica*, 3(2):147–150, 2016.

[142] Houkun Liang, Peter Krogen, Zhou Wang, Hyunwook Park, Tobias Kroh, Kevin Zawilski, Peter Schunemann, Jeffrey Moses, Louis F. DiMauro, Franz X. Kärtner, and Kyung-Han Hong. High-energy mid-infrared sub-cycle pulse synthesis from a parametric amplifier. *Nature Communications*, 8(1), 2017.

[143] Patrick Whalen, Paris Panagiotopoulos, Miroslav Kolesik, and Jerome V. Moloney. Extreme carrier shocking of intense long-wavelength pulses. *Physical Review A*, 89:023850, 2014.

[144] P Malevich, G Andriukaitis, T Flöry, A J Verhoef, A Fernández, S Ališauskas, A Pugžlys, A Baltuška, L H Tan, C F Chua, and P B Phua. High energy and average power femtosecond laser for driving mid-infrared optical parametric amplifiers. *Optics Letters*, 38(15):2746–2749, 2013.

[145] M Hemmer, D Sánchez, M Jelínek, Vadim Smirnov, H Jelinkova, V Kubeček, and J Biegert. 2 μm wavelength, high-energy Ho:YLF chirped-pulse amplifier for mid-infrared OPCPA. *Optics Letters*, 40(4):451–454, 2015.

[146] Lorenz von Grafenstein, Martin Bock, Uwe Griebner, and Thomas Elsaesser. High-energy multi-kilohertz Ho-doped regenerative amplifiers around 2 m. *Optics Express*, 23(11):14744–14752, 2015.

[147] Lorenz von Grafenstein, Martin Bock, Dennis Ueberschaer, Uwe Griebner, and Thomas Elsaesser. Picosecond 34 mJ pulses at kHz repetition rates from a Ho:YLF amplifier at 2 μm wavelength. *Optics Express*, 23(26):33142–33149, 2015.

[148] Yanchun Yin, Andrew Chew, Xiaoming Ren, Jie Li, Yang Wang, Yi Wu, and Zenghu Chang. Towards Terawatt Sub-Cycle Long-Wave Infrared Pulses via Chirped Optical Parametric Amplification and Indirect Pulse Shaping. *Scientific Reports*, 7:45794, 2017.

[149] R C Eckardt, H Masuda, Y X Fan, and R L Byer. Absolute and relative nonlinear optical coefficients of KDP, KD*P, BaB_2O_4, $LiIO_3$, MgO:$LiNbO_3$, and KTP measured by phase-matched second-harmonic generation. *IEEE Journal of Quantum Electronics*, 26(5):922–933, 1990.

[150] F Rotermund, V Petrov, and F Noack. Difference-frequency generation of intense femtosecond pulses in the mid-IR (4-12 μm) using HgGa2S4 and AgGaS2. *Optics Communications*, 185(1):177–183, 2000.

[151] P Kupecek, C Schwartz, and D Chemla. Silver thiogallate ($AgGaS_2$) - Part 1: Nonlinear optical properties. *IEEE Journal of Quantum Electronics*, 10(7):540–545, 1974.

[152] B C Ziegler and K L Schepler. Transmission and damage-threshold measurements in AgGaSe2 at 2.1 μm. *Applied Optics*, 30(34):5077–5080, 1991.

[153] Norman P Barnes, Donald J Gettemy, Jack R Hietanen, and Rebecca A Lannini. Parametric amplification in AgGaSe2. *Applied Optics*, 28(23):5162–5168, 1989.

[154] G Boyd, H Kasper, J McFee, and F Storz. Linear and nonlinear optical properties of some ternary selenides. *IEEE Journal of Quantum Electronics*, 8(12):900–908, 1972.

[155] K L Vodopyanov. Parametric generation of tunable infrared radiation in ZnGeP2 and GaSe pumped at 3 μm. *Journal of the Optical Society of America B*, 10(9):1723–1729, 1993.

[156] G. B. Abdullaev, L. A. Kulevskii, A. M. Prokhorov, A. D. Savel'Ev, E. Y. Salaevs, and V. V. Smirnov. GaSe, a new effective material for nonlinear optics. *Journal of Experimental and Theoretical Physics Letters*, 16:90–95, 1972.

[157] Jin Guo, Ji-Jiang Xie, Laiming Zhang, Chen F, Ke Jiang, Sergei V. Alexeev, Yu.M. Andreev, Konstantin Kokh, Grigory Lanskii, Valery F. Losev, Dmitrii Lubenko, Anna V. Shaiduko, and V Svetlichnyi. *GaSe damage threshold under IR pulse pumping.* Jan 2012.

[158] Andre Peremans, Dan Lis, Francesca Cecchet, Peter G Schunemann, Kevin T Zawilski, and Valentin Petrov. Noncritical singly resonant synchronously pumped OPO for generation of picosecond pulses in the mid-infrared near 6.4 μm. *Optics Letters*, 34(20):3053–3055, 2009.

[159] Peter G Schunemann, Kevin T Zawilski, Thomas M Pollak, David E Zelmon, Nils C Fernelius, and F Kenneth. Hopkins. New Nonlinear Optical Crystal for Mid-IR OPOs: $CdSiP_2$. In *Advanced Solid-State Photonics*, OSA Technical Digest Series (CD), page MG6, 2008.

[160] Anne Hildenbrand, Christelle Kieleck, Aleksey Tyazhev, Georgi Marchev, Georg Stöppler, Marc Eichhorn, Peter Schunemann, and Valentin Petrov. Laser damage

studies of $CdSiP_2$ and $ZnGeP_2$ nonlinear crystals with nanosecond pulses at 1064 and 2090 nm. volume 8964, pages 896417–896418, 2014.

[161] Ichiro Shoji, Takashi Kondo, Ayako Kitamoto, Masayuki Shirane, and Ryoichi Ito. Absolute scale of second-order nonlinear-optical coefficients. *Journal of the Optical Society of America B*, 14(9):2268–2294, 1997.

[162] Yi Li, Feng Liu, Yanfeng Li, Lu Chai, Qirong Xing, Minglie Hu, and Chingyue Wang. Experimental study on GaP surface damage threshold induced by a high repetition rate femtosecond laser. *Applied Optics*, 50(13):1958–1962, 2011.

[163] G D Boyd, E Buehler, and F G Storz. Linear and nonlinear optical properties of ZnGeP2 and CdSe. *Applied Physics Letters*, 18(7):301–304, 1971.

[164] R D Peterson, K L Schepler, J L Brown, and P G Schunemann. Damage properties of ZnGeP2 at 2 μm. *Journal of the Optical Society of America B*, 12(11):2142–2146, 1995.

[165] V Petrov Noack, F Rotermund, and F. Generation of high-power femtosecond light pulses at 1 kHz in the mid-infrared spectral range between 3 and 12 μm by second-order nonlinear processes in optical crystals. *Journal of Optics A: Pure and Applied Optics*, 3(3), 2001.

[166] Anthony E. Siegman. *Lasers*. University Science Books, 1986.

[167] Peter W. Milonni and Joseph H. Eberly. *Laser Physics*. Wiley, 2010.

[168] C H Henry, R A Logan, and K A Bertness. Spectral dependence of the change in refractive index due to carrier injection in GaAs lasers. *Journal of Applied Physics*, 52(7):4457–4461, 1981.

[169] Chin Yi Tsai, Chin Yao Tsai, Chih Hsiung Chen, Tien Li Sung, Tsu Yin Wu, and Fang Ping Shih. Theoretical model for intravalley and intervalley free-carrier absorp-

tion in semiconductor lasers: Beyond the classical drude model. *IEEE Journal of Quantum Electronics*, 34(3):552–558, 1998.

[170] Edward D. Palik. *Handbook of optical constants of solids*. Academic Press, 1998.

[171] Derrek J. Wilson, Adam M. Summers, Giriaj Jnawli, J. H. Edjar, Christopher M. Sorensen, and Carlos Trallero-Herrero. Wavelength scaling of strong field interactions in semiconductors. *in preparation*, 2018.

[172] Derrek Wilson, Adam M Summers, Giriraj Jnawali, Christopher M Sorensen, J H Edgar, and Carlos Trallero-Herrero. Wavelength scaling of strong field effects in GaAs. In *Nonlinear Optics*, OSA Technical Digest (online), page NW2A.6, Waikoloa, Hawaii, 2017. Optical Society of America.

[173] G Vampa, T. J. Hammond, N Thiré, B. E. Schmidt, F Légaré, C. R. McDonald, T Brabec, D. D. Klug, and P. B. Corkum. All-Optical Reconstruction of Crystal Band Structure. *Physical Review Letters*, 115(19):193603, 2015.

[174] A A Lanin, E A Stepanov, A B Fedotov, and A M Zheltikov. Mapping the electron band structure by intraband high-harmonic generation in solids. *Optica*, 4(5):516–519, 2017.

[175] Mengxi Wu, Yongsing You, Shambhu Ghimire, David A. Reis, Dana A. Browne, Kenneth J. Schafer, and Mette B. Gaarde. Orientation dependence of temporal and spectral properties of high-order harmonics in solids. *Physical Review A*, 96:063412, 2017.

[176] V E Gruzdev. Analysis of the transparent-crystal ionization model developed by L. V. Keldysh*. *Journal of Optical Technology*, 71(8):504–508, 2004.

[177] V E Gruzdev. Features of the laser ionization of crystalline broad-band insulators. *Journal of Optical Technology*, 73(6):385–390, 2006.

[178] P. A. Zhokhov and A. M. Zheltikov. Field-cycle-resolved photoionization in solids. *Physical Review Letters*, 113:133903, 2014.

[179] G. Vampa, C. R. McDonald, G. Orlando, P. B. Corkum, and T. Brabec. Semiclassical analysis of high harmonic generation in bulk crystals. *Physical Review B*, 91:064302, 2015.

[180] C. R. McDonald, G Vampa, P. B. Corkum, and T Brabec. Intense-Laser Solid State Physics: Unraveling the Difference between Semiconductors and Dielectrics. *Physical Review Letters*, 118(17):173601, 2017.

[181] Vaidya Nathan, A H Guenther, and S S Mitra. Review of multiphoton absorption in crystalline solids. *Journal of the Optical Society of America B*, 2(2):294–316, 1985.

[182] W C Hurlbut, Yun-Shik Lee, K L Vodopyanov, P S Kuo, and M M Fejer. Multiphoton absorption and nonlinear refraction of GaAs in the mid-infrared. *Optics Letters*, 32(6):668–670, 2007.

[183] Shaul Pearl, Nir Rotenberg, and Henry M van Driel. Three photon absorption in silicon for 2300-3300 nm. *Applied Physics Letters*, 93(13):131102, 2008.

[184] Ting Wang, Nalla Venkatram, Jacek Gosciniak, Yuanjing Cui, Guodong Qian, Wei Ji, and Dawn T H Tan. Multi-photon absorption and third-order nonlinearity in silicon at mid-infrared wavelengths. *Optics Express*, 21(26):32192–32198, 2013.

[185] Martin Schultze, Krupa Ramasesha, C D Pemmaraju, S A Sato, D Whitmore, A Gandman, James S Prell, L J Borja, D Prendergast, K Yabana, Daniel M Neumark, and Stephen R Leone. Attosecond band-gap dynamics in silicon. *Science*, 346(6215):1348 – 1352, 2014.

[186] O Schubert, M Hohenleutner, F Langer, B Urbanek, C Lange, U Huttner, D Golde, T Meier, M Kira, S W Koch, and R Huber. Sub-cycle control of terahertz high-harmonic generation by dynamical Bloch oscillations. *Nature Photonics*, 8:119, 2014.

[187] F Langer, M Hohenleutner, U Huttner, S W Koch, M Kira, and R Huber. Symmetry-controlled temporal structure of high-harmonic carrier fields from a bulk crystal. *Nature Photonics*, 11:227, 2017.

[188] Derrek J. Wilson and Carlos Trallero-Herrero. Simulation for improving the performance of frequency domain optical parametric amplifiers. *in preparation*, 2018.

[189] Qingbin Zhang, Eiji J Takahashi, Oliver D Mücke, Peixiang Lu, and Katsumi Midorikawa. Dual-chirped optical parametric amplification for generating few hundred mJ infrared pulses. *Optics Express*, 19(8):7190–7212, 2011.

[190] A Dubietis, G Jonušauskas, and A Piskarskas. Powerful femtosecond pulse generation by chirped and stretched pulse parametric amplification in BBO crystal. *Optics Communications*, 88(4):437–440, 1992.

[191] I N Ross, P Matousek, M Towrie, A J Langley, and J L Collier. The prospects for ultrashort pulse duration and ultrahigh intensity using optical parametric chirped pulse amplifiers. *Optics Communications*, 144(1):125–133, 1997.

[192] Giulio Cerullo and Sandro De Silvestri. Ultrafast optical parametric amplifiers. *Review of Scientific Instruments*, 74(1):1–18, 2003.

[193] V V Lozhkarev, G I Freidman, V N Ginzburg, E V Katin, E A Khazanov, A V Kirsanov, G A Luchinin, A N Mal'shakov, M A Martyanov, O V Palashov, A K Poteomkin, A M Sergeev, A A Shaykin, I V Yakovlev, S G Garanin, S A Sukharev, N N Rukavishnikov, A V Charukhchev, R R Gerke, and V E Yashin. 200 TW 45 fs laser based on optical parametric chirped pulse amplification. *Optics Express*, 14(1):446–454, 2006.

[194] J Rothhardt, S Hädrich, E Seise, M Krebs, F Tavella, A Willner, S Düsterer, H Schlarb, J Feldhaus, J Limpert, J Rossbach, and A Tünnermann. High average and peak power few-cycle laser pulses delivered by fiber pumped OPCPA system. *Optics Express*, 18(12):12719–12726, 2010.

[195] Bruno E Schmidt, Nicolas Thiré, Maxime Boivin, Antoine Laramée, François Poitras, Guy Lebrun, Tsuneyuki Ozaki, Heide Ibrahim, and François Légaré. Frequency domain optical parametric amplification. *Nature Communications*, 5(3643):1–8, 2014.

[196] P Lassonde, N Thiré, L Arissian, G Ernotte, F Poitras, T Ozaki, A Larameé, M Boivin, H Ibrahim, F Légaré, and B E Schmidt. High Gain Frequency Domain Optical Parametric Amplification. *IEEE Journal of Selected Topics in Quantum Electronics*, 21(5):1–10, 2015.

[197] Charles G Durfee, Michael Greco, Erica Block, Dawn Vitek, and Jeff A Squier. Intuitive analysis of space-time focusing with double-ABCD calculation. *Optics Express*, 20(13):14244–14259, 2012.

[198] Newport Corporation. https://www.newport.com/b/richardson-gratings, 2018.

[199] R Dabu. Very broad gain bandwidth parametric amplification in nonlinear crystals at critical wavelength degeneracy. *Optics Express*, 18(11):11689–11699, 2010.

Appendix A

Fourier transformation in Matlab

Of course, Matlab has an fast Fourier transform (FFT) function available, as most programs do nowadays. However, if you want to have the full electric field to be complete, with the correct phase and calibration, you need to do be careful with your calibration. The first function, **Speck2PulseFreq.m**, takes an electric field specified in angular frequency and yields a time-domain electric field. The second, **Speck2PulseLamb.m**, takes a pulse specified linearly in wavelength, and finds the time-domain electric field. Because we use spectrometers, and the XFROG.3.2.2. code likes to specify everything in wavelength as well, the second code is the one that you will typically use.

A.1 Speck2PulseFreq

```
function [Time,Pulse,pulseo,Phase,freqc]=Speck2PulseFreq(Spec,Freq,pad)

%Created by Derrek Wilson: March 2015

%%%%%%%%%%%%%%%%%%%%%%%%%%%%%%%%%%%%%%%%%%%%%%%%%%%%%%%%%%%%%%%%%%%%%%%
%Speck2PulseFreq is for a spectrally amplitude generated from a linearly
%spaced array!  Check that you are doing this!
%%%%%%%%%%%%%%%%%%%%%%%%%%%%%%%%%%%%%%%%%%%%%%%%%%%%%%%%%%%%%%%%%%%%%%%
%Amplitude should be input as a FIELD (you measure intensity)!
%Freq is input in rad/sec.
%Pad is a number for 2^PAD # of elements in output vectors.
%Spec and Freq must have the SAME EVEN # of elements.
%%%%%%%%%%%%%%%%%%%%%%%%%%%%%%%%%%%%%%%%%%%%%%%%%%%%%%%%%%%%%%%%%%%%%%%

n=numel(Spec);
N=2^pad; %# of points for padding
Zero=zeros(1,N);

df=(Freq(n)-Freq(1))/n;%Frequency spacing
SumNum=sum(Freq.*real(Spec)*df);
SumDen=sum(real(Spec)*df);
freqc=real(SumNum/SumDen);%Carrier wavelength (nm)

padfreq=horzcat(Zero,Spec,Zero);
pulseo=fftshift(fft(ifftshift(padfreq)));%pulse
deltime=2*pi/((2*N+n)*df);
Time=-(2*N+n)/2*deltime:deltime:(2*N+n-1)/2*deltime;%padded time axis (s)

centerline=freqc*Time;%Center the phase on carrier
haze=unwrap(angle(pulseo));%unwrapped fft phase
Phase=haze+centerline;%absolute phase
Pulse=real(pulseo.*exp(1i*centerline))/max(abs(pulseo));
```

A.2 Speck2PulseLamb

```
function [Time,Pulse,pulseo,Phase,Freq,freqc,spectrumas]=Speck2PulseLamb(spectrum,lambda,pad)

%Created by Derrek Wilson: October 2014

%%%%%%%%%%%%%%%%%%%%%%%%%%%%%%%%%%%%%%%%%%%%%%%%%%%%%%%%%%%%%%%%%%%%%%%
%Spectrum for Speck2PulseLamb is typically given from a spectrometer
%(i.e., the amplitude spacing goes 1/lambda and not linearly spaced
%in frequency. Check that you are doing this!
%%%%%%%%%%%%%%%%%%%%%%%%%%%%%%%%%%%%%%%%%%%%%%%%%%%%%%%%%%%%%%%%%%%%%%%
%Amplitude should be input as a FIELD (you measure intensity)
%Lambda is input in NANOMETERS.
%Pad is a number for 2^PAD # of elements in output vectors.
%spectrum and lambda must have the SAME EVEN # of elements.
%%%%%%%%%%%%%%%%%%%%%%%%%%%%%%%%%%%%%%%%%%%%%%%%%%%%%%%%%%%%%%%%%%%%%%%
c=3*10^17;%(nm/s)
freq=2*pi*c./lambda;%(rad/s)
```

```
n=numel(freq);%for padding
delfreq=(freq(n)-freq(1))/n;%freq spacing (rad/s*div)

Freq=linspace(freq(n),freq(1),n);
spectrumas=fliplr(interp1(freq,spectrum,fliplr(Freq)));

df=abs((Freq(n)-Freq(1))/n);
SumNum=sum(Freq.*spectrumas*df);
SumDen=sum(spectrumas*df);
freqc=SumNum/SumDen;%Carrier wavelength (nm)

alpha=numel(find(Freq>freqc));
beta=numel(find(Freq<freqc));
NUMba=abs(alpha-beta);
if alpha>beta
    spectrums=horzcat(zeros(1,NUMba),spectrumas);
else
    spectrums=horzcat(spectrumas,zeros(1,NUMba));
end

Zeros=zeros(1,pad*n);
padspeck=horzcat(Zeros,spectrums,Zeros);
pulseo=fftshift(fft(ifftshift(padspeck)));%spectrum

N=numel(pulseo);
deltime_pad=2*pi/(N*delfreq);
Time=-N/2*deltime_pad:deltime_pad:(N/2-1)*deltime_pad;%padded time axis (s)

haze=unwrap(angle(pulseo));
centerline=freqc.*Time;
Phase=haze+centerline;
Pulse=abs(pulseo)/max(abs(pulseo)).*cos(Phase);
```

Appendix B

Code for propagating intense laser fields in solids

There are two equations used in the thesis for determining the photoionization rates in band gap materials. The first, is Keldysh's original derivation, which uses the Kane band model[17]. The second, is Gruzdev's derivation with the cosine band[58]. Both of these functions are executed in the same script, which is shown in the first section.

Much of this code was written by Carlos Trallero-Herrero. I added the cosine band derivation and made some modifications to the laser propagation script.

B.1 Calc_mod_depth_Thesis.m

This is the script used to propagate an intense laser field in a solid. It finds the depletion of the laser field as it propagates through the material.

```
%Ths program propagates a pulse through a chosen material, assuming
%assuming no focusing in the material and calculates the absorption using a
%chosen theory.

%Can use either Keldysh_solids_full_function or Modified_Keldysh_solids_full_function

%The code takes into account changing effective mass which is taken fom
%theory

%The ouput is the changing intensity with respect to propagation distance
%for a series of initial intensities.
%output the modulation depth in transmission due to changing polarization
%angle and changing effective mass.
%outputs the lawnmower curve, changing transmissino with input intensity

%v2 also saves the transmission and carrier density which the v1 does not.
%v3 saves the maximum ionization rate for each intensity. Uses full Keldysh
%theory
%v4 (also known as newm) uses the higher values for effective mass using the derivative of
%bandstructure
%v8 This is for comparing Gruzdev's cosine band to Keldysh's original model.
clear all
close all

% Plots different stuff through the code
Debug = 'no';
%%%CONSTANTS%%%%%%%%%%%%%%%%%%%%%%%%%%%%%%%%%%%%%%%%%%%%%%%%%%%%%%%%%%%%%%%%%%%%
hbar = 1.054e-34;                   % [J*s]
me = 9.11e-31;                      % electron mass [kg]
perm = 8.85e-12;                    % electric permittivity [F/m]
e = 1.6e-19;                        % elementary charge [C]
d = 5.6535E-10;                     % lattice separation (m)
c = 3e8;                            % speed of light [m/s]
L = 500e-6;                         %length of medium
No = 30;                            % number of intensity points to plot
Nr = 25;                            %number of radius points
Nt = 25;                            %number of time points
Nz = 100;                           %number of length points

%-------------------------------------------------------------------
%%%LASER PARAMETERS%%%%%%%%%%%%%%%%%%%%%%%%%%%%%%%%%%%%%%%%%%%%%%%%%%%%%%%%%%%%%

I0 = 0.395E12;%   %peak laser pulse intensity [W/cm^2]

% Laser Parameter Sets:
 %lambda = 1180*1e-9;          % laser wavelength [m]
 %tauFWHM = 39e-15;            %FWHM intensity pulse duration [s]
 %w0 = 45e-6;                  % 1/e beam waist in field [m]

```

```
50  %lambda = 1580*1e-9;          % laser wavelength [m]
51  %tauFWHM = 30e-15;            % FWHM intensity pulse duration [s]
52  %w0 = 45e-6;                  % 1/e beam waist in field [m]
53
54  lambda = 2000*1e-9;          % laser wavelength [m]
55  tauFWHM = 67e-15;            % FWHM intensity pulse duration [s]
56  w0 = 47e-6;                  % 1/e beam waist in field [m]
57
58 %lambda = 2400*1e-9;          % laser wavelength [m]
59 %tauFWHM = 108e-15;           % FWHM intensity pulse duration [s]
60 %w0 = 45e-6;                  % 1/e beam waist in field [m]
61
62 %-------------------------------------------------------------------------
63
64 %%MATERIAL PARAMETERS%%%%%%%%%%%%%%%%%%%%%%%%%%%%%%%%%%%%%%%%%%%%%%%%%%%%%%%%
65 [a,D,N,EgeV,n0,n2, R] = GaAs_lambda(lambda);          %load variables for material used
66 %-------------------------------------------------------------------------
67 %%UPLOAD%%%%%%%%%%%%%%%%%%%%%%%%%%%%%%%%%%%%%%%%%%%%%%%%%%%%%%%%%%%%%%%%%%%%
68 %upload effective mass
69 mass = dlmread('110429 - GaAs effective mass.txt','\t',2,0);
70 Angle90 = mass(:,1);%vertcat(mass(1,1),mass(11,1));
71 mc = mass(:,2);%vertcat(mass(1,2),mass(11,2));
72 mv = mass(:,3);%vertcat(mass(1,3),mass(11,3));
73 mr = mass(:,4);%vertcat(mass(1,4),mass(11,4));
74 %mvl = mass(:,5);    %light hole valence
75 %mrlh = 1./(1./abs(mr) + 1./abs(mvl)); %reduced mass from light hole and conduction
76 mrhh = 1./(1./abs(mr) + 1./abs(mv));
77 m = abs(mrhh*me);                                  %use reduced effective mass
78 whichweuse = 'mrhh';
79 round = '06';
80 %-------------------------------------------------------------------------
81
82 %CONVERSION AND DECLARATIONS%%%%%%%%%%%%%%%%%%%%%%%%%%%%%%%%%%%%%%%%%%%%%%%%
83 %everything in SI
84 Eg = EgeV*e;                      % [J]
85 I0 = I0*1e4;                        %[W/m^2]
86 omega = 2*pi*c/lambda;            % angular frequency
87 N = N*1e6;                        % [m^-3]
88 tau = tauFWHM/sqrt(4*log(2));    % [s, 1/e] in intensity
89
90 dz = L/Nz;
91 z = linspace(0,L,Nz);
92 rrange = 3;                       %range of radius, multiples of w0
93 trange = 3;
94 t = linspace(-trange*tau, trange*tau, Nt);
95 dt = 2*trange*tau/Nt;
96 r = linspace(0,rrange*w0, Nr);
97 dr = rrange*w0/Nr;
98
99 %-------------------------------------------------------------------------
100
101 %CALCULATIONS%%%%%%%%%%%%%%%%%%%%%%%%%%%%%%%%%%%%%%%%%%%%%%%%%%%%%%%%%%%%%%
102 %assumed that the pulse duration is much shorter than the
103 %recombination/relaxation time of the material
104
105 Ne = zeros(length(z),length(r));    %density of electrons ionized
```

```
Iz = zeros(length(I0),length(z));   %peak intesnity wrt z
Nmax = zeros(length(I0),length(z)); %peak Ne wrt z
wmax = zeros(length(I0),1);         %peak ionization rate

Ein = I0*sqrt(pi)*pi*w0^2*tau/2;   %total input energy of the pulse

%create intensity tensor
for ti = 1:length(t)
    for ri = 1:length(r)
        I_normalized(ri, ti) = exp(-t(ti)^2/tau^2)*exp(-2*r(ri)^2/w0^2);
    end
end

for ii = 1:length(I0)
    tic
    ii
    wmax(ii) = 0;


    for mm = 1:length(m)                    % repeat for every different effective mass
        %%%%%%%%%%%%%%%%%%%%%%%%%%%%%%%%%%%%%%%%%%%%%%%%%%%%%%%%%%%%%%%%%%%%%%%%%%%%
        Eabs(mm) = 0;                       % energy absorbed
        Eout(mm) = 0;
        EZ = ones(1,length(z+1));
        EZ(1) = EZ(1)*Ein(ii);
        I=I_normalized*I0(ii);
        for zz = 2:length(z)+ 1


            Iz(ii, zz-1) = max(max(I));        %for plotting and diagnostics
            Nmax(ii,zz-1)= max(Ne(zz-1,:));
            %account for change in intensity due to absorption
            %use the carry over value of I

            for rr = 1:length(r)
                Fabs = 0;                   %flux absorbed

                for tt = 1:length(t)

                    F = sqrt(I(rr,tt)*2/(n0*perm*c));       % peak electric field [V/m]
                    w = 0;
                    gamma = omega*sqrt(m(mm)*Eg)/(e*F); %Keldysh parameter
                    %w = Keldysh_solids_full_function(gamma, F, Eg, m(mm), omega, n0);%ionization rate per
                        unit volume, per unit time
                    w = Keldysh_solids_full_function(gamma, F, Eg, m(mm), omega);%ionization rate per unit
                        volume, per unit time
                    dNe = w*dt;                 %change in electrons absorbed
                    di = Eg*dNe*dz/dt;          %change in intensity
                    Inew = I(rr,tt) - di;

                    if Inew < 0
                        dNe = N - Ne(zz-1,rr);
                        di = I(rr,tt);
                        Inew = 0;
                    end

```

```
                    I(rr,tt) = Inew;
                    Ne(zz-1,rr) = Ne(zz-1,rr) + dNe;     %electron density absorbed
                    Fabs = Fabs + di*dt;

                    %find max ionization rate
                    if w > wmax(ii)
                        wmax(ii) = w;
                    end

                end
                Eabs(mm) = Eabs(mm) + Fabs*2*pi*r(rr)*dr;
            end %end r loop
            EZ(zz) = EZ(1)-Eabs(mm);
        end   % end z loop
            TZ(:,mm) = EZ/Ein(ii);
            Eout(mm) = Ein(ii) - Eabs(mm);
            Trans(mm) = Eout(mm)/Ein(ii);

    end %end m loop

%find the relative modulation depth

    AvgTrans(ii) = mean(Trans);
    depthTrans(ii) = abs(Trans(1) - Trans(2))./AvgTrans(ii)';
    TTrans(ii,:) = Trans;
    AvgT(ii,:) = mean(TZ,2);
    depth(ii,:) = squeeze(TZ(:,1))./squeeze(TZ(:,2));%relative modulation depth
    TT(ii,:,:)=TZ;
toc
end  %end intensity loop

filename=['keldysh_parabolic_2_',num2str(lambda*1E9),'_gamma0.6_MrDependence.mat'];

save(filename)
```

B.2 Keldysh_solids_full_function.m

This is the Kane band equation. You can specify either the full Keldysh, or approximate Keldysh for the tunneling or multi photon regimes.

```
%calculates the ionization rate of electrons for an electromagnetic wave inside a solid.
%Keldysh 1965 eqn (37 - general)

function [w,x] = Keldysh_solids_full_function(Kgamma, F, Eg, m, omega)

%clear all
%%%CONSTANTS%%%%%%%%%%%%%%%%%%%%%%%%%%%%%%%%%%%%%%%%%%%%%%%%%%%%%%%%%%%%%%%%%%%%
hbar = 1.054e-34;               % [J*s]
me = 9.11e-31;                  % electron mass [kg]
perm = 8.85e-12;                % electric permittivity [F/m]
e = 1.6e-19;                    % elementary charge [C]
```

```
c = 3e8;                          % speed of light [m/s]
%n0 = 3.313;                       %index
N = 4.42e28;                      % number density [m^-3]
%-------------------------------------------------------------


full = 1;           % full keldysh?

if full

    Kgammaf = 1/sqrt(1+Kgamma^2);
    Kgammaff = Kgamma/sqrt(1+Kgamma^2);

    C1 = 2*omega*(m*omega/hbar)^1.5/(9*pi);
    %E elliptic integrals of the second kind
    %[K,E] = ellipke(M) ellipic integral of the 1st and second kind

    [K1,E1] = ellipke(Kgammaf^2);
    [K2,E2] = ellipke(Kgammaff^2);

    %input modulus must be squared for this form of elliptic integral
    Egeff = (2*Eg/pi)*(1/Kgammaff)*E1; % effective ionization potential
    x = Egeff/(hbar*omega);
    intbracket = floor(x + 1);

    if F == 0
        w = 0;
    else

        max_iteration = 1e6;
        Q = 0;
        dQ = 0;
        %tic

        n = 0;
        accuracy = 0;
        while n<max_iteration && accuracy ==0

            z = sqrt(pi^2*(2*floor(x+1) - 2*x + n)/(2*K1*E1));
            fun = @(y)exp(y.^2 - z^2);
            phiz = quad(fun, 0, z);                %integrating function for Phi(z)
            %phiz = mfun('dawson',z);

            dQ = exp(-pi*(K2-E2)*n/E1)*phiz;
            Q = Q + dQ;
            n = n+1;

            if dQ/Q < 1e-6
                accuracy = 1;
                %display(['Converged in ', num2str(n), ' steps']);
            end
        end
        Q = Q*sqrt(pi/(2*K1));
        w = C1*(1/Kgammaff)^1.5*Q*exp(-pi*(intbracket/E1)*(K2-E2));
        %toc

```

```
    end
else
    %lambda = 3100nm, GaAs
    if str2double(sprintf('%5.4e',omega)) == 6.0805e+014 && str2double(sprintf('%5.4e',Eg)) == 2.2784e-019
        if Kgamma(i) <= 1                    %tunneling regime
            K = (2/(9*pi^2))*(Eg/hbar)*(m*Eg/hbar^2)^1.5*(e*hbar*F(i)/(m^0.5*Eg^1.5)).^(5/2); %constant
            wexp = exp(-(0.5*pi*m^0.5*Eg^1.5./(e*hbar*F(i))).*(1 - m*omega^2*Eg./(8*e^2*F(i).^2)));
            w = K.*wexp;

        elseif Kgamma(i) > 1.6               %multiphoton regime
            dEg = e^2*F(i).^2/(4*m*omega^2);
            Egbar = Eg + dEg;
            intbracket = floor(Egbar/(hbar*omega) + 1);      %integer bracket in formula

            z = sqrt(2*intbracket - 2*Egbar/(hbar*omega));
            fun = @(y)exp(y.^2 - z^2);                       %integrating function for Phi(z)
            phiz = quad(fun, 0, z);                          %integrate to sove for phi(z)

            K1 = (2*omega/(9*pi))*(m*omega/hbar)^1.5*phiz;
            wexp = exp(2*intbracket.*(1 - dEg/Eg));
            K2 = (dEg/(4*Eg)).^intbracket;
            w = K1.*wexp.*K2;

        else %this is wrong
            slope = -5.5523;
            b =  84.2991;
            w = exp(slope*log(Kgamma(i)) + b);
        end
    else
        display('Need to define ionization rate in Tunneling/MPI intersection');
    end
end

end
```

B.3 Modified_Keldysh_solids_full_function.m

This is the Cosine band equation.

```
%calculates the ionization rate of electrons for an electromagnetic wave inside a solid.
%Gruzdev PRB 2008

function [w,x] = ModifiedKeldysh_solids_full_function( F, Eg, d, m, omega)

%clear all
%%%CONSTANTS%%%%%%%%%%%%%%%%%%%%%%%%%%%%%%%%%%%%%%%%%%%%%%%%%%%%%%%%%%%%%%%
hbar = 1.054e-34;               % [J*s]
me = 9.11e-31;                  % electron mass [kg]
perm = 8.85e-12;                % electric permittivity [F/m]
e = 1.6e-19;                    % elementary charge [C]
c = 3e8;                        % speed of light [m/s]
%n0 = 3.313;                     %index
```

```
N = 4.42e28;                        % number density [m^-3]
%-------------------------------------------------------------


    chi = e*F*d/(hbar*omega);
    uc = 1+m*d^2*Eg/hbar^2;
    u0 = acosh(uc);
    J0 = besselj(0,chi);

    fun = @(xi)cosh(u0*xi)./sqrt(chi^2+u0^2*xi.^2);
    f1 = integral(fun, 0, 1);
    f2 = u0/(uc-1)*f1-sqrt((uc+1)/((uc-1)*(chi^2+u0^2)));

    %input modulus must be squared for this form of elliptic integral
    Egeff = Eg*(1+hbar^2/(m*d^2*Eg)*(1-J0)); % effective ionization potential
    x = Egeff/(hbar*omega);
    intbracket = floor(x + 1);

    C1 = 2*2*omega/(9*pi)*sqrt(omega^3/(hbar*Eg))*m/(d*J0);
    P = exp(-2*(uc-1)/J0*(intbracket-x)*f2);
    R = exp(-2*Eg/(hbar*omega)*uc/(uc-1)*(asinh(u0/chi)-u0/uc*f1));

    C2 = sqrt(sqrt((uc-1)/(uc+1)*(chi^2+u0^2)));

    if F == 0
        w = 0;
    else

        max_iteration = 1e4;
        Q = 0;
        dQ = 0;
        %tic

        n = 0;
        accuracy = 0;
        while n<max_iteration && accuracy ==0

            %z = sqrt(pi^2*(2*floor(x+1) - 2*x + n)/(2*K1*E1));
            z = sqrt(2*(uc-1)/J0*(intbracket-x+n)*sqrt((uc+1)/((uc-1)*(chi^2+u0^2))));
            fun = @(y)exp(y.^2 - z^2);
            phiz = quad(fun, 0, z);                 %integrating function for Phi(z)
            %phiz = mfun('dawson',z);

            dQ = exp(-2*n*f2*(uc-1)/J0)*phiz;
            Q = Q + dQ;
            n = n+1;

            if dQ/Q < 1e-6
                accuracy = 1;
               % display(['Converged in ', num2str(n), ' steps']);
            end
        end
        Q = Q*C2;
        w = C1*P*Q*R;
        %toc

```

```
70          end
71
72
73      end
```

Appendix C

Introduction to the SNLO software

In this appendix I all give a basic introduction to operating the Software for Nonlinear Optics (SNLO). The basic GUI version of this software is open sourced from Arlee Smith at AS-Photonics. I will only go over the aspects of this program that I have personally used, there is much more that you can do with SNLO than I will present here. Specifically, my use is limited to three-wave mixing for standard phase matching (i.e. *not* quasi-phase matching) for femtosecond-picosecond, high pulse energy systems.

I should also mention that SNLO is based on many approximations. Many of these are adequate, such as Gaussian pulses in time, transform limited or linear chirp, etc. while others can be very far from what we have in the laboratory (i.e. gaussian modes in the OPA signal and idler). So, while SNLO is a great way to provide an estimate for your nonlinear optics, you must not try to use it for detailed engineering of a setup. For example, do not use SNLO to choose between a 1 mm thick and a 1.2 mm thick crystal, as your crystal is very sensitive to the peak fluence of your laser.

SNLO is a quick download available from the link above. Once you have it installed, you can locate the icon, as shown in figure C.1a. Afterwards, a panel will show up like the one shown in figure C.1b. This is a list of all the available programs SNLO offers. They are loosely categorized as crystal properties functions ("Ref. Ind." - "GVM"), nonlinear optics propagation ("PW-mix-LP" - "2D-cav-LP"), optics ("Focus" - "Cavity"), and help/exam-

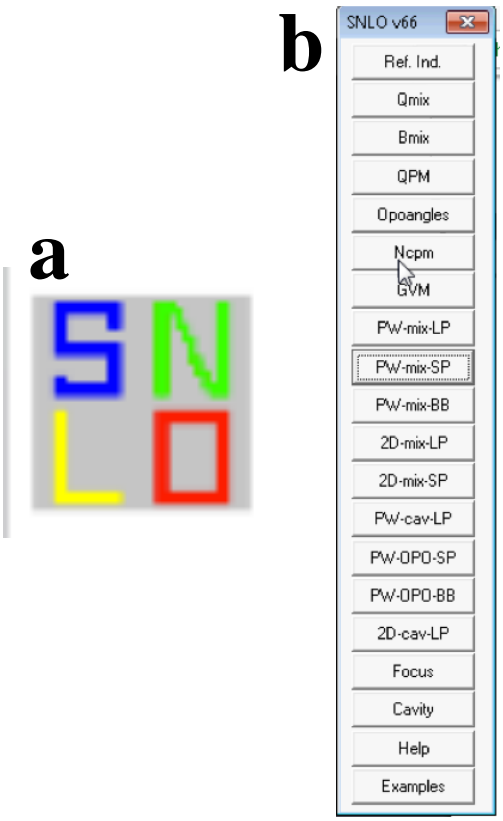

Figure C.1: **a)** The classic SNLO icon. **b)** The start panel for SNLO.

ples.

Let's start with an example. Say we want to run a calculation on our NIR, BBO based OPA. We are pumping with a 30 fs, Ti:Sapph laser (790 nm); and we want to see how well the OPA performs when pumping a 1400 nm signal. We could go and look up all the crystal properties from a website like RefractiveIndex.info, which can be useful under some scenarios. For this calculation, however, you will find it much easier to start with SNLO's "Qmix" program.

So, go ahead and click on "Qmix" (second option down in the SNLO V66), you will see a window open up like the one in figure C.2. The scroll down menu on the top of the panel has a list of crystal options. Select "BBO" from the menu. Before clicking on anything else, you get a chance to see a number of properties of the chosen crystal at a glance. For instance, we can see the transmission profile on a window to the right, as well as the d matrix elements,

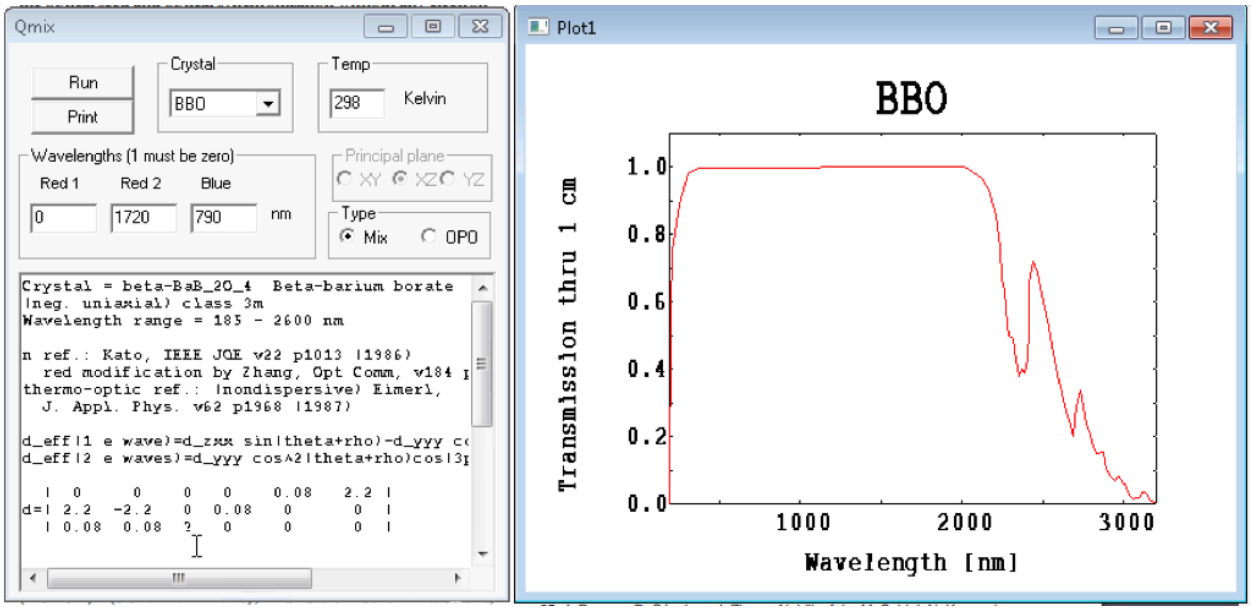

Figure C.2: The Qmix program.

amongst other crystalline properties, and their citations.

The the boxes label "Red 1", "Red 2", and "Blue" are where we enter the wavelengths for the three wave mixing process. Note that SNLO only wants you to give it two of the three wavelengths, they want to calculate the their themselves. You must be able to distinguish which wavelength is the shortest, even if it is not the one you enter. For example, in SHG of a Ti:Sapph, I could enter "Red 1" + "Red 2" = 790 nm, and leave "Blue" as zero. Equivalently, I could enter "Red 1" = 0, "Red 2" = 790 nm, and "Blue" = 395, it will give the exact same results.

In our example, the Ti:Sapph is the shortest wavelength, and will be entered in "Blue", and the signal can be entered in either "Red 1" or "Red 2", it does not matter which. Afterwards, hit the "Run" button, you will get a bunch of options, as shown in figure C.3. These are the crystal parameters for various phase matching conditions that you can choose. For example, in BBO under the given conditions, three phase matching conditions are possible: type I ($\lambda_3^{(o)} + \lambda_2^{(o)} = \lambda_1^{(e)}$), type II ($\lambda_3^{(e)} + \lambda_2^{(o)} = \lambda_1^{(e)}$), and type III ($\lambda_3^{(o)} + \lambda_2^{(e)} = \lambda_1^{(e)}$). In this notation, $\lambda_i^{(n)}$, i denotes the wavelength, with the longest wavelength denoted as a "3" and the shortest as "1", while the polarization is denoted by (n) as either

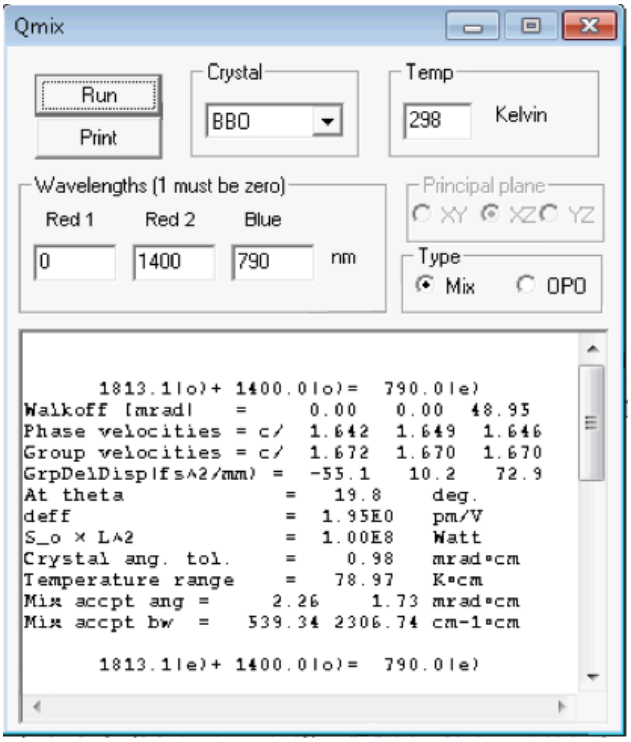

Figure C.3: Qmix results.

along the ordinary (o) or extraordinary (e) axes.

We must choose one of these phase matching conditions. My OPA (HE-TOPAS Prime Plus, see section 4.3) uses type II, so I will use these entries in the next step. Out of all of the nonlinear propagation codes in SNLO, we only need to look at two of them. The first is the "PW-mix-SP", which is short for plane-wave mixing short pulses. It is all in the name, this program is for short ($<$ ns) pulses and uses the plane-wave approximation to run a three wave mixing process. With large diameter beams, the plane-wave approximation is often all we really need, and it can usually run a calculation in just a few seconds.

Open the panel, and you will see something like what is shown in figure C.4. Enter all the data you have from "Qmix", with the phase velocities, group velocities entered as indices, which are just the denominators shown in "Qmix". Enter group delay dispersion as fs^2/mm. Under special conditions, we may be concerned with the higher order nonlinear propagation, such as the Kerr effect and the Beta integral. In this case I will neglect these effects (along with reflectivity's and crystal absorption) and leave the 10 lines in "PW-mix-SP" as zero.

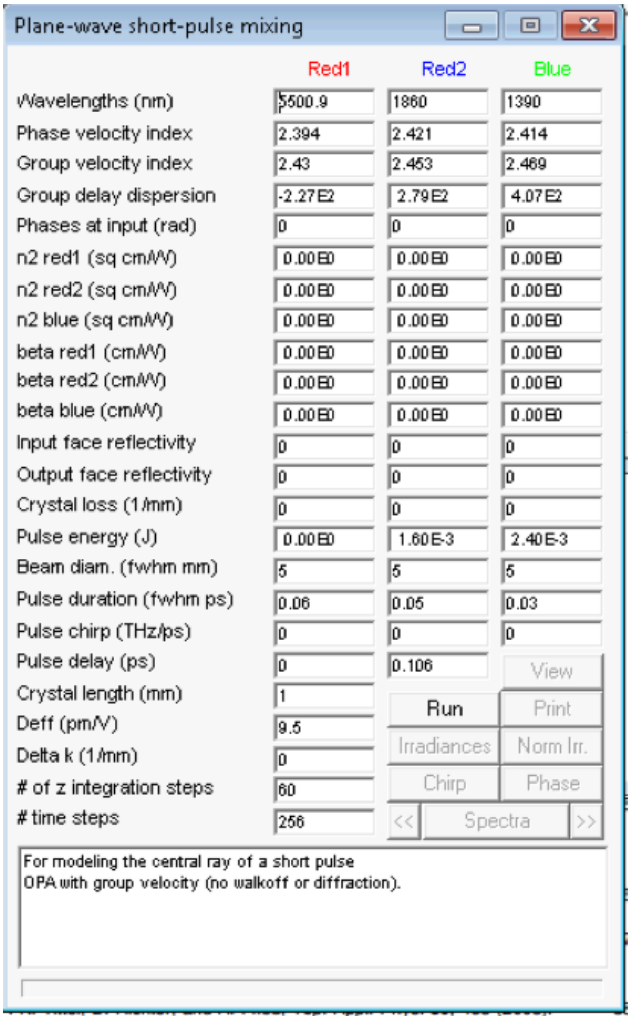

Figure C.4: Start page for PW-mix-SPs.

You are more than welcome to dive into calculations of these to get an idea of when higher peak intensities start to matter. My plan is to simply stay away from this range.

Next, we must consider some initial conditions for the laser. Let's say this is the third stage of the OPA in section 4.3, so that we pump with about 60 μJ at 1400 nm, and 15 mJ at 790 nm (the idler starts with no energy). Let's also say they are approximately 30 fs in duration. The beams are approximately 10 cm in diameter ($1/e^2$), or a FWHM of $\sim$6 mm. Let's also assume no chirp or delay for the moment. The BBO is 1 mm thick, d_{eff} is 1.54 pm/V, and Δk=0, (Because that's what "Qmix" solved everything for).

You can choose alternate numbers for the time steps and z steps, but the default options

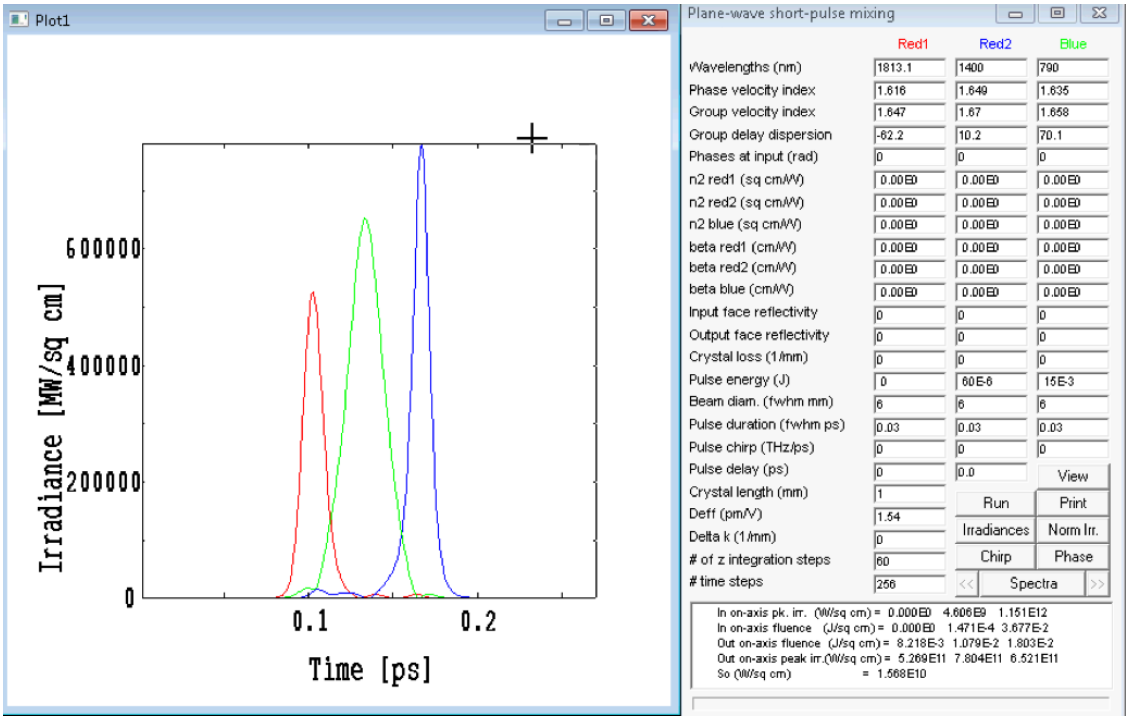

Figure C.5: After running PW-mix-SP.

are usually adequate enough. You can now simply hit the "Run" button and the software will make a calculation. The code propagates the pulses and gives results like those shown in figure C.5. Plot 1, one the left, shows the pulses with their absolute peak intensity, in time. On the bottom of the panel on the right hand side, is the results for the input parameters and the output in both peak intensities and fluence.

From plot 1, we see that the initial delay of 0 actually produces a little walk off between the fields. This is because the group velocities of the three beams cause them to travel at different speeds in the crystal, with the 1400 nm lagging behind the other two. In the lab we would optimize to the maximum extracted pulse energy, and therefore, we would actually introduce a little negative delay (1400 nm comes before 790 nm) to the OPA signal. I played around with this a bit to maximize the peak fluence of the OPA signal.

You can see the results of this in figure C.6. We see that the three beams are closer in time and the pump has undergone fairly significant depletion. To determine the conversion efficiency, we can simply sum up the "Out on-axis fluence" lines on the bottom of the PW-

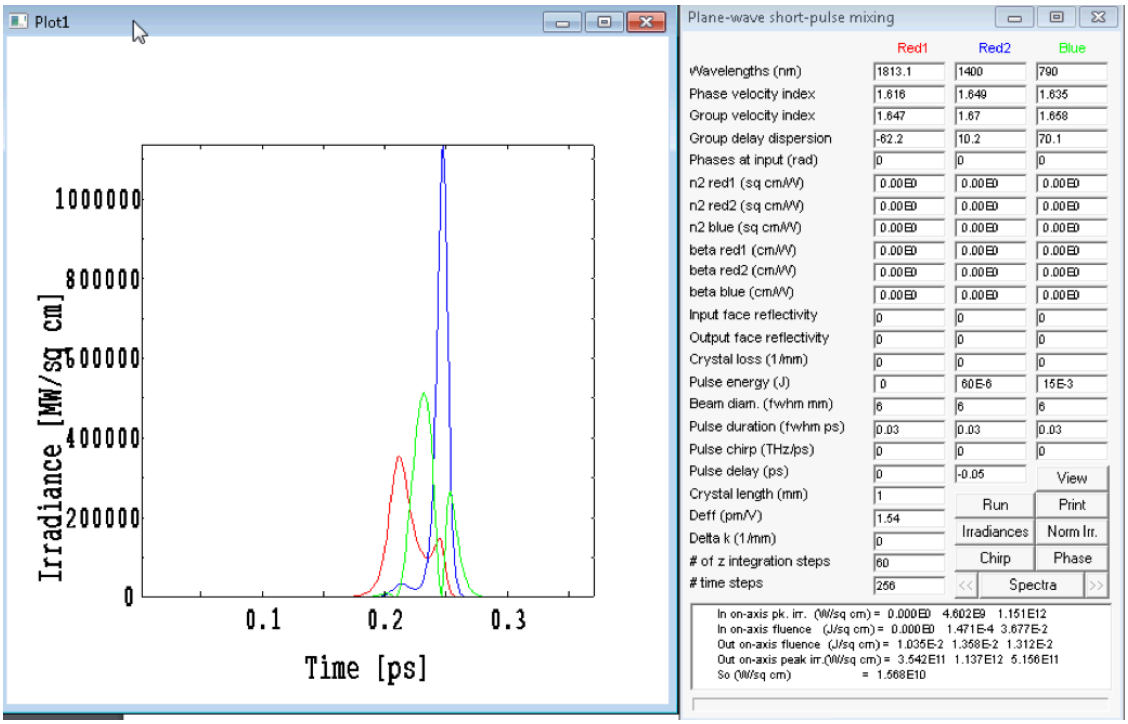

Figure C.6: After running PW-mix-SP with some delay.

mix-SP panel, as they are directly related to the pulse energies, when the three beams are exactly the same diameter. According to this, we get a very optimistic calculation of 5.5 mJ for the 1400 nm and 4.3 mJ for the 1810 nm. This is a combined 65 % efficiency.

Obviously, we cannot expect this to be true, its simply not happening with an OPA of this pulse duration. Let's consider that, in real life, the pump is actually a good amount larger than the 1400 nm. I will keep the FWHM of the signal at 6 mm, but increase the FWHM of the pump to 10 mm. This changes the optimum delay a smidgen, but after doing a simple calculation, shown in figure C.7, to get pulse energy from fluence, we find 2.7 mJ for the signal and 2.1 mJ for the idler, yielding a combined 4.8 mJ, or a conversion efficiency of 32 %. This is remarkably close to the actual values in the lab, and if we wanted to be a little more precise we could expect to get a little closer to the real values.

The final example I will show for SNLO is with the "2D-mix-SP" code. This one is a step more complicated than "PW-mix-SP" as it runs a for two-dimensional propagation of the fields. Because of this, the program is naturally computationally more expensive than

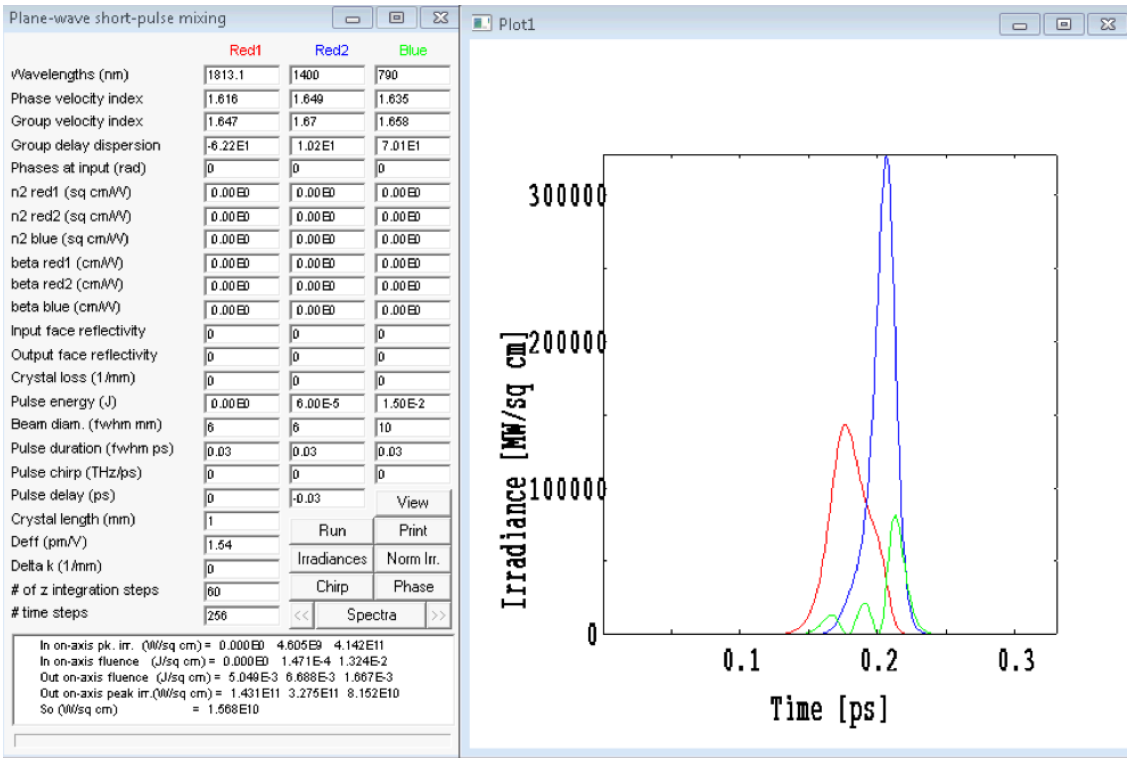

Figure C.7: After running PW-mix-SP with a bigger pump beam diameter and some delay.

"PW-mix-SP". However, even a modern day desktop can expect to run one iteration of this program in ∼1 minute, so it is not necessarily unbearable.

The start panel is shown in figure C.8. To keep things short, I will assume you already read the material from earlier on "PW-mix-SP", so if you are lost, read the rest of the appendix! In addition to the parameters in "PW-mix-SP", the two dimensional code accounts for the walk off angle (given by "Qmix") and needs additional specifications for the grid. A somewhat annoying aspect of SNLO is that the entries are randomly strewn about from one function to the next, and requires some careful searching around to ensure you haven't missed anything. The beam profiles are assumed to be Gaussian unless you specify a super-Gaussian coefficient, which gives the beam a higher order Gaussian profile. You can read through the examples and other SNLO literature to determine how to enter this if you feel you need it.

In addition to the number of z steps and time steps in "PW-mix-SP", we also need to

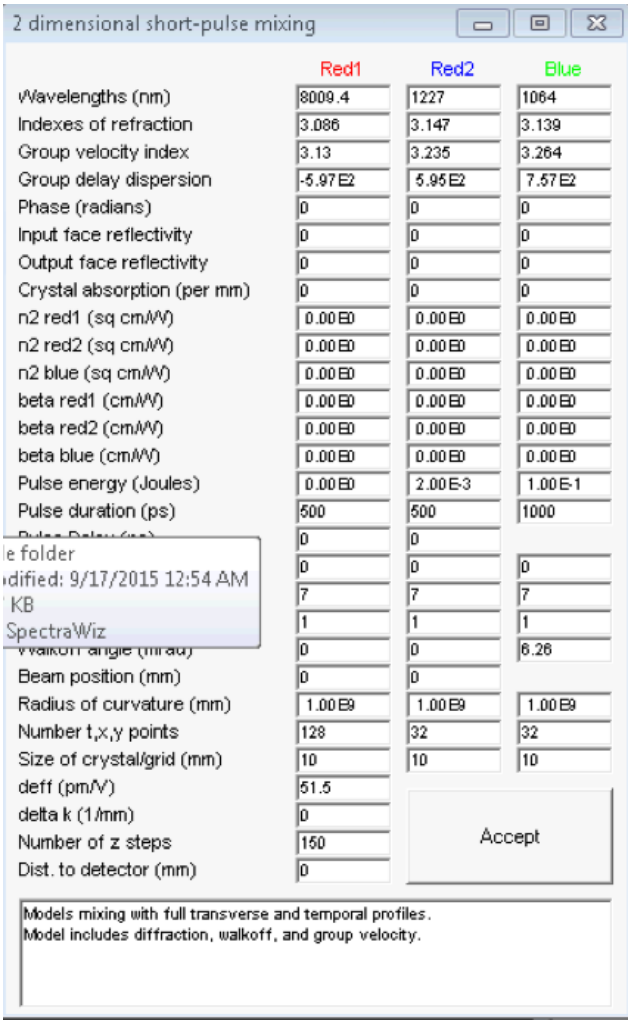

Figure C.8: Start panel for 2D-mix-SP.

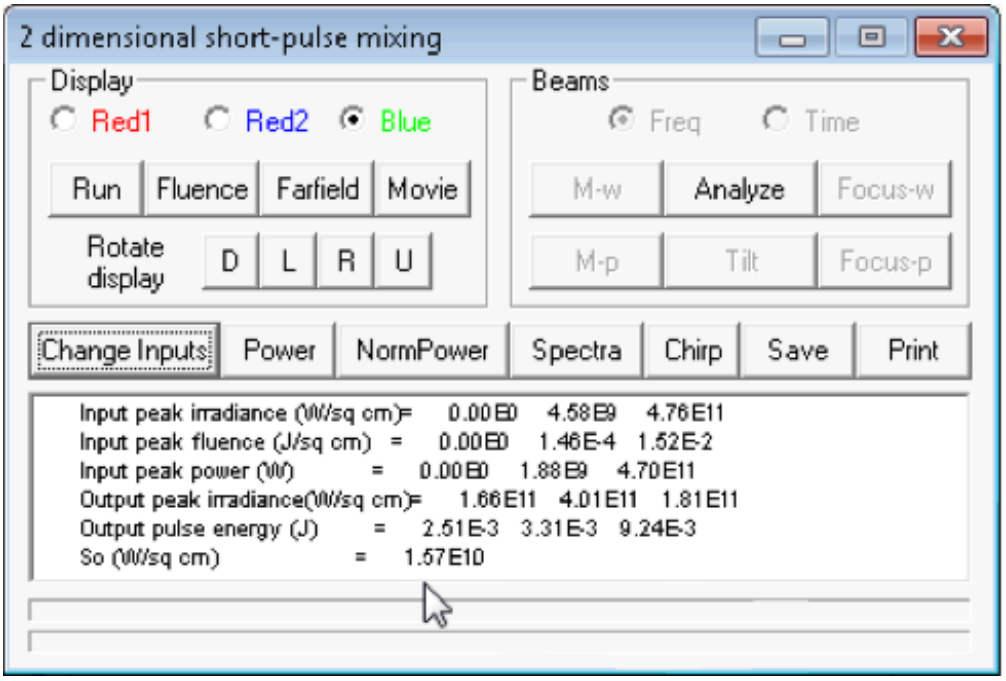

Figure C.9: Run panel for 2D-mix-SP.

specify the x and y points as well. Again, I would just stick with the default values here. You will also want to know the size of the crystal, which should be commensurate with the actual beam diameters so that your x and y grid will accurately represent your beam profile. Finally, you need to accurately determine the beam radius of curvature. If you are working with a focused gaussian beam, this number is something you can calculate using standard Gaussian optics. You can also use the "Focus" program in SNLO, which is fairly self-explanatory. If you are really far from a focus, the radius of curvature is pretty large and the default value of 1 billion millimeters is close enough. Also, if you happen to need to shift your beams to the left or right of one another, you can specify that on the "Beam position" entry. This is rarely needed for our purposes, as walk-off is rarely a concern for us.

Once we have made all the entries we require, we are ready to run the program. Hit the "Accept" button on the bottom right, and you will be taken to a new panel, shown in figure C.9. This panel allows you to run the program and monitor the results as the beams are propagating. The default is to show the fluence profile of the pump beam, but we can also look at this for any field, including the peak intensity in time, spectra, chirp, and so on.

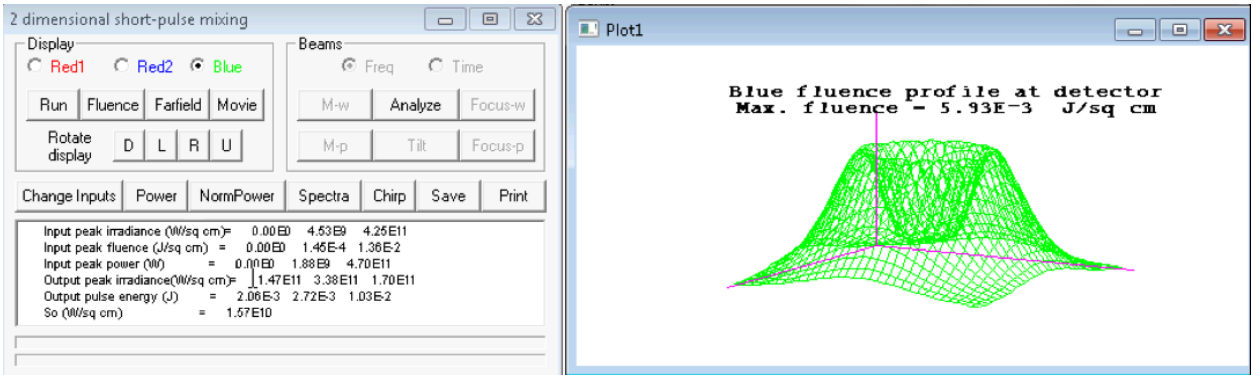

Figure C.10: Results for our example in 2D-mix-SP.

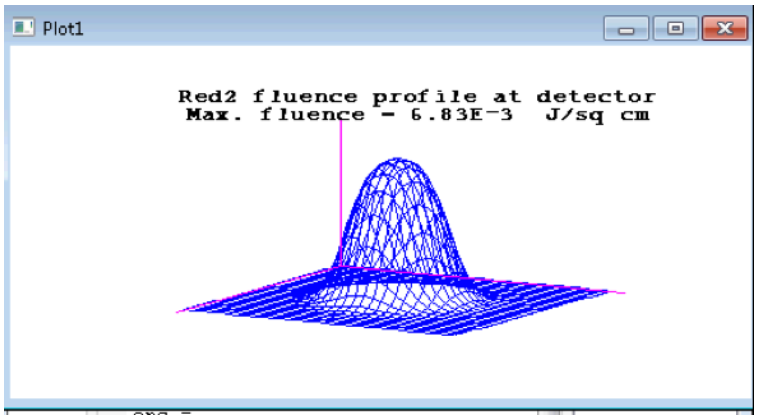

Figure C.11: Results for the signal in our example with 2D-mix-SP.

Figure C.10 shows the results for our example. We see that "2D-mix-SP" gives almost identical results for the pulse energy as compared to "PW-mix-SP". This is not a surprise as the plane-wave approximation is an accurate representation for this example. However, we get some additional insight into the nonlinear optics from this particular program. For instance, we can clearly see the "donut" mode in the pump, while if we switch over to the mode profile of the signal, shown in figure C.11, we find some much closer to a Gaussian beam, just as we observe in the lab.

At this point, you should be ready to start trying out SNLO for yourself! Remember, this is mostly the things that I used SNLO for and if you end up using it a lot, you should expect to run across some new things that I don't show here. In SNLO V66, there are 77 examples provided that covers numerous ways to use the program. Since they are awkward listed in a drop-down menu (why?), take a look at the help menu first. If you are having trouble or a concern about a particular function, you can look it up there, and the example specific to that function are listed at the bottom.

Also, keep in mind that when you run SNLO, it automatically saves .dat files. You can find these files in the same location as where the SNLO program is stored on your computer drive. If you want to save this information and run these files in matlab or origin, you can grab these files and move them to a new location (otherwise, they get overwritten!).

Happy SNLO'ing.

Appendix D

Running FOPA simulations with Matlab SNLO

This appendix will go a step further than appendix C and use the Matlab package for SNLO (mlSNLO). In particular, I will give an overview of how the Matlab package works, and then I will provide the various scripts for FOPA which will double as our examples for running mlSNLO. Keep in mind that there are a lot more things you can do with mlSNLO than what I show here, so please consult the numerous scripts that Jesse Smith has given as examples from mlSNLO.

Ok, so to be completely fair, its been awhile now since I downloaded and installed mlSNLO, so you are going to be on your own there. But its not too difficult to do so I would just go to AS-Photonics and buy it (the current price is only $150, that cheap!). You can also find on the provided link, a list of 8 (sarcastic) reasons why you $SHOULDN'T$ buy mlSNLO, which I like. You will receive a license for the software and you will get a file that installs mlSNO as an app. The app is shown in figure D.1, and in the top bar of Matlab in figure D.1. Once installed, on the top bar of Matlab, you can click on "apps" and it will show up as an icon with the classic SNLO icon.

When you click on the app, the SNLO panel shows up, just like the free software in figure

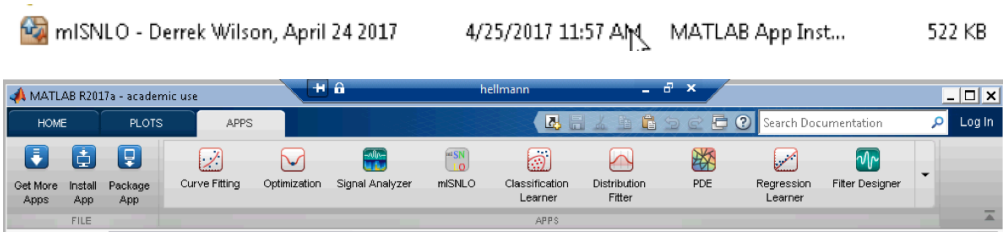

Figure D.1: mlSNLO shows up as an "app" on Matlab 2015 or newer.

```
fcn_handles = snlo_pw_mix_sp_func(problem(K));

run_handle = fcn_handles{1};
accept_handle = fcn_handles{2};
close_handle = fcn_handles{end};
accept_handle();
run_handle();
output = load('pw_mix_sp.dat');
```

Figure D.2: To execute an mlSNLO function, enter the structure with all the inputs into the function, here that structure is called "problem". Next, a series of handles are executed which start the function and run the operation. Afterwards, the data from the operation is collected in the "output" variable.

C.1. In this configuration, you can use mlSNLO exactly the same way that we used the free version. The big difference here is the mlSNLO takes advantage of the nice plotting tools available in Matlab, whereas the free software has cruder plotting tools. At this point, you can reference appendix C to learn more about using this GUI.

The main reason to purchase SNLO, however, is to take advantage of writing scripts that include the functions. Most of the functions available in the free version are available to call in "protected files". You cannot open these files or overwrite them, which has pros and cons, but overall they are fairly simple to work with. To run a function in a script, first, build a structure with all the necessary inputs as sub-elements. Next, you load these inputs into the function, and then run a list of a few commands that execute the function. An example of a line of code performing this for the "PW-mix-SP" function is shown in figure D.2.

Next, I will list out the code for the FOPA in all its details. Just as in regular SNLO, I will loosely divide this into three sections. First, we will initialize the laser parameters, wavelength, energy, pulse duration, etc.

D.1 FROPA_simulator_laser.m

```
clear all
close all

%%%%%%%%%%%%%%%%%%%%%%%%%%%%%%%%%%%%%%%%%%%%%%%%%%%%%%%%%%%%%%%%%%%%%%%%%%%%
%%%%%%%%%%%%%%%%%%%%%%%%%%%%%%%%%%%%%%%%%%%%%%%%%%%%%%%%%%%%%%%%%%%%%%%%%%%%
%Program written for modeling the laser constraints on a FOPA.
%%%%%%%%%%%%%%%%%%%%%%%%%%%%%%%%%%%%%%%%%%%%%%%%%%%%%%%%%%%%%%%%%%%%%%%%%%%%
%Derrek Wilson, February 2018
%%%%%%%%%%%%%%%%%%%%%%%%%%%%%%%%%%%%%%%%%%%%%%%%%%%%%%%%%%%%%%%%%%%%%%%%%%%%
% Place a broadband pulse into a Fourier plane.  The beam is expected to be
% dispersed with some relationship (such as a grating), collimated
% spectrally, and focused on a Fourier plane.
%%%%%%%%%%%%%%%%%%%%%%%%%%%%%%%%%%%%%%%%%%%%%%%%%%%%%%%%%%%%%%%%%%%%%%%%%%%%
%%%%%%%%%%%%%%%%%%%%%%%%%%%%%%%%%%%%%%%%%%%%%%%%%%%%%%%%%%%%%%%%%%%%%%%%%%%%
%This code builds the Fourier Plane, the pulse energy, and the spectral
%density at the FP. It uses Gaussian optics approximations to determine the
%spotsize at the FP for each "beamlet".
%%%%%%%%%%%%%%%%%%%%%%%%%%%%%%%%%%%%%%%%%%%%%%%%%%%%%%%%%%%%%%%%%%%%%%%%%%%%
%%%%%%%%%%%%%%%%%%%%%%%%%%%%%%%%%%%%%%%%%%%%%%%%%%%%%%%%%%%%%%%%%%%%%%%%%%%%

%% Setup the File Path and File names
data_folder = 'J:\Derrek\MatlabCode\FROPA_Model_SNLO\V7';
ExpData_folder = 'J:\Derrek\MatlabCode\FROPA_Model_SNLO\FrancoisandBrunoData';

cd (ExpData_folder)
WAVES = dlmread('Bruno_EmailedData_Gain.txt','\t',[1 0 255 0])/1000;
GAINS = dlmread('Bruno_EmailedData_Gain.txt','\t',[1 3 255 3]);

%Measured FOPA seed spectrum (from Schmidt et. al. Nat Comm (2014))
C = load('Bruno_EmailedData_SeedSpectrum.txt');

cd (data_folder)
%Process FOPA Seed
for i = 1:length(C(:,3));
    if C(i,3) < 0
        Deez(i) = 0;
    else
        Deez(i) = C(i,3);
    end
end

cd('J:\Derrek\MatlabCode\FROPA_Model_SNLO');

Filename ='FOPA_FrancoisandBruno_Simulation_laser.mat';

%% Initialize the FOPA

%spectrum intialization
lamb_p = 0.79; %mum
lamb_min = 1.35; %mum starting FOPA wavelength
lamb_max = 2.3; %mum starting FOPA wavelength
dl = 0.01;%\mum spectrum stepsize
deltl = 0.2; % mum fwhm of spectrum
```

```
54  lambc = 1.825; % mum center wavelenth of spectrum
55  opp = 58000; %mum %desired width of fourier plane
56
57  %crystal parameters
58  t = 4000; %mum crystal thickness
59
60  %grating parameters
61  m = 1;%grating order
62  d = 13.3333;%\mum ruling width on grating
63  B = 3.6*pi/180; %blaze angle
64
65  %focusing element parameters
66  D = 0.5; %cm, width of beam into the grating (beamlet diameter)
67  f = 80; %cm
68
69  %Energy
70  SeedE = 0.000140; %J
71  PumpE = 0.0128; %J
72
73  %Pump Parameters
74  Pump_spotsize = 256; %mum
75  Pump_Tspotsize = 2000; %mum
76  Pump_tau = 2E-12; %s
77
78
79  lambda = lamb_min:dl:lamb_max;%\mum
80  E_lambd = abs(interp1(sortrows(C(:,1)/1000),Deez,lambda));
81
82  c = 3*14; %mum/s
83
84  E_lambds = E_lambd.*2*pi*c./lambda;
85
86  %% Grating Setup
87
88  %grating equation (Littrow configuration)
89  theta = asin(m*lambda./d-sin(B))*180/pi;
90
91  %angular spread off of the grating
92  Dtheta = pi/180*(theta(length(theta))-theta(1));
93
94  %separation of grating and focusing element
95  h = sqrt(opp^2/(2*(1-cos(Dtheta)))); %mum
96
97  %% Beamlet Setup
98
99  %set the gridsize to the shortest wavelength
100 LAMB = lambda(1); %mum
101 w0 = 2*LAMB*f/(pi*D); %mum
102 zr = w0.^2*pi./LAMB; %mum
103 dr = w0/10; %mum
104 dz = zr/150; %mum
105 r = 0:dr:3*w0; %mum
106 z = -0.1*zr:dz:0.1*zr; %mum
107 NN = round(opp/dr); %number of beamlet steps
108
109 %% Beamlet Grid for F.P.
```

```
110
111 Guass = zeros(length(r),length(z));
112 GUASS = zeros(length(r)+length(r)-1,length(z));
113 FourierPlane = zeros(length(r)+NN+length(r)-1,length(z));
114 dthetp = atan(dr/h);%angular step off of grating to give wavelength of next beamlet.
115
116 %beamlet at each dr step
117 ARRAY = 1:1:NN;
118 THETA = theta(1)*pi/180+ARRAY*dthetp;
119 LAMBD = d/m*(sin(THETA)+sin(B));
120
121 %Horizontal position of each beamlet (X=0 is position of LAMBD(1))
122 X = h*(tan(THETA)-tan(theta(1)*pi/180));
123 dX = (X(length(X))-X(1))/numel(X);
124
125 E_lambd_2 = interp1(lambda,E_lambd,LAMBD);
126
127 E_lambd_2(isnan(E_lambd_2)) = 0;
128 %
129 HH = hamming(numel(LAMBD))-min(hamming(numel(LAMBD)));
130
131 E_lambd_2 = E_lambd_2.*HH';
132
133 W0 = 2*LAMBD*f/(pi*D);
134 ZR = W0.^2*pi./LAMBD;
135 %all input beam waist indentical in this version of FOPA
136 W0 = W0(round(NN/2));
137
138 TransversePoints = 64;
139 Gridsize = TransversePoints*dX;
140
141 factor_seed = W0/(sqrt(2/pi)*dX);%Slice integral
142 factor_pump = Pump_spotsize/(sqrt(2/pi)*dX);%Slice integral
143
144 %% Construct beam profile in F.P
145 tic
146 for i = 1:NN
147     RR(i,:) = z.*(1+(ZR(i)./z).^2); %mum
148     BETA = [];
149     Guass(:,:,i) = 1/(sqrt(pi)*W0).*GaussianBeamGenerator_2(r,z,LAMBD(i),W0,ZR(i));
150     GUASS(:,:,i) = vertcat(flipud(Guass(:,:,i)),Guass(2:length(r),:,i));
151
152     BETA = vertcat(zeros(ARRAY(i)-1,length(z)),E_lambd_2(i)*squeeze(GUASS(:,:,i))...
153         ,zeros(ARRAY(length(ARRAY))-ARRAY(i)+1,length(z)));
154     FourierPlane = FourierPlane+BETA;
155 end
156 toc
157     % In this version of the FOPA, all input R.O.C are the same
158     RR(:,isnan(RR)) =10^7; %mum
159     RRstart = RR(round(NN/2),numel(find(z<-t/2))); %m The input radius of curvature
160
161  %% Find Pulse duration at each F.P step
162
163 tic
164 for j = 1:NN
165     for i = 1:NN
```

```
        I_freq_fropa(i,j) = abs(E_lambd_2(i).*exp(-2*((X(i)-X(j))/W0).^2));% equation 8.8 in D.J.W. thesis
    end
time = 0;
pulse = 0;

[time,pulse] = Speck2PulseLamb(sqrt(I_freq_fropa(:,j)'),LAMBD*1000,16);

pulse(isnan(pulse)) =0;

if pulse(round(numel(pulse)/2))==0

tau(j) = 1E-12;

else

tau_init = find(abs(pulse/max(pulse)).^2 > 0.5);

tau(j)=abs(time(tau_init(length(tau_init)))-time(tau_init(1)));

end

end
toc

%input pulse duration will be tau for central wavelenght in this FOPA
%version
tau = tau(round(numel(tau)/2));

%% Setup input pulse energies for each F.P step

FPSpeck = abs(FourierPlane(:,numel(find(z<0))));

array_1 = ones(1,length(X));
PUMP_TProf = exp(-((ARRAY-round(numel(array_1)/2))/Pump_Tspotsize).^8);

%Energy at each F.P. step
Seed_EnergyDensity = SeedE/trapz(FPSpeck(31:length(X)+30,:)).*FPSpeck(31:length(X)+30,:);
Pump_EnergyDensity = PumpE/trapz(PUMP_TProf).*PUMP_TProf;

%Input Energy for SNLO at each F.P. step
Total_SeedEnergy = Seed_EnergyDensity*factor_seed;
Total_PumpEnergy = Pump_EnergyDensity*factor_pump;

%% Save data in work file
cd(data_folder);
save(Filename)
```

D.2 FROPA_simulator_crystal.m

The next section of code constructs the parameters associate with the crystal, such as phase matching angle, phase velocity, group velocity, and group velocity dispersion.

```
%%%%%%%%%%%%%%%%%%%%%%%%%%%%%%%%%%%%%%%%%%%%%%%%%%%%%%%%%%%%%%%%%%%%%%%%%%%%%%%%
```

```
%%%%%%%%%%%%%%%%%%%%%%%%%%%%%%%%%%%%%%%%%%%%%%%%%%%%%%%%%%%%%%%%%%%%%%%%%%%%
%Program written for modeling the constraints on a FOPA for LWIR. The
%program operates the Qmix function in mlSNLO
%%%%%%%%%%%%%%%%%%%%%%%%%%%%%%%%%%%%%%%%%%%%%%%%%%%%%%%%%%%%%%%%%%%%%%%%%%%%
%Derrek Wilson, February 2018
%%%%%%%%%%%%%%%%%%%%%%%%%%%%%%%%%%%%%%%%%%%%%%%%%%%%%%%%%%%%%%%%%%%%%%%%%%%%
% This program sets up the problem parameters for the 2d short-pulse mixing function
% 2D-MIX-SP, call the SNLO 2D-MIX-SP function with the parameters.  In
% particular, we need to calculate the phase matching for all wavelengths
% used in the FOPA.  This code will employ a bandwidth for a given
%number of crystals and assume a phase mismatch for all but the center
%wavelength.
%%%%%%%%%%%%%%%%%%%%%%%%%%%%%%%%%%%%%%%%%%%%%%%%%%%%%%%%%%%%%%%%%%%%%%%%%%%%
%%%%%%%%%%%%%%%%%%%%%%%%%%%%%%%%%%%%%%%%%%%%%%%%%%%%%%%%%%%%%%%%%%%%%%%%%%%%
%%%%%%%%%%%%%%%%%%%%%%%%%%%%%%%%%%%%%%%%%%%%%%%%%%%%%%%%%%%%%%%%%%%%%%%%%%%%
%We will use four BBO's in this calculation
%%%%%%%%%%%%%%%%%%%%%%%%%%%%%%%%%%%%%%%%%%%%%%%%%%%%%%%%%%%%%%%%%%%%%%%%%%%%
clear all
close all

%% Setup the File Path and File names

Main_folder = 'J:\Derrek\MatlabCode\FROPA_Model_SNLO';
SNLO_folder = 'J:\Derrek\MatlabCode\FROPA_Model_SNLO\SNLO';
data_folder = 'J:\Derrek\MatlabCode\FROPA_Model_SNLO\V5';

load('FOPA_FrancoisandBruno_Simulation_laser.mat')

%% Initialize the crystal parameters

C = 2.99792E17; %nm/s
c = 2.99792E14; %mum/s

Nc = 4; %number of crystals in FOPA
BW = (lamb_max-lamb_min)*1000; %BW of seed entering FOPA
BW_per_c = BW/Nc; %BW per crystal
delt=2*pi*C*2E-6;%rad/s
nf = 5001; %points for the derivatives made later one
LAMBP = lamb_p*1000; %pump wavelength (nm)
freq_p = 2*pi*C./LAMBP; %pump frequency (rad/s)
Freq_p = linspace(0.8*freq_p,1.2*freq_p,nf);% pump array for derivatives (rad/s)

cd(Main_folder)

[GV_or_p,N_or_p] = NOD_BBO_no(Freq_p,1); %Refractive indices for pump (ordinary axis)
[GV_ex_p,N_ex_p] = NOD_BBO_ne(Freq_p,1); %Refractive indices for pump (extraordinary axis)


%% Calculate central wavelengths on each crystal and find phase matching angle with Qmix

cd(SNLO_folder)

for i=1:Nc

centerwave(i) = lamb_min*1000+BW_per_c/2+BW_per_c*(i-1); %central wavelength for each crystal
edgewave(i) = lamb_min*1000+BW_per_c*i; %edgewavelength between crystals
```

```
58
59  qmix_crystal_list = importdata('crystal_list.txt');
60  inputs.qmix_wavelength_red1 = 0;
61  inputs.qmix_wavelength_red2 = centerwave(i);
62  inputs.qmix_wavelength_blue = lamb_p*1000;
63  inputs.qmix_temperature = 298;
64  inputs.currentCrystalPopupName = 'BBO';
65  inputs.qmix_selected_crystal = find_selection_number_from_string(qmix_crystal_list...
66      ,inputs.currentCrystalPopupName); % find the crystal you specified
67  inputs.qmix_type = 'Mix';
68  handles = snlo_qmix_func(inputs);
69   run_fcn = handles{1};   % the function handle of the 'Run' button r
70   run_fcn();                  % call the 'Run' button callback - equivalent to clicking the run button
71   outputs = importdata('Qmix.dat'); %load Qmix file with outputs
72
73  walkoff_t1(i,:) = outputs.data(1,:);  %mrad
74  phase_vel_1(i,:) = outputs.data(2,:); % phase velocity (c/frac)
75  group_vel_1(i,:) = outputs.data(3,:); % group velocity (c/frac)
76  GDD_1(i,:) = outputs.data(4,:); % GDD
77  theta_crystal (i) = outputs.data(5,1)*pi/180; %theta (rad)
78  inputs = [];
79
80  end
81
82  %% Calculate the values of v_phase v_group, and GVD at each FP position.
83
84  %% This is Type I phase matching, so only the pump has a component along n_e
85
86  cd(Main_folder)
87
88  for i=1:length(LAMBD)
89     i
90      freq_s(i) = 2*pi*C./(LAMBD(i)*1000);
91      Freq_s(:,i)=linspace(0.95*freq_s(i),1.05*freq_s(i),nf);
92      [GV_ex_s,N_or_s(:,i)] = NOD_BBO_no(Freq_s(:,i)',1);
93      GV_s(:,i) = GV_(Freq_s(:,i),N_or_s(:,i),1);
94      GVD_s(:,i) = GV_(Freq_s(:,i),N_or_s(:,i),2);
95      VP_S(i) = N_or_s(round(length(N_or_s(:,i))/2),i);
96      GV_S(i) = C*GV_s(round(length(GV_s(:,i))/2),i);
97      GVD_S(i) = GVD_s(round(length(GVD_s(:,i))/2),i)*10^36;
98
99      freq_i(i) = freq_p-freq_s(i);
100     Freq_i(:,i)=linspace(0.95*freq_i(i),1.05*freq_i(i),nf);
101     [GV_ex_i,N_or_i(:,i)] = NOD_BBO_no(Freq_i(:,i)',1);
102     GV_i(:,i) = GV_(Freq_i(:,i),N_or_i(:,i),1);
103     GVD_i(:,i) = GV_(Freq_i(:,i),N_or_i(:,i),2);
104     VP_I(i) = N_or_i(round(length(N_or_i(:,i))/2),i);
105     GV_I(i) = C*GV_i(round(length(GV_i(:,i))/2),i);
106     GVD_I(i) = GVD_i(round(length(GVD_i(:,i))/2),i)*10^36;
107
108          %Pump changes with each crystal, we must change theta depending
109          %on what crystal
110
111          if LAMBD(i) < edgewave(1)/1000
112
```

```
113             N_ex_P(:,i) = sqrt(1./((sin(theta_crystal(1))./N_ex_p).^2+(cos(theta_crystal(1))./N_or_p).^2))
                    ;
114             GV_p(:,i) = GV_(Freq_p',N_ex_P(:,i),1);
115             GVD_p(:,i) = GV_(Freq_p',N_ex_P(:,i),2);
116             VP_P(i) = N_ex_P(round(nf/2+1),i);
117             GV_P(i) = C*GV_p(round(nf/2+1),i);
118             GVD_P(i) = GVD_p(round(nf/2+1),i)*10^36;
119
120         elseif LAMBD(i) < edgewave(2)/1000
121
122             N_ex_P(:,i) = sqrt(1./((sin(theta_crystal(2))./N_ex_p).^2+(cos(theta_crystal(2))./N_or_p).^2))
                    ;
123             GV_p(:,i) = GV_(Freq_p',N_ex_P(:,i),1);
124             GVD_p(:,i) = GV_(Freq_p',N_ex_P(:,i),2);
125             VP_P(i) = N_ex_P(round(nf/2+1),i);
126             GV_P(i) = C*GV_p(round(nf/2+1),i);
127             GVD_P(i) = GVD_p(round(nf/2+1),i)*10^36;
128
129         elseif LAMBD(i) < edgewave(3)/1000
130
131             N_ex_P(:,i) = sqrt(1./((sin(theta_crystal(3))./N_ex_p).^2+(cos(theta_crystal(3))./N_or_p).^2))
                    ;
132             GV_p(:,i) = GV_(Freq_p',N_ex_P(:,i),1);
133             GVD_p(:,i) = GV_(Freq_p',N_ex_P(:,i),2);
134             VP_P(i) = N_ex_P(round(nf/2+1),i);
135             GV_P(i) = C*GV_p(round(nf/2+1),i);
136             GVD_P(i) = GVD_p(round(nf/2+1),i)*10^36;
137
138         else
139
140             N_ex_P(:,i) = sqrt(1./((sin(theta_crystal(4))./N_ex_p).^2+(cos(theta_crystal(4))./N_or_p).^2))
                    ;
141             GV_p(:,i) = GV_(Freq_p',N_ex_P(:,i),1);
142             GVD_p(:,i) = GV_(Freq_p',N_ex_P(:,i),2);
143             VP_P(i) = N_ex_P(round(nf/2+1),i);
144             GV_P(i) = C*GV_p(round(nf/2+1),i);
145             GVD_P(i) = GVD_p(round(nf/2+1),i)*10^36;
146         end
147
148 end
149
150 %% K vectors mismatch
151
152 K_S = freq_s/C.*VP_S*10^6;
153 K_I = freq_i/C.*VP_I*10^6;
154 K_P = freq_p/C.*VP_P*10^6;
155
156 DeltK = K_P-K_S-K_I;
157
158 cd(data_folder)
159 save('FOPA_FrancoisandBruno_Simulation_crystal.mat','walkoff_t1','VP_S','VP_I','VP_P','GV_S'...
160     ,'GV_I','GV_P','GVD_S','GVD_I','GVD_P','theta_crystal','DeltK')
```

D.3 FROPA_IC_Francois_pw.m

The initial conditions for inputs not being looped over in the PW-mix-SP function.

```
input.pw_mix_sp_wavelengths = [1064,1064,532];  % wavelengths (in nm)
input.pw_mix_sp_ref_inds = [1.654,1.654,1.654]; % refractive indices
input.pw_mix_sp_gvi = [1.60,1.60,1.61];         % group velocity indices
input.pw_mix_sp_gdd = [0,0,0];                  % group delay dispersion (in fs^2/mm)
input.pw_mix_sp_phases = [0,0,0];               % input phases (in radians)
input.pw_mix_sp_n2_red1 = [0,0,0];              % nonlinear refractive indices from red1 wave (in cm
    ^2/W)
input.pw_mix_sp_n2_red2 = [0,0,0];              % nonlinear refractive indices from red2 wave (in cm
    ^2/W)
input.pw_mix_sp_n2_blue = [0,0,0];              % nonlinear refractive indices from blue wave (in cm
    ^2/W)
input.pw_mix_sp_beta_red1 = [0,0,0];            % two-photon absorptions from red1 wave (in cm/W)
input.pw_mix_sp_beta_red2 = [0,0,0];            % two-photon absorptions from red2 wave (in cm/W)
input.pw_mix_sp_beta_blue = [0,0,0];            % two-photon absorptions from blue wave (in cm/W)
input.pw_mix_sp_input_refl = [0,0,0];           % input face power reflectivity coefficient (0-1)
input.pw_mix_sp_output_refl = [0,0,0];          % output face power reflectivity coefficient (0-1)
input.pw_mix_sp_crystal_losses = [0,0,0];       % linear crystal absorption (in 1/mm)
input.pw_mix_sp_pulseenergy = [1e-8,1e-8,0];    % input pulse energies (in J)
input.pw_mix_sp_beam_diameters = [4,4,4];       % beam diameters (in fwhm mm)
input.pw_mix_sp_pulse_durations = [0.05,0.05,0.05;1,1,1].'; % input pulse durations (in fwhm ps); and
    temporal supergaussian coefficient (1-10) or 0 for hyperbolic secant shape
input.pw_mix_sp_pulse_chirp = [0,0,100];          % linear chirps of the input pulses (in THz/ps)
input.pw_mix_sp_pulse_delay = [0,0];            % pulse delays relative to pump (in ps)
input.pw_mix_sp_crystal_length = 10;            % nonlinear crystal length (in mm)
input.pw_mix_sp_deff = 1.95;                       % crystal nonlinear coefficient (in pm/V)
input.pw_mix_sp_deltak = 0;                     % phase mismatch (in rad/mm)
input.pw_mix_sp_nz = 100;                       % number of z points
input.pw_mix_sp_nt = 512;                       % number of time points
```

D.4 FROPA_IC_Francois_2dsp.m

The initial conditions for inputs not being looped over in the 2D-mix-SP function.

```
inputs.mix_2d_sp_wavelengths = [1550,1550,775];
inputs.mix_2d_sp_ref_inds = [2.142,2.142,2.184];
inputs.mix_2d_sp_gvi = [2.1875,2.1875,2.2811];
inputs.mix_2d_sp_gdd = [1.04e2,1.04e2,3.99e2];
inputs.mix_2d_sp_phase = [0,0,0];
inputs.mix_2d_sp_input_refl = [0,0,0];
inputs.mix_2d_sp_output_refl = [0,0,0];
inputs.mix_2d_sp_crystal_losses = [0,0,0];
inputs.mix_2d_sp_n2_red1 = [0,0,0];
inputs.mix_2d_sp_n2_red2 = [0,0,0];
inputs.mix_2d_sp_n2_blue = [0,0,0];
inputs.mix_2d_sp_beta_red1 = [0,0,0];
inputs.mix_2d_sp_beta_red2 = [0,0,0];
inputs.mix_2d_sp_beta_blue = [0,0,0];
inputs.mix_2d_sp_pulseenergy = [5e-8,5e-8,0];
```

```
inputs.mix_2d_sp_pulse_durations = [0.1,0.1,0.1;1,1,1].'; %ps
inputs.mix_2d_sp_pulse_delays = [0,0];
inputs.mix_2d_sp_pulse_chirps = [0,0,0];
inputs.mix_2d_sp_beam_diameters = [1,1,1]';%[beam_size,beam_size,beam_size].';
inputs.mix_2d_sp_supergaussian_coeff = [1,1,1];
inputs.mix_2d_sp_wo_angles = [0,0,0];
inputs.mix_2d_sp_offset_wodir = [0,0];
power = 8;
inputs.mix_2d_sp_rad_curv = [1.7*10^power,1.7*10^power,1.7*10^power,1.7*10^power,1.7*10^power,1.7*10^power].';
inputs.mix_2d_sp_nt= 128;
inputs.mix_2d_sp_nxny = [32,32];
inputs.mix_2d_sp_crystal_length = t/1000;
inputs.mix_2d_sp_lx_ly = [5,5];
inputs.mix_2d_sp_deff = 1.95;
inputs.mix_2d_sp_deltak = 0;
inputs.mix_2d_sp_nz = 32;
inputs.mix_2d_sp_dist_to_image = 0;
```

D.5 FROPA_simulator_pwPropagator.m

This section of the code runs the mlSNLO simulation that determines the spectral gain across the FP using the PW-mix-SP function.

```
clear all
close all
%%%%%%%%%%%%%%%%%%%%%%%%%%%%%%%%%%%%%%%%%%%%%%%%%%%%%%%%%%%%%%%%%%%%%%%%%%%%%
%%%%%%%%%%%%%%%%%%%%%%%%%%%%%%%%%%%%%%%%%%%%%%%%%%%%%%%%%%%%%%%%%%%%%%%%%%%%%
%Program written for modeling the constraints on a FOPA for LWIR. The
%program operates several function in mlSNLO
%%%%%%%%%%%%%%%%%%%%%%%%%%%%%%%%%%%%%%%%%%%%%%%%%%%%%%%%%%%%%%%%%%%%%%%%%%%%%
%Derrek Wilson, February 2018
%%%%%%%%%%%%%%%%%%%%%%%%%%%%%%%%%%%%%%%%%%%%%%%%%%%%%%%%%%%%%%%%%%%%%%%%%%%%%
% This program runs the pw_mix_sp function from mlSNLO. We assume that
% each step contains a thin "slice" of the FP in the FOPA. We extract
% a total pulse energy from each step and pull out the thin slice at
% and use this to determine the total pulse energy.
%%%%%%%%%%%%%%%%%%%%%%%%%%%%%%%%%%%%%%%%%%%%%%%%%%%%%%%%%%%%%%%%%%%%%%%%%%%%%
%%%%%%%%%%%%%%%%%%%%%%%%%%%%%%%%%%%%%%%%%%%%%%%%%%%%%%%%%%%%%%%%%%%%%%%%%%%%%

load('FOPA_FrancoisandBruno_Simulation_laser.mat')
load('FOPA_FrancoisandBruno_Simulation_crystal.mat')

FROPA_IC_Francois_pw

Main_folder = 'J:\Derrek\MatlabCode\FROPA_Model_SNLO';
SNLO_folder = 'J:\Derrek\MatlabCode\FROPA_Model_SNLO\SNLO';
ExpData_folder = 'J:\Derrek\MatlabCode\FROPA_Model_SNLO\FrancoisandBrunoData';

cd (ExpData_folder)
A = load('FrancoisData_Gain.txt');
```

```
28      GAIN = load('Bruno_EmailedData_AmplifiedSeedSpectrum_Pump12.8mJ.txt');
29      SEED = load('Bruno_EmailedData_SeedSpectrum.txt');
30
31      seed_wavelength = 1./(1/lamb_p-1./LAMBD); %(m)
32
33      cd (Main_folder)
34
35      FWHMcoeff = sqrt(2*log(2));
36      %% call pw mix sp, run model, load output
37      clear problem
38      factor = 20;
39      cd(SNLO_folder)
40      output = cell(size(LAMBD));
41
42      for alpha = 1:floor(length(LAMBD)/factor)
43
44          K = alpha*factor
45          problem(K) = input;
46
47          problem(K).pw_mix_sp_wavelengths = [seed_wavelength(K)*10^3,LAMBD(K)*10^3,lamb_p*10^3]; %
                wavelengths (in nm)
48          problem(K).pw_mix_sp_ref_inds = [VP_I(K),VP_S(K),VP_P(K)]; % refractive indices
49          problem(K).pw_mix_sp_gvi = [GV_I(K),GV_S(K),GV_P(K)];          % group velocity indices
50          problem(K).pw_mix_sp_gdd = [GVD_I(K),GVD_S(K),GVD_P(K)];                % group delay dispersion
                (in fs^2/mm)
51          problem(K).pw_mix_sp_pulseenergy = [0,Total_SeedEnergy(K),Total_PumpEnergy(K)];    % input pulse
                energies (in J)
52          problem(K).pw_mix_sp_beam_diameters = [W0/1000*FWHMcoeff,W0/1000*FWHMcoeff,Pump_spotsize/1000*
                FWHMcoeff;...
53              0.5,0.5,0.5].';        % beam diameters (in fwhm mm)
54          problem(K).pw_mix_sp_pulse_durations = [tau*10^12, tau*10^12, Pump_tau*10^12; 1,1,1]';% input
                pulse durations
55              %(in fwhm ps); and temporal supergaussian coefficient (1-10) or 0 for hyperbolic secant shape
56          problem(K).pw_mix_sp_crystal_length = t/1000;            % nonlinear crystal length (in mm)
57          problem(K).pw_mix_sp_deltak = DeltK(K);                     % phase mismatch (in rad/mm)
58
59          fcn_handles = snlo_pw_mix_sp_func(problem(K));
60
61          run_handle = fcn_handles{1};
62          accept_handle = fcn_handles{2};
63          close_handle = fcn_handles{end};
64          accept_handle();
65          run_handle();
66          output = load('pw_mix_sp.dat');
67
68        red1_energies(alpha) = trapz(output(:,1),output(:,2))*1e-12*pi/(2*FWHMcoeff)*Pump_spotsize^2/
              factor_seed;
69        red2_energies(alpha) = trapz(output(:,1),output(:,3))*1e-12*pi/(2*FWHMcoeff)*Pump_spotsize^2/
              factor_seed;
70        blue_energies(alpha) = trapz(output(:,1),output(:,4))*1e-12*pi/(2*FWHMcoeff)*Pump_spotsize^2/
              factor_pump;
71
72        gain(alpha) = red2_energies(alpha)/Seed_EnergyDensity(K);
73        Wave(alpha) = LAMBD(K);
74        SpeckIn(alpha) = Seed_EnergyDensity(K);
75        SpeckOut(alpha) = red2_energies(alpha);
```

```
        output = [];
    end
cd(Main_folder)

GG = GAIN(:,2)./SEED(:,2);
```

D.6 FROPA_simulator_2DPropagator.m

This section of the code runs the mlSNLO simulation that determines the spectral gain across the FP using the 2D-mix-SP function.

```
    clear all
    close all

    %%%%%%%%%%%%%%%%%%%%%%%%%%%%%%%%%%%%%%%%%%%%%%%%%%%%%%%%%%%%%%%%%%%%%%%%%%%%
    %%%%%%%%%%%%%%%%%%%%%%%%%%%%%%%%%%%%%%%%%%%%%%%%%%%%%%%%%%%%%%%%%%%%%%%%%%%%
    %Program written for modeling the constraints on a FOPA for LWIR. The
    %program operates several function in mlSNLO
    %%%%%%%%%%%%%%%%%%%%%%%%%%%%%%%%%%%%%%%%%%%%%%%%%%%%%%%%%%%%%%%%%%%%%%%%%%%%
    %Derrek Wilson, February 2018
    %%%%%%%%%%%%%%%%%%%%%%%%%%%%%%%%%%%%%%%%%%%%%%%%%%%%%%%%%%%%%%%%%%%%%%%%%%%%
    % This program runs the 2d_mix_sp function from mlSNLO.  We assume that
    % each step contains a thin "slice" of the FP in the FOPA.  We extract
    % a total pulse energy from each step and pull out the thin slice at
    % and use this to determine the total pulse energy.
    %%%%%%%%%%%%%%%%%%%%%%%%%%%%%%%%%%%%%%%%%%%%%%%%%%%%%%%%%%%%%%%%%%%%%%%%%%%%
    %%%%%%%%%%%%%%%%%%%%%%%%%%%%%%%%%%%%%%%%%%%%%%%%%%%%%%%%%%%%%%%%%%%%%%%%%%%%

    load('FOPA_FrancoisandBruno_Simulation_laser.mat')
    load('FOPA_FrancoisandBruno_Simulation_crystal.mat')

    data_folder = 'J:\Derrek\MatlabCode\FROPA_Model_SNLO\V6';
    SNLO_folder = 'J:\Derrek\MatlabCode\FROPA_Model_SNLO\SNLO';
    ExpData_folder = 'J:\Derrek\MatlabCode\FROPA_Model_SNLO\FrancoisandBrunoData';

    seed_wavelength = 1./(1/lamb_p-1./LAMBD); %(m)

    FROPA_IC_Francois_2dsp
    FWHMcoeff = sqrt(2*log(2));
    %% call 2d mix sp, run model, load output
    clear problem
    factor = 20;
    cd(SNLO_folder)
    output = cell(size(LAMBD));

    for alpha = 1:floor(length(LAMBD)/factor)

        K = alpha*factor
        problem(K) = inputs;
        problem(K).mix_2d_sp_wavelengths = [seed_wavelength(K)*10^3,LAMBD(K)*10^3,lamb_p*10^3];
        problem(K).mix_2d_sp_ref_inds = [VP_I(K),VP_S(K),VP_P(K)];
```

```
        problem(K).mix_2d_sp_gvi = [GV_I(K),GV_S(K),GV_P(K)];
        problem(K).mix_2d_sp_gdd = [GVD_I(K),GVD_S(K),GVD_P(K)];
        problem(K).mix_2d_sp_pulseenergy = [0,Total_SeedEnergy(K),Total_PumpEnergy(K)];
        problem(K).mix_2d_sp_pulse_durations = [tau*10^12, tau*10^12, Pump_tau*10^12; 1,1,1]';
        problem(K).mix_2d_sp_beam_diameters = [W0/1000*FWHMcoeff,W0/1000*FWHMcoeff,Pump_spotsize/1000*
            FWHMcoeff;...
            0.5,0.5,0.5].';
        %problem(K).mix_2d_sp_supergaussian_coeff = [1,1,2];
        problem(K).mix_2d_sp_rad_curv = [RRstart/1000,RRstart/1000,RRstart/1000;RRstart/1000,RRstart
            /1000,...
            RRstart/1000].';
        problem(K).mix_2d_sp_nxny = [TransversePoints,TransversePoints];
        problem(K).mix_2d_sp_lx_ly = [Gridsize/1000,Gridsize/1000];
        problem(K).mix_2d_sp_deltak = DeltK(K);
        fcn_handles = snlo_2d_mix_sp_func(problem(K));

        run_handle = fcn_handles{1};
        accept_handle = fcn_handles{2};
        close_handle = fcn_handles{end};
        accept_handle();
        run_handle();
        output = load('mix_2d_sp_output.mat');

      red1_energies(alpha) = trapz(output.power(:,1),output.power(:,2))/factor_pump;
      red2_energies(alpha) = trapz(output.power(:,1),output.power(:,3))/factor_pump;
      blue_energies(alpha) = trapz(output.power(:,1),output.power(:,4))/factor_pump;

      gain(alpha) = red2_energies(alpha)/Seed_EnergyDensity(K);
      Wave(alpha) = LAMBD(K);
      SpeckIn(alpha) = Seed_EnergyDensity(K);
      SpeckOut(alpha) = red2_energies(alpha);
        output = [];
    end
cd(data_folder)

SeedEnergy = sum(red2_energies)*factor
TotalEnergy = (sum(red1_energies)+sum(red2_energies)+sum(blue_energies))*factor
```

D.7 NOD_BBO_no.m

Run in **FROPA_simulator_crystal.m** for the ordinary refractive indices.

```
function [GVD,nr]=NOD_BBO_no(Omega,N)
%%%%%%%%%%%%%%%%%%%%%%%%%%%%%%%%%%%%%%%%%%%%%%%%%%%%%%%%%%%%
%Written by Derrek Wilson May 2015
%For generating the refractive index based on the Sellmeier Equations
%Omega is linearly spaced
%Data from: Zhang, et. al. Optic. Comm. 184, 485,(2000) 0.64-3.18 mum
%%%%%%%%%%%%%%%%%%%%%%%%%%%%%%%%%%%%%%%%%%%%%%%%%%%%%%%%%%%%
n=numel(Omega);
%Sellmeir Coefficients
c=3*10^14; %mu/s
```

```
coeff01=2.7359;
coeff11=0.01878;
coeff12=0.01822;
coeff21=0.01471;
coeff31=0.0006081;
coeff41=0.00006740;

%refractive Index
n0=coeff01;
n1=coeff11./((2*pi*c./Omega).^2-coeff12);
n2=-coeff21*(2*pi*c./Omega).^2;
n3=coeff31*(2*pi*c./Omega).^4;
n4=-coeff41*(2*pi*c./Omega).^6;
nr=sqrt(n0+n1+n2+n3+n4);
Vp=c./nr; % Phase Velocity (mum/s)
K=Omega./Vp; % Reduced Wavenumber (rad/mum)

D2k=diff(K,N);
stepo=abs((Omega(1)-Omega(n))/n);

GVDs=D2k/stepo.^N; %s^2/(rad*mum)
GVD=horzcat(GVDs,GVDs(n-N)*ones(1,N)); %Group Velocity s^2/(rad*mum)
```

D.8 NOD_BBO_ne.m

Run in **FROPA_simulator_crystal.m** for the extraordinary refractive indices.

```
function [GVD,nr]=NOD_BBO_ne(Omega,N)
%%%%%%%%%%%%%%%%%%%%%%%%%%%%%%%%%%%%%%%%%%%%%%%%%%%%%%%%%%%%%%%%%%%%%%%%%%%%%%%
%Written by Derrek Wilson May 2015
%For generating the refractive index based on the Sellmeier Equations
%Omega is linearly spaced
%Data from: Zhang, et. al. Optic. Comm. 184, 485,(2000) 0.64-3.18 mum
%%%%%%%%%%%%%%%%%%%%%%%%%%%%%%%%%%%%%%%%%%%%%%%%%%%%%%%%%%%%%%%%%%%%%%%%%%%%%%%
n=numel(Omega);
c=3*10^14; %mu/s
%Sellmeir Coefficients
coeff01=2.3753;
coeff11=0.01224;
coeff12=0.01667;
coeff21=0.01627;
coeff31=0.0005716;
coeff41=0.00006305;

%refractive Index
n0=coeff01;
n1=coeff11./((2*pi*c./Omega).^2-coeff12);
n2=-coeff21*(2*pi*c./Omega).^2;
n3=coeff31*(2*pi*c./Omega).^4;
n4=-coeff41*(2*pi*c./Omega).^6;
nr=sqrt(n0+n1+n2+n3+n4);

```

```
26 Vp=c./nr; % Phase Velocity (mum/s)
27 K=Omega./Vp; % Reduced Wavenumber (rad/mum)
28
29 D2k=diff(K,N);
30 stepo=abs((Omega(1)-Omega(n))/n);
31
32 GVDs=D2k/stepo.^N; %s^2/(rad*mum)
33 GVD=horzcat(GVDs,GVDs(n-N)*ones(1,N)); %Group Velocity s^2/(rad*mum)
```

D.9 GV_.m

Run in **FROPA_simulator_crystal.m** for group velocity and GVD.

```
1  function [GVD]=GV_(Omega,nr,N)
2  %%%%%%%%%%%%%%%%%%%%%%%%%%%%%%%%%%%%%%%%%%%%%%%%%%%%%%%%%%%%%%%%%%%%%%%
3  %Written by Derrek Wilson October 2015
4  %Takes an input refractive index, nr, and writes the Group velocity for the
5  %frequency range, Omega.
6  %Omega is linearly spaced
7  %%%%%%%%%%%%%%%%%%%%%%%%%%%%%%%%%%%%%%%%%%%%%%%%%%%%%%%%%%%%%%%%%%%%%%%
8  c=3E17;%nm/s
9  n=numel(Omega);
10 Vp=c./nr; % Phase Velocity (nm/s)
11 K=Omega./Vp; % Reduced Wavenumber (rad/nm)
12
13 D2k=diff(K,N);
14 stepo=abs((Omega(1)-Omega(n))/n);
15
16 GVD=D2k/stepo.^N; %s/(rad*nm)
17 end
```

D.10 Gaussian.m

Run in **FROPA_simulator_laser.m** for the Gaussian beam profile.

```
1  function [Guass,Rz] = GaussianBeamGenerator_2(r,z,lambda,w0,zr)
2
3  wz = w0*sqrt(1+(z/zr).^2);
4
5  Rz = z.*(1+(zr./z).^2);
6
7  phiz = atan(z/zr);
8
9  k = 2*pi/lambda;
10
11 for m=1:length(r)
12
13     for j=1:length(z)
```

```
14              if z(j) == 0
15               Guass(m,j) =exp(-(r(m)/w0).^2);
16              else
17              Guass(m,j) = w0./wz(j).*exp(-r(m).^2./wz(j).^2).*exp(-1i*k*r(m).^2./(2*Rz(j))).*exp(-1i*phiz(j));
18              end
19
20          end
21
22  end
```